Late burial, hydrothermal dolomitization of the Cambrian Láncara Fm., Cantabrian Zone (NW Spain): origin of the dolomitizing fluids and relation to the geodynamic setting

Fabio Lapponi

Late burial, hydrothermal dolomitization of the Cambrian Láncara Fm., Cantabrian Zone (NW Spain): origin of the dolomitizing fluids and relation to the geodynamic setting
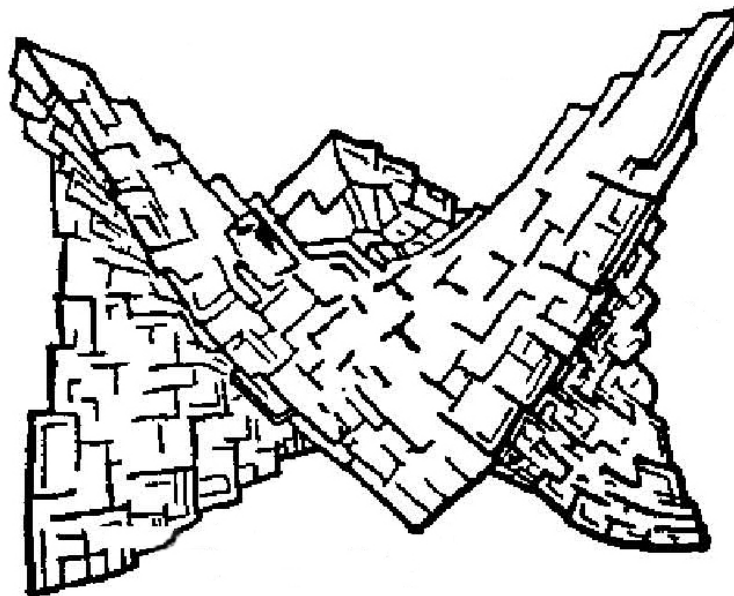
Inaugural-Dissertation

zur Erlangung der Doktorwürde

der Naturwissenschaftlich-Mathematischen Gesamtfakultät

der Ruprecht-Karls Universität Heidelberg

Vorgelegt von

Fabio Lapponi

In the front cover: saddle dolomite morphological figure (from Dana, 1955)

Gutachter: **Prof. Dr Thilo Bechstädt**

Prof. Dr. Ronald Bakker

Promotionsprüfung: 21/12/2007

Acknowledgments

Everybody wants to arrive on the peak of the mountain, but the real happiness consists on how the mountain was climbed

Table of contents

Abstract

Several petrographic and geochemical methods have been applied in order to distinguish and characterize the late epigenetic dolomitization event occurring in the Cambrian Carbonate succession of the Láncara Formation, Cantabrian Zone, NW Spain. The phenomenon is volumetrically not impressive but has a large spatial distribution, affecting different tectonic units. Furthermore, this dolomite type is petrographically similar to the volumetrically more extensive dolomite replacing the thick Namurian and Westfalian succession, which was the object of a previous Ph.D thesis (Gasparrini 2003). New data from dolomitized Carboniferous samples have also been integrated for comparison.

The contact between dolomitized and undolomitized lithologies is very sharp in the outcrops, usually crosscutting the bedding surface. The dolomitization affects mostly the calcareous members of the Láncara Formation (glauconitic packstone, birdseye limestone). Rarely, the stromatolitic dolostone, which forms the upper part of the lower member of the Láncara Formation, is also replaced by the epigenetic event.

The dolomite is fabric-destructive with only rare remnants of former sedimentary features left. At the hand specimen scale, two different generations of dolomite can be easily distinguished: a matrix-replacive dolomite (Dol A), which is usually grey to beige in colour, and a void-filling coarser, white saddle dolomite (Dol B). Usually, Dol B is volumetrically less important relative to matrix-replacive Dol A, but locally it may reach 30-35 % of the dolomitized bodies. The transition between the matrix-replacive Dol A and the void-filling Dol B is gradual, never corresponding to a reaction boundary. The polimodal grain size distribution allows subdivision of Dol B in different sub-generations, with the last one (Dol B II) consisting of a clear inclusion-free rim. In CL, Dol B is characterised by the same red to red-dull luminescence of Dol A, with the exception of the last Dol B II generation (the clear rim), which is non-luminescent. Millimetre-scale pores are abundant in the dolomitized bodies whereas they are practically absent in the undolomitized lithologies.

This dolomite generation has a burial origin, as indicated by coarse cristallinity, abundant saddle dolomite cement, zebra structures, high Fe-Mn concentrations and low Sr concentrations, low $\delta^{18}O$, radiogenic $^{87}Sr/^{86}Sr$ and fluid inclusions T_H between 80 and 120°C.

Raman Spectroscopy combined with microthermometry and crush-leach analyses have been applied to identify the main ion species present in individual inclusions. Eutectic and other phase change temperatures are correctly established, in addition to the identification of metastable phase assemblages that can lead to erroneous interpretation of the salinity of the fluids.

Crush-leach analyses reveal that the dolomitizing fluids are highly evaporated seawater which has been modified through water-rock interaction only at a minor degree. For comparison, crush-leach tests were performed on samples from the dolomitized Namurian and Westphalian limestones. The data reveal that a possible coeval fluid flow with similar composition affected both the Cambrian and the Carboniferous carbonate successions. It can be assumed that a local fluid source is mainly defined by the adjacent host rock; consequently, different dolomitized rock formations would reveal different fluid

systems. The similarity between dolomitizing fluids affecting the Cambrian as well as the Carboniferous limestones favours an external fluid source, which flooded both rock types.

This fluid flow event affected the Cantabrian Zone presumably during the late stages of the Variscan orogeny, as indicated by indirect geological evidences (i.e. temporal relationship with dated ore minerals and main Variscan structures). This period was characterized by an extensional tectonic regime and by a high geothermal gradient which might have favoured the onset of convective cells in the study area.

Keywords: Cantabrian Zone, fluid flow, epigenetic dolomitization, Variscan orogeny, zebra structures, saddle dolomite, hypersaline brines, fluid inclusions.

_____

Zusammenfassung

In dieser Arbeit wurden die Phasen spät-epigenetischer Dolomitisierung in der kambrischen Karbonatabfolge der Láncara Formation (Kantabrische Zone, NW Spanien) anhand verschiedener petrographischer und geochemischer Methoden unterschieden und charakterisiert. Während das Dolomitisierungsvolumen nicht bedeutsam ist, ist seine Verbreitung über verschiedene tektonische Einheiten hinweg bemerkenswert. Überdies bestehen petrographische Ähnlichkeiten zu jenen großvolumigen Dolomitvorkommen, welche die mächtigen Namur- und Westphal-Abfolgen ersetzten (vgl. Doktorarbeit Gasparrini 2003). Zum Vergleich wurden neue Daten von dolomitisierten Karbon-Gesteinen integriert.

In den Aufschlüssen ist der Kontakt zwischen dolomitisierten und nicht dolomitisierten Lithologien abrupt und verläuft meistens über Schichtgrenzen hinweg. Vor allem die kalkhaltigen Lithologien der Láncara Formation (glaukonitischer Packstone und Kalkstein mit *birdseyes*) sind von der Dolomitisierung betroffen. Örtlich ist auch der stromatolitische Dolomit, aus dem der obere Teil der unteren Láncara Formation besteht, von der epigenetischen Dolomitisierung betroffen.

Die Dolomitisierung wirkt gefügezerstörend; somit sind nur selten sedimentäre Strukturen erhalten. Schon im Handstück können zwei verschiedene Dolomitgenerationen unterschieden werden: ein grau- bis beigefarbener Dolomit, der die Matrix ersetzt (Dol A), sowie ein weißer „Satteldolomit", der in Hohlräumen Platz nimmt (Dol B). Dol B hat generell ein viel kleineres Volumen als Dol A, wobei Dol B lokal bis zu 30-35 % der dolomitisierten Gesteine ausmachen kann. Der Übergang vom matrixersetzenden Dol A zum hohlraumfüllenden Dol B ist graduell und ohne Bezug zu Reaktionsgrenzen. Dol B ist aufgrund seiner polymodalen Korngrößenverteilung in mehrere Generationen zu unterteilen, deren letzte (Dol B II) eine klare einschlussfreie Randzone des Satteldolomits ist. Unter dem Kathodolumineszenzmikroskop (CL) zeigen Dol B und Dol A die gleichen rot bis mattroten Lumineszenzfarben; nur Dol B II luminesziert nicht. Der dolomitisierte Körper ist von millimetergroßen Poren durchsetzt, die im nicht dolomitisierten Bereich fehlen.

Die Dolomitisierung hat sich während der Versenkungsphase ereignet. Dies ist aus der Grobkristallinität des Dolomits, dem häufig auftretenden Satteldolomit-Zement, den Zebra-Strukturen, den hohen Fe-Mn- und geringen Sr-Konzentrationen, dem geringen $\delta^{18}O$, dem radiogenen $^{87}Sr/^{86}Sr$ Verhältnis und den ermittelten Homogenisierungs-Temperaturen (T_H) von 80 bis 120°C zu schließen.

Durch eine Kombination von Raman-Spektroskopie, Mikrothermometrie und *crush-leach* Analysen wurden die wichtigsten Ionenspezies individueller Flüssigkeitseinschlüsse bestimmt. Desweiteren wurden die Eutektika und weitere Phasenübergangs-Temperaturen bestimmt, sowie metastabile Paragenesen identifiziert, die zur falschen Interpretation der Salinität führen können.

Die *crush-leach* Analysen zeigen, dass die Dolomitisierungfluide aus stark evaporiertem Meerwasser (gering modifiziert) bestanden. Vergleiche mit *crush-leach* Daten von Namur- und Westphal-Kalksteinen führten zur Annahme, dass sowohl die kambrischen als auch die karbonischen Karbonatabfolgen von Fluiden ähnlicher Zusammensetzung alteriert wurden. Es wird eine externe

Zusammenfassung

Fluidquelle, die beide Einheiten gleichzeitig durchströmte, bevorzugt. Es kann nicht davon ausgegangen werden, dass die jeweils lokalen Nebengesteine die Fluidquellen waren, da die unterschiedlichen Lithologien unterschiedliche Fluidsysteme generiert hätten.

Der Fluidfluss in der Kantabrischen Zone, der zur Dolomitisierung führte, ereignete sich in der Spätphase der Variszischen Orogenese. Dies ist aus indirekten geologische Indizien zu schließen ist (z.B. enge zeitliche Beziehung zu datierten Erzmineralen). Das extensionale tektonische Regime und der hohe geothermische Gradient während dieser orogenen Spätphase waren möglicherweise Voraussetzung für die Entwicklung von Fluidkonvektionszellen im Arbeitsgebiet.

Schlüsselwörter: Kantabrische Zone, Fluidfluß, epigenetische Dolomitisierung, Variszische Orogenese, Zebrastrukturen, Satteldolomit, salzreiche Laugen, Fluideinschlüsse

Chapter 1 - Introduction

1.1. Aim and approach of the study

The main subject of this study are the processes responsible for a late stage dolomitization which affected large volumes of rocks of Cambrian age, the Láncara Formation, in the Cantabrian Zone, NW Spain.

The study has a multidisciplinary approach which combines petrographic and geochemical methods, in order to better understand the genesis of the dolomite bodies and the origin of the dolomitizing fluids. Analyses on trace elements (particularly Fe, Mn, Sr), stable (O and C) and radiogenic (Sr) isotope composition have been carried out on different dolomite phases, in order to constrain the physical and chemical environment in which the dolomite formed. The dolomitizing paleofluids, preserved inside the dolomite crystals as fluid inclusions, have been analysed by classical fluid inclusion petrography and microthermometry techniques and more sophisticated analytical techniques. In particular, the combination of Raman spectroscopy and low temperature microthermometry has been an extremely powerful non-destructive technique in order to investigate the low temperature behaviour of the fluid inclusions and individuate and correctly interpret the different stable and metastable phase changes into the fluid inclusions, which are usually difficult to observe with standard microthermometry studies. Quantification of the major and minor trace elements present in the fluid inclusions was possible by means of chemical analyses of the fluids liberated after crush-leach of the inclusions. In particular, the ratios between conservative (Br) and non-conservative (Cl) elements gave important information about the origin and the evolution of the formation waters. Crush-leach analyses were carried out not only for the samples of the dolomitized Láncara Formation carbonates (Cambrian) but, for comparison, also for dolomitized Barcaliente and Valdeteja Formations (Carboniferous).

In addition to the Láncara Formation, also the Carbonifeorous Barcaliente and Valdeteja Formations were intensely dolomitized. The dolomitization event affecting the latter two formations was the object of a previous study (Gasparrini 2003). A comparison between the two data sets was carried out in order to detect possible similarities and eventually to relate the two dolomitization processes to a single fluid flow event. When necessary, the data from the Barcaliente and Valdeteja Formations were integrated with new data obtained from different methodologies.

The timing of the dolomitization event was deduced from the direct field observation of the temporal relationship between the dolomitized bodies and the Variscan structures and the age derived from uranium bearing ore minerals occurring in the same district. The results were integrated into the geological setting of the Cantabrian Zone at the time of dolomitization.

This study gives a better insight into the origin and the composition of the fluid responsible for regional dolomitization of carbonate platforms as well as the hydrological regime which characterized the Cantabrian Basin during the latest stage of the Variscan orogeny.

1.2. The dolomite problem

Since Deódat de Dolomieu gave the first description of a rock consisting chiefly of the mineral dolomite (Dolomieu 1791), the origin of this mineral has attracted the attention of earth scientists. After 200 years of intense research, many hydrological and geochemical conditions of the formation of dolomite are still poorly understood (Machel 2004).

In 1957, Fairbridge pointed at the complexity of the dolomitization process, later called "dolomite problem" by McKenzie (1991). The core of the "problem" consists of the fact that dolomite, despite being the second most abundant carbonate mineral (after calcite) in the sedimentary record, is rare in modern marine depositional environment. Although normal seawater is supersaturated with respect to both dolomite and calcite, precipitation of dolomite is inhibited by several kinetic factors.

Dolomite is generally considered a diagenetic phase, forming in the subsurface, at depths starting from only few centimetres below the surface, down to several kilometres. Dolomite directly precipitates as cement from pore fluids but the volume of dolomite formed in such a way probably represents only a minor part. Most of the ancient massive dolomitic bodies, occurring in the sedimentary record, have been interpreted as secondary, as replacement of a previous calcium carbonate (Morrow 1990a, Tucker and Wright 1990, Purser et al. 1994a).

Dolomite is a highly ordered mineral that is very difficult to precipitate in laboratory experiments under common P-t diagenetic conditions. Consequently, the physical and chemical controls on dolomite precipitation are extrapolated from high temperature experiments (Gaines 1980, Morrow 1990a, Usdowsky 1994).

The solution of the problem of the dolomite formation is not only a very fascinating academic task. In carbonate systems dolomite often constitutes one of the best reservoirs for oil and gas as well as for base metals (MVT ore deposits). Dolomitization of carbonate sediments usually increases crystal size and pore throat size and decreases roughness, resulting in a permeability increase. In addition, dolomite is less reactive than calcite, so dolomitic units are more resistant to porosity loss by diagenesis and re-crystallization than limestone. In particular, structurally-controlled hydrothermal dolomite reservoir are major hydrocarbon producers in North America and are receiving increasing attention globally over the last 25 years (Davies and Smith 2006). Dolomite reservoirs developed along structural lineaments are exemplified by the Ordovician-hosted Lima-Indiana and Albion-Scipio fiends of the north-western United States (Huley and Burdos 1990, Wickstrom et al. 1992, Wickstrom 1996). The hydrologic systems that dolomitize a limestone control the geometry of the dolomite bodies. A firm understanding of the dolomitization process plays a crucial role in the recognition and the delimitation of dolomite reservoirs.

1.3. Dolomite terminology

The term dolomite refers to the mineral whose ideal formula is $CaMg(CO_3)_2$, whereas the dolostone is a rock composed for more than 75% by dolomite crystal. The term "hydrothermal", which is often associated to dolomite to describe a paragenetic phase forming at high temperature (>100°C), is more contradictory, as pointed out by Machel and Lonnee (2002). These authors recommended the definition proposed by White (1957, p.1638): "of or pertaining to any water that is appreciably warmer (5°C or more) than the surrounding environment". The term "hydrothermal" dolomite should be restricted to mineral products emplaced into a host formation at temperature higher than the ambient temperature of the host. It represents evidence to a geothermal anomaly and requires a mechanism or conduit for fluid movement.

The term *saddle dolomite* (Dana 1955, Radke and Mathis 1980, Gregg 1883, Barber et al. 1985, Searl 1989, Kretz 1992) indicates a particular type of dolomite characterised by curved crystal faces and wavy extinction. This morphology is commonly considered an indicator of hydrothermal dolomitization (Davies and Smith 2006), but it is not necessary diagnostic of a hydrothermal setting (Machel 1987).

1.4 The dolomite chemistry

1.4.1. Dolomite crystallography

The crystal of dolomite has a symmetry structure 3 in the trigonal subsystem of the hexagonal crystallographic system. The unit cell is a rhombohedron elongated parallel to the c crystallographic axis, similar to that of calcite but more highly ordered, and has a lower degree of symmetry. Like calcite, the dolomite crystal is built up of cation layers (Ca^{2+} and Mg^{2+}) alternating with anions (CO_3^{2-}) perpendicular to the c axis direction, with the distinction that half of the cation layers consist of magnesium that regularly alternate with calcium (Fig. 1.1). Dolomite crystals are better represented by the formula

$$Ca_{(1+x)} Mg_{(1-x)} (CO_3)_2 \qquad (1.1)$$

Ideal, stoichiometric dolomite

Carbonate   Magnesium   Calcium

Fig. 1.1. Ideal stoichiometric structure of the dolomite crystal, built up of a regular repetition of layers of Ca^{2+} and Mg^{2+}, alternating with anions of CO_3^{2-}.

However, dolomite crystals commonly depart from the ideal composition and structure by the degree to which calcium and magnesium are segregated into the respective layers. Most natural dolomites display a degree of mixing of calcium and magnesium between cation layers, which does not affect the composition. Dolomite departs from the stoichiometric composition because of an excess of calcium which is accommodated in the magnesium layers and, less commonly, for an excess of magnesium. Furthermore, a multitude of cations, primarly Fe, Sr, Na, Mn, substitutes for calcium in many dolomites; iron in particular can be present in concentrations up to 4-5 mole % in ferroan dolomite.

Intracrystalline variations in composition and degree of order are also common, above all in larger crystals; there are some evidences that compositional variations have influenced the shape of the coarse crystals with curved faces ("saddle" type) that are common in some late diagenetic dolostones (Radke and Mathis 1980). The degree of disorder and the departure from the stoichiometric composition also affect the unit cell dimensions and the solubility of dolomite (Land 1980).

1.4.2. Dolomitization reactions

The condition of dolomite formation is difficult to determine in the laboratory as dolomite does not experimentally precipitate at low temperature from natural waters. For direct precipitation one can write

$$Mg^{2+} + Ca^{2+} + 2CO_3^{2-} \Leftrightarrow CaMg(CO_3)_2 \qquad\qquad (1.2)$$

The equilibrium constant, derived from the activities of the dissolved and crystalline species, is not precisely known for low temperature and can be approximated to $1*10^{-17}$ (Hsü 1967). Knowing approximately the ion activities of Mg^{2+}, Ca^{2+} and CO_3^{2-} of seawater, the equilibrium constant shows that normal seawater is supersaturated with respect to dolomite by nearly two orders of magnitude (Lippmann 1973). However, for kinetic reasons outlined below, dolomite rarely precipitates out of normal seawater; most dolomite forms preferentially by replacing $CaCO_3$ (dolomitization). Under a wide range of surface and near-surface environment, dolomite is thermodynamically favoured over co-existing calcite: the dolomitization reaction, as it is commonly expressed (Bathurst 1975)

$$2CaCO_3 + Mg^{2+} \Leftrightarrow 2(Ca,Mg)\,CO_3 + Ca^{2+} \qquad\qquad (1.3)$$

This reaction is characterized by a free energy change of $\Delta_r G° = -7.66$ kJ/mole, for the transition from aragonite to dolomite with an ideal composition and structure, which means that this reaction has a thermodynamic drive to dolomite under standard conditions and unit molar concentrations.

It is possible that a part of the CO_3^{2-} does not derive from the dissolution of $CaCO_3$ but is supplied from an external source; according to this idea another reaction has been proposed (Lippman 1973):

$$CaCO_3 + Mg^{2+} + CO_3^{2-} \Leftrightarrow Ca,Mg(CO_3)_2 \qquad\qquad (1.4)$$

which is thermodynamically more favourable than reaction (2). This formula has also the advantage that the calcium liberated by dissolution of $CaCO_3$ is completely removed from solution whereas reaction (2) poses the problem of Ca^{2+} removal, which would increase the Ca/Mg ratio and lower the thermodynamic drive toward dolomitization if present at the reaction site (Morrow 1990a).

1.4.3. Origin of magnesium

Dolomitization, like the other diagenetic reactions, is entirely a chemical wet process; solid state reactions between carbonates in absence of an aqueous phase proceed prohibitively slowly at temperatures lower than several hundred degrees Celsius.

The magnesium in the dolomitization reactions is necessarily supplied in solution from an external source. The only abundant source of Mg^{2+} ions for early diagenetic surface or near-surface dolomitization is seawater. It contains 1290 ppm Mg and 411 ppm Ca, a Mg/Ca weight ratio of 3.14 and a molar ratio of 5.2. Land (1985) has calculated that in order to dolomitize a cubic meter of a typical Recent marine carbonate sediment (i.e. 40% porosity, 6.3 mole % $MgCO_3$) would require around 650 pore volumes of seawater. If seawater is diluted with meteoric water, then the volume needed increases dramatically (6500 pore volumes for seawater diluted 10 times). Much less water is needed if seawater is evaporated; at halite saturation only 30 pore volumes are required. Without an external source of Mg^{2+}, the amount of dolomite that can form is very limited, being dependent on the amount of high Mg calcite present.

Many diagenetic brines are mixtures of meteoric and marine waters modified by burial processes. They are commonly supersaturated with respect to dolomite even when undersaturated with calcite. Very dilute solutions are undersaturated with both phases. The dolomite-calcite equilibrium is shifted towards higher Ca/Mg ratios at higher temperature (Rosenberg and Holland 1964). The increase of temperature during progressive burial in sedimentary basins will increase the saturation level of dolomite with respect to that of calcite in solution with constant Ca/Mg ratios.

1.4.4. A kinetic problem

Several kinetic factors impede the precipitation of dolomite from supersaturated solutions. These are

(1) rapid crystallization rate of non-dolomite carbonate minerals from supersaturated, concentrated solutions;

(2) pronounced differences in the hydration behaviour in aqueous solution of the constituent ions of dolomite, promoting precipitation of calcium-rich phases;

(3) the low activity or concentration of CO_3^{-2} relative to Ca^{+2} or Mg^{+2} in most natural solutions, which strongly inhibits the precipitation of magnesium-bearing carbonate minerals in general.

The speed of crystallization influences the degree of order because ions that adhere to incorrect lattice positions on the surfaces of rapidly growing crystals are more likely to be entombed in these positions.

The strength of the electrostatic ion of magnesium to water molecular bond is about 20% greater than that of calcium and much greater than that of the carbonate ion. Calcium carbonates, which are less strongly hydrated, are more readily incorporated into growing Ca-Mg carbonates and will tend to occupy sites in the Mg layers as well. Another important kinetic effect, related to the strength of the magnesium ion hydratation sheath, is the inability of the carbonate ions to come in contact with the crystal surface breaking through the hydration barrier; only a part of the CO_3^{-2} in solution has sufficient energy of motion.

Consequently, the three parameters affecting the kinetic of the growth of the dolomite crystals are the **Ca^{+2}/Mg^{+2} ratio**, the **salinity** and the **CO_3^{-2}/Ca^{+2} ratio**. These three parameters can be plotted in a block diagram (Fig. 1.2); the boundary between calcite and dolomite is shown as a plane.
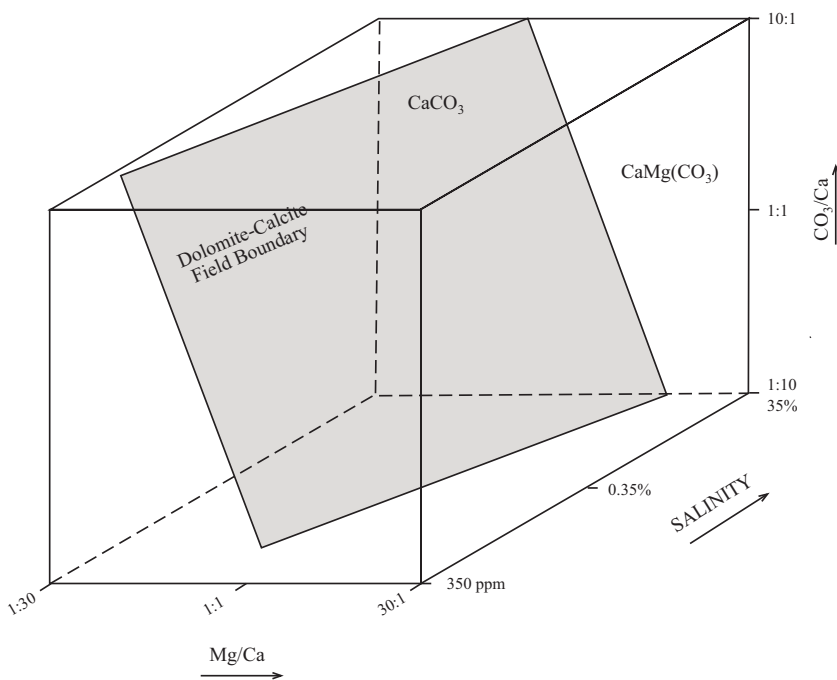
Fig. 1.2. Block diagrams showing the effect of changing the parameters Mg/Ca ratio, salinity and CO₃/Ca ratio. The plane represents the calcite/dolomite kinetic boundary (redrawn after Morrow 1988).

A solution in the calcite field can move into the dolomite field by increasing the Mg/Ca ratio, decreasing the salinity and increasing the CO_3^{-2} content. An increase in the Mg/Ca ratio favours the uptake of magnesium into a precipitating carbonate. The disordering effect caused by rapid precipitation may be overcome by a reduction in the rate of precipitation by dilution of these solution.

Mixing a wide variety of solution compositions can induce limestone dissolution; however it is less clear if this could directly induce dolomitization. Dolomitization may take place in solutions that are saturated or supersaturated in both phases in geological settings such as sabkhas or evaporitic lagoons, because of an appropriate increase of the Mg/Ca ratio through the precipitation of gypsum. Dilution of saline brines favours dolomite precipitation simply because of the kinetic effect of the attendant decrease in the rate of precipitation.

High CO_3^{-2} activity promotes dolomitization, as confirmed by several experimental studies (Liebermann 1967, Lippmann 1968, Davies et al. 1977). Sources of naturally occurring alkaline solutions containing high CO_3^{-2} concentrations include continental ground water that have been

involved in the weathering of siliceous rocks or that have dissolved continental alkali-rich minerals, or marine and continental waters that have been involved in anaerobic bacteria sulphate reduction. Generation of the CO_3^{-2} by anaerobic sulphate reduction may occur in many burial environments from depth less than one meter to several hundreds of meters below the sediment-water interface. This process has been suggested as a factor in the dolomitization of some Recent burrow fillings (Brown and Farrow 1978). A supply of SO_4^{-2} is probably necessary because the initial rise in the alkalinity will precipitate $CaCO_3$ before proceeding to dolomitization (Lippman 1973).

The presence of certain cations, such as lithium and possibly iron, has a catalytic effect on the precipitation of dolomite (Carpenter 1980, Gaines 1980). Because the proportion of strongly hydrated Mg ions decreases with increasing salinity, dolomitization should be favoured by high salinity

Fig. 1.3. Calculated equilibrium of Ca-Mg activity ratios as a function of temperature for calcite plus dolomite using thermodynamic data from Robie at al. (1978). Redrawn after Carpenter (1980).

(Carpenter 1976); it appears that the dolomites formed under conditions of higher salinity and higher solution Mg/Ca ratios tend to be less calcium-rich and hence more stoichiometric (Füchtbauer and Goldschmidt 1965; Glover and Sippel 1967). The degree of disorder introduced by the faster rate of precipitation from more saline solutions (see above) overshadows the effect of the diminution of the hydration barrier of the Mg ions with increasing salinity so that, although the Ca/Mg carbonates that are formed approach a dolomite composition, they tend to be disordered (Glover and Sippel 1967, Folk and Land 1975, Morrow 1978).

The temperature increase that occurs with burial is of dominant importance; it probably reduces the kinetic inhibition to dolomitization and cause dolomite to become more saturated relative to calcite (Fig. 1.3). The amount of dolomite formed will depend on the rate with which magnesium is provided and the time available.

1.5. Dolomitization models

In order to dolomitize a limestone, two requirements are essential:

1) a source of Mg;

2) a transport mechanism able to carry the Mg to the site of dolomitization.

Mass balance calculation indicates that hundreds of pore volumes of fluids must be exchanged in order to complete the dolomitization reaction (Land 1980).

The main dolomitization models proposed in the literature are briefly described in this paragraph: They represent substantially hydrological models that try to predict an efficient mechanism for pumping Mg-rich fluids into carbonate formations.

1.5.1. Near surface models

Most dolomites at the present time form in or near hypersaline environments from highly evaporated seawater with an elevated Mg/Ca ratio (Shinn et al. 1965, Shinn 1968, Deffeyes et al. 1965). Precipitation of gypsum and anhydrite can preferentially remove Ca from seawater while leaving the Mg concentration unchanged. **Sabkha dolomite** (Fig. 1.4A) forms where storm surges force seawater landward over peritidal sediments in arid regions (McKenzie et al. 1980, Patterson and Kinsman 1982). Evaporation results in the precipitation of evaporites. The increased density of the brines concentrated by evaporation forces them to flow downward and dolomitize the underlying sediments. Sabkha dolomites are usually easy to identify because they are always associated with supratidal sediments and contain many different distinctive features such as algal stromatolites, nodular anhydrites and eolian interbeds.

Reflux dolomites (Fig. 1.4B) form beneath restricted lagoons and basins where evaporation is intense and leads to brine concentration and evaporate precipitation. The model was applied by Adams and Rhodes (1960) to account for the dolomitization of the Permian Reefs of West Texas. The Zechstein (Upper Permian) dolomites of Northwest Europe have been interpreted as seepage-reflux in origin by Smith (1981) and Clark (1980). Downward and seaward density-driven flow of brines once again leads to dolomitization of underlying sediment, which in this case are not exclusively supratidal but can represent any depositional facies.

The **marine-meteoric mixing zone model** (Fig. 1.4C) is based on the idea that mixing meteoric water with sediments produces a fluid that is undersaturated with respect to calcite and supersaturated with respect to dolomite (Folk and Land 1975). The Mg is supplied by seawater and the hydrodynamic head provides the hydrologic pump. This model has been invoked to explain ancient dolomite sequences not associated with evaporites but the model has received much criticism in part related to the lack of dolomitization in all but a few modern mixing zone environment (Land 1985, Machel and Mountjoy, 1986, 1987, Hardie 1987).

_____

Strong evidence for dolomitization by seawater (Fig. 1.4D) has been proposed in many recent papers (Carballo et al. 1987, Land 1991). Seawater is supersaturated with respect to dolomite, more than any other meteoric water-seawater mixture. For the **normal seawater model**, the Mg is delivered either by tidal pumping or by inflow and buoyant rise of geothermally heated seawater at continental margins.

1.5.2. Subsurface models

Geochemical and petrographical evidence supports the hypothesis that many of the massive dolomite successions might have formed in the subsurface after lithification (burial dolomite). As temperature increases, kinetic requirements for dolomitization are more easily satisfied and the many subsurface brines may become dolomitizing solutions. These burial, subsurface dolomites are usually referred as "hydrothermal" in the literature, although this term is ambiguous and has no precise definition, as previously discussed (see paragraph 1.3). In general, hydrothermal dolomites are considered to consist of a large proportion of open-space filling dolospar cements within breccia bodies, fractures and large vugs, commonly associated to subsurface replacement dolomites (Drivet and Mountjoy 1997).

Mattes and Mountjoy (1980), Zenger (1983), Mountjoy and Amthor (1994) have shown a widespread replacement of limestones at burial depth estimated to be in the order of at least 1000 m. The most cited fluid sources for burial dolomitization are Mg-rich residual evaporite brines, modified seawater and shale compaction waters. The fluids can be delivered to the dolomitization site through porous aquifers or along faults by a number of transport mechanism, including squeezing due to sediment compaction, thermal convection and topographically or tectonically driven flow.

The **topographic recharge model** (Graven and Freeze 1984a and b) and the **tectonically driven compaction flow model** (Oliver 1986), have the potential to explain many laterally extensive dolomite bodies. In the topographic recharge model (Fig. 1.4E), the elevated topography of the thrust belt provides the hydrodynamic potential for gravity-driven meteoric fluids to circulate rapidly into the foreland basin, in front of the thrust belt, across distances of several hundreds of kilometres. This model has been applied by Garven (1985) to explain the Pine Point Pb-Zn deposit in the Middle Devonian carbonates of the Keg River Barrier during the post-Cretaceous rise of the Rocky Mountains. Also the MVT deposits of the Late Permian of the US mid-continent (such us the Viburnum Trend) have been explained with the same model (Garven et al., 1993): the Knox dolomite was considered the aquifer and the Ouachita Fault Belt the topographic recharge area.

Tectonic loading and compression during the development of orogenic thrust belts (**tectonic compression model**, Fig. 1.4F) may cause expulsion of formational fluids outward into the foreland basins (Oliver 1986). The thrust belt behaves like a giant "squeeze" and can represent a contributing factor (Qing and Mountjoy 1994, Montañez 1994, Machel et al. 1996), or the dominant driver (Amthor et al. 1993, Drivet and Mountjoy, 1997) for the fluid movement responsible for the emplacement of some regional subsurface dolomites.

Free convection in subsurface sedimentary settings is driven by buoyancy forces related to temperature and salinity gradients **The thermal convection model** (Wood and Hewett 1982, Wilson et
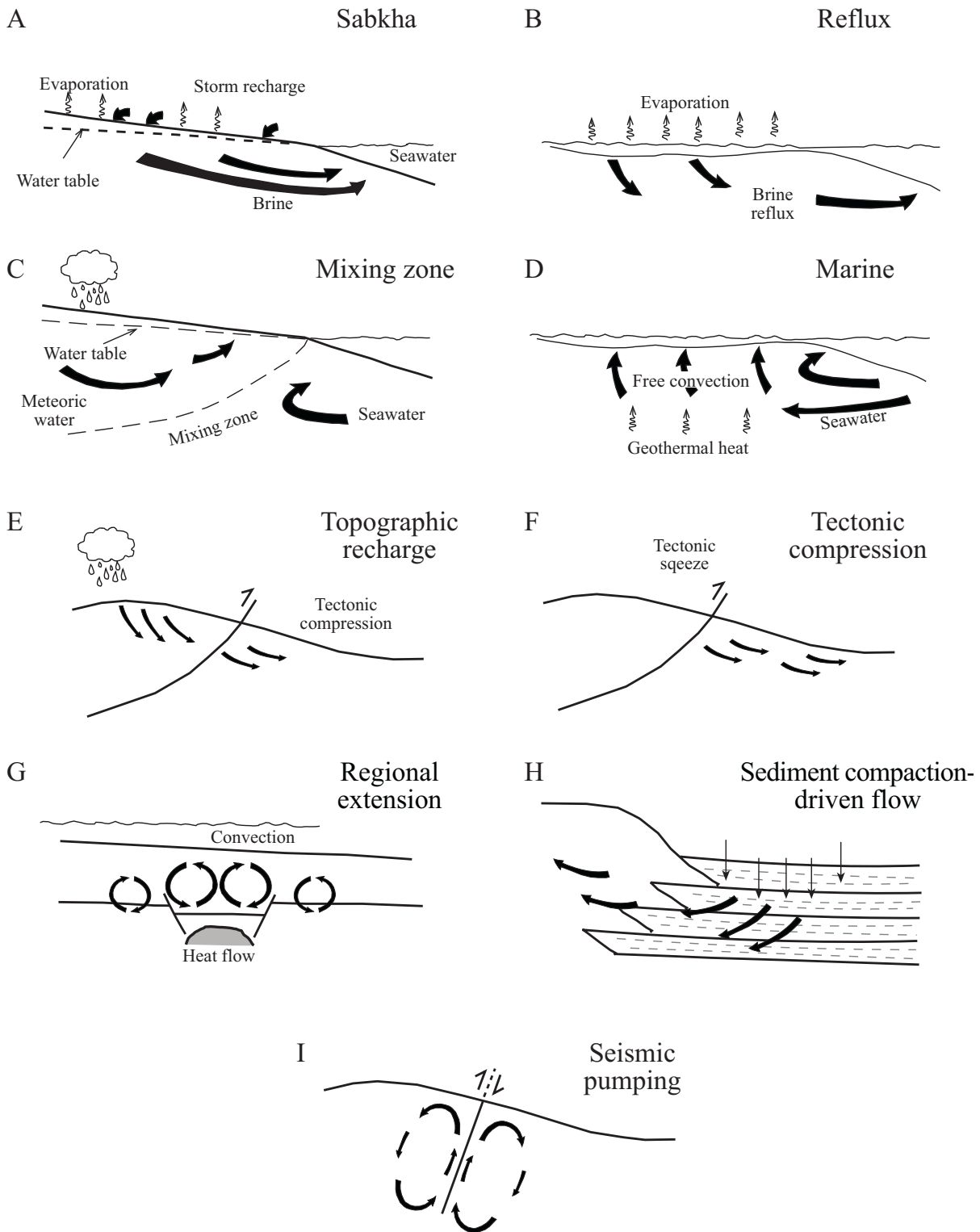
Fig. 1.4. Illustration of the different hydrologic models typical of dolomitizing environments: (A) sabkha model, (B) reflux model, (C) marine-meteoric mixing zone model, (D) normal seawater model, (E) topographic recharge model, (F) tectonically driven flow model, (G) free convection cell flow model, (H) sediment compaction flow model, and (I) seismic pumping fluid flow model. See text for explanation.

al. 2001, Fig. 1.4G) received less attention in comparison with the other models, due to the fact that several recent basinal settings seem to be dominated by topographic recharge mechanism, as in Western Canada Sedimentary Basin and the U.S. Mid Continent (Garven 1995). It is well known, however, that free convection in subsurface sedimentary settings can be driven by buoyancy related to temperature and salinity gradients. In many cases a magmatic intrusion was invoked as the main heat source for the onset of the convective cells (Morrow et al. 1990, Spencer-Cervato et Mullis 1992, Coniglio et al. 1994, Morrow and Aulstead 1995, Wendte et al. 1998). Some Mesozoic carbonate build-ups of northern Italy may represent examples of hydrothermal dolomitization by convection of sea water on a regional scale (Wilson et al. 1990; Cervato 1990).

The **sediment compaction model** (Illing 1959, Fig. 1.4H) has never become very popular. It is local in scope because of the limited supply of fluids available for dolomitization (Machel and Mountjoy 1986). According to this model, seawater, or its subsurface derivates buried along with the sediments, are pumped through the rocks as result of compaction dewatering.

The **seismic pumping hydrologic model** (Fig. 1.4I, Garven 1995, Machel 2004) is also local in scope but it may provide a very efficient way of focussing big amount of hydrothermal fluids into relatively small volumes of limestone. The dolomitized rock bodies usually are limited to plumes in the vicinity of faults and fractures, but the process may be also effective on a basinal scale, eventually combined with other hydrological models, i.e. free convection.

1.6. Secular distribution of dolostones

In young carbonate platforms, such as the Bahamas Banks, rocks younger than Pliocene are almost devoid of dolomite. This absence has been explained as a result of the reduced amount of time during which the limestone has been in contact with seawater (Nordeng and Silbey 2003). The relative abundance of dolostones that originated by replacement of marine limestones appears to have varied cyclically through time. Maxima of early diagenetic replacive dolomite occurred during Early Ordovician-Silurian and Early Cretaceous (Given and Wilkinson 1987). The reasons of these secular variations in the abundance of dolostones during Phanerozoic time are very debated. Several explanations have been proposed, including relationship with plate tectonics which changed the atmosphere and seawater composition, i.e. increase of atmospheric CO_2, high eustatic sea levels, decrease of the saturation state of calcite relative to dolomite, changes in the Mg/Ca ratio or decrease of the atmospheric O_2 levels which coincided with enhanced rates of bacterial sulphate reduction (Stanley and Hardie 1999, Burns et al. 2000 and references therein).

Several carbonate platform have been massively dolomitized by means of basinal brines during late burial diagenetic stages, tens of millions of years after the limestone deposition; two examples are the Upper Devonian carbonate successions of the West Canadian Sedimentary Basin and the Triassic succession of the Dolomites in Northern Italy. The absolute age of formation of these dolostones is not easy to be inferred, due to the lack of radiometric dating methods which can be directly applied to dolomite. Geological evidence supports the hypothesis that these dolomitization events are related to a

particular tectono-thermal evolution of the sedimentary basins, which favoured the onset of hydrothermal fluid flow into the sedimentary succession. The spatial association between intensely dolomitized rocks and hydrothermal mineralizations (such as the Mississippi Valley Type Pb-Zn deposits, which are often hosted by dolomitized lithologies), point to a common origin between the two processes, which might be linked to the same hydrothermal fluid circulation system effective in the sedimentary basin as a result of particular tectonic conditions.

Chapter 2 - Geological setting

2.1. Introduction

The study area is located in the NW part of the Iberian Peninsula, within the Cantabrian Mountain Range (Fig. 2.1). The geodynamic evolution and geological characteristics of the north-western part of Iberia are briefly outlined below, with special emphasis on the episodes related to the Variscan orogeny.
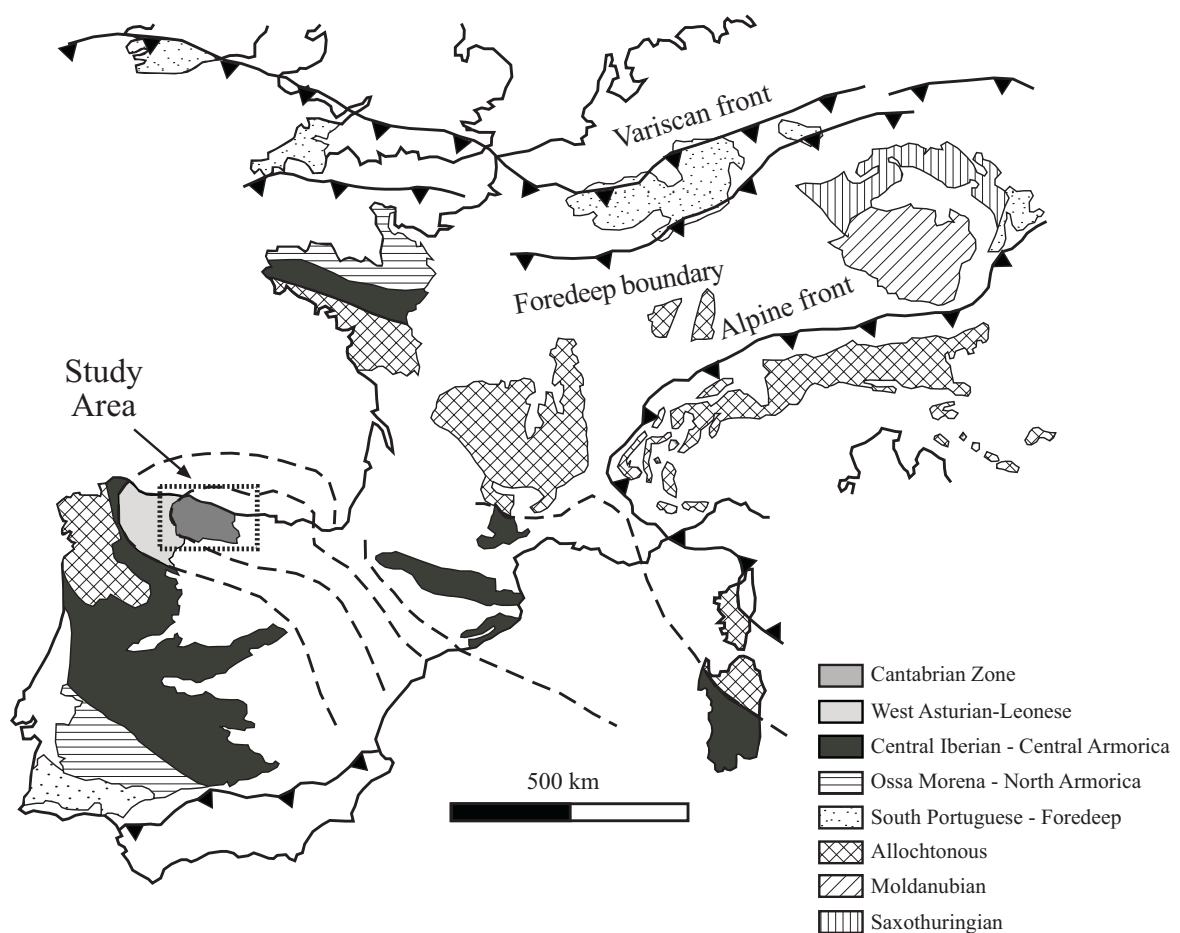
Fig. 2.1. Geological sketch of the European Variscan Belt of Western Europe (modified from Schönenberg and Neugebauer 1997). The study area is located within the Cantabrian Zone, in the Northwestern part of the Iberian Peninsula.

2.2. Geodynamic evolution of Iberia

2.2.1. Early Paleozoic

During the late Neoproterozoic/Early Paleozoic Iberia was part of the northern margin of Gondwana. An angular unconformity, which is possibly related to a Cadomian compressional deformation phase (Diéz Balda el al. 1990) or to a rifting stage connected to the opening of the Iapetus Ocean around the Precambrian to Cambrian boundary, separates the Neoproterozoic from the Cambrian sediments (Aramburu 1995).

During the Cambrian the Iberian Peninsula formed a promontory extending from the shelf of northern Gondwana. In the Late Ordovician, further extension let to the opening of the Rheic Ocean between the Avalonia Terrane and the Iberian Block (Fig. 2.2, Fernández Suárez et al. 2002, Robardet 2002, Tait et al. 1997). According to Leeder (1988), Linnemann and Heuse (2000), Matte (1991, 2001) and Tait et al. (1997) the Iberian Block was part of the Armorican terrane. These authors postulated the existence of another oceanic basin , the Galicia-Massif Central Ocean (Matte 1991) or

Fig. 2.2. Paleogeographic reconstruction of land-to-sea distribution in Europe during the Ordovician (modified from Arumburu and Bastida 1995).

Proto-Tethys, (Matte 1986, Leeder 1988) between Armorica and the margin of northern Gondwana.

The tensional tectonic regime continued during the Silurian, with the Iberian Peninsula drifting northward (Tait et al. 1997), but still belonging to the north Gondwana shelf (Robardet and Gutiérrez Marco 2002).

2.2.2. Late Paleozoic - The Variscan Orogeny

The Variscan orogeny is the consequence of the Late Paleozoic collision between two continental blocks, Gondwana in the south and Laurentia-Baltica in the north (e.g. Matte 1991, Gutiérrez Marco et al. 2002). The collision caused the closing of the Rheic Ocean and the Proto-Tethys and the amalgamation of the microplates present between the two main continental blocks.

The European Variscan Belt (the "Variscides") represents the pre-Mesozoic basement of large parts of western Europe, including Portugal and western Spain (the so called Iberian Massif) (Fig. 2.1). The Variscan deformation was contemporaneous with the Acadian orogeny in the United States, which gave rise to the Appalachian Mountains.

The Rheic Ocean possibly closed during the Late Devonian (Tait et al. 2000). The continental collision took place around 380 Ma (Eifelian-Givetian), as indicated by crustal melting in Brittany, Massif Central and southern Spain (Windley 1995). The subduction probably started in south-western Iberia and then moved progressively to the north-east (Dias and Ribeiro 1995), as indicated by the I-type magmatism north and east of the suture zone (Ribeiro et al. 1990). The collision was the result of a crustal wedge moving to the north and the north-west (Dias and Ribeiro 1995, Matte 1986, 1991), with a predominance of a sinistral transpressive strike-slip system.

Another theory, proposed by Matte (1991), includes the symmetrical subduction of opposite lithospheric plates, with deformation and metamorphism migrating northward and southward from the suture toward the forelands.

2.2.3. The Iberian Massif

The Iberian Massif is the westernmost exposure of the European Variscides in the Iberian Peninsula and represents the largest tectonic element of the Armorican plate. Lotze (1945) distinguished six different domains in the Iberian Massif, based on differences in facies, structure, metamorphism and magmatism. This subdivision, which was subsequently modified by Julivert et al. (1972), includes, from northeast to southwest, the following zones (Fig. 2.1):

1. **Cantabrian;**
2. **West Asturian-Leonese;**
3. **Central Iberian;**
4. **Ossa-Morena;**
5. **South Portuguese**

The Cantabrian, West Asturian-Leonese and Central Iberian Zones occupy the autochthonous position relative to the chain suture and have the thrust and fold vergence predominantly towards the north, the Ossa-Morena and South Portuguese zones are characterized by thrusts and folds whose vergence is predominantly towards the south (e.g. Silva et al. 1990, Apalategui et al. 1990).

2.3. The Cantabrian Zone

The Cantabrian Zone (Fig. 2.3) constitutes the most external part of the Iberian Massif and occupies the core of the so-called Ibero-Armorican Arc, defined by the trace of the Variscan structure. It represents the foreland thrust-and-fold belt and it is characterized by a thin-skinned type geometry complicated by its arcuate shape.

In the Cantabrian Zone, the Variscan deformation took place practically without metamorphism. Penetrative cleavage is generally absent.

The western boundary of the Cantabrian Zone corresponds to the boundary to the more internal zone of the orogen (the West Asturian-Leonese Zone) and is represented by Precambrian rocks forming an antiform structure (the Narcea Antiform). The other boundaries are constituted by Meso-Tertiary rocks in the south and east and by the Cantabrian Sea (Golf of Biscay) in the north.

2.3.1.Tectono-stratigraphic evolution

The Cantabrian Zone is characterized by an incomplete and comparatively thin Cambro-Ordovician sedimentary sequence, a Siluro-Devonian succession which is complete in the west and absent in the east, and a very well developed Carboniferous sequence.

From the stratigraphic point of view, the Cantabrian Zone (Fig. 2.3) can be divided into two areas (Pérez-Estaún 1990):

1) **the Asturian Leonese Domain** (not to be confused with the West Asturian-Leonese Zone);

2) **the Palentian Domain**.

The Asturian Leonese Domain comprises the following allochthonous tectonic units (Julivert 1971, Pérez-Estaún et al. 1988):

1) **Somiedo-Correcilla Unit;**
2) **Sobía-Bodon Unit;**
3) **Aramo Unit;**
4) **Central Coal Basin Unit;**
4) **Ponga Unit;**
5) **Picos de Europa Unit.**

The Palentiane Domain corresponds to the Pisuerga-Carrión Unit (Julivert 1971) and has been interpreted as an allochthonous unit coming from the West Asturian-Leonese Zone (Marcos 1979, Frankenfeld 1983, Marquínez and Marcos 1984, Rodríguez Fernández et al. 1985).
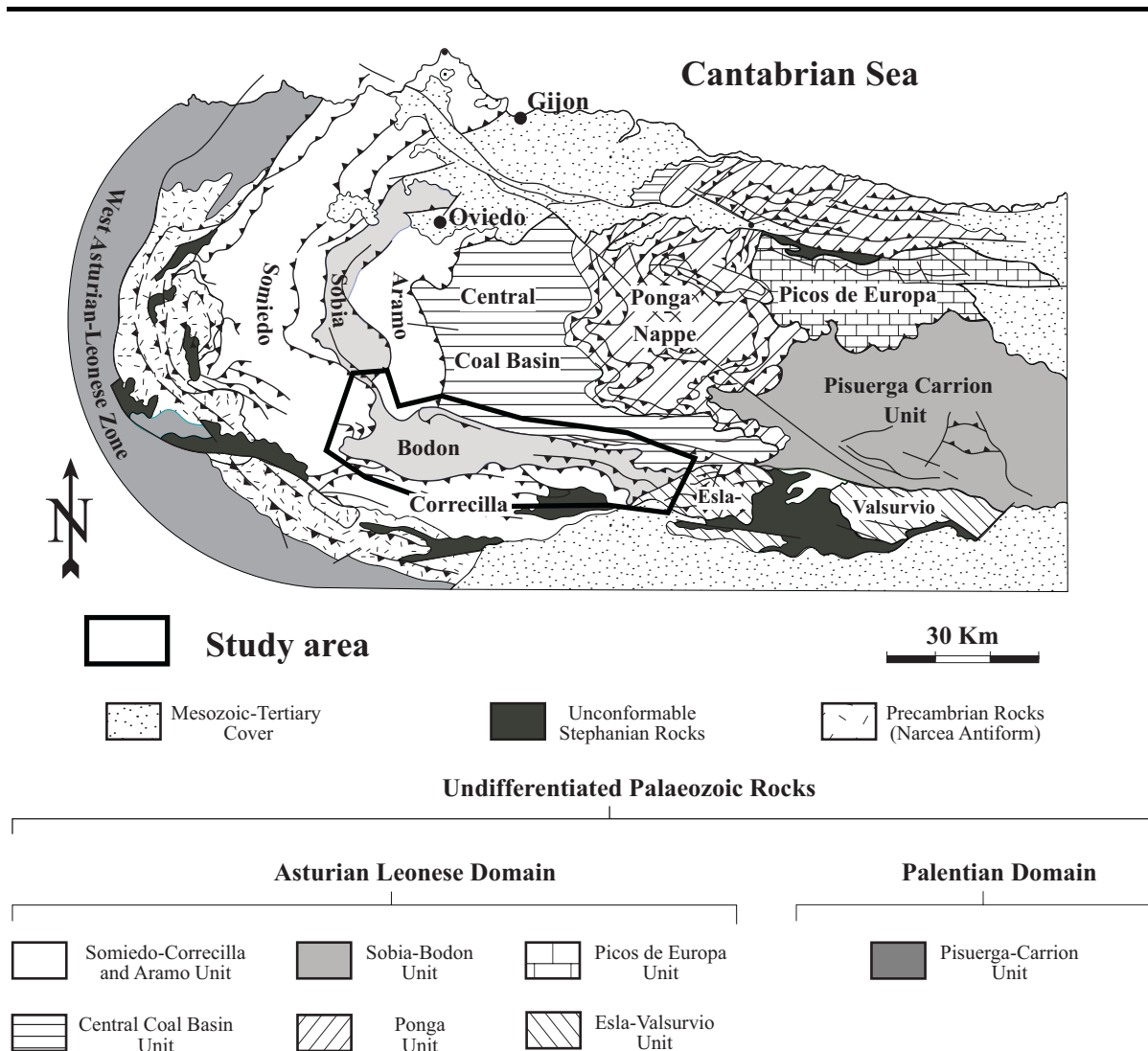
Fig. 2.3. Gelogical map of the Cantabrian Zone showing the different thrust units and the location of the study area (modified from Pérez-Estaún and Bastida 1990).

The Asturian Leonese Domain shows the most complete Paleozoic succession of the Iberian Massif, reaching from Lower Cambrian to Lower Permian. The sedimentary pile rests unconformably on the Precambrian basement, which crops out in the Narcea Antiform. The sedimentation was quite uniform all over the Cantabrian Zone up to Early Ordovician.

From Late Ordovician to Late Devonian, an uplifted area, located in the north-eastern part of the Cantabrian Zone (the so-called "Cantabrian Block" or "Asturian Uplift"), limited the sedimentation in the basin and acted as main source area.

After the Late Devonian peneplanation, a regional eastward tilting eliminated the Cantabrian Block as a source area and the more extensive Carboniferous basin received its siliciclastic input from the West Asturian-Leonese Zone (Truyols et al. 1990).

The Paleozoic starts with a thick clastic succession of pinkish feldspatic quarzites, sandstones and conglomerates, the **Herrería Formation** (Vendian-Lower Cambrian, Comte 1937). It frequently contains a dolomitic horizon near the base.

The Herrería Formation is overlain by ca. 40 m of shallow water limestones, the **Láncara Formation** (upper Lower Cambrian- lower Middle Cambrian, Comte 1937), constituted by yellow stromatolitic dolomite and grey fenestral (birdseye) limestone in the lower part, and by nodular, generally red limestone in the upper part, the Cambrian "griotte" (Zamarreño 1972). The boundary of Lower-Middle Cambrian corresponds to the lithological change mentioned before.

After the carbonate deposition of the Láncara Formation, the siliciclastic sedimentation was restored with the **Ovílle** (Middle Cambrian-Tremadocian, Comte 1937) and the **Barrios Formations** (Tremadocian-Arenigian, Comte 1937), consisting of ca. 150-400 m of white quartz sandstone, which were deposited in shallow water.

In the study area the Barrios Formation is mostly paraconformably overlain by the Silurian shales of the **Formigoso Formation** (Llandovery-Wenlock, Comte 1937), consisting of about 100-300 m of black shales, deposited in an euxinic environment not far from the coast. The Formigoso Formation is overlain by the **San Pedro Formation** (Wenlock-Early Lochkovian, Comte 1937), consisting of ca. 80-200 m of red ferruginous sandstones, with thin-bedded, shaly intercalations and sandy limestone lenses. These sediments were deposited in more agitated and oxygenated waters.

The Devonian stata consists of alternating terrigenous and calcareous, sometimes reefal units (Truyols et al. 1990). The Devonian succession thins out and finally disappears towards the Asturian Uplift, which was located, during the Devonian, in the area of the present-day Central Coal Basin. The sediments were generally deposited in the shallow marine neritic realm and only locally in deeper shelf conditions. In the southern part of the Cantabrian Zone, the San Pedro Formation is overlain by the **La Vid Group** (Comte 1936), which can be divided into four informal members (García Alcalde et al. 2002): dolomitic marls and dolostones, sometimes with stromatolites (Felmín dolomite); argillaceous limestones and shales (Pedrosa limestone); olive green shales with limestone lenses (Valporquero shales); red detrital limestones and marlstones interbedded with shales (Coladilla limestone). Keller (1997) proposed a somewhat different subdivition.

Although sparse bioherms are found in the La Vid Group (Stel 1975), important reef buildups are only present in the **Santa Lucía Formation** (Late Emsian-Eifelian) and the **Portilla Formation** (Late Givetian, Truyóls et al. 1990). A major sedimentary change is represented by the siliciclastic **Huergas Formation** (Upper Eifelian-Lower Giventian), which is intercalated between the two reefal successions.

In Late Devonian time, siliciclastic input increased again due to the renewed uplift of the northern landmass (Truyóls et al. 1990), resulting in the deposition of the **Nocedo** and **Fueyo Formations** (Frasnian, Comte 1936) and of the **Ermita Formation** (Famennian, Comte 1936).

The **Baleas**, **Vegamian** and **Alba Formations** overlay more or less conformably the Devonian succession and indicate the successive deepening of the basin in the Early Carboniferous (Truyóls et al. 1990). The structural setting became increasingly unstable due to the influence of the Variscan orogeny. The basin geometry underwent continuous changes related to the movement of the compressional front from west to east, which gradually involved the different parts of the foreland basin (Sanchéz de la Torre 1983, Colménero and Prado 1993).

In the Namurian A, the sedimentary basin consisted of a large, somewhat deeper carbonate platform succession, the **Barcaliente Formation**. Contemporaneously, the Variscan foredeep was established in the western part, as recorded in the study area by the turbidites of the **Olleros**

Formation (Fig. 2.4A). Facies differentiation continued in front of the migrating Variscan orogen and in Namurian B-Westphalian time a less extensive carbonate platform (**Valdeteja Formation**), surrounded by basinal deposits (**San Emiliano Formation**), was positioned in more open marine environments (Fig. 2.4B). The siliciclasctic input continued and, starting from the Westphalian A, the basin was completely filled by terrigenous sediments, terminating the carbonate platform deposition.

Only in the northeast, in the Picos de Europa Unit, the carbonate production continued up to the Stephanian, with the development of the **Picos de Europa Formation**. In contrast, Stephanian continental sediments overlay with an angular unconformity the western and the southern tectonic units.

Permian deposits outcropping in the northern part of the Cantabrian Zone formed presumably under a post Variscan extensional tectonic regime. The **Viñon Formation** (Autunian) consists of a shallow water limestone, deposited in isolated basins controlled by normal faults. This limestone is intercalated with alkaline volcanites, conglomerates and shales associated with gypsum deposits (Prado 1972, Sanchéz de la Torre et al. 1977, Martínez Garcia 1983). The **Villaviciosa Formation** (Saxonian) is composed of conglomerates, sandstones, caliche limestones and shales containing gypsum and indicates sedimentation in a continental environment under semiarid conditions (Sancéz de la Torre et al. 1977, Martínez Garcia 1983).
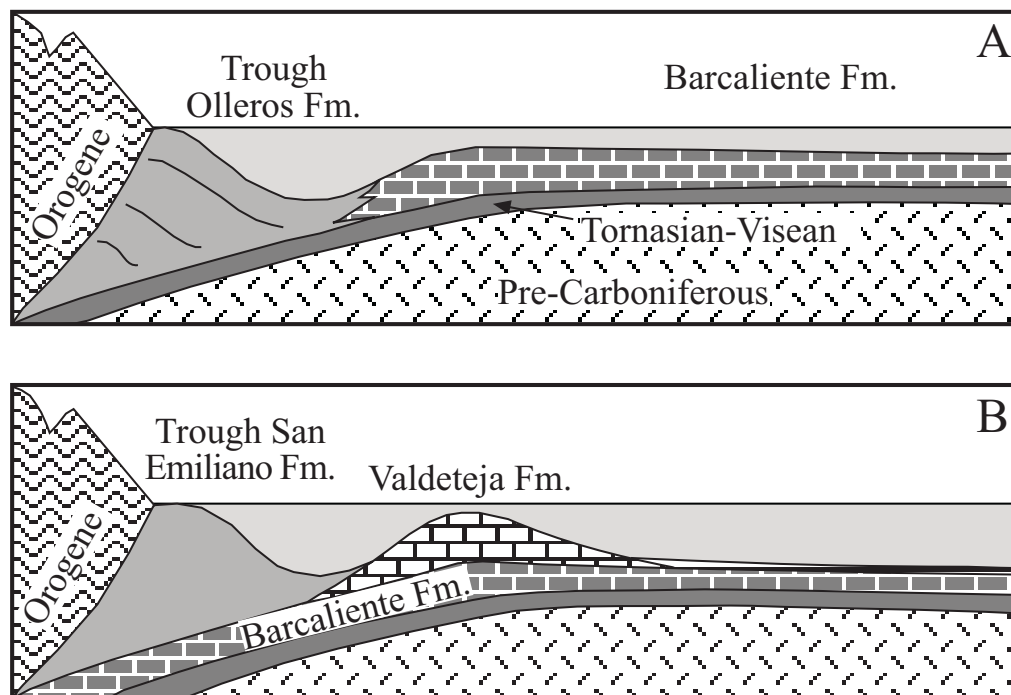
Fig. 2.4. Tectono-sedimentary evolution of the Variscan foreland basin during the Carboniferous (modified after Fernández 1995). A) Namurian A time. B) Namurian B - Westphalian A time.

Arid conditions characterized the transition to the Triassic, during which shales, marls and evaporitic successions containing gypsum were deposited in brackish lagoonal environments (Sánchez de la Torre et al. 1977, Orti et al. 1996).

During the Jurassic and the Cretaceous the sea covered most of the area, although continental conditions persisted locally. Mesozoic deposits cover wide areas in the N, S and E of the Cantabrian Zone.

2.3.2. Structure

The general structure of the Cantabrian Zone shows the characteristic features of thin-skinned tectonics, including the general ramp-flat staircase geometry as well as associated folds (Fig. 2.5). The Variscan faulting migrated generally from the hinterland to the foreland in a forward-type sequence (Pérez-Estaún and Bastida 1990, Alonso and Pulgar 1995). The thrust surfaces mostly diverged from a *decollément* which is usually located at the base of the limestones and dolostones of the Láncara Formation (although in the western part of the Cantabrian Zone it also affects the Precambrian rocks). The first units to be emplaced were the westernmost Somiedo, la Sobia and Aramo Units in Namurian to early Westphalian time, followed by the Central Coal Basin and the Ponga Unit. The Picos de Europa Unit was the last to be deformed during Stephanian time.
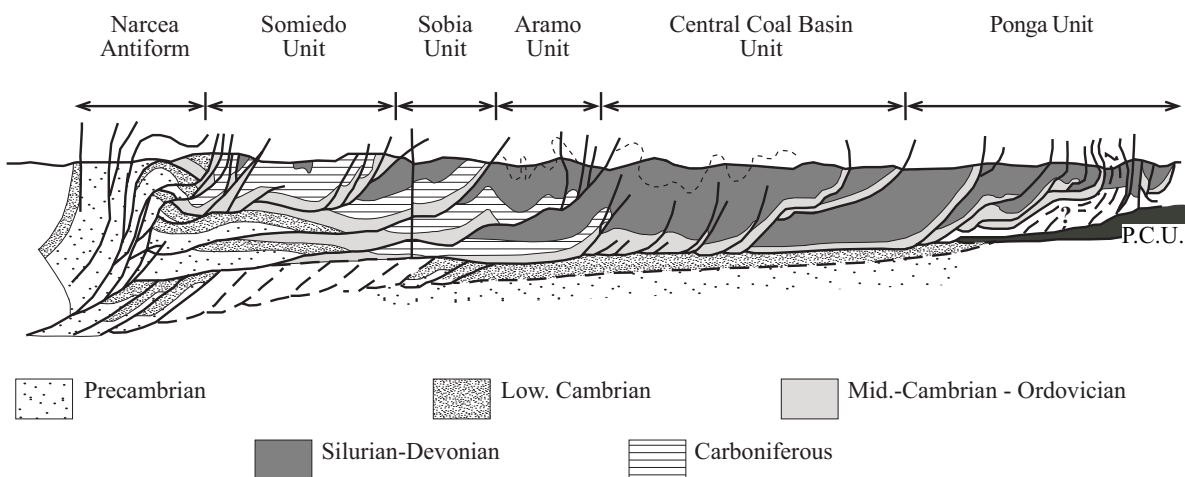
Fig. 2.5. Geological cross section showing the general structure of the Cantabrian Zone, including the general ramp-flat geometry and the associated folds.

There are several faults that have long traces and affect different tectonic units. In the southern part of the Cantabrian Zone the main faults, the **León Line** and the **Sabero-Gordón Line**, have an E-W direction and affect the Stephanian Basin. These faults have a composite history, implying initial strike-slip displacement (Marcos 1979, Julivert 1971) and a later reactivation as reverse faults during the successive emplacement of the different nappes (Bastida et al. 1976, Aller 1986, Alonso 1987). In the northern part of the Cantabrian Zone there are also E-W faults, which represent an Alpidic reactivation of previous thrusts. (Tosal 1968). The **Ventanilla fault**, a prominent structure crossing the Cantabrian Zone from NW to SE, has been interpreted as a post-Variscan wrench fault (Julivert et al. 1971).

The origin of the Cantabrian Arc was controversially debated. Pérez-Estaún and Bastida (1990) and Pérez-Estaún et al. (1988) proposed a two phase emplacement of the tectonic units, with a first thrust system causing the emplacement of the westernmost units and a second system developing

beneath the first one and responsible for the thickening of the orogenic wedge, the steepening and local overturning of thrust planes and the progression of the deformation towards the foreland. A progressive series of rotational displacements led to the final arrangement of the major tectonic units.

Paleomagnetic studies of Weil et al. (2000, 2001 and 2003) and the work of Gutiérrez-Alonso (2004) are in agreement with an originally completely linear N-S belt during thrust development and a post-orogenic bending around a vertical axis. This oroclinal bending caused the thickening of the lithospheric root in the inner part of the arc and a thinning in the outer part of the arc. The process led subsequently to lithospheric delamination of the lithospheric mantle.

2.3.3. Metamorphism

In most of the Cantabrian Zone diagenetic conditions are dominant. However, very low grade (anchizonal) metamorphism developed locally (Aller and Brime 1985, Aller 1986, Raven and Van der Plujim 1986, Aller et al. 1987, Colmenero and Prado 1993, Keller and Krumm 1993, Warr and Marschik 1996, Bastida et al. 1999, Gárcia-López et al. 1997, 1999, Brime et al. 2001, Frings 2002, Frings et al. 2004, Aller et al. 2005).

In addition to the Variscan metamorphism recognized in the Precambrian rocks and contact metamorphism developed around the post-Variscan granite intrusions, three distinct metamorphic events affected the Cantabrian Zone.

1) The first event corresponds to the burial metamorphism, which predates the emplacement of the main Variscan thrusts (as evidenced by the break in the thermal trend across tectonic lineaments) and gives rise to anchizonal conditions in the basal part of thrust units. Cooling took place during the rise and erosion of the hanging wall.

2) The second episode occurred at the Stephanian–Early Permian boundary in an extensional tectonic regime. The metamorphism is restricted to the northern part of the study area, where anchizonal to epizonal condition were reached, associated with subhorizontal cleavage. The spatial distribution of the event is controlled by the León Line, with the highest metamorphic grades located in the northern wall of the fault (in the Westphalian rocks of the Central Coal Basin).

3) The third metamorphic event is registered in the unconformable Stephanian B-C rocks of the Ciñera-Matallana and La Magdalena Coal Basins. The metamorphic event can be explained as a result of intense hydrothermal activity of Permian age, facilitated by the structural location of the basins (which are partly bounded by faults), and a high thermal gradient, confirmed by the high coal rank and small magmatic bodies which intruded the sedimentary succession.

2.3.4. Igneous activity

The Cantabrian Zone underwent a qualitatively important igneous activity. Volcanic activity is abundant in the Cambrian-Upper Devonian and Permian horizons. An alkaline association occurs as lava flows, sills and volcanoclastic rocks particularly abundant in Mid- to Upper Cambrian and Lower Ordovician

rocks, whereas alkaline volcanic necks and pyroclastic rocks are mainly found in Ordovician and Silurian formations. A horizon of kaolinite tonstein, derived from volcanic ash falls, occurs in Lower Ordovician strata (García Ramos et al 1984). According to the data provided by Loeschke (1983, 1986, Loeschke and Zeidler 1982) the alkaline volcanic activity extended into the Late Silurian.

Tholeiitic activity started during the Middle Ordovician and had a second pulse during the Upper Ordovician. Finally, volcanic activity of probably alkaline character was present during the Permian (Martínez-García and Tejerina 1985).

In the Cantabrian Zone, numerous post-kinematic plutonic stocks also occur, which show a variety of characteristics. The most important area in this respect is the Palentian Zone, where more than 200 bodies have been described (Corretgé et al. 1987). These have a tonalite-granodiorite-monzogranite composition, are associated with mafic to intermediate dykes (e.g. Gallastegui et al. 1990, Fernández-Suárez et al. 2000) and were formed by melting of lower crust with varying involvement of mantle derived melts (Galán and Suárez 1989, Galán et al. 1996). Granodioritic to gabbroic stocks, which are located along deep late-Variscan faults of considerable extension (Julivert 1971, Loeschke 1982, Corrétge and Suárez 1990), also occur in the northwestern part of the Cantabrian Zone (Infieto Group and Salas-Belmonte Group). Fernández-Suárez et al. 2000 favoured a delamination model to explain the high heat flow, which is reflected by the widespread magmatic activity in the Cantabrian Zone in post-Variscan time.

2.3.5 Metallogenesis

Over 300 metallic ores are known in the Cantabrian Zone. The metals include copper, cobalt, nickel, lead, zinc, mercury, arsenic, antimony, gold, iron, and manganese. Among the non-metallic substances there are fluorite, barite, talc, magnesite, kaolinite and gypsum. Nearly 75% of the ore deposits are located in Carboniferous rocks (Luque and Martínez García 1983).

Cu-Co-Ni deposits are usually hosted by Carboniferous carbonate rocks and in terrigenous sediments of the same age near granodioritic and gabbroic igneous rocks (Corretgé et al. 1970). The usual paragenesis is arsenopyrite-chalcopyrite-pyrite with occasional tetrahedrite, sphalerite, galena, molybdenite, and gold (García de Figuerola and Peña 1964, Loredo and García-Iglesias 1988). When the intrusions cut carbonate rocks of Cambrian (Boinás), Devonian (Carlés, Ancellana) or Carboniferous age (Infiesto), these ores are contained in a skarn-like paragenesis. In the western Cantabrian Zone, the ores are hosted by intensely dolomitized Carboniferous rocks. Complex associations of Cu-Co-Ni minerals are found, with an extensive development of supergene alteration (Ypma et al. 1968, Paniagua et al. 1988a, Paniagua and Rodriguez Pevida 1988).

Pb-Zn-Ba deposits are more abundant in the eastern extremity of the Cantabrian Zone, in the Picos de Europa Unit. The most widespread paragenesis includes sphalerite, galena, pyrite, greenockite, and chalcopyrite. Gangue minerals are calcite, dolomite, ankerite, aragonite, barite, quartz and chert. In the supergenic paragenesis, smithsonite, hydrozincite, hemimorphite, cerussite, malachite, anglesite, cinnabar and goethite occur (Luque et al. 1990). These occurrences are hosted usually in dolomitized rocks of Carboniferous age (Fernández Fernández et al. 1985). There are also small showings of Pb-Zn associated with Middle Cambrian Láncara limestones in the western part of

the Cantabrian Zone, as, for example, in the localities of Torre de Babia, Riolago, Villasecino, Rabanal, Rodiezmo (Paniagua 1993).

As-Sb-Au deposits are hosted by Carboniferous dolomitized limestones and bituminous shales, associated to an E-W fracture system belonging to the León Line (Paniagua 1998, Paniagua et al. 1996, Crespo et al. 2000). Other deposits are associated with late Hercynian basic igneous rocks and deposited in shear zones and related fractures (Paniagua 1988). The most common paragenesis consists of gold-bearing arsenopyrite, pyrite, berthierite, stibnite, Pb-Sb sulfosalts and barite.

Hg-As deposits are hosted by limestones of Carboniferous, Middle Cambrian and Devonian age and are also associated with siliceous breccias and/or conglomerates, quarzites, and sandstones (Luque et al. 1990). The most common paragenesis includes (1) cinnabar, pyrite melnikovite and marcasite; (2) cinnabar, realgar and orpiment; 3) cinnabar, stibnite and fluorite (Luque 1985). These mineralizations usually occur as fracture and cavity filling (Luque et al. 1990).

Talc deposits are related to faults cutting Ordovician Barrios sandstones and Carboniferous limestones in the eastern Cantabrian Zone (Galán-Hertos and Rodas 1973, Hardy et al. 1980, Hardy and Ildefonse 1981, Tornos and Spiro 2000).

Most mineralizations in the Cantabrian Zone are of hydrothermal origin, hosted in carbonate rocks in intensely faulted and folded areas, showing strong control by the main late Variscan fracture direction (Luque and Martinez García 1985), suggesting a common age. Sometimes these mineralizations are associated to post-Variscan intrusive rocks or Early Permian volcanism, suggesting a relation with (ascending or descending) hydrothermal fluids (Martínez García 1981). As no younger strata are mineralized, their age should be Permian (Martínez García 1983). Many deposits are also related to enhanced porosity and reducing environment, associated to alteration phenomena, such as dolomitization and silicification (Fernández Fernández 1985).

2.3.6. Dolomitization

Extensive occurrences of apparently the same type of epigenetic dolomite (I will be describing in this work) were observed in several tectonic units of the Cantabrian Zone (Sobia-Bodón, Somiedo-Correcilla, Picos de Europa, Pisuerga-Carrion Units), affecting different carbonate successions.

In the southern Cantabrian Zone, the most intensely dolomitized sediments are the Namurian-Westphalian carbonates, which are particularly well exposed in the Bodón Unit (Gasparrini 2003), and the Cambrian Láncara Formation, which contains numerous but volumetrically less impressive dolomite bodies.

In the study area, dolomites have never been observed in the carbonate levels of the San Emiliano Formation, or in the carbonate clasts contained in the conglomerates of the Stephanian Basin. Furthermore, the dolomitized rock bodies were never involved in the main Variscan thrusting phase.

Dolomitized rocks of different type occur in the lower member of the Láncara Formation and in the Felmín member of the La Vid Group. These dolomites probably have a "less exotic" origin than the former one. They surely formed before the onset of the Variscan orogeny and are probably related to early diagenetic stages, as demonstrated by their fine crystal size and their fabric preservative character.

_____

Chapter 3 - Methods

3.1. Field methods

Over 200 rock samples of dolomitized and undolomitized rocks from the Láncara Formation were collected for standard petrographic and geochemical studies in a region of about 1000 km^2, in the southern part of the Cantabrian Zone. The study area is approximately delimited by the Rio (River) Luna in the west and the Rio Curueño in the east, and includes the Correcilla and Bodón Units (see Fig. 2.4, chapter 2).

The spatial distribution of the dolomite bodies in the study area was qualitatively mapped in order to evaluate the volumes of the dolomitized rocks related to the undolomitized rocks. This was possible only for the Barcaliente and Valdeteja Formations of the Bodón Unit, where the dolomitization is much more widespread and the recognition is facilitated by the clear colour contrast between the light grey limestone and the dark grey dolostone.

3.2. Petrographic methods

Ninety polished thin sections were prepared (60 μm thick) from the most representative samples of both dolomitized and precursor lithology. Observations in transmitted light were performed using a Leica MPV-SP microscope.

Cathodoluminescence microscopy was carried out using a Leica DM-RP microscope equipped with a Citl cold cathode apparatus of the type CCL 8200mk3. In order to visualize compositional heterogeneity and recognize the different phases, a scanning electron microscope (SEM Leo 440) was used in reflection mode (backscattered emission), together with an energy discriminating system (EDS) for X-ray micro-analysis of target areas.

Cathodoluminescence microscopy is a powerful method to recognize fabric and textural characteristics of minerals, especially in recrystallized carbonate rocks, in order to better characterize the growth history of different diagenetic phases. The principle is based on the luminescence property of many minerals under electron bombardment. The energy of a beta ray (electron) is sufficient to excite an atom or molecule and cause a quantum jump, with the input energy being totally absorbed. After a short delay time (10^{-8} s) the exited atom or molecule returns to its former energy state and may emit a radiation in the form of light or other emissions (alpha, beta or gamma rays). The intensity of the CL is the function of current density at the specimen and of the voltage (acceleration potential) of the applied electron beam. A beam voltage of 20 kV and a current of 300 to 400 μm were used and maintained constant during the observations.
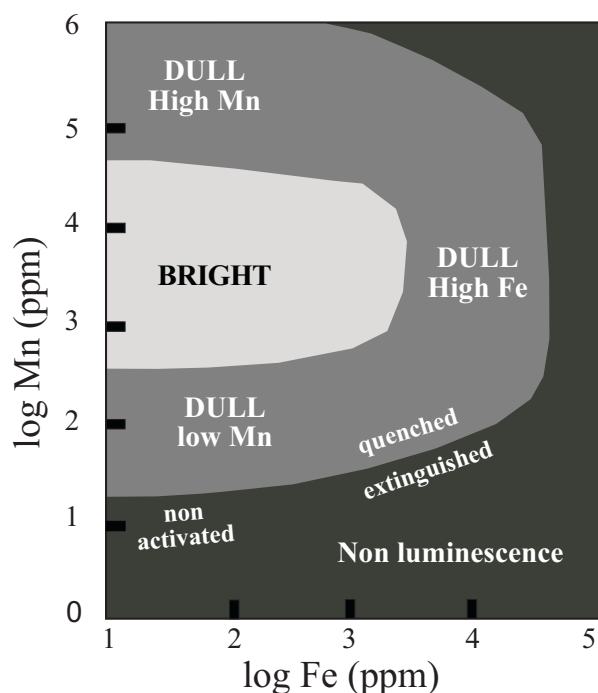
Fig. 3.1. Field of CL in calcite and dolomite (Machel and Burton 1991). Non-luminescence is due to low Mn (activator) concentration (lower left) and extinction is due to Fe-quenching as well as self-quenching by Mn (right ad upper right).

At any temperature, a crystalline solid is in a state of dynamic unrest (ground state), with all the atoms in the lattice vibrating around their mean positions. Upon excitation by an electron beam, such local sites of crystal imperfections are more liable to absorb energy from the beam than are the neighbouring lattice sites. The domains of imperfections become luminescence centres. The centres may occur in two general forms: intrinsic and extrinsic. Intrinsic centres are due to lattice imperfections such as growth distortions and other electronic lattice defects, acquired independently of the composition of the precipitating medium. Extrinsic centres are those acquired from the parent medium during growth, such as impurities in surface, regular lattice and interstitial sites, or compositional heterogeneities between different parts of a crystal. In practice, it may be very difficult to determine the principal causes of CL in a mineral, as there are often complex interactions between extrinsic and intrinsic centres.

Extrinsic luminescence centres may behave differently depending on their response to electron beam excitation .The following types can be distinguished:

1) activator centres, where the luminescence is highly probable;

2) trap centres, where additional energy is required to raise the energy state sufficiently to produce luminescence on transition to the ground state;

3) quencher centres, where the exited state of the centre is close to the transition level, so little or no luminescence is emitted.

Extrinsic luminescence centres are the best known and easiest to detect by geochemical analysis. Luminescence is controlled by the balance between activators and quenchers. Impurities of transition metal ions are the most common activators causing extrinsic CL. Rare earth elements, such as Eu^{3+}, Sm^{3+} and Dy^{3+} are also implicated as inducing activator centres (Mariano and Ring 1975).

Mn^{2+} is the main activator causing luminescence in carbonate minerals such as calcite and dolomite (Long and Agrell 1965, Sommer 1972, Ebers and Kopp 1979, Person 1981), producing a yellow to red emission. Minor activators are also REEs such as Sm^{3+}, Eu^{2+} and Eu^{3+}. Fe^{2+}, Ni^{2+} and Co^{2+} are quenchers in the same minerals.

Fe^{2+} and Mn^{2+} tend to co-precipitate in the lattice of carbonate minerals and varying degrees of quenching occur reducing the intensity of Mn^{2+} emission and inducing a brownish colouration according to the quenching (Fig. 3.1)

Amieux (1982) has related Mn/Fe ratios and their emission colours to chemical environments, particularly to the redox potential changes during crystallization.

3.3. X-ray diffraction analyses

X-ray diffraction (XRD) is commonly used in the study of dolostones. X-rays are produced by bombardment of a metal anode (the target) by high-energy electrons from a heat filament in a Roentgen X-ray tube. The resulting radiation consists of a broad band of continuous radiation (white radiation) produced by the electrons of the filaments which convert their kinetic energy to X-ray on collision with the atoms of the anode target, and a number of discrete lines of varying intensity (which represent the energy released by the rearrangements of the orbital electrons of the atoms of the target) and which are usually removed by the use of a filter.

The X-rays are first collimated to produce a subparallel beam and then directed at the samples, which is positioned on a motor driven mount to rotate at a regular speed in degrees per minute. When the mineral planes in the samples attain an appropriate angle, they will diffract the X-rays according to Bragg's law

$$n\lambda = 2d \sin\theta \tag{3.1}$$

where n is an integer, λ is the wavelength of the x-rays, d is the lattice spacing in ångstroms and θ is the angle of diffraction.
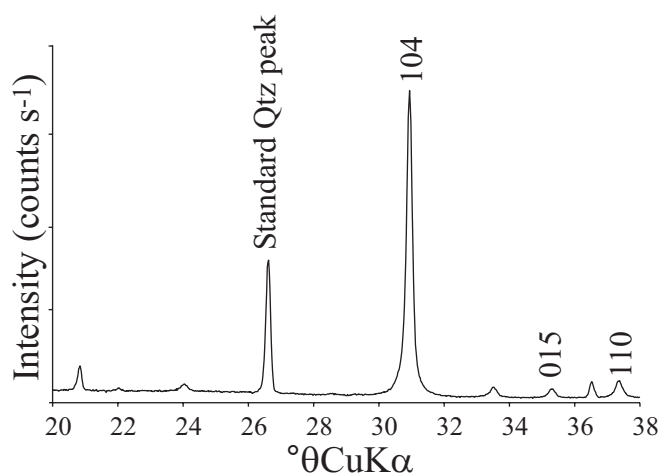
Fig. 3.2. X-ray diffractometry of dolomite showing the peaks used to calculate the stoichiometry (d_{104}) and the degree of ordering (d_{101} and d_{015}).

The diffracted beam is than passed through a receiving slit to the monochromator and than to the detector, where the signal is amplified and recorded.

The conventional X-ray pattern output is a strip chart where the horizontal scale is calibrated in °2θ and the vertical scale shows the intensity of the diffracted peaks (Fig. 3.2).

Deflections recorded can be easily converted into lattice spacing (d) by applying Bragg's law. Minerals can be identified by comparison with

a set of standard patterns compiled by the Joint Committee of Powder Diffraction Standards (JCPDS).

XRD gives information on the Ca or Mg excess of dolomite and can be used to determine the ordering of the dolomite crystals.

The mineral dolomite, $CaMg(CO_3)_2$ is commonly non stoichiometric, but has an excess of Ca^{2+}, up to Ca:Mg = 58:42, or less commonly an excess of Mg up to Ca:Mg = 48:52 (Hardy and Tucker 1988). The effect of Ca^{2+} substitution for Mg^{2+} is to increase the cation lattice spacing, which can be measured from the XRD. The excess of calcium is then calculated from the equation of Lumsden (1979), relating the mole percent of $CaCO_3$ (N) to the d_{104} spacing measured in ångstroms (d)

$$N=Md+B \tag{3.2}$$

where M is 333.33 and B is - 911.99.

The d_{104} spacing for ideal stoichiometric dolomite is taken as 2.886 Å and for 55% $CaCO_3$ as 2.901 Å (Goldsmith and Graf 1958a, 1958b).

XRD of dolomites also gives information on the ordering of the crystals. As a result of the segregation of the cations into separate sheets in the dolomite crystal, a set of superstructure reflections corresponding to d_{021}, d_{015} and d_{101} is revealed with the XRD. The sharpness and the relative intensity of these ordering peaks can be used to give a measure of the degree of ordering (OR) of the dolomite crystals:

OR = intensity 015 peak/intensity 110 peak

The greater the ratio of the heights of the ordering peaks 015 to the diffraction peak 110 is, the higher is the degree of order (OR).

XRD analyses were performed at the Geological-Paleontological Institute of the University of Heidelberg (Germany), in order to determinate the stoichiometry and the degree of order of different dolomite phases. A Bragg-Brentano X-ray diffractometer (Siemens D 500), with a Cu tube and graphite monochromator was used. The diffractometer operated at 40 kV and 30 µA and scanned the samples in the 2θ range from 2.0° to 70.0° with increments of 0,02°[2θ]/sec. Aperture and detector diaphragm were 1° and 0.15° respectively. Data analyses were performed employing the Mac Diff 4.2 software. The peaks were fitted with the Split Pearson VII method. Quartz powder was added to the dolomite samples as internal standard in order to correct the position of the peaks by referring to the known d_{101} reflection of the internal quartz standard.

3.4. Trace element geochemistry

Sample powders (0.5 g) were analysed at ACME Analytical Laboratories Ltd. (Vancouver, Canada) with ICP-ES. Each sample was digested in Aqua Regia for one hour in a hot water bath (>95 °C). After

digestion, the sample solutions were aspirated into a Jarrel Ash AtomComp 800 Inductively Coupled Plasma Atomic Emission Spectrometer (ICP-AES) to determine the element concentrations.

The analysis package includes 32 elements. The trace elements usually measured in dolomite studies are Fe, Mn, Sr and Na. The lower and upper detection limits for each element are summarized in Tab. 3.1. The data are usually expressed in ppm for the minor trace elements and in wt % for the major elements.

Trace elements in dolomite are commonly used to give information about the nature of the dolomitizing fluids. The trace elements concentrations are determined by the concentration in the fluid, the water/rock ratio of the system, and the distribution coefficient k_e of the element (M_e) between dolomite and the aqueous fluid, expressed by the relation:

$$\left(\frac{^mM_e}{^mCa}\right)_{dolomite} = k_{e_{dol}}\left(\frac{^mM_e}{^mCa}\right)_{water} \tag{3.3}$$

	Detection limit	Upper limit
Ag	0.3ppm	100 ppm
Al	0.01%	10%
As	2 ppm	10000 ppm
Au	2 ppm	100 ppm
B	3 ppm	2000 ppm
Ba	1 ppm	1000 ppm
Bi	3 ppm	2000 ppm
Ca	0.01 %	40%
Cd	0.5 ppm	2000 ppm
Co	1 ppm	2000 ppm
Cr	1 ppm	10000 ppm
Cu	1 ppm	10000 ppm
Fe	0.01 %	40 %
Hg	1 ppm	100 ppm
K	0.01 %	10 %
La	1 ppm	10000 ppm
Mg	0.01 %	30 %
Mn	2 ppm	10000 ppm
Mo	1 ppm	2000 ppm
Na	0.01 %	10 %
Ni	1 ppm	10000 ppm
P	0.001 %	5 %
Pb	3 ppm	10000 ppm
Sb	3 ppm	2000 ppm
Sr	1 ppm	10000 ppm
Th	2 ppm	2000 ppm
Ti	0.01 %	10 %
Tl	5 ppm	1000 ppm
U	8 ppm	2000 ppm
V	1 ppm	10000 ppm
W	2 ppm	100 ppm
Zn	1 ppm	10000 ppm

Tab. 3.1. ICP-ES detection and upper limits.

where M is the molar concentration. For k>1 the guest ion will be preferentially partitioned into the solid. Elements with distribution coefficient lower than 1 will fractionate in the fluid.

There has been much discussion over the real meaning of the values of distribution coefficients in carbonates (e.g. Brand and Veizer 1980, Kretz 1982, Veizer 1983a and 1983b) due to the fact that the theoretical k only applies to substitution of the element in the lattice sites. There are other modalities of incorporation of trace elements into a crystal, for example trapped along crystal boundaries, included in solid or liquid inclusions. Furthermore, experimental values for dolomite are difficult to obtain, since dolomite cannot be precipitated directly in the laboratory at realistic diagenetic temperatures.

3.5. Microprobe analyses

Electron microprobe analysis (EMPA) is a technique for chemical analysis of small selected areas of solid samples, in which X-rays are excited by a focused electron beam. By comparing the X-ray pattern with those emitted by standards, it is possible to obtain quantitative analysis.

Microprobe analyses were performed on 4 thin sections at the Electron-microprobe laboratory of the University of Göttingen, Germany. Analyses were obtained in a Jeol JXA-8900RL, equipped with a wavelength dispersive (WD) X-ray spectrometer. Ca, Mg, Fe, Mn and Sr were measured with an acceleration voltage of 20.0 kV and a beam current of 20mA. A beam diameter of 10 µm was chosen, in order to minimize the systematic error due to decomposition of the dolomite under electron bombardment. The standards used are Dolomite UNNM for Ca and Mg, Siderite USNM for Fe, Rodonite for Mn and Strontianite USNM for Sr. Detection limits and other parameters are reported in Tab. 3.2.

Elements	Ca	Mg	Fe	Mn	Sr
Standards	Dolomite USNM	Dolomite USNM	Siderite USNM	Rodonite	Strontianite USNM
Acceleration voltage [kV]	20.0	20.0	20.0	20.0	20.0
Beam current [nA]	20.0	20.0	20.0	20.0	20.0
Beam diameter [µm]	10	10	10	10	10
Detection limits [ppm]	107	130	85	80	70
Count time [s]	15	15	30	30	60

Tab. 3.2. Microprobe parameters, detection limits and standards.

3.6. Stable isotope geochemistry

Isotope fractionation is a consequence of the fact that isotopes of the same element have slight differences in mass and energy, which cause differences in the physical and chemical properties. Such differences are generally greatest for elements of low atomic number, such as C and O. In addition, a given molecule that contains the lighter of two isotopes has weaker chemical bonds and is more reactive than a similar molecule containing the isotope with heavier mass.

Isotopic fractionation is indicated by the fractionation factor α, which is defined as

$$\alpha = \frac{R_A}{R_B} \tag{3.4}$$

where R_A is the heavy/light isotopic ratio for phase A and R_B is the same in phase B.

The fractionation factor for any given system is temperature dependent and generally approaches unity at increasing temperature.

Oxygen and carbon isotope geochemistry is used to define the conditions of carbonate precipitation and diagenesis. Oxygen has three isotopes: ^{16}O (99.763%), ^{17}O (0.0375%) and ^{18}O (0.1995 %); carbon has two stable isotopes: ^{12}C (98.89 %) and ^{13}C (1.11%).

The oxygen and carbon composition of a sample (spl) are expressed by mean of the δ notation, which indicates the per mil differences relative to a standard (st):

$$\delta^{18}O = \left[\frac{(^{18}O/^{16}O)_{spl} - (^{18}O/^{16}O)_{st}}{(^{18}O/^{16}O)_{st}} \right] 10^3 \tag{3.5}$$

$$\delta^{13}C = \left[\frac{(^{13}C/^{12}C)_{spl} - (^{13}C/^{12}C)_{st}}{(^{13}C/^{12}C)_{st}} \right] 10^3 \tag{3.6}$$

Positive δ indicates an enrichment of the heavy isotope relative to the standard.

The reference standard for carbonates is the CO_2 gas obtained by reacting a particular belemnite (*Belemnita americana*) of the Peedee Formation in South Carolina with 100% phosphoric acid (PDB standard of the University of Chicago). In actual practice a working standard is used which has been compared to V-PDB. The isotope composition of the fluids is expressed relative to the SMOW (Standard Mean Ocean Water) international standard. The conversion between $\delta^{18}O_{SMOW}$ and $\delta^{18}O_{PDB}$ is expressed by the equations of Coplen (Coplen et al. 1983)

$$\delta^{18}O_{SMOW} = 1.03091\delta^{18}O_{PDB} + 30.91 \tag{3.7}$$

$$\delta^{18}O_{PDB} = 0.97002\delta^{18}O_{SMOW} - 29.98 \tag{3.8}$$

The oxygen isotopic composition of dolomites reflects the temperature of formation and the isotopic composition of the dolomitizing fluid, which can be influenced by the isotopic composition of the $CaCO_3$ that is being replaced only at very low water/rock ratios and/or closed systems.

Both the elevated temperature and the "meteoric effect" (i.e. decreasing $\delta^{18}O$ of rainfall and fresh groundwater, the increasing latitude, altitude and distance from the ocean), drive the oxygen isotopic composition of diagenetic carbonates negative. (Fig.3.3).

Carbonate minerals always concentrate ^{18}O relative to the fluid from which they precipitate (i.e. the $\delta^{18}O$ is higher than the parent fluid). Fractionation becomes less and less efficient at increasing temperatures.

$\delta^{18}O$ values that have not been reset during dolomite neomorphism reflect both the temperature and composition of the parent fluid (Land 1992, Allan and Wiggins, 1993, Emery and Robinson, 1993). The relation among temperature, $\delta^{18}O_{water}$ and $\delta^{18}O_{dolomite}$ is imprecisely known. Experimental works, carried out mainly at high temperature, have resulted in different fractionation equations (Northrop and Clayton, 1966, O'Neil and Epstein 1966, Sheppard and Schwarcz 1970, Fritz and Smith 1970, Friedman and O'Neil 1977).

Land (1983) published temperature vs. $\delta^{18}O_{dolomite}$ curves for various $\delta^{18}O_{water}$ and temperature vs. $\delta^{18}O_{water}$ for various $\delta^{18}O_{dolomite}$, both based on the equation

$$10^3 \ln\alpha_{dol-water}=3.2*10^6 T^{-2}(°K)-3.3 \tag{3.8}$$

which is a compromise between the experimental data and observation of the real fractionation of existing coeval calcite-dolomite and represents probably the best approximation for diagenetic temperature conditions. With constant fluid composition, lower $\delta^{18}O$ values generally reflect higher temperature of crystallization.

In contrast, $\delta^{13}C$ values of dolomite are strongly influenced by the values of the precursor $CaCO_3$. In addition, there is little isotopic fractionation of $^{13}C/^{12}C$ with temperature. The $\delta^{13}C$ values give information about the source of the carbon in the carbonate (marine, derived from organic matter, methanogenesis, Fig. 3.3). The isotope fractionation in the system CO_2- HCO_3-$CaCO_3$ results in calcite that is enriched in ^{13}C by about 10‰ relative to CO_2 at 20°C. Marine carbonate rocks typically have $\delta^{13}C$ values very close to PDB (ie, 0 ± 5 ‰). Lacustrine carbonates usually have lower $\delta^{13}C$ values due to incorporation of CO_2 derived from the decay of plant material in soil. Carbonates formed by oxidation of biogenic CH_4 (which is very depleted in ^{13}C) also have light

Fig.3.3. Summary of the effects of temperature, evaporation and dilution of the dolomitizing fluids plus input of CO_2 derived from methanogenesis and organic matter oxidation on the isotope composition of dolomite (modified after Lohmann 1988).

(more negative) $\delta^{13}C$ values, whereas carbonates formed in organic-rich systems (where methanogenesis has reduced and removed significant portions of the total DIC into the gas phase) can have very positive values (> +20‰).

Oxygen and carbon isotope ratios were measured at the University of Erlangen (Germany). Carbonate powders as small as 0.2 mg, drilled with a dental-drill, were extracted from rock slices. The powders were reacted with 100% phosphoric acid at 75 °C (Wachter and Hayes 1985) in an online carbonate preparation line, connected to a Finnigan Mat 252 mass spectrometer. $^{18}O/^{16}O$ and $^{13}C/^{12}C$

ratios were measured simultaneously on the CO_2 gas produced. Calibration was accomplished by assigning a δ ^{18}O value of –2.20‰ and a δ ^{13}C value of 1.95‰ to the NBS-19 standard. All of the δ ^{18}O and δ ^{13}C values for carbonates are reported in ‰ V-PDB. Reproducibility was checked by replicate analysis of laboratory standards and is better than ±0.02. As suggested by Land (1980), the δ^{18}O values of dolomite samples were not corrected for the phosphoric acid fractionation.

3.7. Strontium isotope geochemistry

Strontium has four naturally occurring stable isotopes: ^{88}Sr (82.53%), ^{87}Sr (7.04%), ^{86}Sr (9.87%), and ^{84}Sr (0.56%). ^{88}Sr, ^{86}Sr and ^{84}Sr are not part of any decay series, while ^{87}Sr is generated by the decay of ^{87}Rb.

Dolomite excludes rubidium from its structure and incorporates strontium as a substitute for calcium. As no significant fractionation occurs during precipitation, the ^{87}Sr/^{86}Sr of dolomite is the same as the one in the fluids from which it precipitated (or subsequently reequilibrated). The ^{87}Sr/^{86}Sr of the fluids from which the dolomite formed is in turn related to the minerals which provided strontium through water-rock interaction.

Carbonate samples were measured for their strontium isotopic composition and concentration at the University of Giessen (Germany). Sample powders were totally spiked with a mixed ^{87}Rb-^{84}Sr tracer and dissolved in 6 N HCl. Rubidium and strontium were separated with 3N HNO_3 using EICHROM Sr resin (Horwitz et al. 1991a, 1991b) on 50μm Teflon columns. Sr was loaded with $TaCl_5$-HF-H_3PO_4 solution (Birck 1986) onto W single filaments. Rb was loaded with de-ionized water onto the evaporation ribbon of a Ta double-filament assemblage. All isotopic analyses were performed on a six collector FINNIGAN MAT 261 mass spectrometer running in static multicollector mode. Repeated static measurements (n = 36) of the NBS 987 standard over the duration of the study yielded ^{87}Sr/^{86}Sr = 0.71025 ± 4 (2σ mean).

3.8. Fluid inclusion study

One of the crucial problems in understanding the dolomite origin is the definition of the hydrological and chemical conditions of the fluids responsible for its precipitation (see chapter 1, paragraphs 1.2 amd 1.5).

Fluid inclusions are fluid-filled vacuoles sealed within minerals during crystal growth (**primary inclusions**) or in a later stage during crack-healing mechanism (**secondary inclusions**), and represent the only direct means of examining the fluids present in ancient diagenetic environment.

Fluid inclusions (FI) give the only direct information about the temperature and the composition of the paleofluids active during the dolomitization process; for this reason fluid inclusion analyses have been systematically applied as a routine method in the most important dolomitization studies (see also

Morrow and Aulstead 1990, Qing & Mountjoy 1994, Coniglio et al. 1994, Zeeh et al. 1995, Boni et al. 2000, Gasparrini et al. 2006a).

Simple petrographic observations combined with microthermometric analyses and more quantitative geochemical analyses of the inclusion content can provide valuable information about the temperature and pressure of mineral precipitation, the composition and origin of fluids and the after-mineral precipitation history of the fluid system.

The theory of the fluid inclusion studies and its application are exhaustively discussed in Roedder (1984), Shepherd et al. (1985), Goldstein and Reynolds (1994) and Samson et al. (2003).

3.8.1. Microthermometry

The determination of temperatures of thermodynamic phase changes within fluid inclusions during heating and cooling of samples is termed microthermometry. At P-t conditions typical of the diagenetic realm, aqueous fluids can be trapped as single-phase (liquid or vapour) or two-phase fluid inclusions. If the inclusion satisfies few basic requirements, (i.e. remains a closed system and maintains a constant volume), as the inclusion experiences decrease in temperature (for example from the entrapment temperature to the ambient temperature), the P-t condition within the inclusion are constrained to follow lines of constant volume (the so called "isochores"), until the liquid/vapour saturation line or field is intersected. At that temperature a minuscule vapour bubble (for inclusion trapped as liquid phase) or a liquid film (in the case that the inclusion was trapped as vapour phase) will form. During subsequent cooling of the inclusion, the inclusion conditions remains on the liquid-vapour curve.

The natural cooling path of the fluid inclusion can be reversed in the laboratory heating the inclusion under microscopic observation: the vapour bubble (or the liquid film) will gradually shrink during heating and finally disappear and the inclusion will once again become a single homogeneous phase. This phase-change temperature, called homogenization temperature (T_H) gives a minimum estimate of the entrapment temperature of the inclusion.

One of the effects of adding electrolytes to pure H_2O is to lower the temperature at which ice can exist (freezing point depression). The measurements of the final melting temperature of ice (T_M ice) and of other salt-hydrates (such as species, which may nucleate during freezing experiments) give important information about the total salinity of the inclusion. The salinity is generally expressed in equivalent weight percentage of a determined salt species (eq. wt. %). In this study, the equivalent mass percentage notation is preferred, as weight is a measure of a force (Bakker, private communication).

The determination of the salt species present in the fluid inclusions is connected to another important phase change used in low temperature microthermometric studies: the first melting temperature, also called eutectic temperature (T_e).

Eutectic melting of an inclusion is the temperature at which one solid phase (either ice or salt-hydrate) melts completely. In practice this phase has to be present in a quantity sufficient for the melting to be observed under the microscope. Each solid phase, which nucleates in the inclusion, is characterized by its typical eutectic temperature, the identification of which allows to select the appropriate model composition for calculation of the salinity.

_____

The fluid inclusion study was conducted on double polished 100-120 µm thick sections prepared with cold technique, reaching the maximum temperature of 35 °C in order to prevent re-equilibration and/or decrepitation of the inclusions by preparation heat.

Microthermometric measurements were carried out using a Linkam MDS 600 heating-freezing stage (University of Heidelberg, Germany). Calibration was performed using synthetic fluid inclusions and chemical compounds at -56.6°C, 0.0 °C and 213 (i.e. melting point of CO_2, triple point of H_2O and melting temperature of $AgNO_3$ respectively).

Thick section chips were placed on a sample port controlled by X-Y manipulators, which rests directly on a silver block within the stage chamber. The silver block can be heated by thermal conduction and cooled by a constant flux of liquid N_2 through the chamber.

A videocamera is mounted onto the microscope and connected to a computer, which runs Linksys software. Volumetric proportion of the vapour phase relative to the total volume of the FI was calculated from digital image at ambient temperature, assuming that the area fraction is equal to the volume fraction (Bakker and Diamond 2006).

3.8.2. Raman spectroscopy

Limitations of the optical microscope makes the identification of the mentioned phase changes sometimes impossible. Furthermore, it is generally difficult to be confident that all the phase assemblages, observed during the heating of a frozen inclusion, represent a stable phase configuration (see also Bakker 2004).

The combination of Raman spectroscopy with microthermometry represents a powerful method to overtake some of these limits and carefully identifies the major ion species present in individual fluid inclusions (Dubessy et al. 1982, Bakker 2004).

When light falls on a molecule of a chemical compound, two kinds of scattering take place: Reyleigh, in which the frequency of the scattered beam does not alter from the incident beam, and Stocks and Antistocks, in which the frequency of the scattered beam is different from the incident beam, as the light either imparts rotational or vibrational energy to the molecules or takes energy away. The spectrum of the scattered light will have one prominent line corresponding to the original wavelength of the incident radiation, plus additional lines to each side of it (Raman effect).

Raman spectroscopy can be applied to the study of fluid inclusion: in fact the most important salt-hydrates that nucleate at low temperature ($NaCl_2 \cdot H_2O$, $CaCl_2 \cdot 6H_2O$, etc.) can be identified using Raman spectroscopy. This permits a careful identification of the thermal phase change on individual fluid inclusions. Another positive aspect is the non-destructive nature of the method, which allows repeatable experiments.

Liquid and gas phases in the fluid inclusions were analysed with a LABRAM confocal-Raman spectrometer (University of Leoben, Austria) using a 100 mW frequency-doubled Nd-YAG laser. A 532.2 nm wavelength (green laser) was used for radiation. The laser beam was focused within the inclusions through an Olympus BX 40 microscope, applying a 40x and 100x magnification, combined with a confocal optical arrangement. A Linkam TMS 93 stage, attached to the Raman microprobe, enabled spectroscopic analysis at controlled temperatures. Raman spectra were measured in a time

span of 20 seconds at selected temperatures. The spectra were analysed for the peak positions with the LabSpec v.2.08 software. The background signal of the dolomite was subtracted from the fluid inclusion spectra for every spectrogram (Fig.3.4). The results were compared with already compiled tables for the most common substances (Samson & Walker 2000, Bakker 2002, 2004).
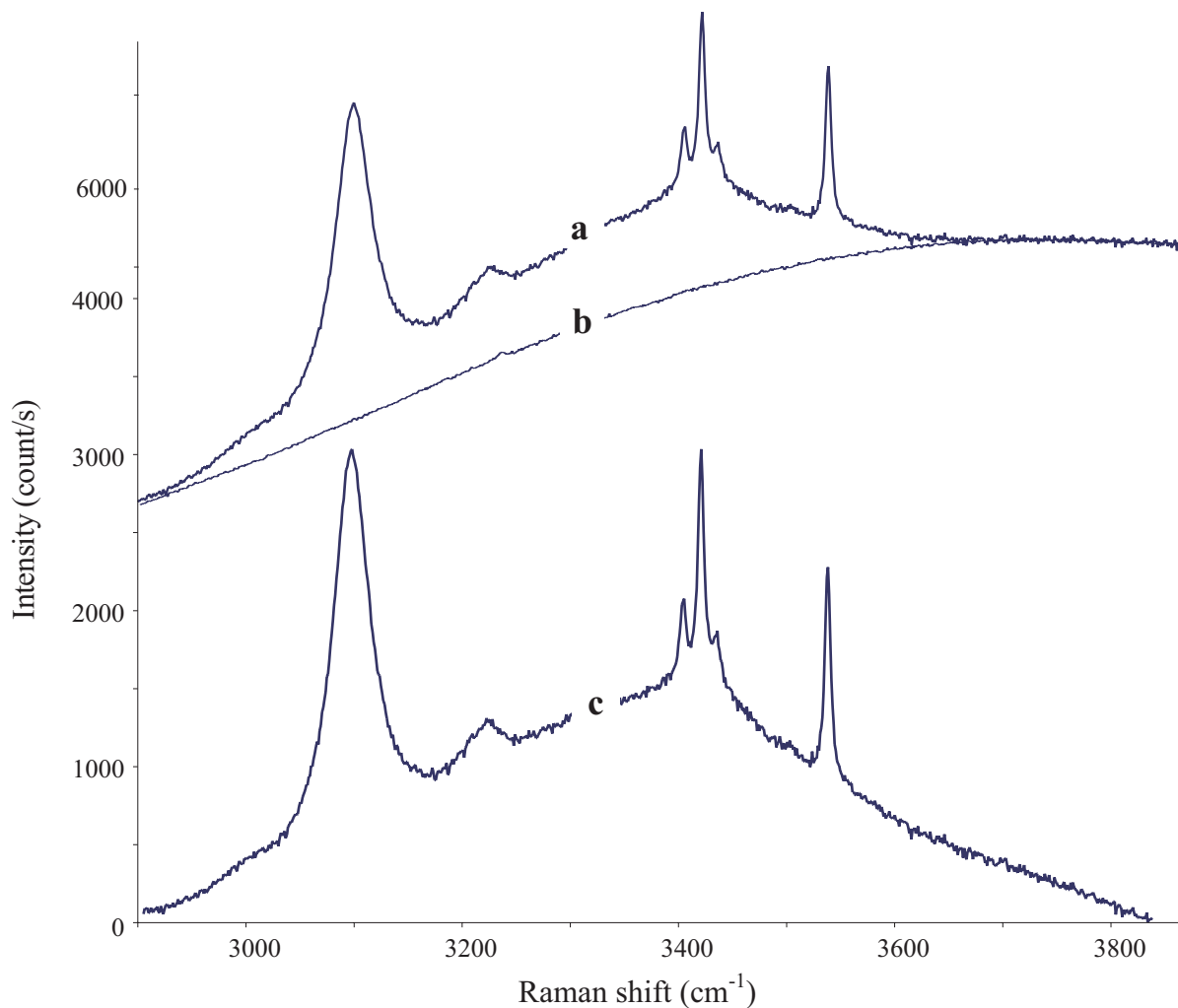
Fig. 3.4. Raman spectra measured (A) and calculated (C) by subtracting the background signal of the host mineral (B).

The measurements were performed on fluid inclusions near to the sample surface in order to reduce the high background signal of the host. Twelve inclusions were selected from a database of more than 100 inclusions where microthermometric data are available.

Two different types of heating/cooling experiments were carried out for comparison, in order to recognize different stable and metastable assemblages:

1) **normal heating-cooling procedure**, including fast cooling down to -190°C and then reheating up to the temperature of melting a specific phase;

2) **composite heating-cooling procedure**, during which reheating reached -50°C, followed by cooling down again to -190°C.

The composite procedure enhances nucleation and generates stable phase configurations at selected temperatures. Exact melting temperatures are obtained from the analysis of Raman spectra at low temperatures, after rapid cooling following a supposed melting event. This method uses the metastable absence of phases to identify melting temperatures.

3.8.3. Crush-leach analyses

The crush-leach analysis procedure (Roedder 1984, Banks and Yardley 1992) is a bulk destructive method, which permits determination of the solute content of all the fluid inclusion populations present in a mineral. In particular, the halogen ratios (such as Br/Cl) give important information about the origin and the water/rock interaction of the fluid system.

The crush-leach method has some limitations: it is a bulk analytical method, which cannot discriminate between the presence of more than one fluid inclusion generation. This limitation can be overcome by working with very well characterized material containing only a single fluid inclusion population. Furthermore, it is a destructive method, which does not allow repetitive measurements.

Crush-leach does not provide absolute values but only elemental ratios, due to the inability of calculating the amount of fluid leached during the laboratory procedure. Absolute concentration can only be estimated using the model salinity calculated by means of low temperature microthermometry. These values usually represent an approximation, especially when dealing with complex diagenetic systems.

Crush-leach analyses were performed at the University of Leeds, UK, on 18 dolomite samples. The samples were crushed and handpicked under a binocular microscope in order to remove contaminant material. Samples were then boiled three times in 18.2 MΩ deionized water and dried prior to analysis. About 0.5 grams were crushed in an agate mortar and the powder transferred to a small polycarbonate container. Between 5 and 7 ml of water was added to the sample, which after shaking was filtered through a 0.2 µm nylon filter prior to analysis. For Ca and Mg analyses, samples were crushed in a pestle and mortar containing 10-15 mls of dried methanol. As water and methanol are miscible, the content of the inclusions when opened are dissolved in the methanol. The methanol will not dissolve sample matrix, as carbonates are not soluble in it. The methanol is then separated by filtering through 0.2 micron nylon filter and evaporated slowly to dryness. Once dry, the residue is re-dissolved in 5 ml of Milli Q de-ionised water and treated as per normal crush leach solutions. Cl and Br were measured by ion chromatography and Na, K, Ca, Mg and Li were analysed by flame emission spectroscopy ($LaCl_3$ was added to give concentration of 200 ppm La to prevent ionization of the alkalis during analysis).

3.8.4. P-t trapping condition modelling

The burial depth of dolomite formation can be estimated by mean of thermodynamic properties of the fluid trapped into inclusions. The fluid inclusions must, however, fulfill several requirements:

1) the volume of the inclusions remains constant (isochoric) since entrapment;

2) the inclusions represent a closed (isoplethic) system from the time of entrapment.
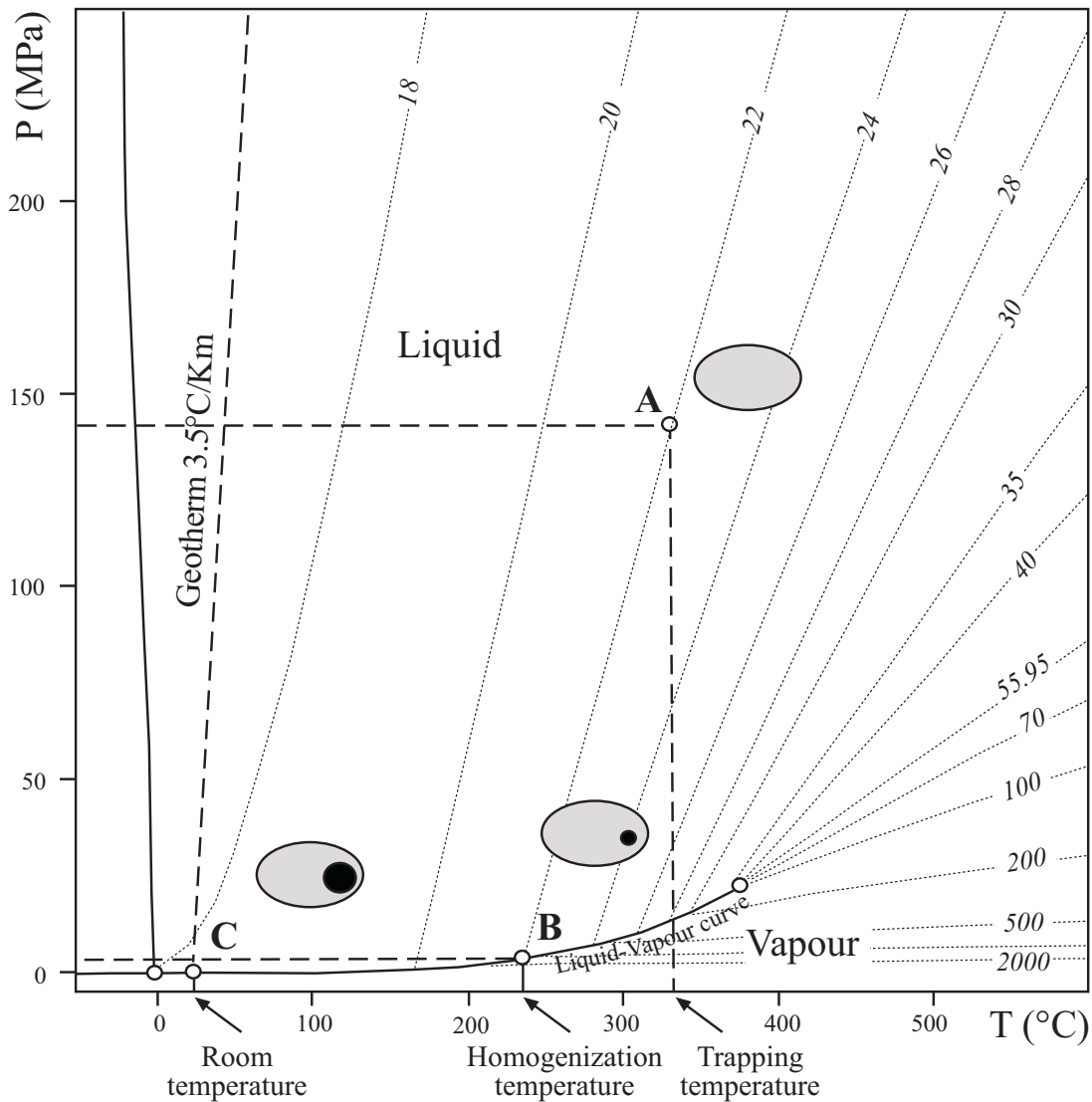
Fig. 3.5. P-T plot showing the cooling path of an imaginary FI from trapping conditions (A) towards surface conditions (C).

This thermodynamic model is of course applicable only within certain approximation but these requirements are most likely present in the diagenetic environment. At the time of trapping, an aqueous fluid inclusion, which homogenizes into liquid at a temperature lower than 374°C (the critical temperature of water), consists of a single homogeneous liquid phase (point A in Fig.3.5). During subsequent cooling, for example as a consequence of uplift, the fluid inclusion is forced to follow a determinate P-t path called isochore (a line of constant molar volume), until it crosses the liquid-vapour curve (point B in Fig.3.5). At this point a vapour bubble should theoretically segregate into the inclusion

(in practice, for kinetic reason, the vapour bubble will form at lower temperature). From this point the fluid inclusion will follow the liquid-vapour curve until it reaches the room P-t conditions.

This process is reversed in the laboratory to measure the homogenization temperature, which corresponds to a minimum trapping temperature of the inclusion. To calculate the real trapping temperature of the inclusions it is necessary to apply the so-called "pressure-correction". Knowing the density and the composition of the fluid inclusions, it is possible to construct the isochores for the systems by mean of thermodynamic equations. It is necessary to assume a thermobaric gradient consistent with the geological setting. The trapping pressure and temperature of the fluid inclusions will result from the intersection between the isochores and the gradient.

3.8.5. Thermodynamic calculations and computer modelling

Microthermometry data were used to determine the bulk composition and density of the fluids trapped within the inclusions, by means of the computer package *FLUIDS* (Bakker 2003). Salinities were calculated in the ternary H_2O–$NaCl$-$CaCl_2$ (Nader 1996), and in the binary H_2O-$CaCl_2$ systems, using the program *AqSo2*. The bulk fluid properties (density) were calculated using the *Bulk* program, using a purely empirical thermodynamic model (Krumgalz et al. 1996) and the volume fractions of the liquid phase of the inclusions at room temperature. Isochores were calculated with the *ISOC* program and the equation of state of Zhang and Frantz (1987), which requires the homogenization temperature (T_H), the salinity of the inclusions and the bulk fluid density. Thermodynamic modeling depends on microthermometry (homogenization temperature and model composition) and petrographic data (fluid/gas ratios), particularly in complex fluid systems. Therefore, a careful petrographic and microthermometric study represents the starting point for any accurate and meaningful fluid inclusion study.

Chapter 4 - Dolomite distribution and petrography

4.1. The study area

The study area is located in the Correcilla and Bodón Units, in the southern part of the Cantabrian Zone (Fig. 4.1). To the west the working area is approximately delimited by the River (Rio) Luna, to the east by the River (Rio) Curueño, to the north by the León Line and the Central Coal Basin Unit, and to the south by the Meso-Cenozoic cover of the Duero Basin (Fig. 4.2).
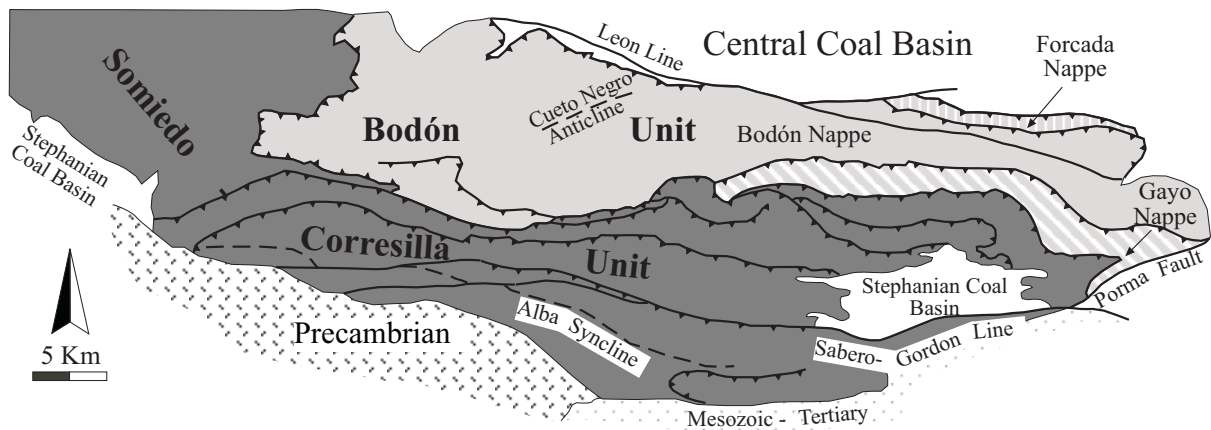
Fig. 4.1. Structural sketch of the southern branch of the Cantabrian Zone, showing the different tectonic units present in the study area.

The main topic of this thesis is the epigenetic dolomitization event which affected the Láncara Formation (Lower-Middle Cambrian) in this area. Dolomites with similar characteristics, from the the Namurian-Westphalian A carbonates of the Barcaliente and Valdeteja Fms., have also been described by Gasparrini (2003) and Gasparrini et al. (2006b). For my study, rocks of dolomitized and undolomitized lithologies were sampled in 29 different localities in the Correcilla and Bodón Units (Fig. 4.2 and Tab. 4.1).

In the study area, the Láncara Fm. crops out in the Bodón Unit along the thrusts which separate the Central Coal Basin from the the Bodón and the Forcada Nappes and the Bodón Nappe from the Gayo Nappe (Fig. 4.1). Inside the Bodón Nappe, the Láncara Fm. crops out in the Cueto Negro anticline (Fig. 4.1). The Láncara Fm. is present continuously at the base of the Correcilla Unit, corresponding to the thrust front of this unit over the Bodón Unit. In the southern part of the Correcilla Unit, the Láncara Fm. overlays the Herrería Formation, which has a regional intra-Proterozoic unconformity at its base (along the flank of the Narcea Antiform).

4.2. Stratigraphy of the Láncara Fm.

n.	Locality	Tectonic Unit
1	Torrestio	Somiedo-Correcilla
2	Genestosa	Somiedo-Correcilla
3	Cospedal	Somiedo-Correcilla
4	Torre de Babia	Somiedo-Correcilla
5	Riolago	Somiedo-Correcilla
6	Villasecino	Somiedo-Correcilla
7	Rabanal de Luna	Somiedo-Correcilla
8	Barrios de Luna	Somiedo-Correcilla
9	Láncara de Luna	Somiedo-Correcilla
10	Aralla (Tunnel)	Somiedo-Correcilla
11	Viadango	Sobia- Bodón
12	Casares de Arbas	Somiedo-Correcilla
13	San Martín de la Tercia	Somiedo-Correcilla
14	Rodiezmo (Cruz)	Somiedo-Correcilla
15	Campolongo	Sobia- Bodón
16	Fontún	Somiedo-Correcilla
17	Ciñera	Somiedo-Correcilla
18	Valle de Vegacervera	Somiedo-Correcilla
19	Gete	Somiedo-Correcilla
20	Carmenes	Sobia-Bodón
21	León Line	Sobia-Bodón
22	Villanueva de Pontedo	Sobia-Bodón
23	Canseco	Sobia-Bodón
24	Llamazares	Sobia-Bodón
25	Cueto Arcuno	Sobia-Bodón
26	Valdorría	Somiedo-Correcilla
27	Nocedo de Curueño	Somiedo-Correcilla
28	Montuerto	Somiedo-Correcilla
29	Valdepielago	Somiedo-Correcilla

Tab. 4.1. Sampled localities and the corresponding tectonic units (see Fig. 4.1)

The Láncara Fm. extends throughout all the Cantabrian Zone. It consists of shallow water platform carbonates with a highly variable thickness due to the fact that the lower part usually corresponds to the detachment level of the main Variscan thrusts (Fig. 4.3A).

The Láncara Fm. is divided into two members (Zamarreño 1972), differing in their lithological characteristics and representing two different sedimentary depositional environments, which can be easily visualized in the field due to their different colour (grey for the lower member and red for the upper member, Fig. 4.3B). The two members have the same constant characteristics with certain lateral changes.

The lower member is composed of yellow, laminated, often stromatolitic dolostone and grey birdseye limestone (Figs. 4.3C and 4.3D). The depositional environment corresponds to tidal flats.

The upper member is usually constituted of a few meters of glauconitic echinoderm-rich pack- to grainstone (Fig. 4.3E), overlain by more micritic, nodular, generally red limestone (wacke- to packstone), the so-called Cambrian *griotte* (Fig. 4.3F), which represents a condensed succession in analogy with the Devonian *griotte*.

A generation of epigenetic dolomite is also present throughout the Láncara Fm. It usually replaces the facies originally devoid of dolomites, such as the grey birdseye limestone and the glauconitic crinoidal limestones of the upper member, never affecting the *griotte*.

The dolomite of the lower member is probably of early diagenetic origin, which is consistent with a tidal depositional environment. In this member, laminations, usually due to microbial mats, are easily

Fig. 4.3. A) Variscan detachment level thrusting the Cambrian Láncara Fm. over the Carboniferous San Emiliano Fm.; B) typical succession of the Láncara Fm. composed of two easily recognizable members, the grey lower member and the red upper member; C) yellow, laminated, often stromatolitic dolostone of the lower part of the lower member of the Láncara Fm.; D) grey birdseye limestone typical of the upper part of the lower member of the Láncara Fm., E) glauconitic echinoderm-rich pack- to grainstone, which often occurs in the lower part of the upper member of the Láncara Fm.; F) red nodular limestone (the so-called griotte), which typically constitutes the upper member of the Láncara Fm.

recognizable in the field on weathered surfaces (Fig. 4.4A). These mats are often alternating with more detritic intervals composed of pellets, in part derived from the erosion of the mats (Fig. 4.4B). Birdseyes are abundant in the laminated dolomites and are recognizable only in thin sections.
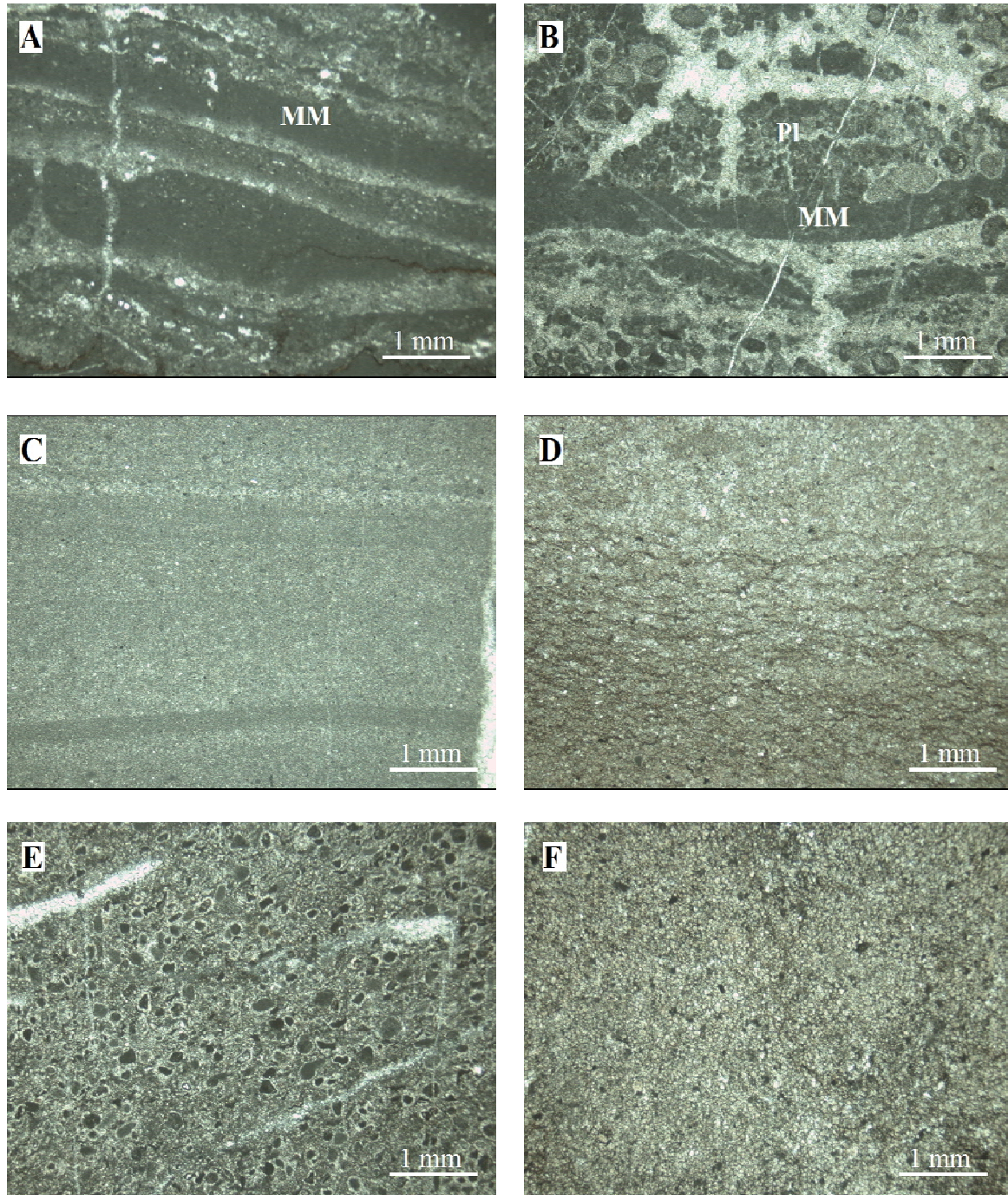
Fig. 4.4. Microphotographs showing different lithological types of the lower member dolostone: A) laminations of organic origin; B) alternation of microbial mats (MM) with more detritic intervals composed of pellets (Pl) with abundant birdseyes (BE); C) laminations of inorganic origin, related to alternating *laminae* of different grain size; D) lamination of inorganic origin, caused by abundant stylolites; E) pelsparite typical of the lower member dolostone; F) more homogeneous textures related to recrystallization of precursor textures.

Laminations can also have an inorganic origin, related to alternating *laminae* of different grain size (Fig. 4.4C), or to the presence of abundant stylolites (Fig. 4.4D). Pelsparite (Fig. 4.4E) occurs frequently. The lower member dolostone shows also more homogeneous textures, which may be
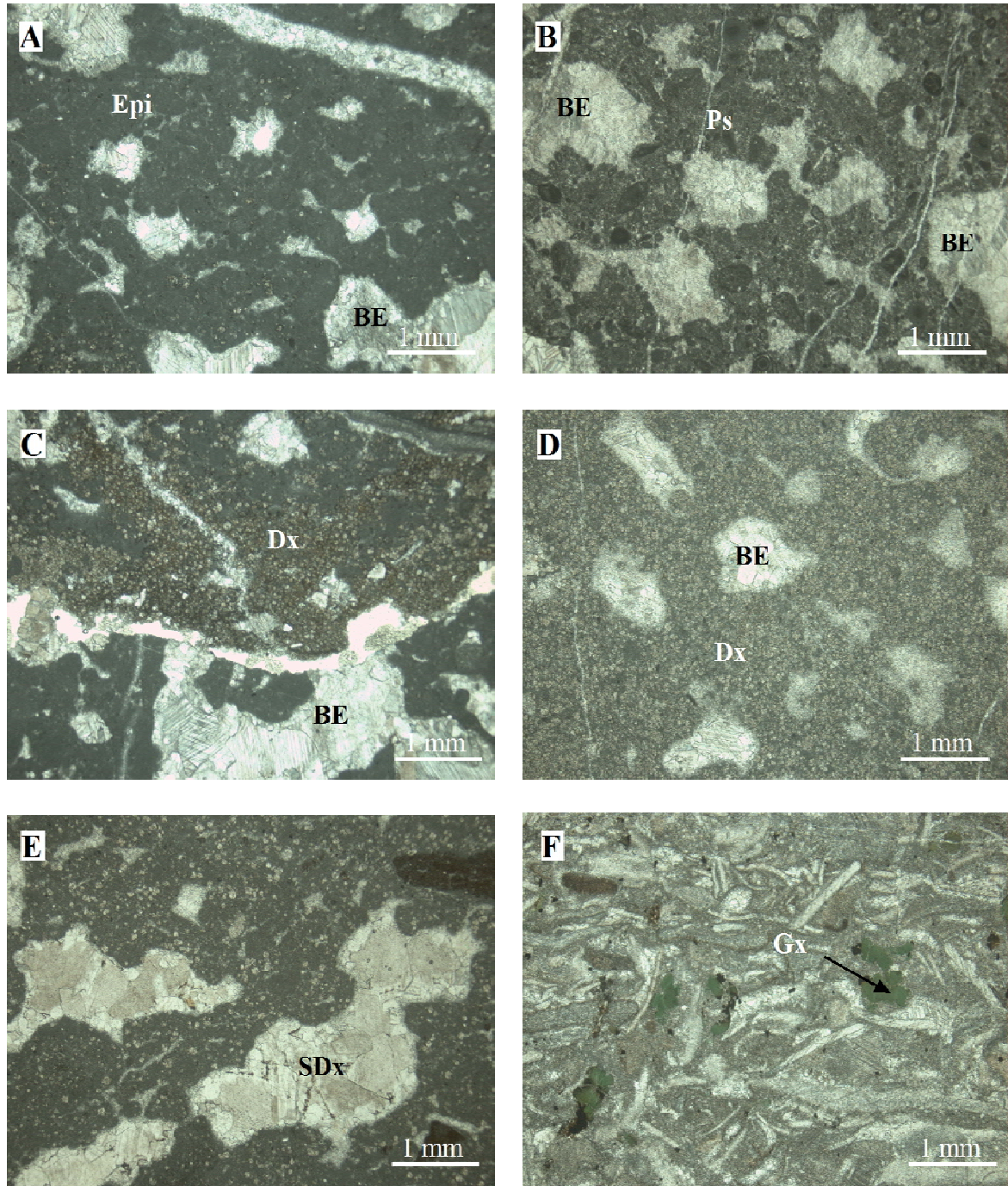
Fig. 4.5. Microphotographs showing different lithological types of the lower and upper member limestones. A) Grey birdseye (BE) limestone consisting mainly of the calcareous algae *Epiphyton* (Epi); B) pisolitic (Ps) grey birdseye limestone, which are also common in the upper part of the lower member of the Láncara Fm.; C) grey birdseye limestone partly replaced by dolomite, in particular along stylolites; D) fine-crystalline dolomite (Dx) totally replacing the precursor limestone: the fenestral cavities, filled by different generations of calcite cements, remain undolomitized; E) fenestral cavities partly or totally filled by coarse saddle dolomite crystals (SDx); F) upper member glauconite-rich (Gx) pack- to grainstone, constituted by fragments of brachiopods, trilobites and echinoderms.

related to recrystallization of precursor fabrics (Fig. 4.4F). Only rarely, the epigenetic dolomitization was observed replacing the lower member dolostone.
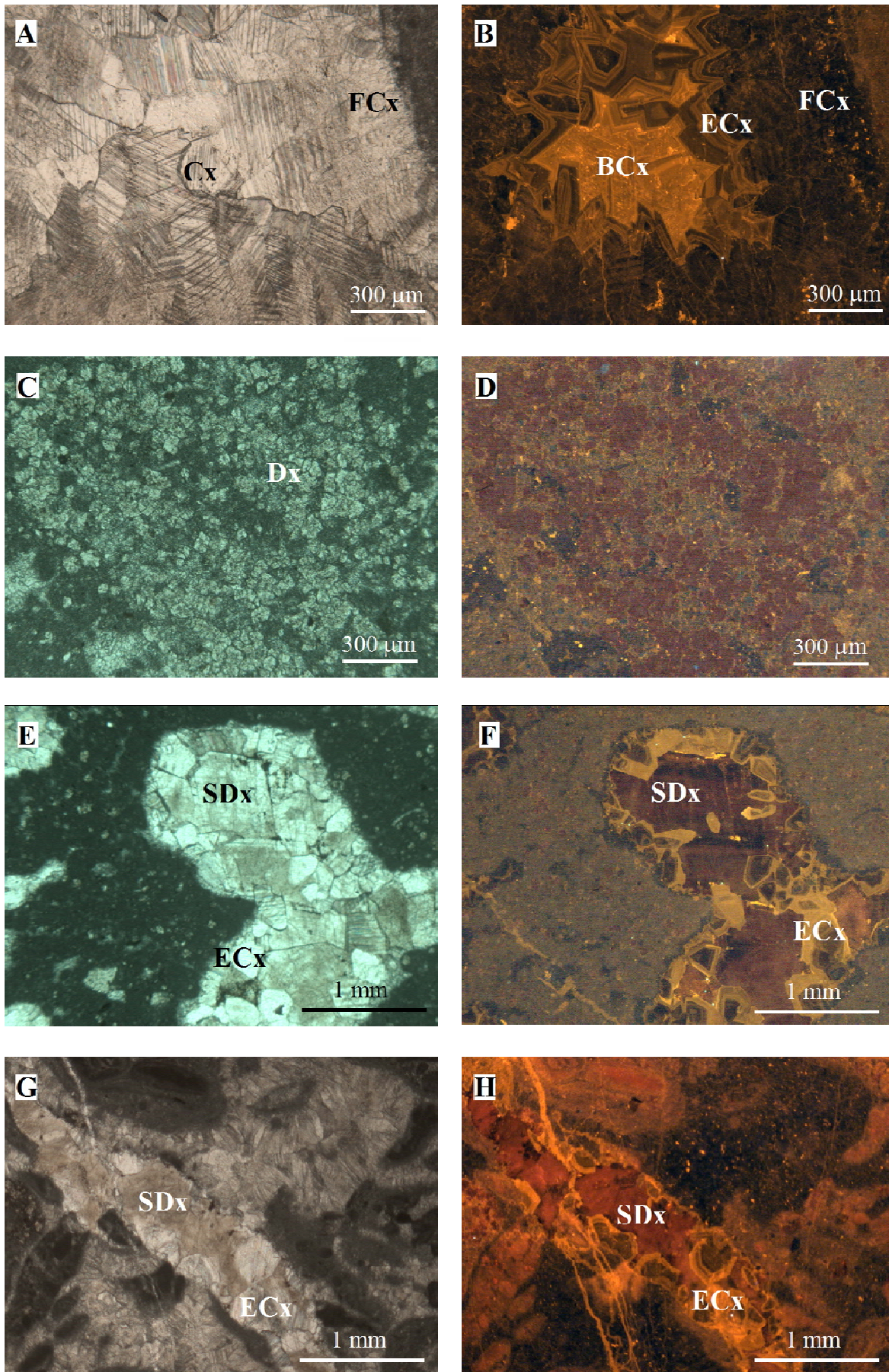
Fig. 4.6. Caption see next page.

The upper part of the lower member consists of the grey birdseye limestone, which overlies the dolostone in some localities. The main component of the limestone is the calcareous algae *Epiphyton* (Fig. 4.5A). Pisolitic layers are also common (Fig. 4.5B).

Birdseyes (*fenestrae)* are abundant and are usually filled with two generations of calcite cements: fibrous calcite, lining the cavity walls, and blocky calcite, completely occluding the remnant volume.

The grey birdseye limestone may be partly replaced by dolomite, in particular along stylolites (Fig. 4.5C). A fine-crystalline dolomite may also totally replace the precursor limestone (Fig. 4.5D). Fenestral cavitiy cements may remain undolomitized in the dolomitized matrix (Fig. 4.5D) or they may be partly or totally filled by coarse saddle dolomite crystals (Fig. 4.5E).

The upper member is constituted by a few meters of glauconite-rich pack- to grainstone, including fragments of brachiopods, trilobites and echinoderms (Fig. 4.5F), overlain by red nodular limestone (the already mentioned Cambrian *Griotte)*. In cathodoluminescence, three generations of fenestral calcite cements can be recognized (Figs. 4.6A and 4.6B): 1) fibrous calcite with a red-dull, non luminescent colour, 2) finely zoned orange luminescent equant calcite, and 3) blocky, homogeneous orange luminescent calcite.

The matrix replacive dolomite crystals show a red dull-non luminescent colour (Figs. 4.6C and 4.6D).

A coarse crystalline dolomite phase, which fill and/or replace previous fenestral calcite cement (Figs. 4.6E and 4.6F) or form veins crosscutting the fenestral cavities, (Figs. 4.6G and 4.6H) also show red dull-non luminescent colour. These dolomite crystals are characterized by curved crystal margins and by sweeping undulose extinction typical of the *saddle dolomites* (Radke and Mathis 1980), and are usually associated with the equant calcite cement phase, but never with the orange luminescent blocky calcite cements.

Fig. 4.6. Microphotographs see previous page. Normal petrographic and cathodoluminescence microphotographs showing different cement phases typical of the Láncara Fm. A) and B) different generation of calcite cements filling the fenestral cavities: fibrous calcite (FCx), characterized by a red-dull, non luminescent colour; finely zoned orange luminescent equant calcite (ECx) and blocky homogeneous orange luminescent calcite (BCx); C) and D) matrix replacive dolomite crystals characterized by a red dull-non luminescent colour; E) and F) saddle dolomite cements (SDx) filling and /or replacing previous fenestral calcite cements; G) and H) red dull-non luminescent saddle dolomite cements in veins, crosscutting the fenestral cavities.

4.3. Epigenetic Dolomitization

4.3.1. Field observations

The late dolomitization event affecting the Láncara Fm. is petrographically distinct from the dolomitization occurring in the stromatolitic carbonates constituting the lower member of this formation. It shows many similarities with the dolomite type replacing the Carboniferous limestones described by Gasparrini et al. (2006b): e.g. presence of zebra structures, coarse crystal size, abundant saddle dolomite cements, destruction of the precursor limestone textures, same weathering colour, distinct secondary porosity.

Volumetrically, the single dolomitized bodies do not exceed a few hundreds of cubic meters but crop out regularly in the study area (Fig. 4.7A). The dolomitization event affects firstly the glauconitic biomicrite facies of the upper member, and secondly the grey limestone facies of the lower member.

The recognition of the dolomite bodies in the field is facilitated by the strong colour contrast between the dark altered dolomitized lithology and the light coloured undolomitized lithology (Fig. 4.7A). The contact between the dolomitized and undolomitized rocks is sharp, resolving in a transition zone of a few centimetres thickness only (Fig. 4.7B). The dolomite front can also follow previous discontinuities of the precursor lithology, such as bedding planes, which probably acted as conduits for the dolomitizing fluids (Fig. 4.7C). On the other hand, the dolomite fronts frequently crosscut the same planes (Fig. 4.7D).

The epigenetic dolomite is always associated with abundant saddle dolomite (Fig. 4.7E). Zebra structures are also common (Fig. 4.7F).

At the hand specimen scale, two different generations of dolomite can be easily distinguished (Fig. 4.8A): 1) a **matrix-replacive** dolomite, which is usually variably grey to beige; 2) a **void-filling** coarser, white dolomite. The two phases are named respectively dolomite A (**Dol A**) and dolomite B (**Dol B**), following the nomenclature used by Gasparrini et al. (2006b) for the description of the dolomite types in the Carboniferous succession. The two phases can be rhythmically repeated in an A-B-A-B succession typical of zebra structures (Fig. 4.8B). Alternatively, Dol B may have irregular shapes (Figs. 4.8A, 4.8C and 4.8D) and may mimic the precursor birdseye limestone texture (Fig. 4.8E).

A dolomitic zebra consists of several tens of parallel veins of dolomite that are often remarkably equidistant. The thickness of the single veins is in the same order of the spacing between them. Each vein consists of two halves that leave a seam (Fig. 4.7G) along the centre, each half consisting of subhedral or euhedral saddle dolomite crystals. Zebra textures are typical of burial dolomites (e.g. Nielsen et al. 1998, Boni et al. 2000) but also of other minerals, such as magnesite (Lugli et al. 2003), talc (Tornos and Spiro 2000), fluorite (Zeeh 1995, Fontboté and Amstutz 1980), and the sulphides in the MVT deposits (Wallace et al. 1994). The remarkable regularity of the veining might indicate that these structures formed by some kind of self-organization (Merino 1984, Fontboté 1993).

Zebras in the dolomitized Láncara Fm. are always associated with macroporosity of secondary origin. The generation of macropores during dolomitization is confirmed by the fact that porosity is very
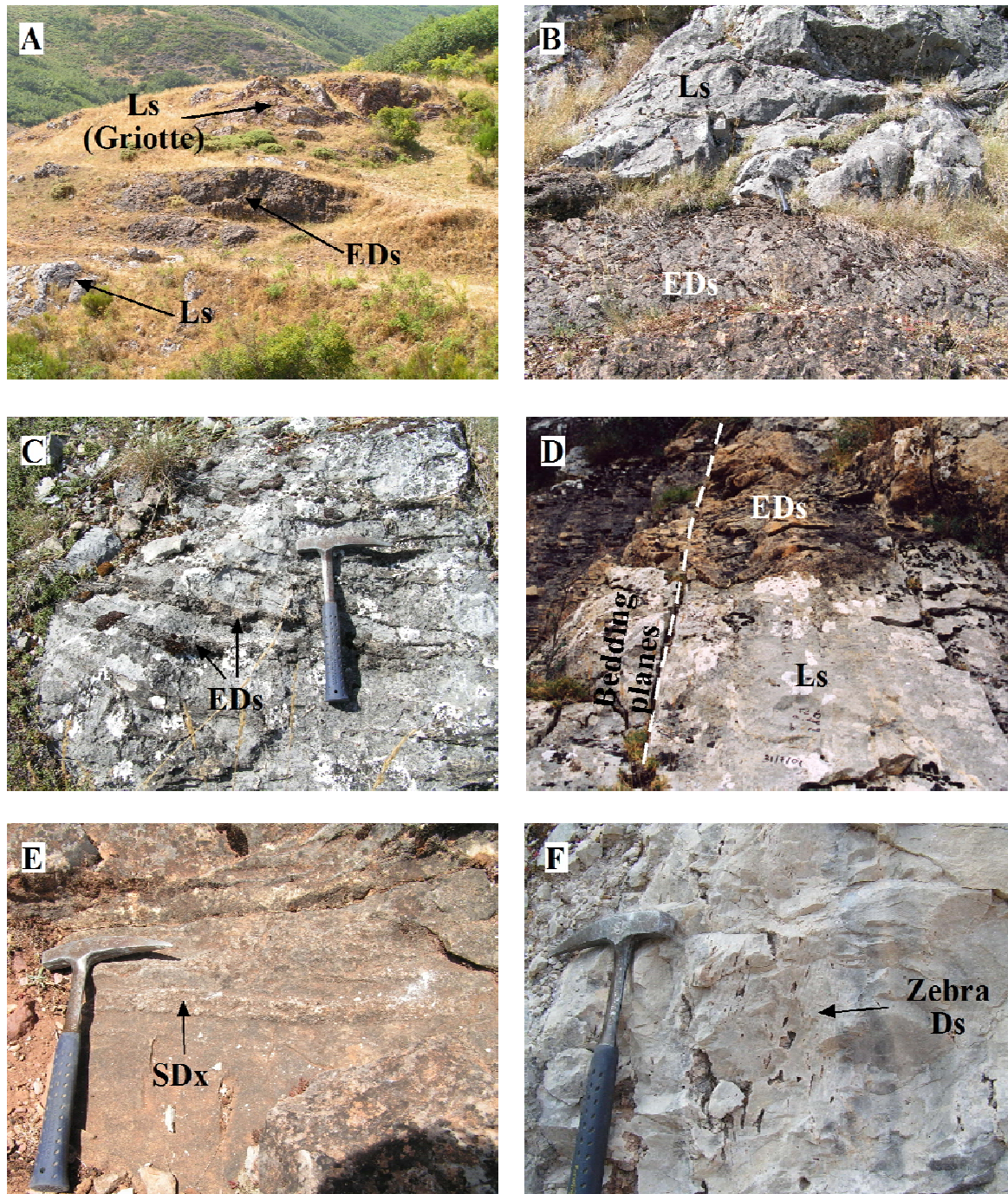
Fig. 4.7. A) Epigenetic dolostone (EDs) replacing the glauconitic biomicrite facies of the upper member (*Griotte*); the recognition in the field of the dolomite bodies is facilitated by the strong colour contrast between the dark altered dolomitized lithologies and the light coloured undolomitized lithologies; B) sharp contact between the dolomitized (EDs) and undolomitized (Ls) rocks; C) dolomite front following previous discontinuities of the precursor lithology, such as bedding planes, which acted as fluid conduits; D) the dolomite front crosscuts bedding plains; E) saddle dolomite associated with the epigenetic dolomitization event; F) zebra structures commonly associated with the epigenetic dolomitization event.

low in the undolomitized lithologies and is limited to rock discontinuities such as stylolites, bedding planes and microfractures.
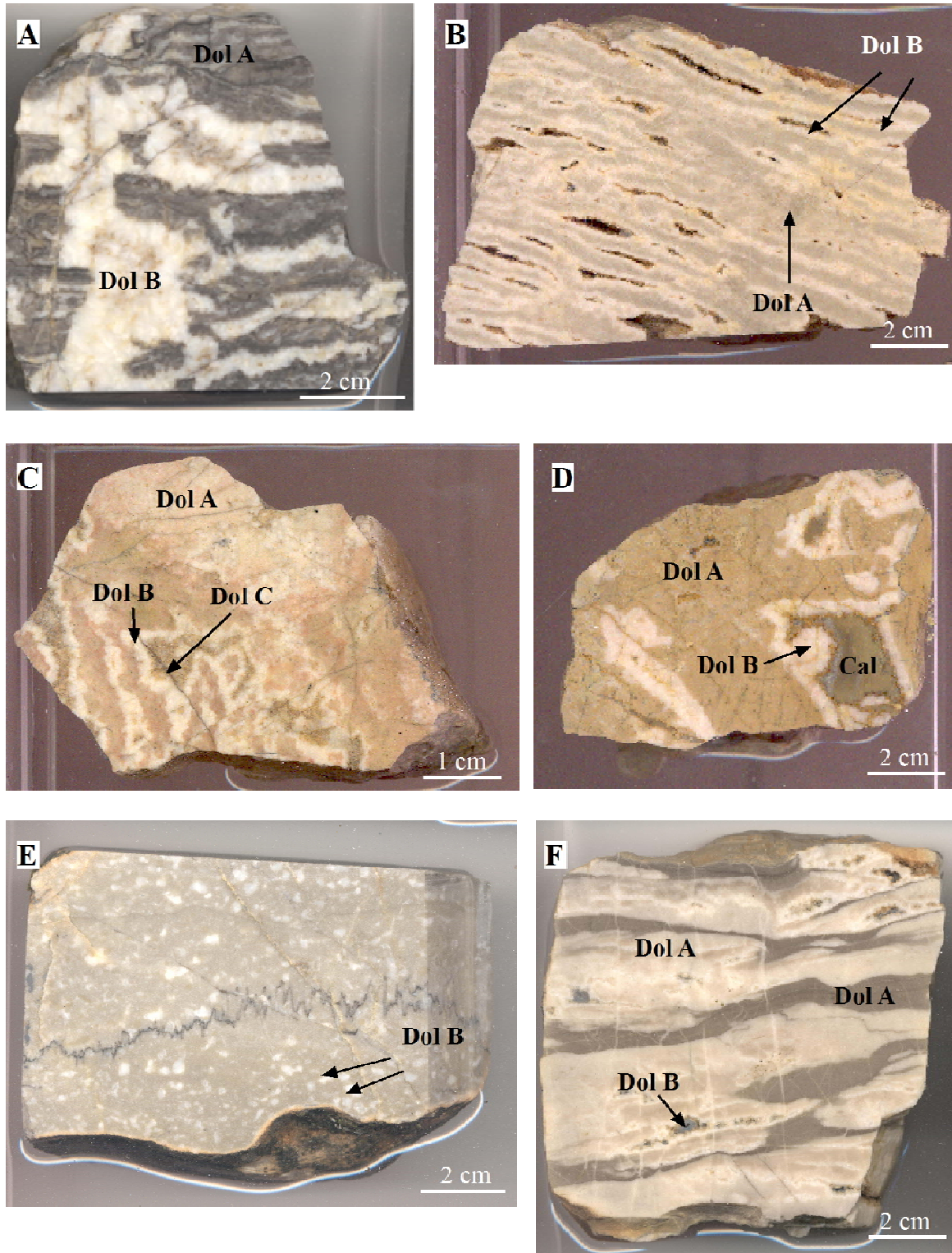
Fig. 4.8. A) Hand specimen showing two different generations of dolomite: a dark beige matrix-replacive dolomite (Dol A), and a void-filling coarser, white dolomite (Dol B); **B)** rhythmically repeated A-B-A-B succession typical of zebra structures, which are common in the epigenetic dolomite; **C)** and **D)** Dol B infill showing irregular (cavity-like) shapes; another generation of dolomite (Dol C) or calcite may follow the Dol B phase; **E)** Dol B mimicking the precursor birdseye texture of the limestone; **F)** epigenetic dolomitization recrystallizing the "early" dolostone facies of the lower member of the Láncara Formation.

Dol B is usually volumetrically less abundant relative to matrix-replacive Dol A, but locally (e.g. in the

sections Torrestio, Genestosa, Cospedal) it may reach 30% of the total dolomitized volume, as in the example shown in Fig. 4.8A.

Millimetre-scale pores and cavities, always associated with the zebra structures (Fig. 4.8B), may be totally occluded by the Dol B phases (Fig. 4.8A) or, alternatively, by a third reddish saddle dolomite generation (Fig. 4.8C) or by calcite cements (Fig. 4.8D).

Occasionally, the epigenetic dolomitization affected (recrystallized) the lower member "early" dolostone of the Láncara Fm. In this case, alternations of light and dark dolomite bands have been observed, which are due to distinctly different crystal sizes (Fig. 4.8F). The dark bands, consisting of tiny crystals, are considered as remnants of the previous fine-grained dolostone of the lower member, which were recrystallized to a minor extent. The Dol B void-filling phase occurs in the light bands, made up of coarser dolomite crystals.

4.3.2. Thin section microscopy

In thin section, Dol A forms a mosaic of medium-sized, coarse, interlocked, cloudy, subhedral to anhedral crystals, commonly characterized by abundant solid inclusions (Figs. 4.9A and 4.9B). These characteristics indicate that Dol A probably formed as replacement of the precursor calcium carbonate or, alternatively, as recrystallization of a preexisting (unstable?) dolomite phases.

According to the dolomite classification proposed by Sibley and Gregg (1987), the Dol A phase can be classified as non-planar. The modal size distribution is usually unimodal. Remnants of the undolomitized precursor lithology are absent. Dol A is fabric destructive; structures inherited from the precursor limestone are limited to components which were probably previously dolomitized (Fig. 4.9C). Stylolites are still visible after dolomitization, as in Fig. 4.8E, but their trace is smoothed and the dolomite crystals do not show any dissolution (Fig. 4.9D).

Dol B is a sparry dolomite (Fig. 4.9A), with a pore-lining, void-filling or fracture-filling fabric. It shows the crystal shape and sweeping extinction typical of saddle dolomite (Fig. 4.9B). The term "void-filling" is preferred to "cement" as the latter is referred exclusively to mineral phases that grow in open spaces; "void-filling" is a more general descriptive term, which can be used for mineral phases forming by replacement of previous cement phases as well. This xenotopic-C type of dolomite (nomenclature of Sibley and Gregg, 1987) usually lacks solid inclusions but may contain abundant fluid inclusions, giving a turbid appearance. The grain size increases gradually from the first crystal generation, which follows Dol A, toward the centre of the cavities. The polymodal grain size distribution may allow subdivision in different sub-generations, with the last one (Dol B II) having a clear inclusion-free rim (Fig. 4.9B) and being the only one where direct growth in an open space is likely.

The transition between the matrix-replacive Dol A and the void-filling Dol B is mostly gradual (not corresponding to a sharp pore-lining surface). Sharp transitions have also been observed, however. In CL, Dol A has a red to red-dull colour (Figs. 4.9E and 4.9F), which varies only slightly over the studied area. The fine-size dolomite bands, which were observed in the recrystallized lower member dolostone, show similar luminescence colour with some darker spots (Figs. 4.9G and 4.9H), probably representing partly recrystallized remnants of early dolomites.

Dol B is characterized by the same red to red-dull luminescence as Dol A, with the exception of the outer clear rim belonging to the mentioned Dol B II phase, which is less luminescent and shows a fine zonation (Figs .4.10A and 4.10B). Numerous micron sized brighter red spots were observed, which are interpreted as coherent planar defects (Barber et al. 1985). A more complex zonation has been locally observed, consisting of alternating inclusion-rich (Z1 and Z3) and inclusion-free (Z2 and Z4) growth zones, characterized by different cathodoluminescence patterns (Figs. 4.10C and 4.10D). This complex zonation is also observed under SEM (Figs. 4.10E and 4.10F) and under back-scatter cathololuminescence image (Figs. 4.10 G and H). The zoning is related to the high iron content of the brighter zones, which acts as quencher for cathodoluminescence.

Dol B II shows a stepwise shape (Fig. 4.11A). The outermost part of the inclusion-free rim of the Dol B II phase is often enriched by brownish iron oxy-hydroxides, which are associated with dedolomitized bands (Fig. 4.11B). The inclusion-free rim can also be replaced by sulphides (Figs. 4.11C, 4.11D, 4.11E and 4.11F). EDX combined with back-scattered images allows the identification of Cu-Fe sulphides (brighter colour in Fig. 4.11F), and oxides derived from the alteration of the sulphides (darker gray in Fig. 4.11F). Traces of Ni (point A in Fig. 4.11F) and As (point B in Fig. 4.11F) have been also detected.

Displacements of zoned Dol B II along microfractures are evident in cathodoluminescence images (Figs. 4.11G and H). The faulting took place during the crystal growth, as indicated by the fact that the displaced areas are subsequently followed by other zones which drape and level the crystal growth planes, indicating that these subsequent zones were clearly not affected by the fracturing. This cathodoluminescent pattern has been interpreted as the result of crystal growth during a tensional tectonic regime, which may account for the formation of zebra structures (Nielsen et al. 1998).

Dolomitization clearly enhanced porosity. Millimetre-scale cavities are abundant in the dolomitized lithologies (Figs. 4.8B and 4.8F) and are absent in the precursor limestone. Void-filling Dol B only locally occludes completely the pores, which may remain open or may be filled by different mineral phases. A third generation of dolomite (Dol C) is locally present, which postdates the Dol B phase (Fig. 4.8C) and fills the remaining open space. This dolomite, reddish in hand specimens (Fig. 4.8C), appears clear in thin section (Figs. 4.12A and 4.12B), due to the almost complete absence of fluid inclusions (only present along thin zones).

Fig. 4.9. Microphotographs see next page. A) and B) Microphotographs in parallel and crossed nicols showing the two different generations of dolomite: Dol A and Dol B. Dol A forms a mosaic of medium sized, coarse, interlocked, cloudy, subhedral to anhedral crystals. Dol B is a sparry dolomite occurring as a pore-lining, void-filling or fracture-filling cement with a sweeping extinction and the crystal shape typical of saddle dolomite. The grain size increases gradually from the first crystal generation, which follows Dol A, toward the centre of the cavities. The polymodal grain size distribution may allow subdivision of Dol B in different sub-generations, with the last one (Dol B II) having a clear inclusion-free rim; C) remnants of the precursor components; D) Stylolites visible in Dol A, showing a smoothed trace; evidence of dissolution of the dolomite crystals is absent; E and F) normal and cathodoluminescence microphotographs showing the typical red to red-dull colour of Dol A; G) and H) thin dolomite bands in the recrystallized lower member dolostone, showing a luminescence colour similar to Dol A with some darker spots.
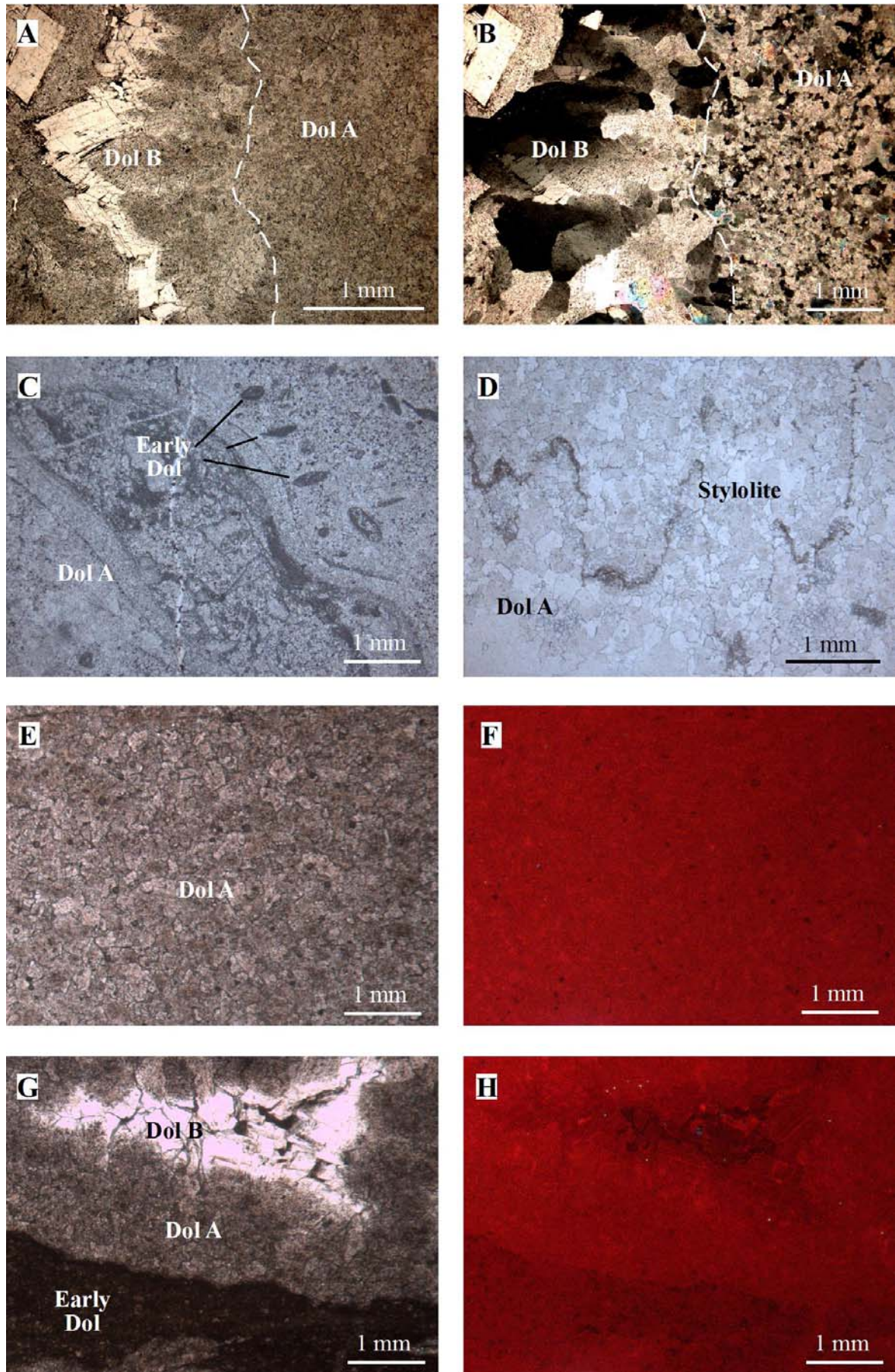
Fig. 4.9. Caption see previous page.
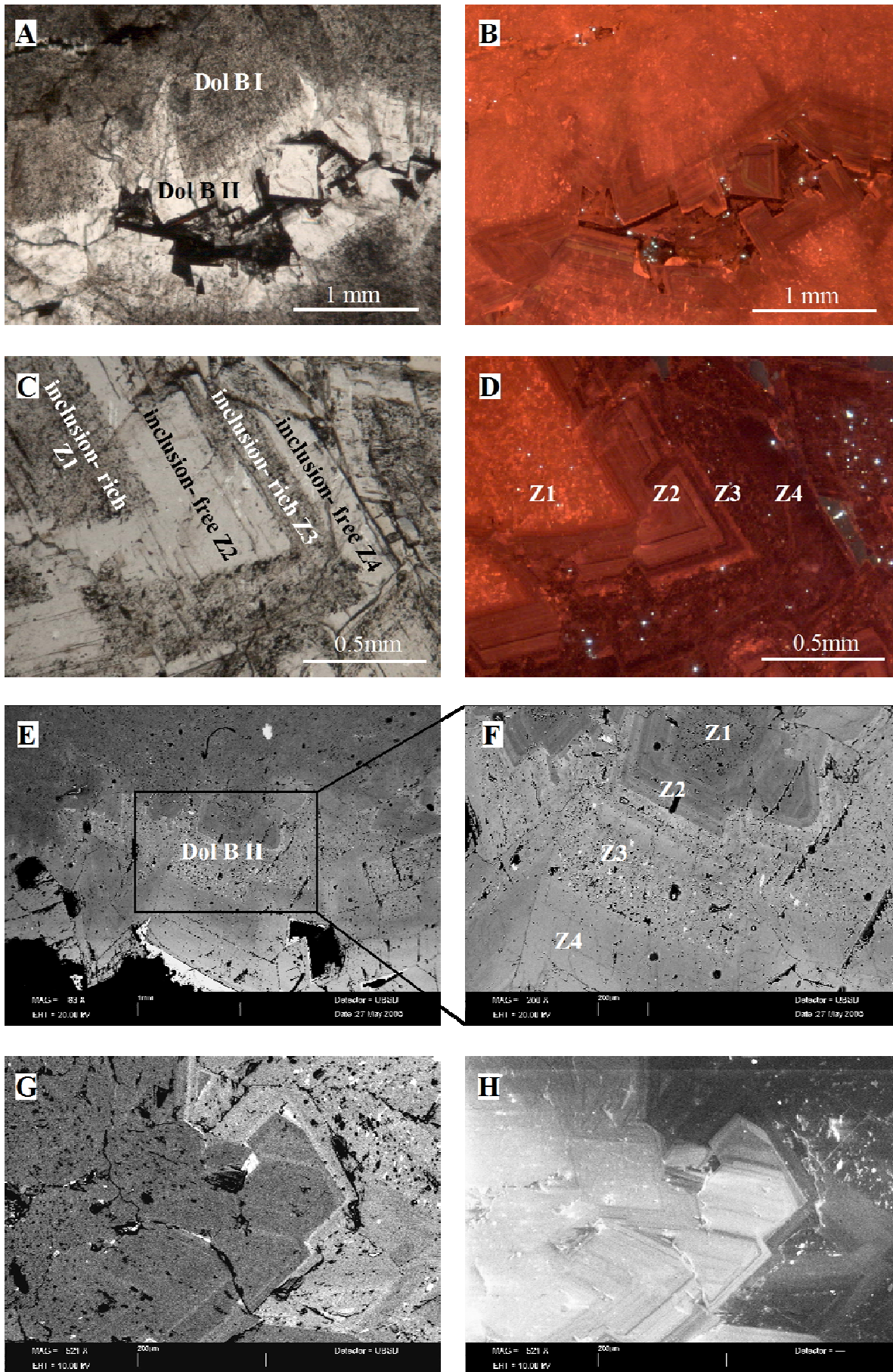
Fig. 4.10. Captions see next page.

The reddish colour is related to the presence of iron oxy-hydroxides associated to dedolomitized crystal zones (Figs. 4.12C and 4.12D), similar to those that characterise the outer rims of the Dol B II phase.

Under CL, the Dol C generally shows a homogeneous non-luminescent colour, with the exception of very tiny growth zones, which show a red to red-dull colour (similar to Dol B) and the inclusion-rich growth zones (Fig. 4.12E and Fig. 4.12F).

Cavities and pores in Dol B may also be filled by at least two different calcite generations (Cal I and Cal II in Figs. 4.13A and 4.13B) or, more rarely, by quartz (Fig. 4.13C). Internal sediments, which are the product of dedolomitization and dissolution of Dol B (Fig. 4.13D), have also been observed.

Fig. 4.10. Microphotographs see previous page. A) and B) Normal and cathodoluminescence microphotographs of Dol B, showing red to red-dull luminescence similar to Dol A, with the exception of the outer clear rim belonging to the Dol B II, which is less luminescent and shows a fine zonation. Numerous μm-sized brighter red spots were observed, which are explained as coherent planar defects (Barber et al. 1985); C) and D) complex cathodoluminescence zonation pattern of alternating inclusion-rich (Z1 and Z3) and inclusion-free (Z2 and Z4) growth zones; E) back scattering scanning electron microscope image showing the complex zonation pattern characteristic of Dol B, which is due to an alternation of Fe-rich (bright) and Fe-poor (dark) layers; F) particular of Fig. 4.10E; G) and H) back-scattering and cathodoluminescence images showing the typical compositional zonation of Dol B.

Fig. 4.11. Microphotographs see next page. A) Microphotograph of Dol B II phase showing a "stepwise" shape; B) microphotograph of the outermost part of the inclusion-free rim of Dol B II enriched by brownish iron oxy-hydroxides and associated with dedolomitized bands; C) and D) transmitted and reflected light microphotographs showing the inclusion-free rim of Dol B II replaced by sulphide phases; E) scanning electron microscope back scattering image of the sulphide phases associated to Dol B II; F) low contrast scanning electron microscope back scattering image showing the different sulphide phases. EDX allowed the identification of the composition of the different phases: Cu-Fe sulphides (brighter colour), and -oxides (darker gray). Traces of Ni (point A) and As (point B) have also been detected; G) and H) normal and cathodoluminescence microphotographs showing Dol B II zonations displaced along microfaults. The faulting took place during crystal growth, as indicated by displaced areas, subsequently followed by zones draping the previously deformed crystal growth planes. The latter, clearly not affected by the fracturing, are post-deformational.
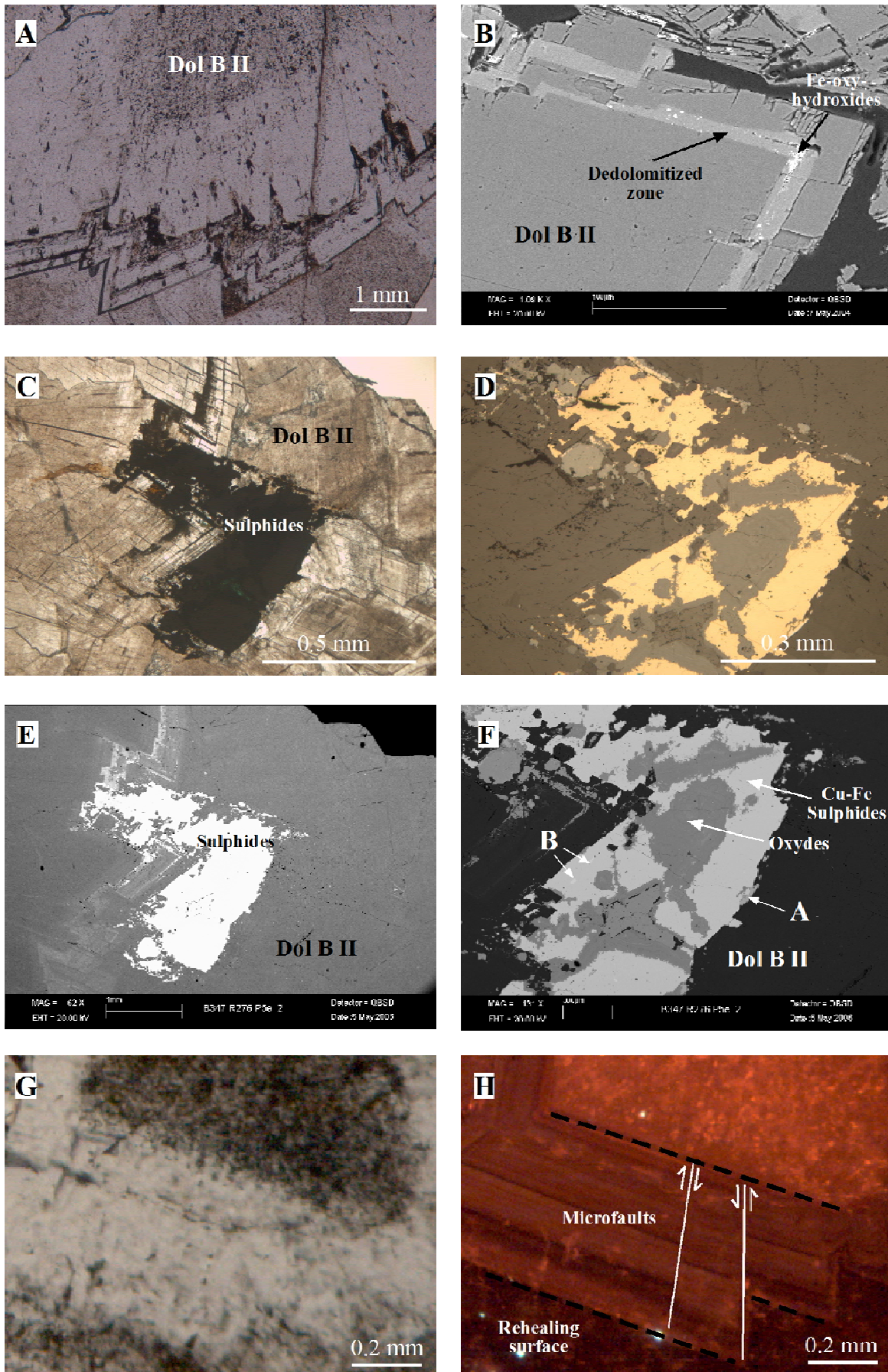
Fig. 4.11. Captions see previous page.
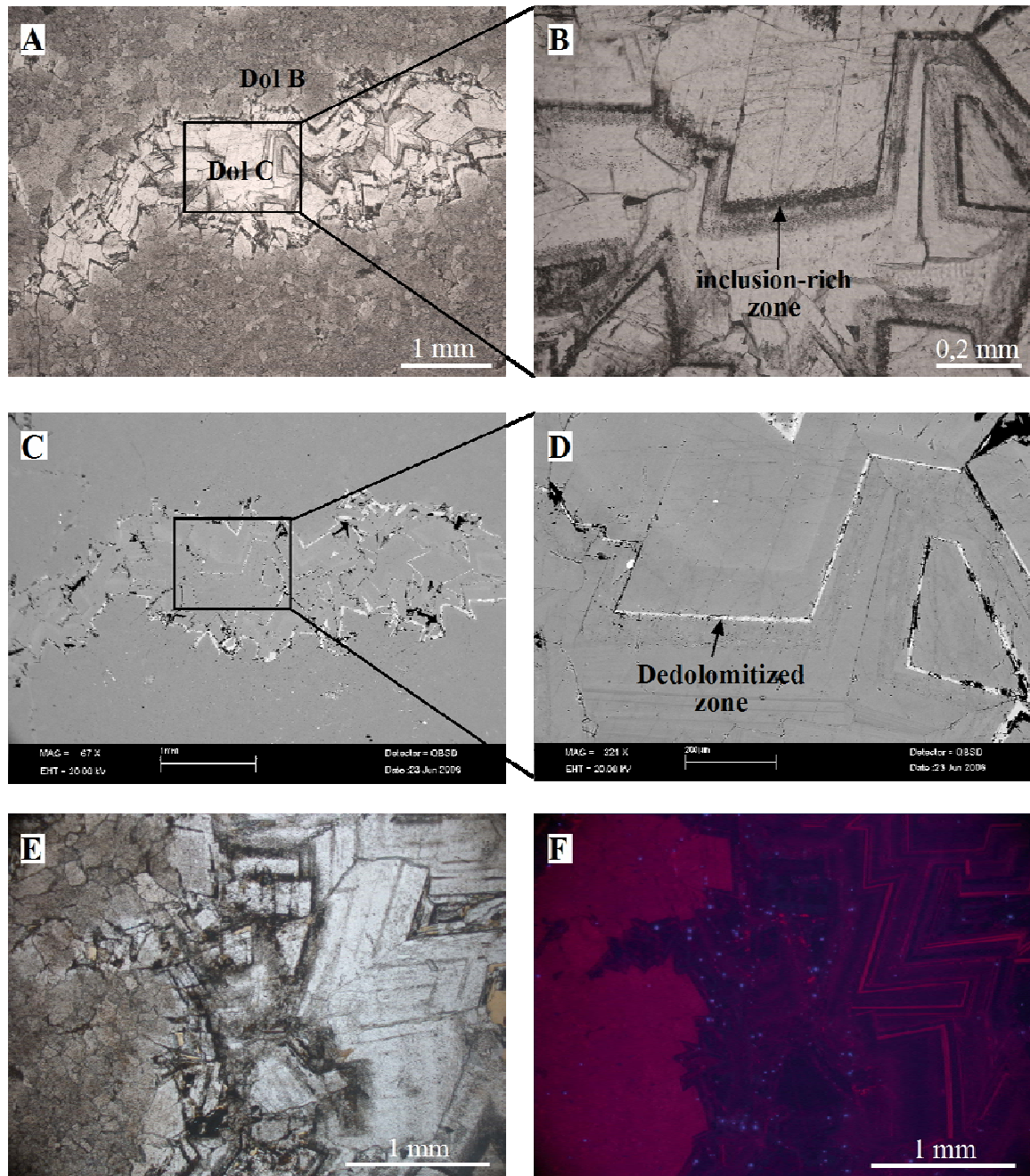
Fig. 4.12. A) Microphotograph showing a local, third generation of dolomite (Dol C) postdating Dol B. This dolomite, reddish in hand specimen, appears clear in thin section; B) particular of Fig. 4.12A; C) scanning electron microscope back scattering image showing the presence of iron oxy-hydroxide zones associated with dedolomitized crystal zones; D) particular of Fig. 4.12C; E) and F) normal and cathodoluminescence microphotograph of Dol C showing a homogeneous non-luminescent colour, with the exception of tiny growth zones, which show a red to red-dull colour, and the inclusion-rich growth zones.
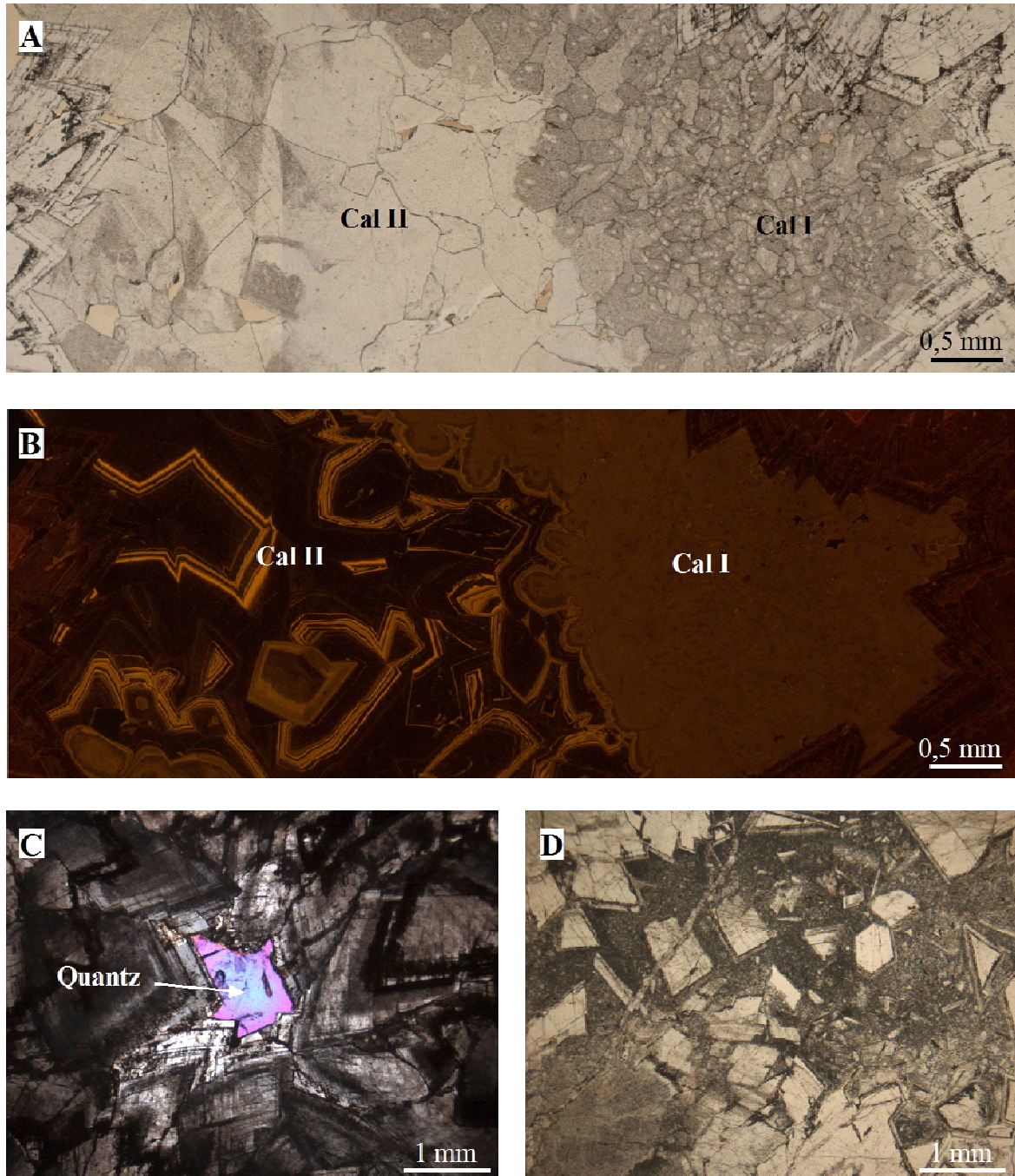
Fig. 4.13. A) and B) Normal and cathodoluminescence microphotographs showing two different calcite generations (Cal I and Cal II), filling the cavities and pores in Dol B; C) microphotographs showing quartz, filling the cavities in Dol B; D) microphotograph showing internal sediments, which are the product of dedolomitization and dissolution of the Dol B phase.

Chapter 5 - Geochemical study

5.1. Introduction

Several mineralogical (XRD) and geochemical methods of analysis (elemental composition, stable and radiogenic isotopic composition) have been applied in order to elucidate the dolomite origin and to distinguish between high temperature (burial) and low temperature (marine or early diagenetic) dolomite. As dolomite is usually a replacive mineral (this is valid in particular for the Dol A generation, see chapter 4), the data obtained are compared with the composition of the precursor carbonate rocks of the Láncara Fm., sampled in the proximity of the dolomite samples, in order to define the diagenetic system and the water/rock ratios. Since the original geochemical signature of the precursor carbonates was modified during burial, the measured data were also compared with the marine geochemical baseline for carbonates precipitated from Cambrian seawater and with other dolomites in other districts, whose origin was previously established by other authors.

5.2. XRD analyses

Fifty-two samples of Dol A, Dol B and fine-grained dolomite from the lower member of the Láncara Fm. were analysed for bulk mineralogy, stoichiometry and degree of order (OR).

The diffractograms obtained exhibit sharp diffraction peaks typical of the carbonates. All the parameters are reported in Appendix 1. The X-ray patterns obtained from the different dolomite phases do not show detectable remnants of the precursor calcite and consist of almost 100% dolomite.

In Fig. 5.1A the frequency histogram of the $CaCO_3$ content of Dol A and Dol B is plotted. The values range between 49.50 and 52.60 mole % (average 50.65). The degree of order (OR) is shown in Fig. 5.1B: the values vary between 0.42 and 0.97 (average 0.58). The values of the lower member dolostone are in general less stoichiometric and less ordered compared to Dol A and Dol B: the $CaCO_3$ content is between 49.60 and 53.10, with an average value of 51.31 (Fig. 5.1A); the degree of order ranges between 0.27 and 0.68 (average 0.51) (Fig. 5.1B).
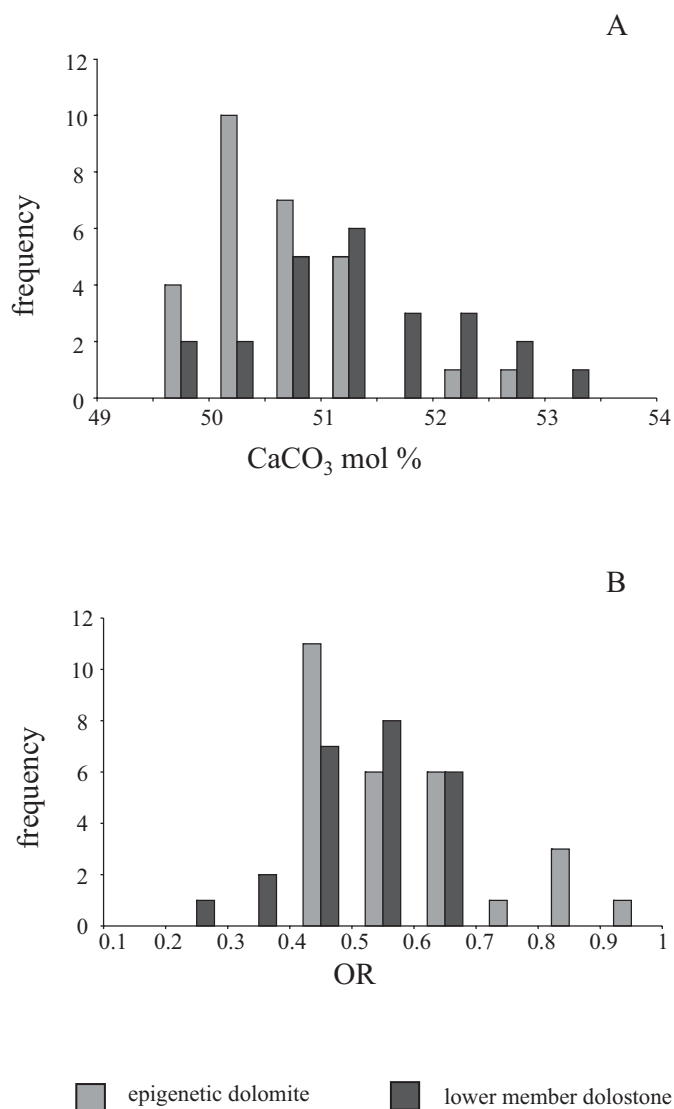
Fig. 5.1. X-ray analyses of different dolomite types of the Cambrian Láncara Fm. A) CaCO₃ content of epigenetic Dol A and Dol B and of the lower member dolostone; B) degree of order of epigenetic Dol A and Dol B as well as of the lower member dolostone.

The degree of order and stoichiometry are related to the precipitation rate, the Mg/Ca ratio and the salinity of the dolomitizing fluids. Near stoichiometric (50.0 to 51.0 mole % $CaCO_3$), well ordered dolomites may reflect slow growth from dilute solutions, possibly aided by relatively high temperature. Early diagenetic dolomites, associated with evaporites are also characterized by near stoichiometry, due to the high Mg/Ca ratios of the pore fluids. Early diagenetic dolostones, not associated with evaporates, are generally Ca-rich (54.0 to 56.0 mole % $CaCO_3$). In dolomites formed at temperatures above 100°C the degree of order should decrease with increasing temperature (Goldschmidt and Graf 1958b). In general, OR values less than 0.4 have been interpreted as typical of early diagenetic fine crystalline dolomite (Patterson 1972).

An effect of poor crystallographic order and non-stoichiometry is the metastability of the dolomite crystals and their more solubility compared to the "ideal" dolomite. The stabilization of Ca-rich dolomites into a more stoichiometric type would take place by dissolution-reprecipitation (solid state processes are usually too slow to be operative in diagenetic conditions) and may result in significant changes in trace element and stable isotope geochemistry of the dolomite.

Several authors (e.g. Füchtbauer and Goldsmith 1965, Sperber et al. 1984) observed a broad correlation between increasing stoichiometry and increasing crystal size. Regardless of the difference in crystal size, no difference has been observed between Dol A and Dol B, which show very similar values (see measured values in Appendix 1).

Petrographic observations indicate a burial origin of Dol A and Dol B. The XRD data are in agreement with this interpretation: the ample spread of the OR values (Fig.5.1B) may be the result of a complex interplay between the precipitation rate and the high salinity of the dolomitizing fluid.
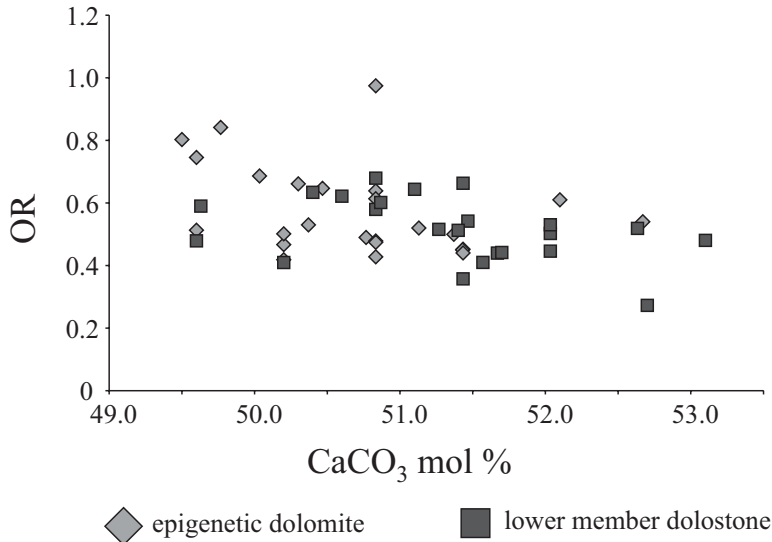
Fig. 5.2. CaCO3 content vs. degree of order (OR) of epigenetic Dol A and Dol B, as well as of the lower member dolostone.

In Fig. 5.2 the $CaCO_3$ content is plotted versus the degree of order of the epigenetic dolomites and the lower member dolostone. The field of the lower member dolostone overlaps partly with that of the epigenetic dolomite phases. No regional trend can be observed in the data set. This dolomite is interpreted as an early diagenetic episode associated to a sabkha environment. The ample spread of the OR values can be explained as result of partial re-equilibration to a more stable, ordered dolomite type during burial.

5.3. Element geochemistry

5.3.1. Microprobe analyses

The values obtained by XRD were verified with microprobe analyses on four thin sections from different localities. Transects across Dol A and Dol B were measured for Ca, Mg, Fe, Mn and Sr. Other trace elements, such as Si, Ni, Co, Ba, Pb and Zn, were also measured but the detection limits of the microprobe for these elements are in general very close to the observed concentrations. All the measurements are reported in Appendix 2.

In Fig. 5.3 the microprobe profiles for Mg, Ca and Fe are shown for different thin sections. The data confirm in part the XRD analyses. Dol A and Dol B have almost stoichiometric composition, with a slight excess in Ca relative to Mg (Fig. 5.3D). The iron content is low in Dol A and Dol B, and variable but distinctly higher in Dol B II. Fe concentrates in particular zones, which are characterized by lighter colour in the BS images, and substitutes preferentially for Mg, due to the very similar atomic
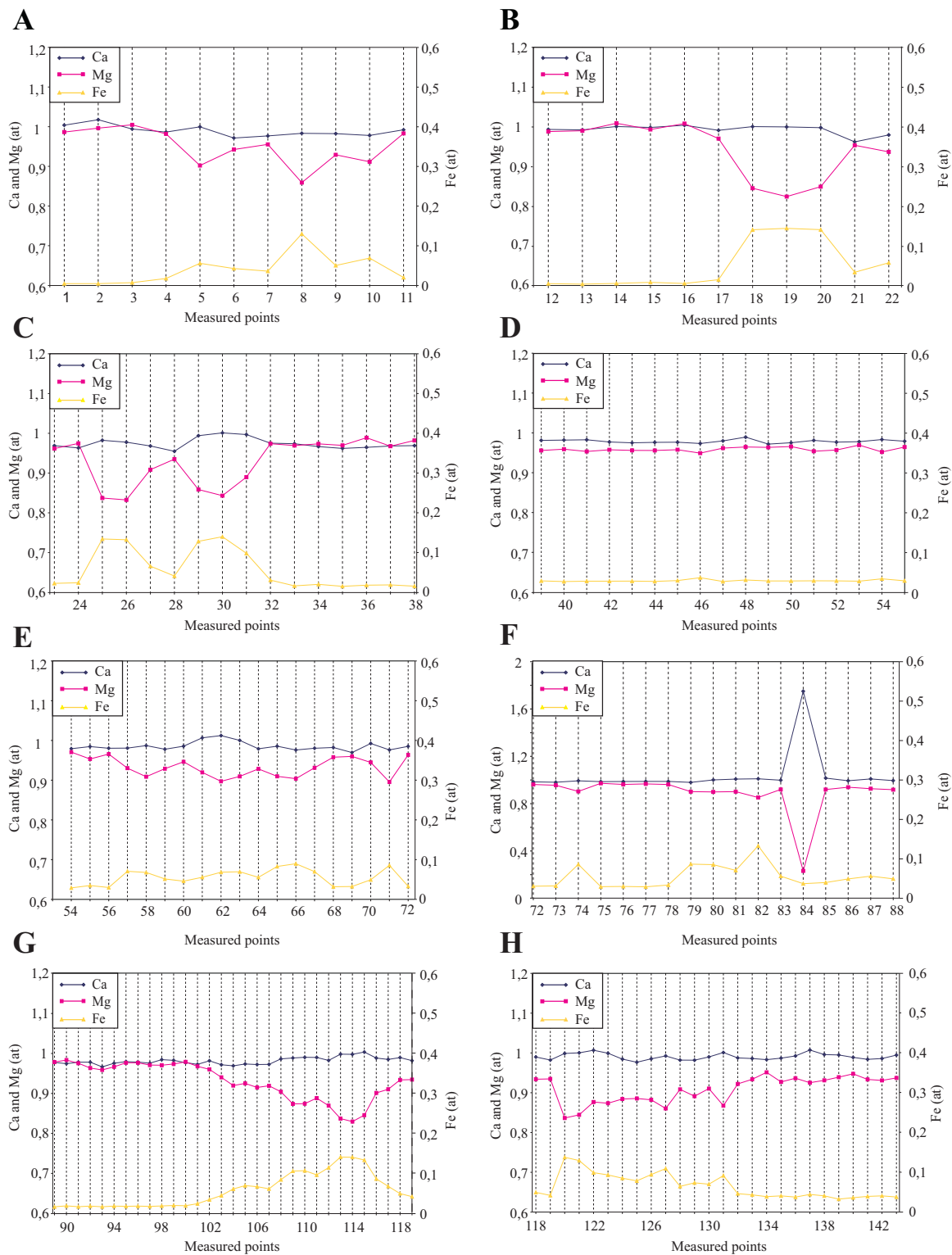
Fig. 5.3. Microprobe (WDS) profiles measured on samples from different localities. The position of the measured points is shown in the BS image in the next page. A) and B) San Martín de la Tercia, sample fc8sm; C) Torrestio, sample fd5torr; D) E) and F) Cospedal, sample fd5cos; G) and H) Genestosa, sample fd1gen. All the data are reported in Appendix 2.
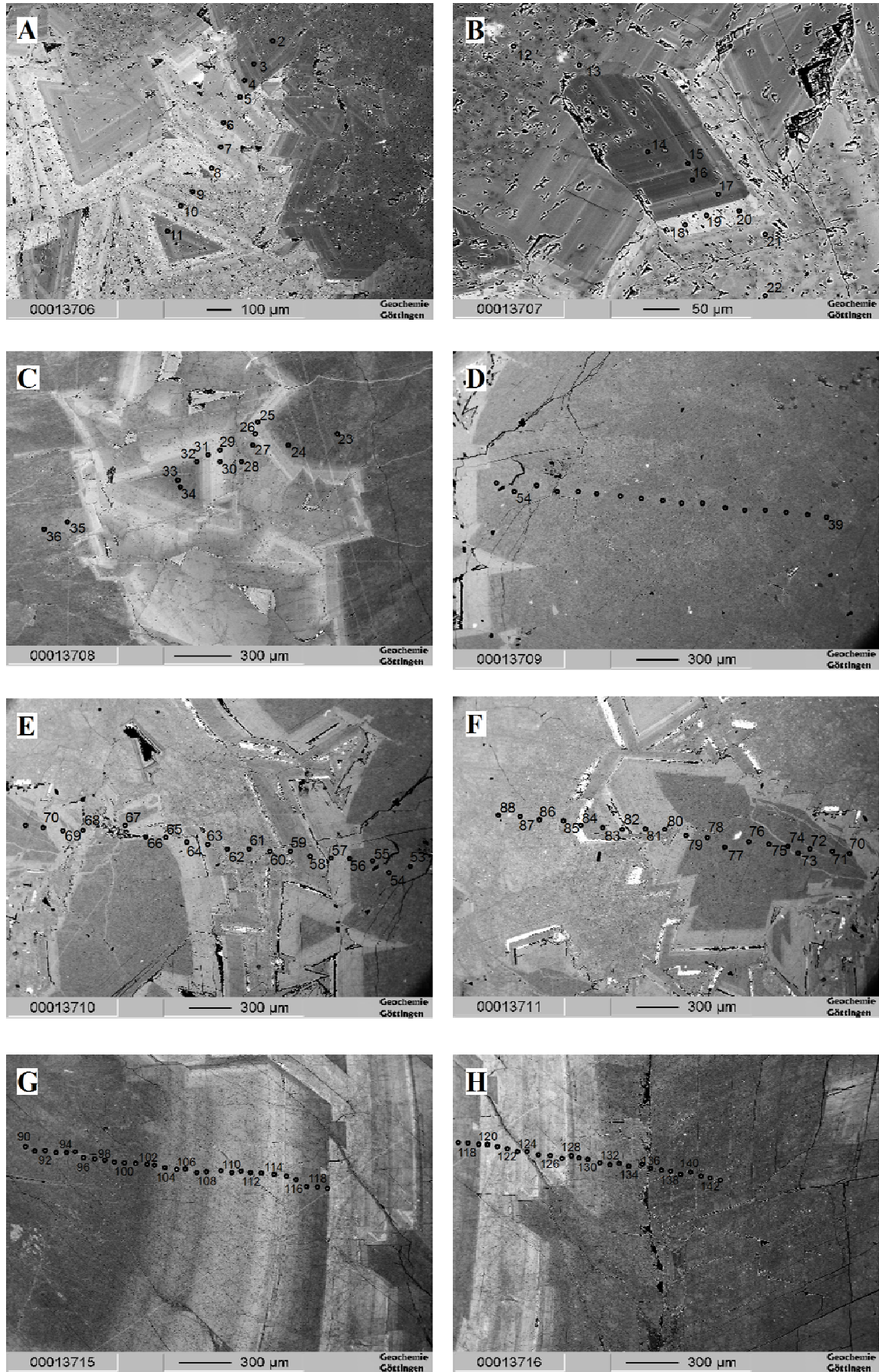
Fig. 5.3. Caption see previous page.
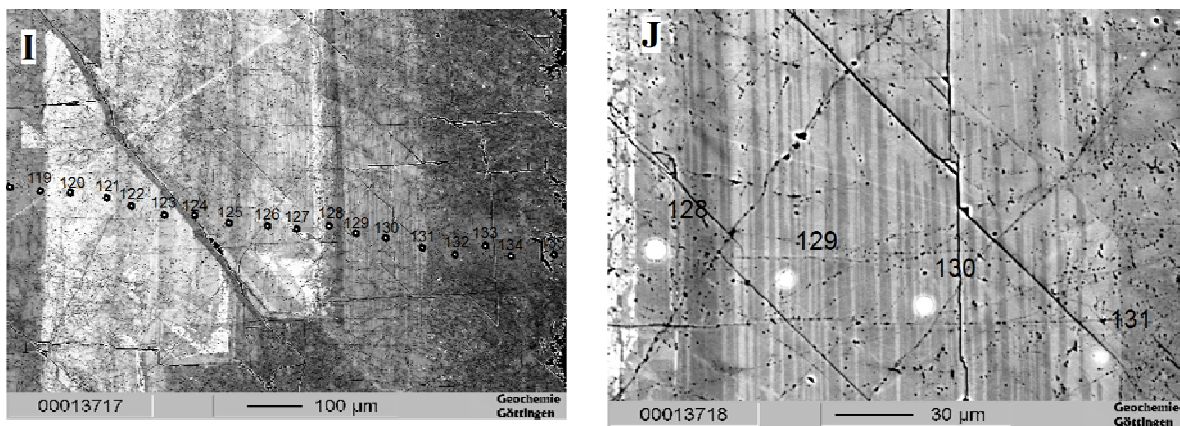
Fig. 5.3. Continuation. I) and J) Details of the zonations of sample fd1gen.

radius (Figs. 5.3A, 5.3B, 5.3C, 5.3E, 5.3F, 5.3G, and 5.3H). The origin of the zonation is probably related to changes in the redox potential of the dolomitizing fluids. Iron substitutes magnesium inside the dolomite lattice only in its bivalent ionic species. The Fe^{2+} activity is controlled by the redox potential of the solutions.

As it has been previously observed in back-scattering images and CL microphotographs, Dol A and the first generation of Dol B reveal a quite homogeneous composition. Sr is usually very close to the detection limits. Very complex and small-scaled compositional zonation is present in the Dol B II phase (Figs. 5.3I and 5.3J). The microprobe diameter of the beam (10µm) was sometimes unable to resolve the very fine-scaled zonation present in some samples (Fig. 5.3J).

The dolomitized lithologies preferentially host several small non-economic ore deposits compared to the mainly barren limestones. (see chapter 2, paragraph 2.4.5). Metallic elements, such as Pb, Zn, Ba, Ni, Co, might have also been incorporated in the dolomite lattice. The metallic concentrations measured are in general under the detection limits but there are a few exceptions in which statistically significant amounts of metals have been detected in the dolomite lattice (and not in small mineral inclusions). For example, in sample fd5tor, 350 to 500 (±40) ppm Co occur.

5.3.2. Minor and trace elements

Minor and trace element contents were analysed with ICP-ES in 73 samples (31 containing Dol A and Dol B, 21 lower member dolostone and 21 precursor limestone). Dol B II was not measured due to the potential contamination during micro-drilling (0.5 gr are required for a reliable ICP-ES measurements).

Strontium, sodium, iron and manganese represent the crucial elements in carbonate diagenetic studies and are discussed in this paragraph. Sr and Na represent elements with a distribution coefficient smaller than 1, while Mn and Fe have a distribution coefficient greater than 1. The data for the latter elements are reported in Appendix 3.
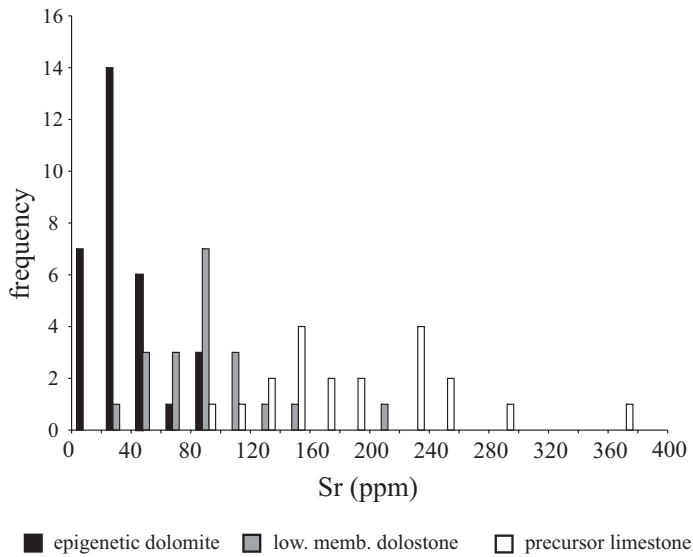
Fig. 5.4. Fraquency histogram of the Sr concentration in the epigenetic dolostone, in the lower member dolostone and in the precursor limestone.

In Fig.5.4 are shown the strontium concentrations of epigenetic dolomites, lower member dolostone and precursor limestone. In Fig.5.5 the Dol A and Dol B values for single sampled sites are plotted. Dol A and Dol B always have Sr concentrations ranging between 15 and 100 ppm, with 90% of the samples having less than 60 ppm. The lower member dolostone values range between 43 and 210 ppm. The strontium concentration of the precursor limestone is between 93 and 375 ppm.

The sodium contents are plotted in Fig. 5.6. The concentrations of the dolomite phases A and B are between 100 and 400 ppm. The lower member dolostone has values between 100 and 200 ppm. The Na concentration of the precursor limestone is between 0 and 200 ppm.

The iron and manganese concentrations of the Dol A and Dol B phases range from 2200 ppm to 45800 ppm for Fe, with 90% between 2200 ppm and 20000 ppm, and from 218 ppm and 2496 ppm for Mn, with 90% of the data less than 1500 ppm (Figs. 5.7A and 5.7B). The lower member dolostone values range from 2100 and 40000 ppm for Fe and from 135 ppm and 3043 ppm for Mn. The precursor limestone shows distinctly lower values, with Fe values ranging from 200 ppm to 4800 ppm and Mn from 42 ppm to 386 ppm.
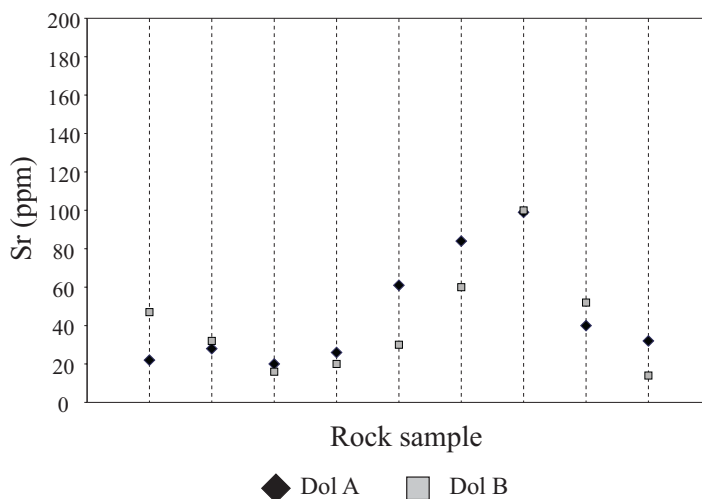
Fig. 5.5. Sr concentration trend of Dol A and Dol B in single sampled sites. The values of the dolomite phases from the same rock samples are plotted on the same vertical line (dashed).

The strontium partitioning coefficient between stoichiometric dolomite and solution is not well constrained because of the lack of laboratory measurements under normal diagenetic conditions. Values available in the literature vary from 0.0600 (Jacobson and Udowsky 1976), to 0.025 (Katz and Matthews 1977) and to
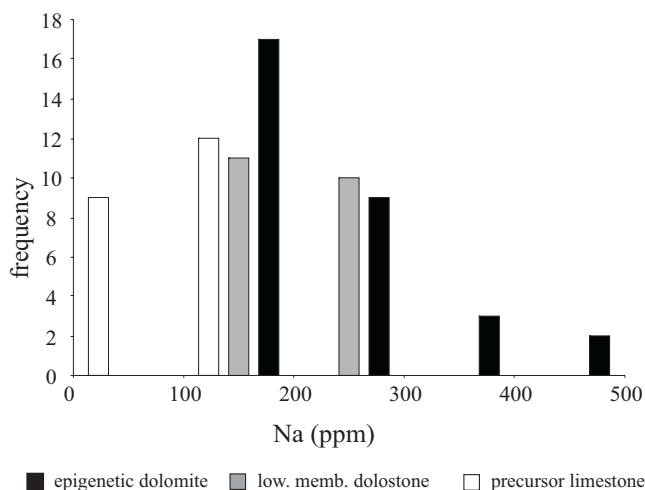
Fig. 5.6. Frequency histogram of the Na concentration in the epigenetic dolostone, in the lower member dolostone and in the precursor limestone.

0.0118 (Vahrenkamp and Swart 1990). The first two values have been calculated from high temperature experimental studies, the latter has been extrapolated from dolomites which formed from waters of normal or near-normal marine composition.

As Sr substitutes principally Ca in the dolomite lattice (Behrens and Land 1972, Kretz 1982), the distribution coefficient for Sr in dolomite should increase by about 0.0039 for every additional mole % $CaCO_3$ (Vahrenkamp and Swart 1990). Assuming a value of about 0.020 for the Sr partitioning coefficient and the Sr and Ca concentration of seawater (8 ppm and 400 ppm respectively, Drever 1982), the Sr concentration of a dolomite in equilibrium with seawater should be about 150 ppm (for a dolomite with about 51% $CaCO_3$). Dolomite precipitating from evaporative seawater (where gypsum precipitation has elevated the Sr/Ca molar ratio) should have even higher values (Behrens and Land 1972, Land and Hoops 1973). On the other hand, early diagenetic dolomite, precipitating from hypersaline evaporitic brines that reached halite saturation, may have a Sr concentration as low as 50 ppm, due to the fractionation of the strontium into the evaporitic minerals (Bein and Land 1983). Due to the very high ionic strength of seawater compared with meteoric water, a mixture with more than 5% seawater has a Sr/Ca molar ratio similar to seawater, and a dolomite precipitated from a mixture of about 20% seawater should have the typical marine Sr concentration (Tucker and Wright 1990).

Dol A and Dol B always have low Sr concentrations, with 90% of the samples having less than 60 ppm (Fig. 5.4). No clear distinction exists between Dol A and Dol B (Fig. 5.5), supporting the hypothesis of a continuous process between matrix-replacive dolomitization (Dol A) and void-filling (Dol B) dolomitization. This is confirmed also by the petrographic evidence. Several authors (e.g. Mattes and Mountjoy 1980, Morrow 1990a) reported Sr concentrations of a few tens of ppm in burial dolomites. The strontium concentration of the precursor limestone (93-375 ppm) is distinctly higher than that of Dol A and Dol B (Fig. 5.4) but depleted relative to calcite and high-Mg calcite in equilibrium with normal seawater, indicating that diagenetic re-equilibration of the precursor limestone was probably completed before the dolomitization event. The lower member dolostone shows higher Sr concentrations relative to dolomite A and B phases. As suggested by petrographic evidence, the lower member dolostone represents the product of an earlier diagenetic episode, probably related to a sabkha environment. Early diagenetic dolomites generally have a higher Sr content than late diagenetic dolomites, due to the very low partition coefficient that discriminates Sr in the fluid.
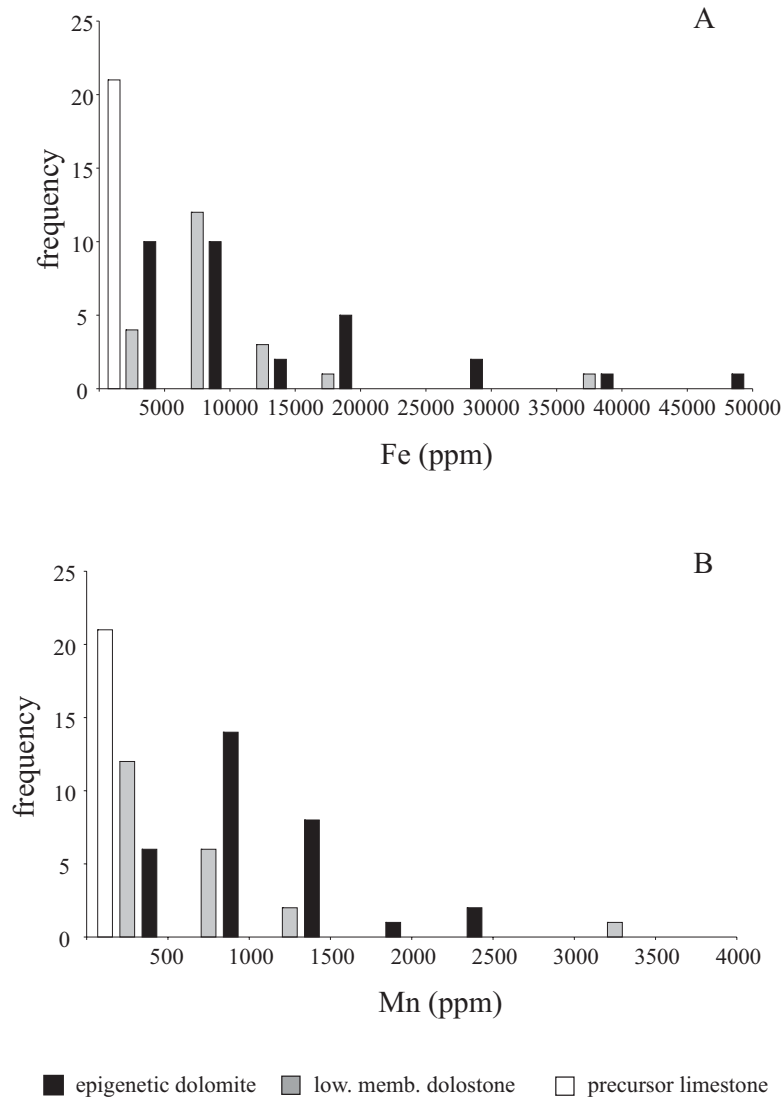
Fig. 5.7. Frequency histogram of the Fe (A) and Mn (B) concentrations in the epigenetic dolostone, in the lower member dolostone and in the precursor limestone.

Also Na fractionates strongly into the fluid during diagenesis and is considered a good indicator of the diagenetic evolution of the system. The low Na concentration values of dolomites A and B are consistent with the data reported in literature for typical burial dolomites (Mattes and Mountjoy 1980, Nielsen et al. 1998), and exclude the presence of inclusions of evaporitic minerals. No clear distinction was observed between the lower member dolostone and the epigenetic dolomites, with the former having Na concentrations only slightly lower than those of the Dol A and B phases (100-300 ppm, Fig. 5.6). The Na concentrations of the precursor limestone are distinctly lower than those of the dolomite phases. This is in disagreement with the behaviour of this element during dolomitization (Na fractionates in the fluids during recrystallization). These values can be strongly influenced by the abundance of fluid inclusions present, which are particularly frequent in the coarser crystals of Dol A and in Dol B. Sodium usually represents one of the major cations present in the saline diagenetic brines. Alternatively, the measured value can be explained assuming a dolomitizing fluid with a distinctly higher salinity than the diagenetic fluid in equilibrium with the precursor limestone.

Fe and Mn values tend to increase during diagenesis (Brand and Veizer 1980), due to their partitioning coefficient (higher than 1) and to the fact that these two elements are particularly abundant in the pore fluids at reducing conditions, typical of deeper diagenetic environment. The Fe and Mn concentrations of the dolomite A and B phases are quite variable. Most of the samples show values less than 20,000 ppm Fe and 1,500 ppm Mn (Fig. 5.7).
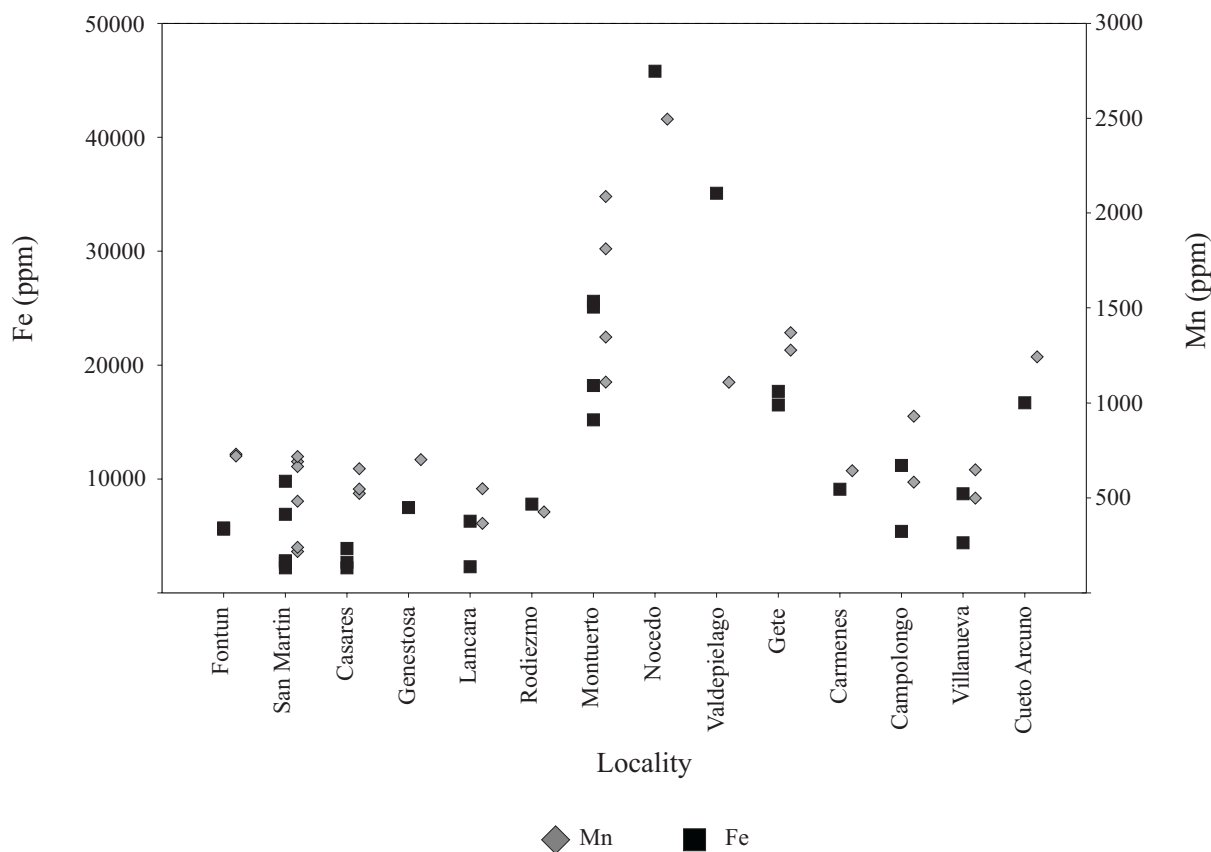
Fig. 5.8. Fe and Mn concentrations of the epigenetic dolomites plotted versus the different localities.

In Fig. 5.8 the iron and manganese concentrations are plotted for the different sampled localities. No clear regional trend can be observed: the highest Fe values are from the Montuerto, Nocedo, Valdepielago and Cueto Arcuno localities, in the eastern part of the Correcilla Unit, with values higher than 15,000 ppm. The lowest values were found in the San Martín, Casares and Láncara de Luna localities, with values (>10,000 ppm). The samples from the Bodón Unit show intermediate values.

In Figs. 5.9A and 5.9B are plotted the Fe and Mn concentrations of Dol A and Dol B in single
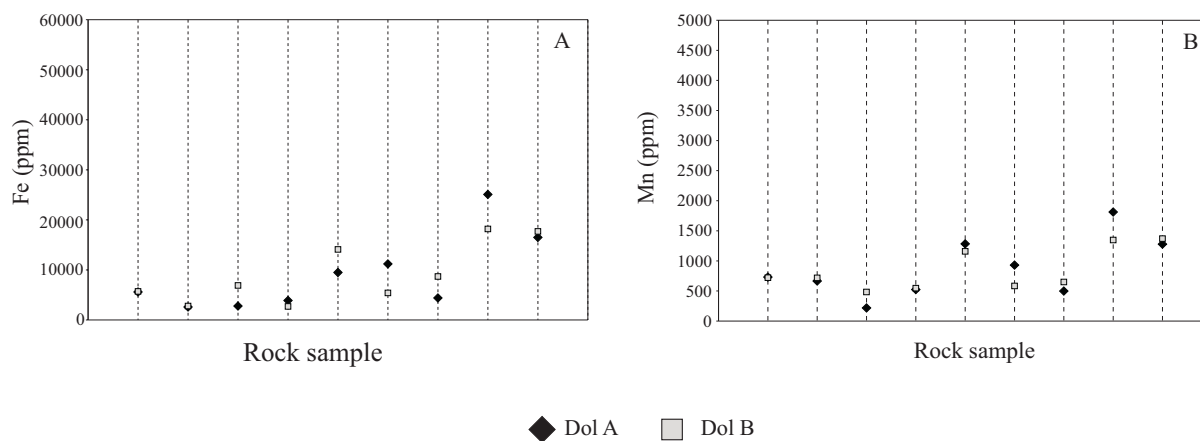
Fig. 5.9. Fe (A) and Mn (B) concentration trend of Dol A and Dol B in single sampled sites. The values of the dolomite phases from the same rock sample are plotted on the same vertical line (dashed).
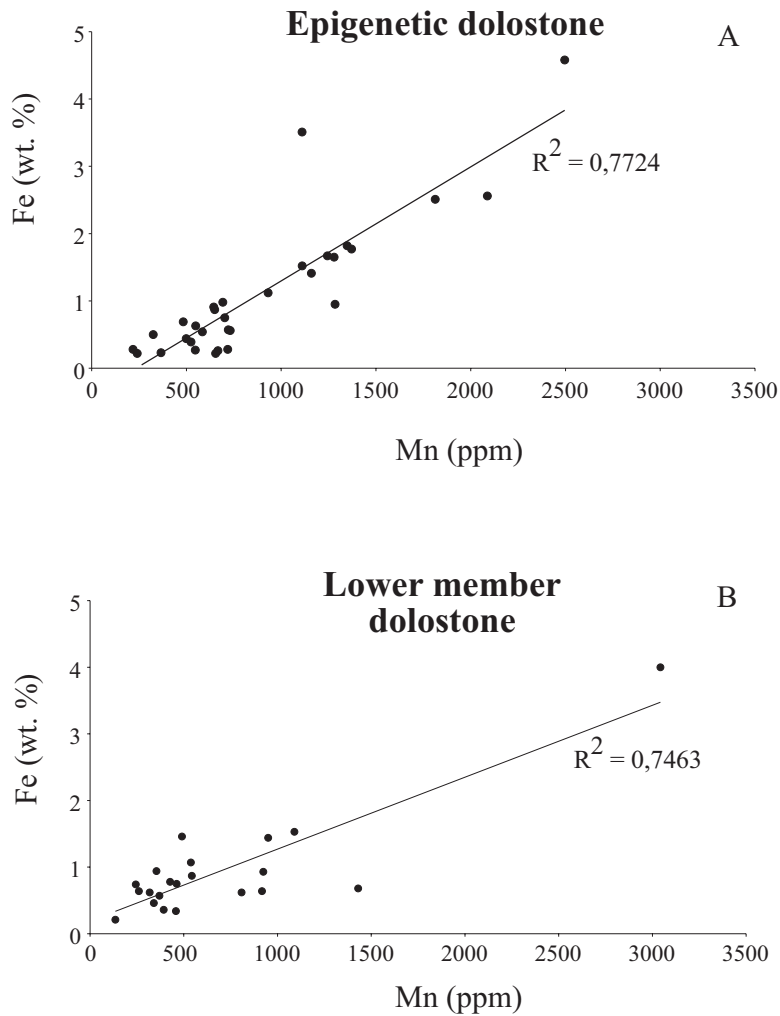
Fig. 5.10. Fe vs. Mn concentration diagram in the epigenetic dolostone (A) and in the lower member dolostone (B).

sampled sites. As for strontium, no clear distinction is observed between the Fe and the Mn content in Dol A and Dol B. Usually the values are very close: Dol B can be either slightly depleted or enriched relative to the associated Dol A.

The lower member dolostone shows comparably high and widespread Fe and Mn as the epigenetic dolomite; on the contrary, the precursor limestone shows distinctly lower values (Figs.5.7A and 5.7B). The mean values in both Dol A and Dol B are higher than those of the lower member dolostone and the precursor limestone, pointing to a late burial input of Fe and Mn.

The Fe and Mn values in Dol A and Dol B correlate positively (Figs. 5.10A and 5.10B). This trend is a common feature of burial dolomites observed in many other areas (e.g. Barnaby and Read 1992).

The 1000*Sr/Ca vs. Mn diagram (Fig. 5.11) does not show any statistically significant correlation. Diagenetic systems in equilibrium with deeper burial settings are characterized by high Mn content and low Sr/Ca ratios. The precursor limestone is, however, characterized by high Sr/Ca and low Mn values compared to the dolomite phases. The lower member dolostone shows intermediate values between the limestones and the epigenetic dolostones, which occupy the lower part of the diagram, with the high but variable Mn values and the lower Sr/Ca ratios.
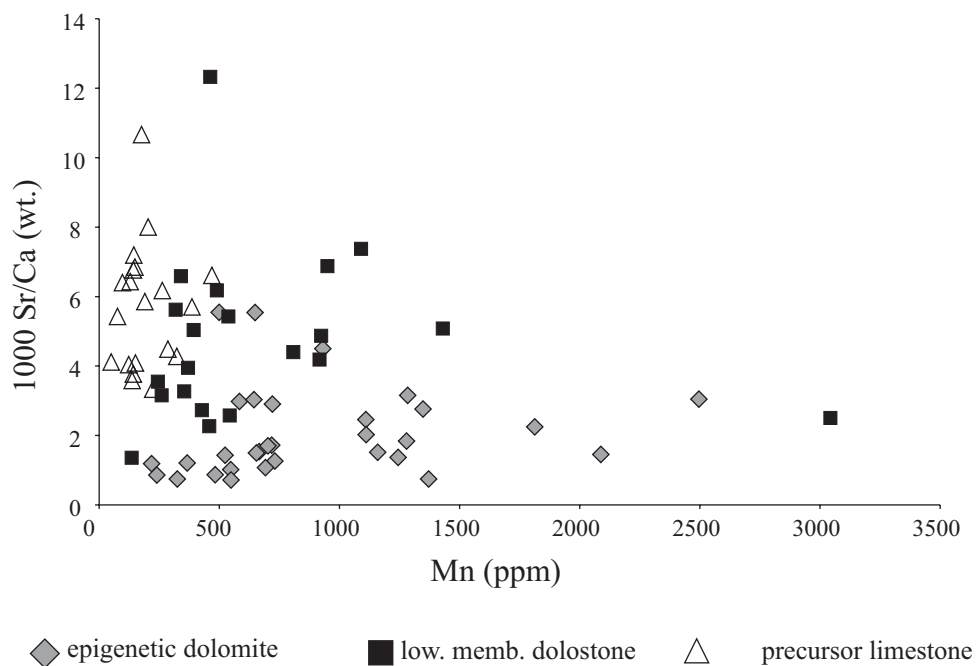
Fig. 5.11. 1000*Sr/Ca vs. Mn concentration diagram of epigenetic dolostone, lower member dolostone and precursor limestone.

5.4. Isotope geochemistry

5.4.1. Oxygen and carbon isotopic composition

Ninety-six samples of Dol A and Dol B were measured for stable isotopes (O and C). Five Dol B II samples and five late calcite cement samples were also analysed. For comparison, samples of the precursor limestone (34), the lower member dolostone (39) and calcite veins (5) were also measured. All the data are reported in Appendix 4.

In Fig. 5.12 the $\delta^{18}O$ versus $\delta^{13}C$ values are plotted for the epigenetic dolomite phases Dol A and Dol B, the lower member dolostone and two different precursor limestone lithologies: birdseye limestone and glauconitic packstone.

The Dol A and Dol B values show an ample regional spread of $\delta^{18}O$ values ranging from -4.02 to -13.29‰ PDB (Fig. 5.12A). No clear distinction is observed between the matrix-replacive Dol A and the void-filling Dol B in their oxygen isotopic signature: the measured values are usually quite similar, with few exceptions. Dol B is rarely considerably depleted in ^{18}O (2-3‰) relative Dol A (see values in Appendix 4).

The highest oxygen isotopic ratios are typical of the southern part of the Somiedo-Correcilla Unit (with the Fontún locality being the only exception; Tab. 5.1). Lower values have been observed in the Bodón Unit and the western part of the Somiedo-Correcilla Unit, which are also characterized by very
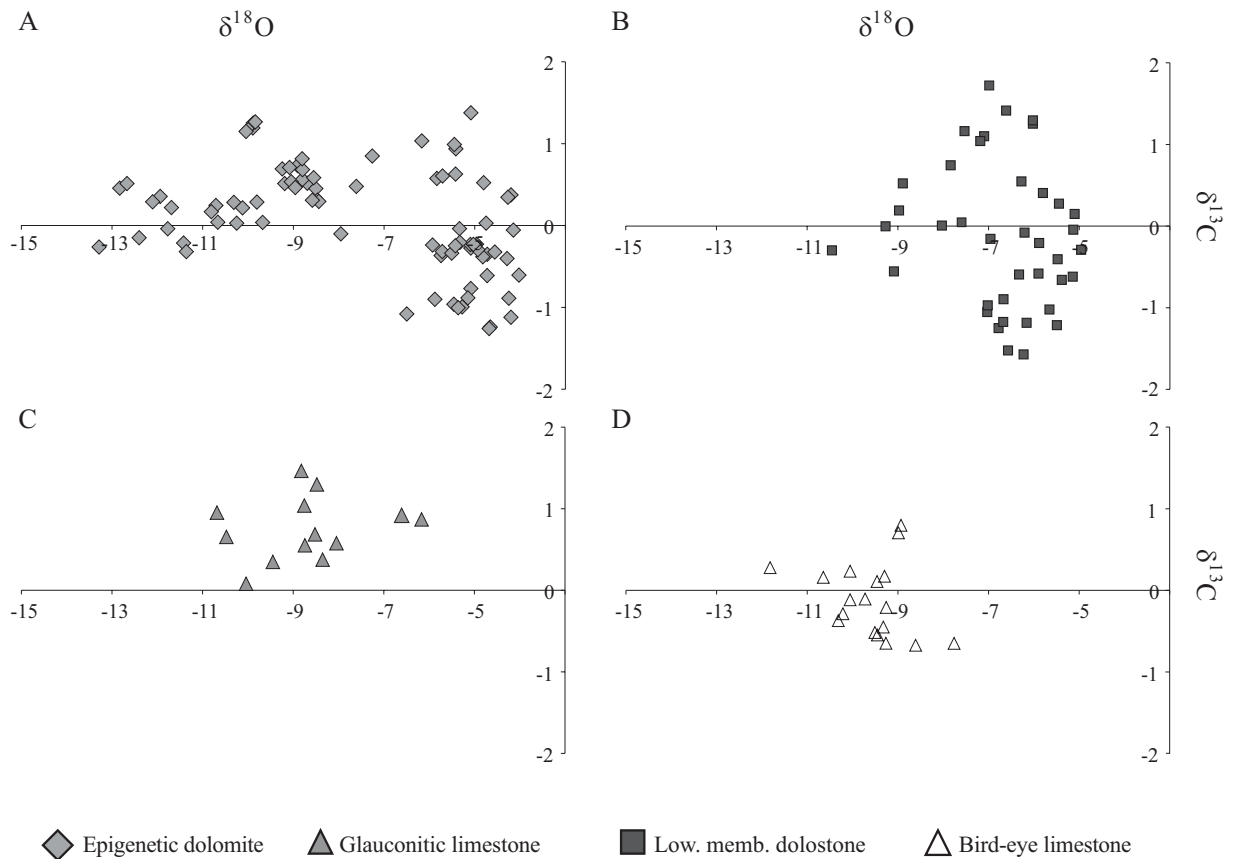
Fig. 5.12. Oxygen vs. carbon isotopic composition diagrams of the epigenetic dolomite (A), lower member limestone (B), glauconitic limestone (C) and birdseye limestone (D).

high Dol B/Dol A ratios and by the lack of open cavities and, therefore, late infilling calcite cements (see chapter 4, paragraph 4.3, Figs. 4.8A and 4.8C).

The lower member dolostone shows also very scattered oxygen isotopic ratios, with values between -4.96 and -10.45‰ PDB (Fig. 5.12B). The oxygen isotopic composition of the precursor limestone ranges from -6.17 to -10.48‰ PDB, for the glauconitic packstone (Fig. 5.12C), and from -7.76 to -11,82‰ PDB for the fenestral limestone (Fig. 5.12D).

The oxygen isotopic composition of dolomite reflects the temperature of precipitation and the isotopic signature of the dolomitizing fluids. In closed diagenetic systems and low water/rock interaction, the latter may be influenced by the isotopic signature of the calcium carbonate being replaced. Dolomite in equilibrium with Cambrian seawater should have values between -3.6 and -7.5‰ PDB (Veizer and Hoefs 1976). Lower values can be due to isotopic fractionation during diagenetic re-equilibration at higher temperature.

Calcite in equilibrium with the Cambrian seawater has $\delta^{18}O$ values between -5.5‰ and -10.5‰ PDB (Veizer and Hoefs 1976). The precursor limestone may have preserved part of the Cambrian seawater composition. The fenestral cements, however, have distinctly lower values (between -10.89 and -12.36‰ PDB), although these cements normally form during early diagenetic stages. It was not possible to distinguish between the different calcite cements, except for a few cases: large fibrous

Bodón Unit			Somiedo-Corresilla Unit		
Locality	$\delta^{18}O$	$\delta^{13}C$	Locality	$\delta^{18}O$	$\delta^{13}C$
Carmenes	-8.80 to -7.26	0.68 to 0.85	Torrestio	-12.40 to -10.25	-0.21 to 0.15
Villanueva de Pontedo	-8.58 to -8.44	0.30 to 0.59	Cospedal	-13.29 to -11.94	-0.26 to 0.51
Viadango	-9.06 to -7.82	0.52 to 1.02	Rabanal de Luna	-7.77 to -7.68	0.87 to 0.96
Campolongo	-9.25 to -8.32	0.53 to 0.73	Láncara de Luna	-6.50 to -4.20	-1.08 to 0.37
Cueto Arcuno	-8.96 to -5.08	0,47 to 1.38	Aralla (Tunnel)	-6.17 to - 4.15	-0.06 to 1.09
			Casares de Arbas	-5.75 to -4.29	-0.61 to -0.32
			San Martín de la Tercia	-7.26 to -4.20	-1.24 to 0.63
			Rodiezmo (Cruz)	-11,75 to -9.54	-1,07 to 0,44
			Campolongo	-9.25 to -8.32	0.53 to 0.73
			Fontún	-11.88 to -9.88	-0.22 to 1.27
			Gete	-9.08 to -8.81	0.71 to 0.82
			Nocedo de Curueño	-8.63	-.097
			Montuerto	-11.77 to -5.71	-0.32 to 0.61
			Valdepielago	-7.95	-0.10

Tab. 5.1. Stable isotope composition of Dol A and Dol B for different sampled localities

calcite cements from Torre de Babia, in the north-western part of the study area, show values between -6.69 and -9.76 ‰ PDB. Late calcite veins, which crosscut the limestone and postdate the fenestral cements, show a very depleted O isotopic composition (between -10.22 and -14.90 ‰ PDB).

The $\delta^{13}C$ values of dolomite are usually strongly influenced by the precursor limestone; in addition, there is little isotopic fractionation of carbon with temperature. The carbon isotopic signature of epigenetic Dol A and Dol B is variable (between -1.36 and +1.38 ‰ PDB, Fig. 5.12A). The $\delta^{13}C$ values of the precursor limestone range between 0.08 and 1.46 ‰ PDB for the glauconitic packstone (Fig. 5.12C), and between -0.80 and 0.80 ‰ PDB for the fenestral limestone (Fig. 5.12D). All the data are in the range of calcite precipitated in equilibrium with Cambrian seawater values (from -3.0 to +2.0 ‰ PDB, Veizer and Hoefs 1976). All of the epigenetic dolomite phases replacing the glauconitic packstone have positive $\delta^{13}C$ values, clearly inherited from the precursor limestone.

The lower member dolostone has a wide ranged carbon isotopic composition between -1.57 and 1.72 $\delta^{13}C$ (Fig. 5.12B). This distribution can be explained by the variable involvement of carbon which was modified during methanogenesis (which strongly fractionates ^{12}C, resulting in an enrichment of the heavy carbon in the carbon reservoir) and from decomposition of organic matter, which has the opposite effect.

Late calcite cements, which partly fill the remnant pores in the dolomitized lithologies (see chapter 4, paragraph 4.3.2), are characterized by distinctly negative but variable $\delta^{18}O$ (between -7.14 and -13.05 ‰ PDB) and by light $\delta^{13}C$ between -1.39 and -9,22 ‰ PDB). An involvement of carbon component derived from decomposition of the organic matter can be assumed.
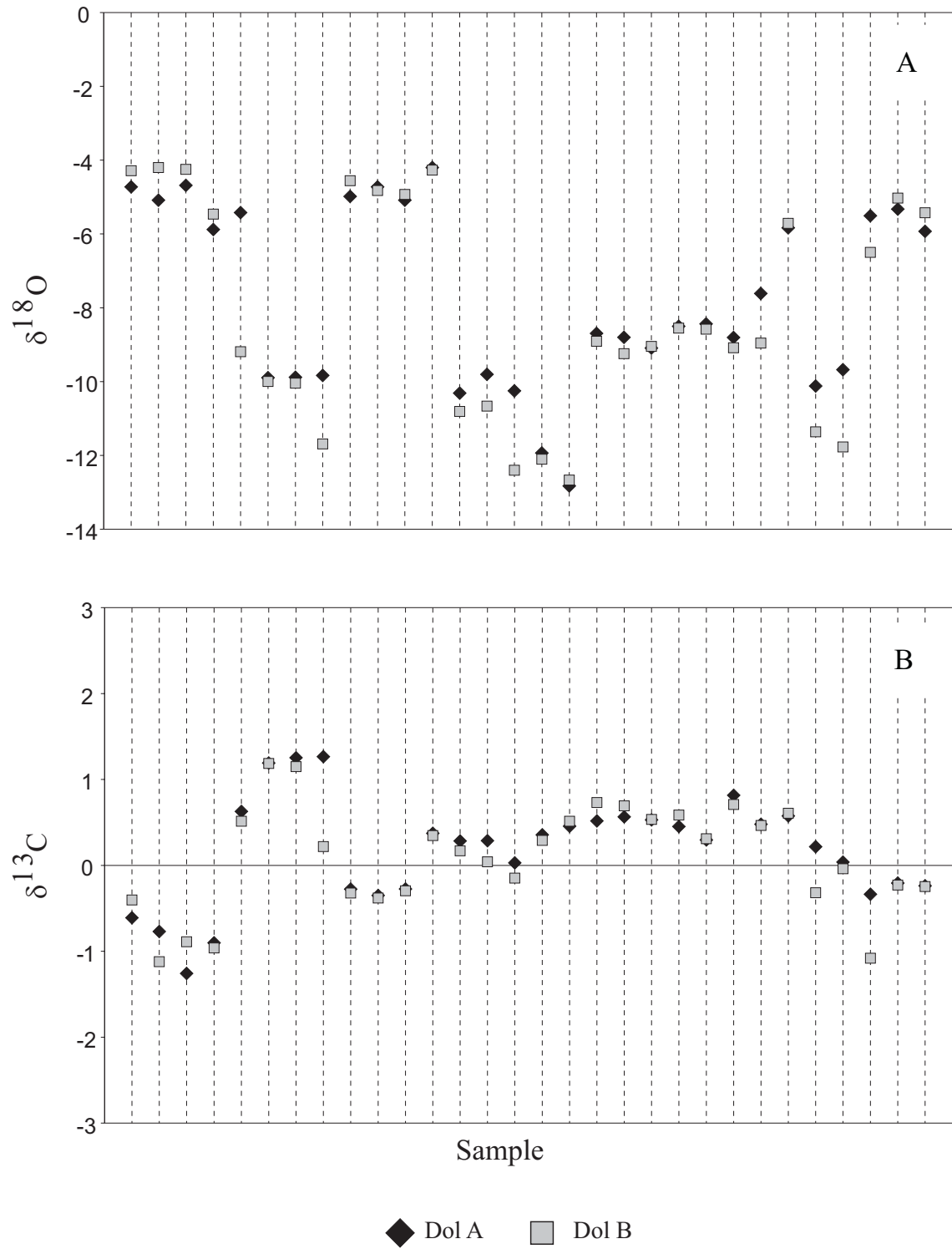
Fig. 5.13. Oxygen (A) and carbon (B) isotopic composition trend of Dol A and Dol B in single sampled sites. The values of the dolomite phases from the same rock sample are plotted on the same vertical line (dashed).

In Fig. 5.13 the oxygen (A) and carbon (B) isotopic ratios of Dol A and Dol B are plotted for single sampled sites. As for Fe, Mn, Sr concentrations (see paragraph 5.3.2), no clear fractionation between Dol A and Dol B can be observed. The values of both $\delta^{18}O$ and $\delta^{13}C$ plot often very close. Alternatively, Dol B can be either enriched or depleted relative to Dol A.
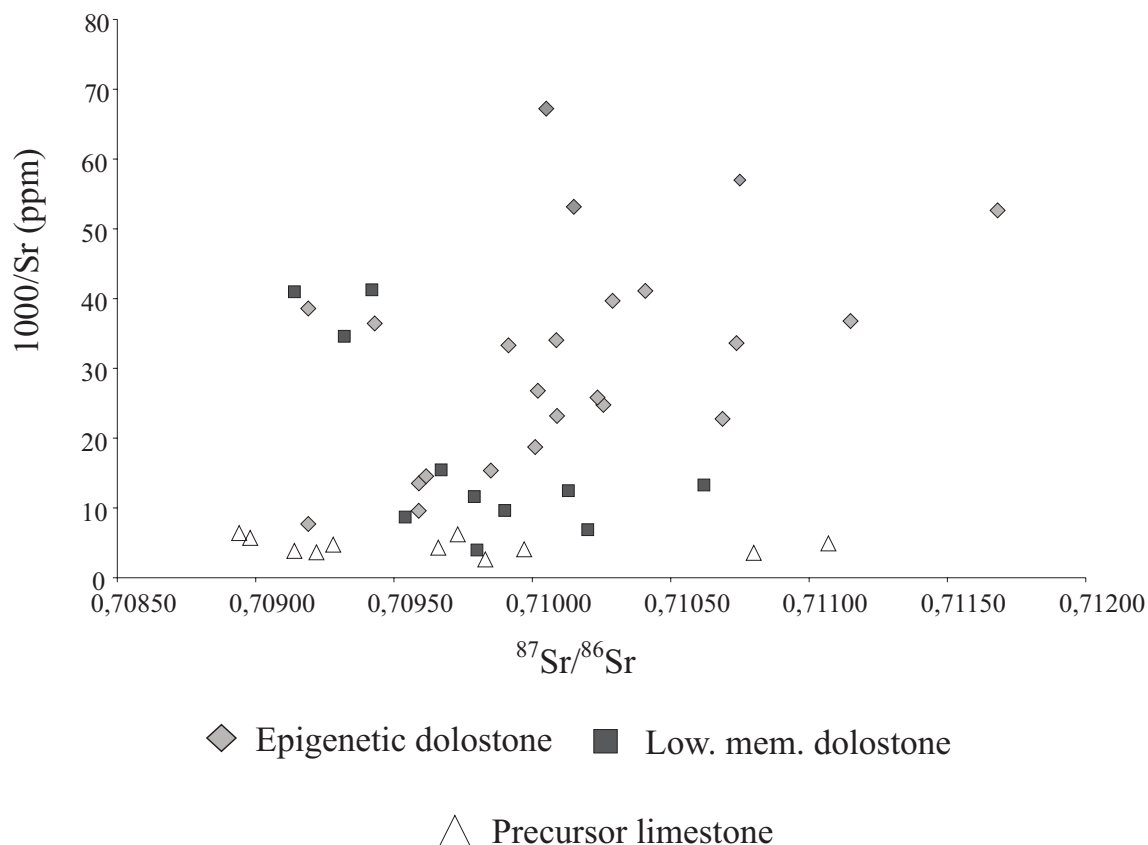
Fig. 5.14. Sr concentration vs. strontium isotopic ratio of epigenetic dolostone, lower member dolostone and precursor limestone.

5.4.2. Strontium isotopic composition

Strontium isotopes can provide useful information on the nature of the fluids from which dolomite was precipitated. As Sr isotopic fractionation during carbonate precipitation can be considered negligible, the Sr isotopic composition of a carbonate is considered identical to that of the fluid (seawater or diagenetic brine) at the time of precipitation. The $^{87}Sr/^{86}Sr$ ratio of ocean water has changed systematically throughout the Phanerozoic, but it can be considered constant at any time, due to the long residence time of Sr in seawater (Burke et al. 1982).

Eleven samples of Dol A and twelve of Dol B from different localities were measured for Sr isotopes and Sr concentration. For comparison, eleven samples of host limestone and ten samples from the lower member dolostone were also analysed.

In order to trace for possible sources of Sr, the siliciclastic rocks from above and below the Láncara Fm. were measured for the $^{87}Sr/^{86}Sr$ and $^{87}Rb/^{86}Sr$ ratios, together with samples from a small granodioritic body, which intruded the Stephanian Ciñera Matallana Coal Basin, outcropping in the study area. All the data are reported in Appendix 5.
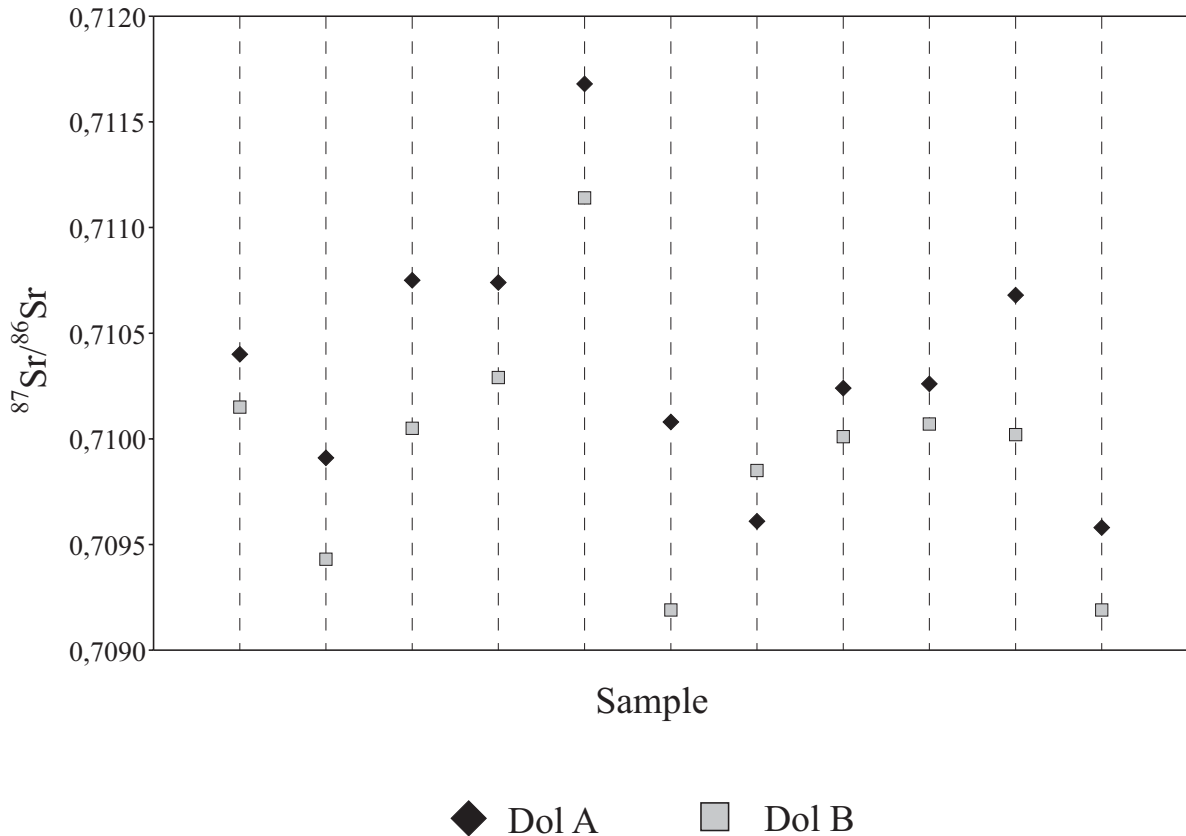
Fig. 5.15. Strontium isotopic composition trend of Dol A and Dol B in single sampled sites. The values of the dolomite phases from the same rock sample are plotted on the same vertical line (dashed).

The $^{87}Sr/^{86}Sr$ ratios of the dolomite phases range between 0.70917 and 0.71168 (Fig. 5.14). As for the oxygen isotopic ratios, there is no clear distinction between the Sr isotopic composition of Dol A and Dol B on a regional scale. Considering the two phases associated in single sampled sites (Fig. 5.15), the Sr isotopic ratios are very close to each another; the $^{87}Sr/^{86}Sr$ values of Dol A are always higher than those of Dol B (there is only one exception).

The values of the dolomites are more radiogenic than Cambrian seawater (0.70886 to 0.70940, Montañez et al. 2000) and any other seawater. Also the host limestone shows variable Sr isotopic compositions. The values are either more radiogenic than Cambrian seawater or close to the highest ones reported in literature. The more radiogenic values plot in the same field as those of Dol A and B but have higher Sr concentrations (Fig. 5.14). The lower member dolomite is also characterized by a large variation of Sr isotopic ratios and by radiogenic values. The original Cambrian seawater signature was probably modified during burial diagenesis, as indicated by the oxygen isotopic composition as well.

Detrital sedimentary rocks are a potential source of radiogenic ^{87}Sr because they contain minerals with relatively high Rb/Sr ratios. Generally, the release of ^{87}Sr is related to dissolution or albitization of alkali-feldspar (Land, 1984), dissolution of micas (Hower et al. 1976), illitization and interlayer cation exchange (Stueber et al. 1987, Chaudhuri and Clauer 1993). The thick siliciclastic successions

underlying and overlaying the Láncara Fm. had the potential to provide enough radiogenic strontium to produce the ample Sr isotopic spread recorded in the dolomitized and undolomitized lithologies. The strontium isotopic signature of the brines in equilibrium with the basinal shales cannot be derived directly from the Sr isotopic composition of the siliciclastic lithologies. The MASIRBAS (Maximum Sr Isotope Ratio of Basinal Shales, Machel and Cavell, 1999) is defined as the highest possible strontium ratio that can be derived from the basinal shales under diagenetic pressure and temperature conditions and it is usually calculated experimentally by stepwise leaching from shale samples. Although the MASIRBAS of the Cantabrian Paleozoic Basin has not been directly calculated, few assumptions can be made in order to constrain the possible strontium isotopic composition of the Cantabrian basinal brines. As previously discussed, all the Cambrian precursor limestones and lower member early dolostones show slightly more radiogenic Sr isotope composition compared to the Cambrian Sr isotopic signature. The data have been interpreted as result of interaction with more radiogenic basinal brines during burial diagenesis. The MASIRBAS value of these brines should not be lower than the highest values of the lower member dolostone and the undolomitized precursor lithologies (0,71107). Different water/rock ratios (resulting in different mixing from the strontium isotopic signature derived from Cambrian seawater and the MASIRBAS) can explain the ample spread of ratios which characterize both the lower member dolostone and the undolomitized precursor limestone.

All the cements precipitated from the basinal brines should have values not exceeding the MASIRBAS. The Dol B strontium isotopic ratios are in a range which would be expected from these cements (with values ranging from 0.70919 to 0.71114). Influx of extra-basinal metamorphic or basement sources can be probably excluded.

Granodioritic intrusions are present in the Stephanian Coal Basin, all over the Cantabrian Zone, but they are usually limited in volume. A small granodiorite body, which intruded the Ciñera-Matallana Coal Basin in the study area, gave a $^{87}Sr/^{86}Sr$ ratio equal to 0.70918. This value has to be corrected according to the $^{87}Rb/^{86}Sr$ ratio of 0.139, resulting in an even lower at the time of the crystallization of the magmatic body. This value is too low to indicate a possible genetic link between the hydrothermalism related to the granodioiritic intrusions and the dolomitizing fluid.

The nearest magmatic body of a certain importance, the Peña Prieta stock in the Palentian Zone, has $^{87}Sr/^{86}Sr$ ratios, corrected for the in-situ decay of Rb, between 0.7045 and 0.7069 (Gallastegui et al. 1990, written communication 2003). These values are again too low and rule out an influence of these magmatites on the epigenetic dolomitization of the Láncara carbonates.

Chapter 6 - Fluid inclusion study

6.1. Fluid inclusion petrography

A careful petrographic description of all the fluid inclusion populations present in the dolomite phases represents the starting point for any accurate and meaningful fluid inclusion study (see chapter 3, paragraph 3.8). Dol A displays a uniform cloudiness due to the presence of small (<4 μm) and possibly primary fluid inclusions densely distributed throughout individual crystals (Fig. 6.1A). Dol B also shows a uniform cloudiness, except Dol B II, which has inclusion-rich cores and inclusion-free rims (Fig. 1B). More complex zonations have also been locally observed, with several successive inclusion-rich and inclusion-free zones repeating (see chapter 4, paragraph 4.3.2). This fluid inclusion distribution commonly occurs in the dolomite during crystal growth or, alternatively, during recrystallization in previously dissolved zones (Goldstein 2003). In many mineral systems, recrystallization is a dissolution-reprecipitation process, which may take place on the submicrometer scale of fluid films or on the scale of wholesale dissolution of a large portion of a crystal, followed by later precipitation within the void that was created. Variation in minor element concentration, stoichiometry or degree of order in dolomite affect the likelihood that a certain growth zone will be recrystallized. Recrystallization is a common mechanism for trapping fluid inclusions, which can still be considered "primary" but only in relation to the "recrystallization phase". In our case, fluid inclusions are mostly concentrated in the crystal cores, which show a red cathodoluminescence (see chapter 4, Figs. 4.10C and 4.10D), and in certain growth zone. Clear secondary inclusions, which commonly align along trails and sealed fractures have never been observed.

Most of the inclusions are 2-phase, liquid-rich with φ^{liq} ranging from 0.80 to 0.97 (Fig. 6.1C). Larger inclusions (up to 12 μm in length) occur preferentially in the outer part of the crystal cores or along crystal growth zones. The inclusions have mostly irregular to lobate shape. Some inclusions are elongated along the direction of growth of the saddle dolomite crystal (Fig. 6.1D), which indicates primary entrapment. The inclusions do not emit fluorescence under UV light, indicating the absence of oil among the components (e.g. Shepherd et al. 1985) and suggesting an aqueous composition of the liquid phase. The presence of an aqueous phase was also confirmed by Raman spectroscopy (see paragraph 6.4). This excludes the presence of other gases inside the inclusions.

Monophase liquid inclusions were also found in the samples. These inclusions may be interpreted in two different ways:

1)   metastable 2-phase fluid inclusions of the type previously described (in which the bubble did not nucleate at normal temperature);

2)   monophase fluid inclusions which were trapped below 50°C (Goldstein and Reynolds 1994).

The Dol C generation, which locally follows Dol B II, is in general inclusion-free, with the exception of numerous small 2-phase (less than 4 µm) liquid-rich fluid inclusions, which are distributed along certain crystal growth zones (Figs. 6.1E, 6.1F and 6.1G). Dol C is non luminescent in CL with the exception of very tiny growth zones and the inclusion-rich growth zones, with are characterised by a red-dull luminescent colour (Figs. 6.1H and 6.1I).

6.2. Microthermometry

Microthermometry was carried out predominantly in Dol B from four different localities in the Correcilla Unit, in the dolomite replacing the Cambrian glauconitic echinoderm-rich limestone facies (fc3lann, fc8sm, fc3fg), in the upper member limestone (fcxsm and fc3cas), and in the dolomite replacing the lower member dolostone (fc3sm). Inclusions suitable for microthermometry were not found in the dolomite samples from the Bodón Unit, which are characterized by a darker colour and small inclusions. Inclusions in Dol C were also measured in the already mentioned sample fc3fg. Inclusions in Dol A are in general too small to be measured. Only a few homogenization measurements could be performed, resulting in the same temperature range as in Dol B. All the phase changes measured in inclusions from the different localities are reported in Appendix 6.

In Dol B the homogenization temperature shows an ample range, with values between 63 and 151 °C, but with 90% of the data ranging between 80 and 110°C (Fig. 6.2A). The latter range can be considered as the interval of minimum trapping temperatures of Dol B. The histogram shows a normal distribution, which excludes thermal re-equilibration of the FIs. The highest and lower, isolated values can be explained respectively as result of stretching of the inclusions (a process which causes an increase of the homogenization temperature) and/or necking-down of the inclusions, causing either increase or decrease of the original homogenization temperature.

A certain variability of the T_H values, sometimes in the range of 10-15 °C, is commonly observed in inclusions from the same samples or even the same crystals. This variability can be related to differences in the trapping temperature during crystal growth, which result in inclusions located in different growth zones as well as in the same growth zone having different homogenization temperatures (Goldstein and Reynolds 1994).

Fig. 6.1. Microphotograph see next page. A) Microphotograph of Dol A; B) microphotograph of Dol B (saddle dolomite); C) microphotograph of two phase liquid-rich fluid inclusion in Dol B; D) microphotograph of Dol B showing the inclusion-rich crystal core with inclusions elongated along the direction of growth of the saddle dolomite; E) microphotograph of Dol C, showing numerous small 2-phase liquid-rich fluid inclusions distributed along certain crystal growth zones; F) particular of Fig. 6.1E; G) microphotograph of aqueous fluid inclusion in Dol C; H) and I) normal and CL microphotograph of Dol C.
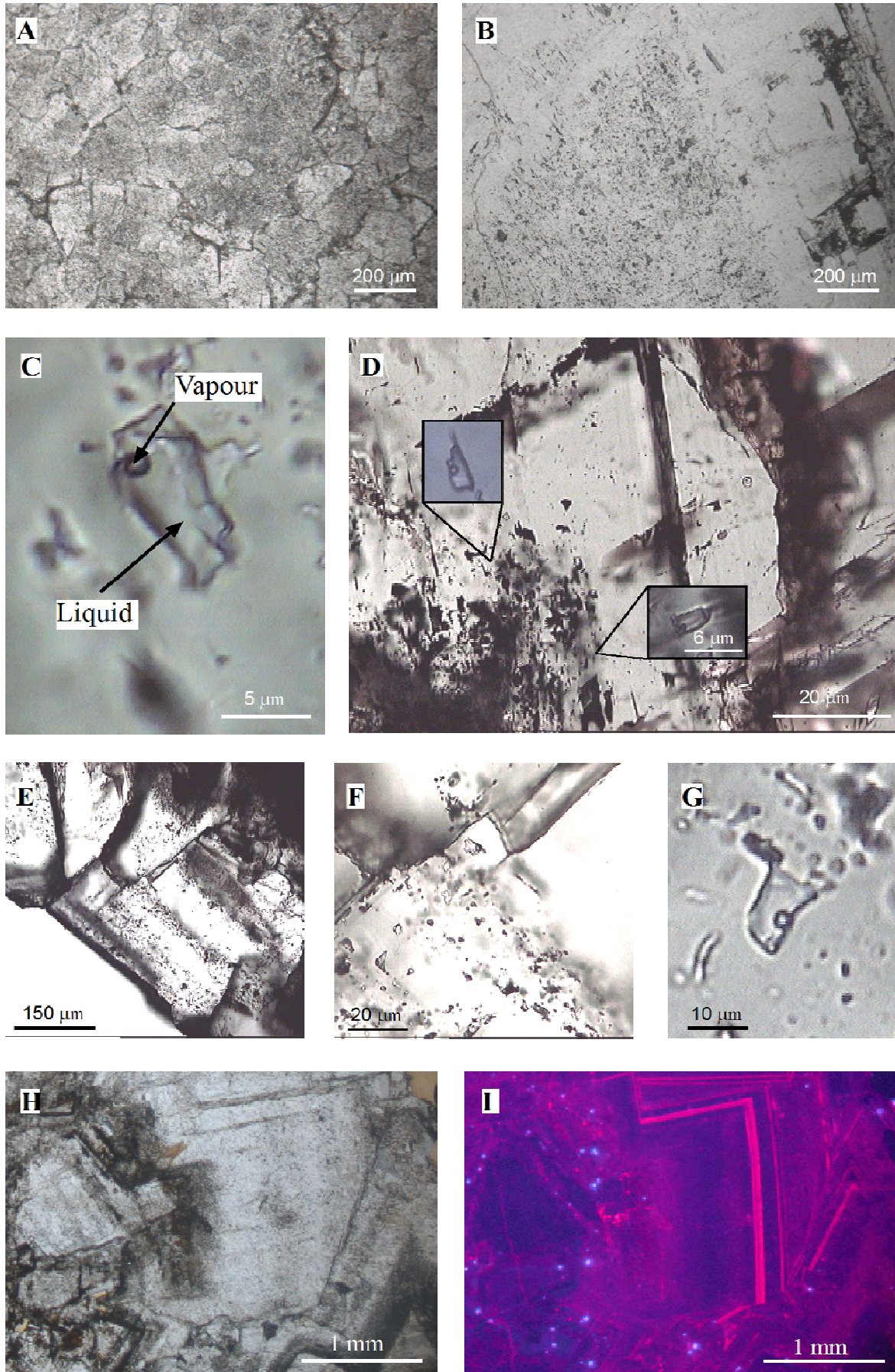
Fig. 6.1. Caption see previous page.
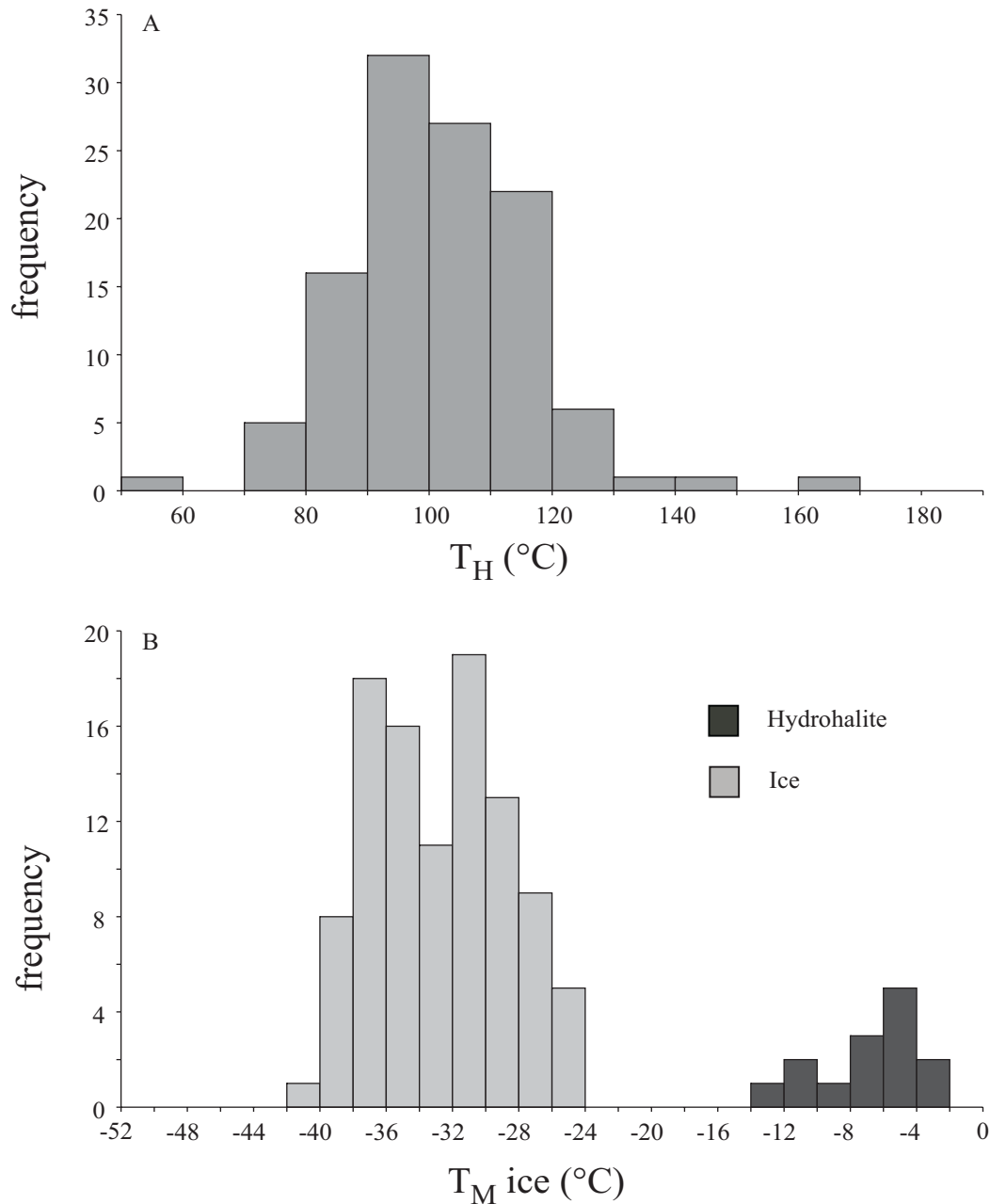
Fig. 6.2. A) Frequency histogram of the homogenization temperature (T_H) in fluid inclusions from Dol; B) frequency histogram of the final melting temperature of ice and hydrohalite in fluid inclusions from Dol B.

Major element composition and salinity are estimated from the eutectic and final melting temperatures, but optical limits make the identification of these phase changes often impossible. Furthermore, the inclusions show a very complex low temperature behaviour. During cooling down to -150°C, no recognizable solid phase has been observed in the inclusions. The enlargement of the bubble is only visible by an optical change during the cooling run. Nucleation starts during subsequent heating between -80°C and -70°C. This behaviour has been already described by Kozlowsky (1984) as typical of Ca-rich brines in fluid inclusions in fluorite from Strzegom pegmatites (Lower Silesia).
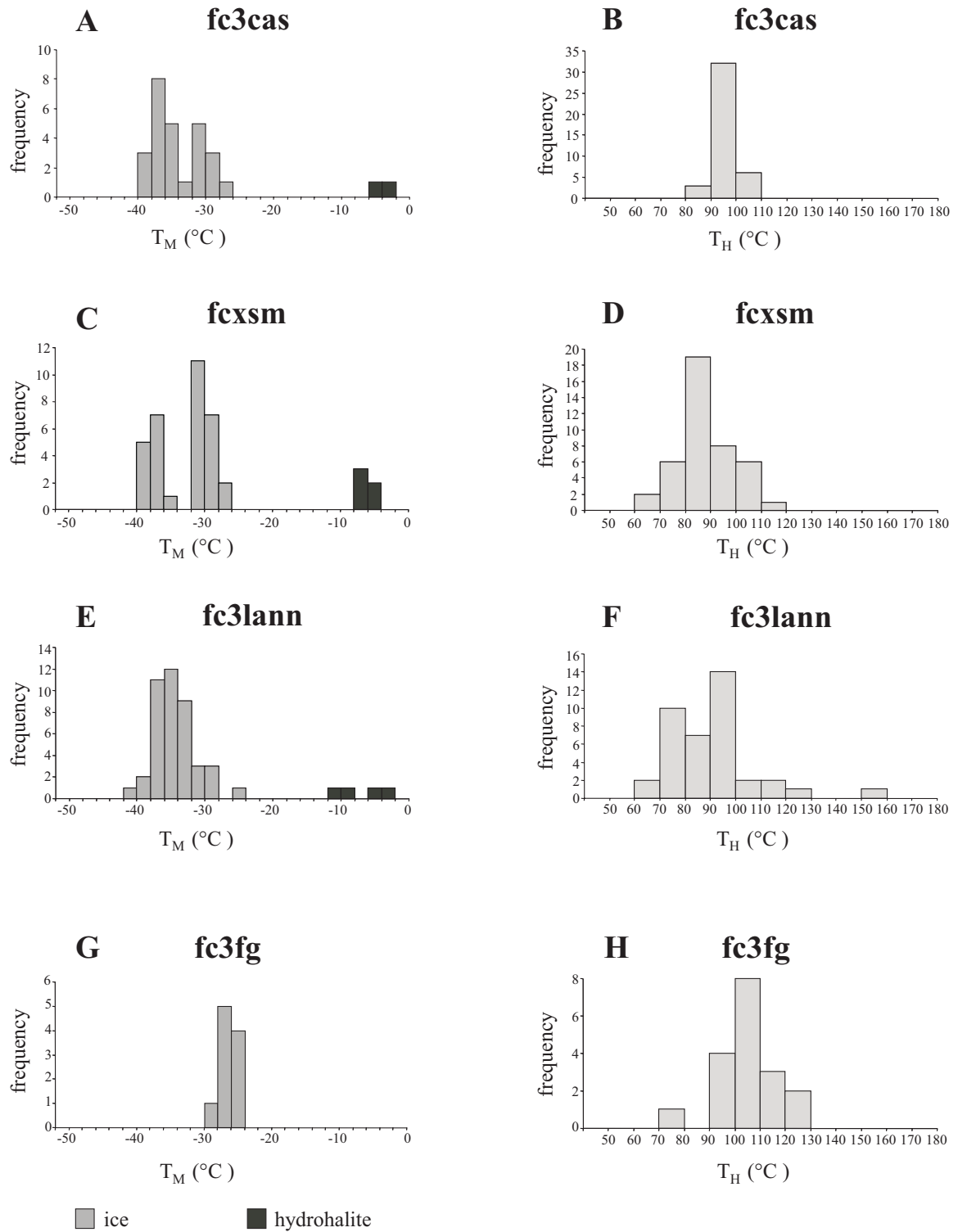
Fig. 6.3. T$_H$ and T$_M$ ice and T$_M$ hydrohalite of fluid inclusions in Dol B for the different localities. A) and B) Casares; C) and D) San Martín de la Tercia; E) and F) Láncara; G) and H) Fontún.

In general, the only recognizable phase observed is ice, which melts between -24 and -39°C (Fig. 6.2B). Only in a few large inclusions it was possible to observe hydrohalite melting between -12 and -2 °C (Fig. 6.2B). This can be due to two different reasons:

1 - hydrohalite is in general very difficult to observe in small, optically not suitable crystals;

2 - hydrohalite can be absent due to metastability during cooling of the inclusions (Bakker 2004).

The observed final melting temperature of ice, distinctly less than the eutectic temperature of hydrohalite (-21.2°C), indicates the presence of cations other than Na in the inclusions. The eutectic temperature, which gives information about the composition of the inclusions, is not clearly constrained by optical observations only. Melt is present in all the measured inclusions at temperatures higher than -40°C. This is consistent with the presence of Ca^{2+} in addition to Na^{2+}.

The stable eutectic temperature for the system $NaCl-CaCl_2-H_2O$ is -52°C (Davies et al. 1990). Alternatively, both Ca^{2+} and Mg^{2+} might be present, because the stable eutectic temperature for the system $NaCl-CaCl_2-MgCl_2.H_2O$ is -57°C (Davies et al 1990). Because of these alternatives, the data are not easy to interpret correctly and will be better described in the next paragraph combining Raman spectroscopy with microthermometry.

In Fig. 6.3, the microthermometric data for Dol B are presented, grouped according to the sample locations. No systematic geographical variation has been observed among the different localities, with one exception only: Dol B of sample fc3fg (Fontún locality, in the Correcilla Unit). The fluid inclusions in this sample show slightly but systematically lower T_M ice and similar T_H (Fig. 6.3G) and a different low temperature behaviour. Nucleation occurred during the cooling run between -80 and -90°C, and was accompanied by the shrinking of the bubble, which almost disappeared. Ice is the only solid phase present in the inclusions. Hydrohalite is lacking: however this phase might have been overlooked because of the exiguous number of measurements, due to the small size of the fluid inclusions and the darker colour of the dolomite crystals.

The only measurable fluid inclusions trapped in Dol C is from the same sample (fc3fg, Fontún locality, see chapter 4, Fig. 4.1). The measurements are again not very numerous, due to the small size and the very flat and irregular shape of the inclusions. The fluid inclusions show a different behaviour compared to those trapped in Dol B. During cooling, the bubble disappears at -40°C. During subsequent heating, no evidence of phase changes has been observed up to -5°C. The melting temperature of ice has been observed between -5 and -1°C (Fig. 6.4A). The melting of the last solid ice phase usually takes place a few decimals of a degree after the reappearance of the bubble. In this case no phase change has been observed before the reappearance of the bubble. These temperatures indicate very diluted solutions or, alternatively, a metastable behaviour.

Generally, high-temperature runs were carried out before the low-temperature runs, in order to avoid cracking of the fluid inclusions. This represents a potential danger when high density fluids are present. This is the case of the fluid inclusions trapped in Dol B phase, where the bubble disappears during cooling.

A   fc3fg Dol C

B   fc3fg Dol C
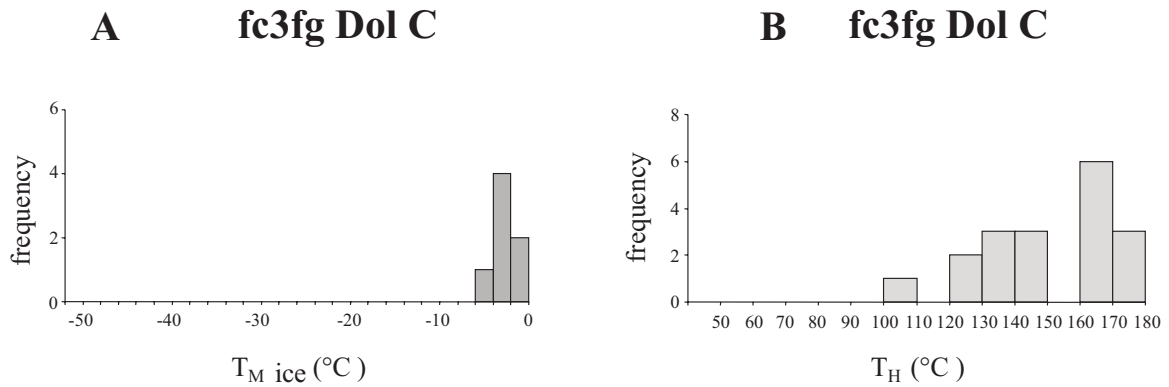
Fig. 6.4. A) Frequency histogram of the final melting temperature of ice in fluid inclusions within Dol C; B) frequency histogram of the temperature of homogenization (T$_H$) of fluid inclusions in Dol C (sample fc3fg).

The homogenization temperatures of Dol C range from 128 to 175 °C (Fig. 6.4B). These values are distinctly higher than those of the fluid inclusions trapped in Dol B.

6.3. Raman spectroscopy

Raman spectroscopy combined with microthermometry provides a helpful methodology to correctly identify and interpret all the phase changes happening during the heating of frozen fluid inclusions. The temperature gradients and the heating-cooling procedures, used during the measurement of the fluid inclusions, play a crucial role in the nucleation of stable assemblages. Raman spectroscopy revealed that different heating-cooling experiments

Fig. 6.5. A) Normal heating-cooling procedure for microthermometry of the fluid inclusions; B) composite heating cooling procedures for microthermometry of fluid inclusions.

might lead the system to stabilize under different assemblages. Consequently, the fluid inclusions displayed different melting behaviours (i.e. different melting temperatures of ice, no nucleation of hydrohalite), which would result in different values of the calculated salinities.
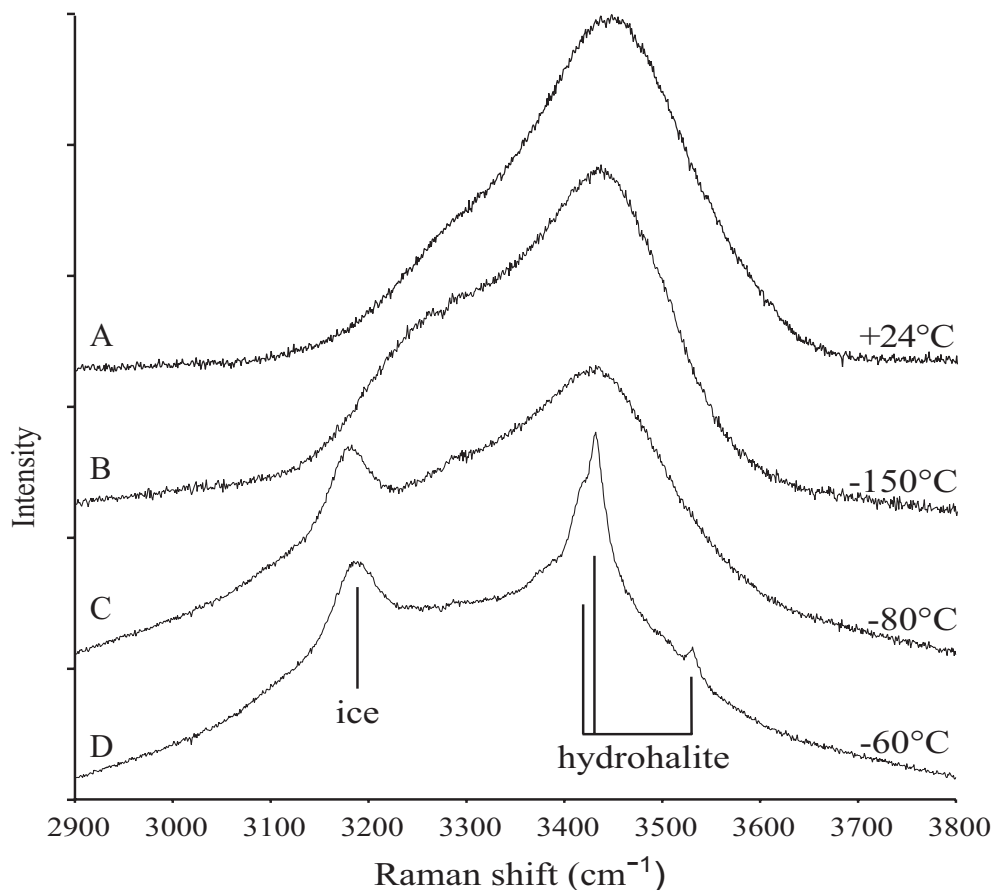
Fig. 6.6. A) Raman spectrum collected at room temperature; B) Raman spectrum collected after normal heating-cooling procedure at -150°C; C) Raman spectrum collected after normal heating-cooling procedure at -80°C; D) Raman spectrum collected after normal heating-cooling procedure at -50°C.
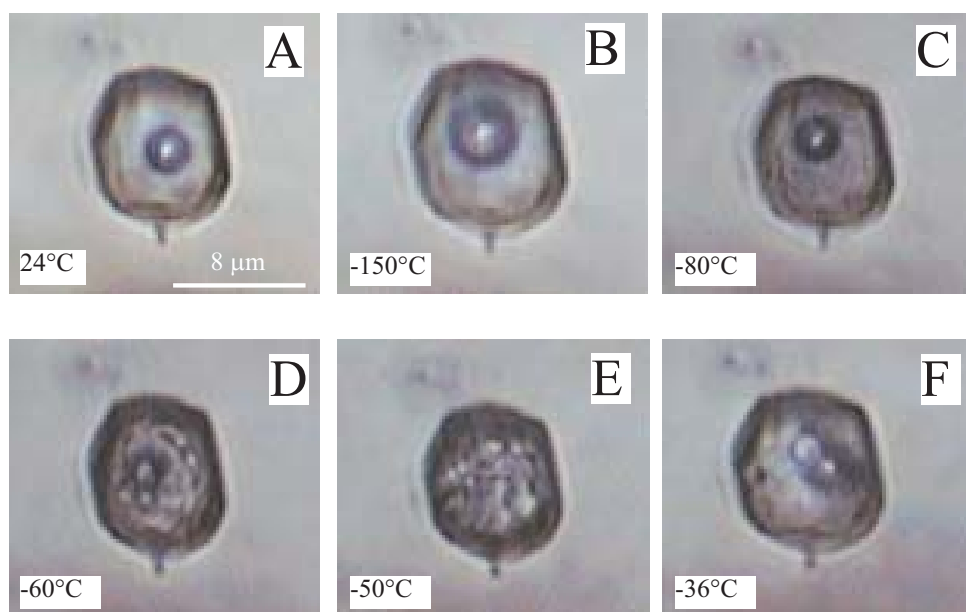
Fig. 6.7. Microphotographs of fluid inclusions collected during heating-cooling procedure. A) 24°C; B) -150°C; C) -80°C; D) -60°C; E) -50°C; F) -36°C.

Eleven suitable fluid inclusions in Dol B were monitored under normal and composite heating cooling procedures (Fig. 6.5). Raman spectra were collected at different temperatures. No Raman spectra are available for inclusions trapped in Dol B and Dol C phases of the above discussed sample fc3fg, due to the small size and the irregular shape of the inclusions. All the phase change temperatures and Raman peak positions are summarized in Tab. 6.1.

T melt (°C)			Peak positions at -190°C		Optical observation
Ice	HH	HX	HX	HH	
-27	-12	no	No HX		Nucleation during cooling at -70°C (ice + HH)
-33.5	no	-41.5	3199, 3364, 3396, 3403, 3425, 3454, 3508	No HH	No nucleation during cooling (glass); nucleation during heating.
-39	no	-39	3199, 3396, 3425, 3506	No HH	No nucleation during cooling (glass); nucleation during heating
-31	-5	-41	3204, 3364, 3396, 3453, 3507	3405, 3422, 3437 (shoulder), 3537	No nucleation during cooling (glass); nucleation during heating
-29.5	-9	-41.5			No nucleation during cooling (glass); nucleation during heating
-29	-6	-47	3202, 3366, 3422, 3459, 3511	3405, 3438 (shoulder), 3538	No nucleation during cooling (glass); nucleation during heating
-31	-3.5	-41			No nucleation during cooling (glass); nucleation during heating; metastable absence of HH
-32.5	-4°C	-42.5			No nucleation during cooling (glass); nucleation during heating
-29	-6	-41	3201, 3367, 3399, 3422, 3454, 3511	3405, 3422, 3437, 3538	No nucleation during cooling (glass); nucleation during heating; metastable absence of HH
-30	-5	-42.5			No nucleation during cooling (glass); nucleation during heating; metastable absence of HH
-29	no	no	No HX	No HH	Nucleation during cooling (ice);
-30	-5	-42.5	3362, 3398, 3511	3405, 3422, 3437, 3536	Nucleation during cooling at -85°C (ice + glass).

Tab. 6.1. Raman spectroscopy mealting temperatures, Raman peak positions and optical observations for different fluid inclusions. HX (hydro-x), HH (hydrohalite).

6.3.1. Normal heating-cooling procedure

The presence of aqueous solutions was confirmed by Raman measurements on the liquid phase of the fluid inclusions at room temperature. Although liquid water is usually difficult to recognise in carbonate crystals due to the high background signal of the host mineral, fluid inclusions close to the sample surface revealed the "typical water hill", a brad peak between 3000 and 3700 cm^{-1} (Fig. 6.6A).

During the normal heating-cooling procedure, the inclusions show a metastable behaviour. During the cooling run, down to -150°C, the inclusions do not nucleate any recognizable crystalline phase, forming an amorphous solid ("glass") with a Raman spectrum similar to the one of liquid H_2O (compare

spectra at room temperature and at -150°C in Fig. 6.6). The only optical change in the inclusion is the size-increase of the bubble (compare microphotograph A and B in Fig. 6.7). During further heating, the "glass" starts crystallizing, which is also visible by the contracting bubble. Between -80°C and -70°C, the mass recrystallizes slowly to a microcrystalline mixture with a granular texture and a brownish colour (Fig. 6.7C). This phenomenon is confirmed by the appearance of the peak of ice and other salt hydrate phases in the Raman spectrum (Fig. 6.6 C). The appearance of the granular texture could have been easily mistaken for the eutectic temperature of the fluid system if Raman spectroscopy had not been applied. At this temperature, it is not possible to distinguish the peaks belonging to different salt hydrate phases due to the small size of the crystals, which are randomly oriented inside the inclusion. After subsequent heating, recrystallization continues and peaks belonging to ice can be identified, sometimes associated with hydrohalite (Fig. 6.6D).

According to their final melting behaviour, two groups of inclusions have been distinguished:

Type 1 final melting behaviour - hydrohalite is the final phase melting, with T_M observed between -12°C and -3.5°C; ice is melting between -33°C and -28°C.

Type 2 final melting behaviour - ice is the final phase melting, with T_M observed between -39°C and -33.5°C; no hydrohalite nucleating.

6.3.2. Composite heating-cooling procedure

In order to generate an assemblage that approaches the stable configuration, all of the inclusions (type 1 and type 2 final melting behaviours described in paragraph 6.3.1), were monitored under a composite heating-cooling procedure. Raman spectra were collected to distinguish the different peak patterns related to the salt-hydrates present in the inclusions.

Type 1 final melting behaviour

After composite heating-cooling procedure, the inclusions that have hydrohalite (HH) as the final phase melting during normal heating-cooling procedure (*type 1 final melting behaviour*) nucleate ice, HH and at least one third phase of unknown origin. At -190°C, it is possible to clearly distinguish in the Raman spectra the peak belonging to ice, the four peaks of the HH (peak-wavenumbers at 3405, 3422, 3437, 3538 cm^{-1}, Fig. 6.8A) and five peaks belonging to one (or maybe more than one) unknown salt hydrate, here called "HX" (peak-wavenumbers at 3200, 3366, 3396, 3425, 3454 and 3510 cm^{-1}). With increasing temperature the peaks become less and less pronounced and difficult to monitor under Raman spectroscopy, due to the increasing background signal (Fig. 6.9).

In order to individuate with accuracy the exact T_M (HX), a cyclic step-wise heating-cooling procedure was applied: the inclusions were heated with increments of 2-3°C and, after any heating step, cooled down to -150°C. Raman spectra were measured at -150°C after any step and compared with the spectrum that shows the original configuration. After the temperature of melting of a salt hydrate is reached, further cooling will nucleate only the phases that did not melt, with the melted phase persisting
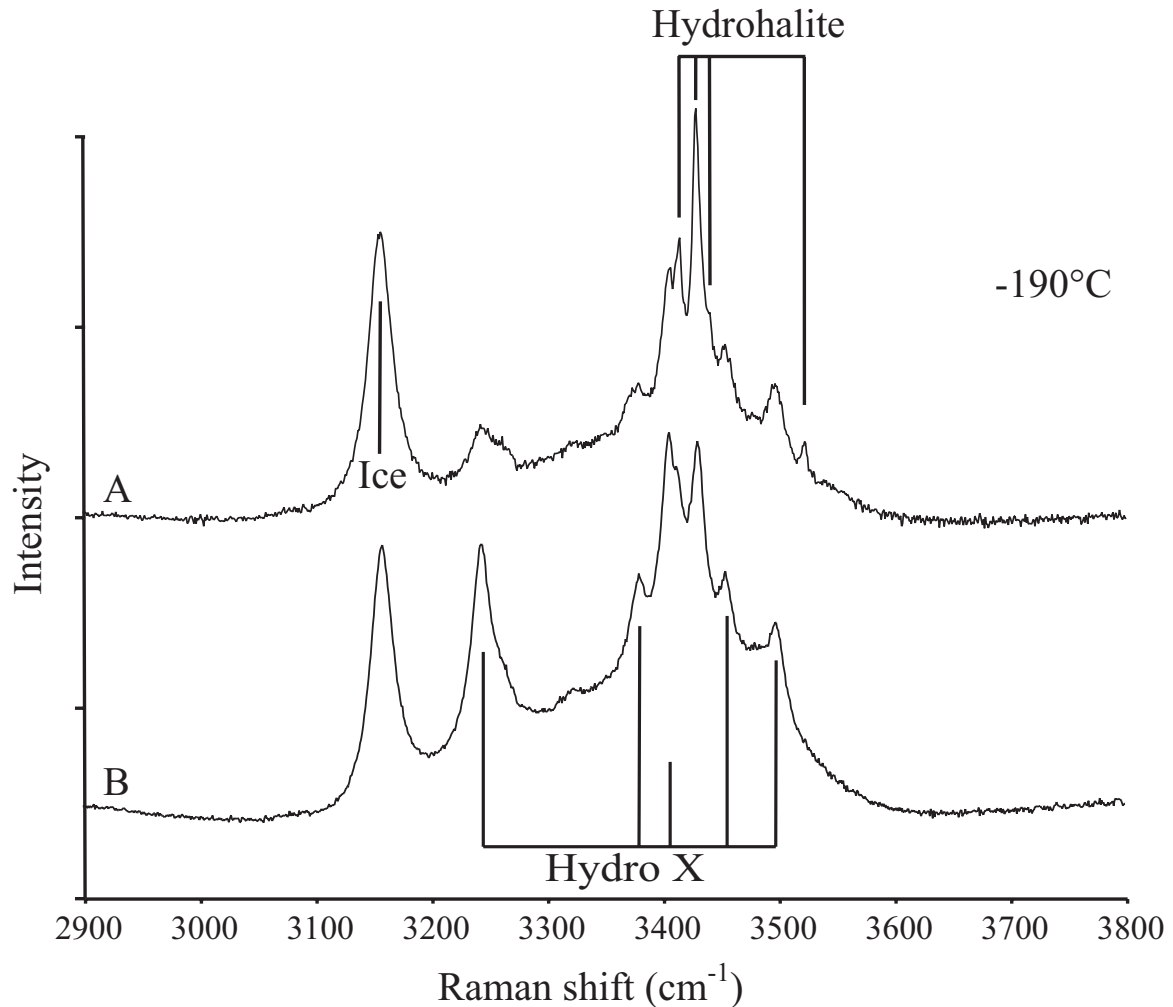
Fig. 6.8. Raman spectra collected at -190°C after composite heating-cooling procedure. One can distinguish the peaks belonging to ice, four peaks characterizing hydrohalite (peak-wave numbers at 3405, 3422, 3437, 3538 cm^{-1}), and five peaks belonging to the unknown salt hydrate "hydro-X" (peak-wavenumbers at 3200, 3366, 3396, 3425, 3454 and 3510 cm^{-1}). The different intensity of the peaks depends on the laser incident orientation on the crystal surface. Two different assemblages can be distinguished, according the final melting behaviour described during normal heating7cooling procedure: A) type 1 final melting behaviour: the inclusions that have hydrohalite (HH) as the final phase melting during normal heating-cooling procedure; B) type 2 final melting behaviour: the inclusions having only ice as the final phase melting during normal heating-cooling procedure (see text for details).

as a metastable liquid. This procedure, which is based on the metastable absence of the solid phases after their melting, is summarized in Fig. 6.10.

The HX is the first phase to disappear, in a temperature range between -47°C and -41°C. The T_M (ice) is observed in the range between -33°C and -29°C. This temperature is consistent with the one measured during normal heating-cooling procedure. The T_M (hydrohalite) has been observed between -6°C and -3.5°C.

Type 2 final melting behaviour

The inclusions that have ice as the last melting phase during the normal heating-cooling procedure and do not show nucleation of hydrohalite (*type 2 final melting behaviour*), nucleate ice and the unknown

phase HX (Fig. 6.8B). The peak positions of HX clearly correspond to the ones of the HX phase that nucleate together with HH. The nucleation of HH in this inclusions is ambiguous. The T_M (HX) is observed between -41.5°C and -39°C. Ice is the last phase melting between -39°C and -33.5°C. No T_M (HH) has been recorded.
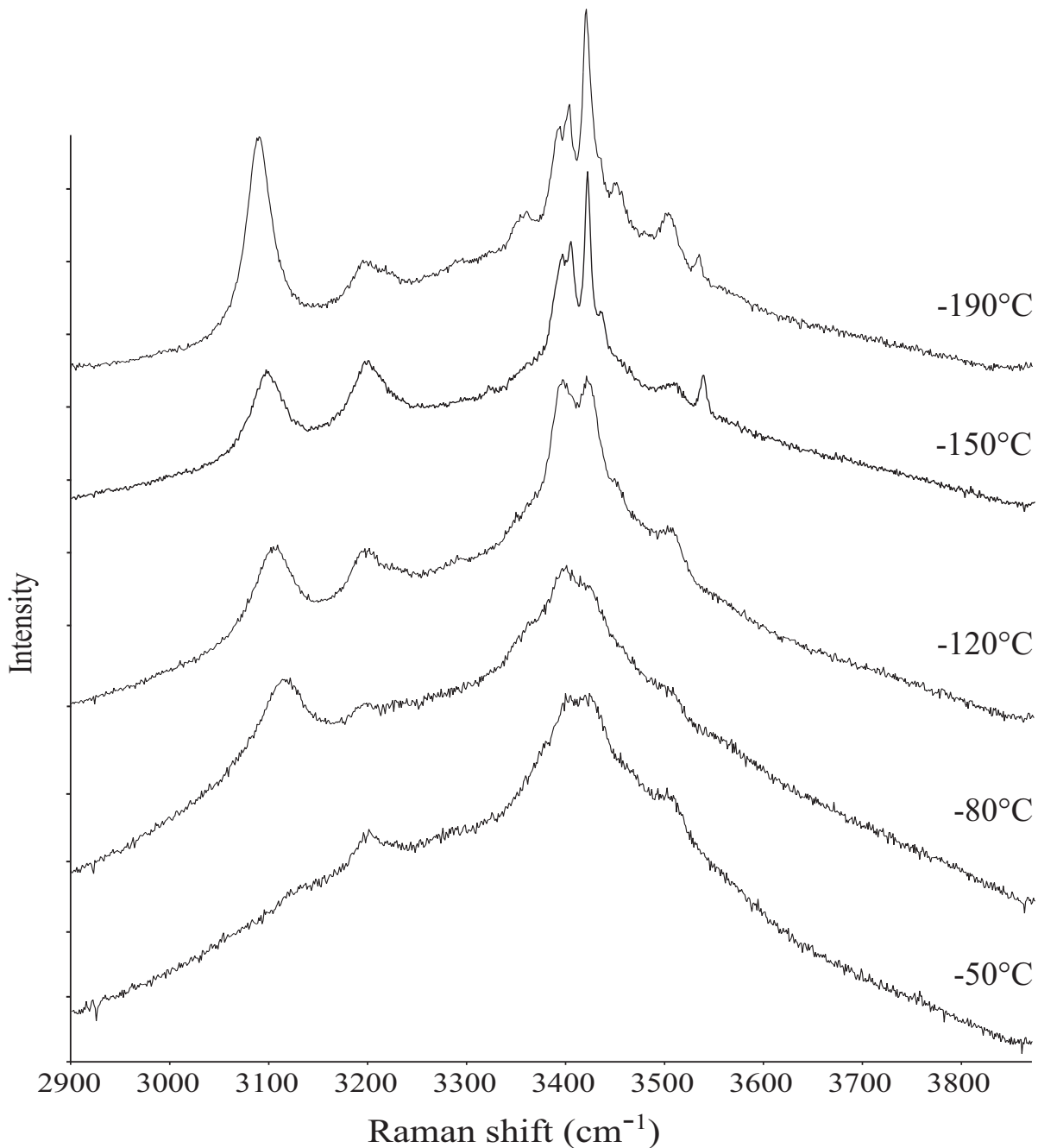
Fig. 6.9. Raman spectra measured at different decreasing temperatures after composite heating-cooling procedures: the peaks become less and less pronounced due to the increasing background signal.

Inconsistent behaviour

Some inclusions that do not nucleate hydrohalite during normal procedure (*type 2 final melting behaviour*) may or may not nucleate it during the composite heating-cooling procedure. Figs. 6.11A and

6.11B are two microphotograph sequences of the same inclusion, monitored during the composite heating-cooling procedure, showing inconsistent final melting behaviour: in sequence A, ice is the final melting phase (metastable absence of hydrohalite); in sequence B hydrohalite is the final melting phase. This phenomenon is always associated with inconsistent T_M (ice), depending on the presence or the metastable absence of HH. An increase of 5°C to 6°C has been systematically measured between the T_M (ice) without nucleation of HH and the T_M (ice) with nucleation of HH.
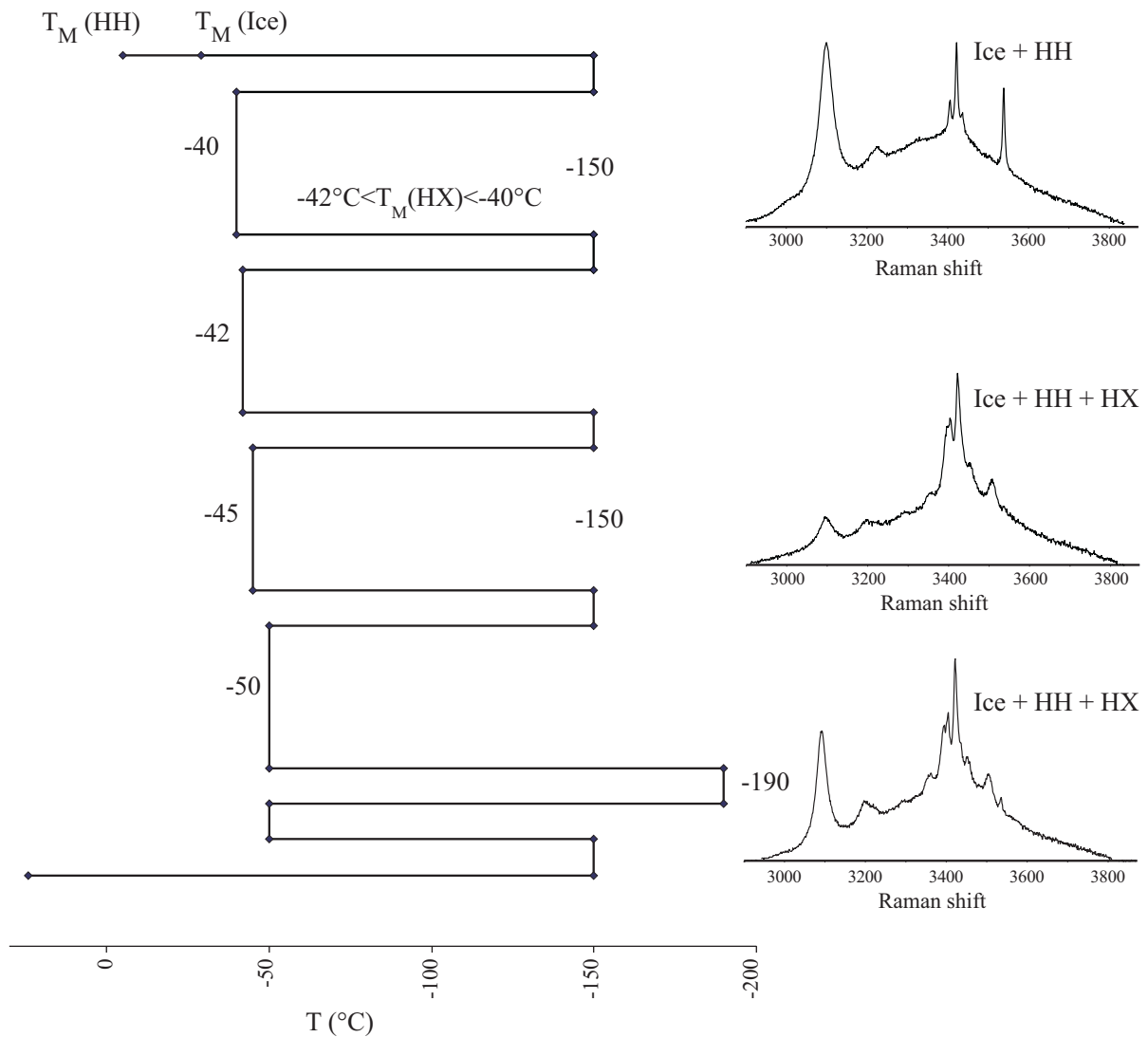
Fig. 6.10. Cyclic step-wise heating/cooling procedure (see text for details).

Fig.6.11. A) Microphotograph sequence of a fluid inclusion with type 1 final melting behaviour (ice as final phase melting) during composite heating/cooling procedure. The inclusion does not nucleate hydrohalite; B) microphotograph sequence of the same inclusion during the same heating-cooling procedure. The inclusion shows an inconsistent behaviour: hydrohalite is present and melts as final phase; T_M ice is decreased of about 5-6°C (see text for details).

6.4. Preliminary discussion of microthermometric data

The fluid trapped in Dol B belongs to a H_2O-salts system. The most likely stable configuration may be represented by the system H_2O–$NaCl$–XCl, where X is an unknown cation. The X cation clearly nucleates as a different salt hydrate phase, together with hydrohalite in a salt mixture or alone. In order to identify the unknown salt-hydrate, it has to be taken into account that the peak positions of the individual phases may be shifted by several wave numbers due to the presence of a mixture of salt-hydrates within the inclusions (see also Bakker 2004). Furthermore, the presence of more than one unknown cation cannot be excluded, and this would add another factor of complexity to the interpretation of the Raman spectra. The peak patterns are compared with the ones obtained from experimental data on synthetic fluid inclusions, in the fluid system $CaCl_2$ + $NaCl$ (Samson and Walker 2000) and in the $MgCl_2$ system (Bakker 2004). No clear similarity is observed between the observed peak configurations and the published data. It may be worthwhile to carry out another series of experiments on synthetic fluid inclusions, for example in more complex systems, such as $MgCl_2$ + $CaCl_2$ + $NaCl$, to discriminate the different possibilities.

The HX phase disappears between -47°C to -41°C. This temperature range, that may be considered the true eutectic temperature of the system, does not correspond to the eutectic temperature of Ca-chloride dominated aqueous solutions (-49.2°C) and Mg-chloride dominated aqueous solutions (-33.6°C, Crawford 1981).

Ice is the second phase melting, in the range between -32.5°C and -29°C. This phase change is the only optically recognizable in almost all of the inclusions measured. Inconsistent T_M (ice) has been observed in the same inclusion, depending on the heating-cooling procedure used. The nucleation of HH is also dependent on the heating-cooling procedure: HH may nucleate only during composite procedure or may not nucleate at all, with the fluid persisting as a metastable assemblage. The metastable absence of HH is probably connected to the inconsistent T_M (ice), which has been observed: the T_M(ice) is systematically increased by 5-6°C relative to the T_M (ice) measured in the same inclusion in metastable absence of HH.

The microthermometric values of the fluid inclusions trapped in Dol B show a quite homogeneous composition and temperature for the different localities (Fig. 6.3). The range of variation observed in inclusions trapped in the same locality and also in the same crystal may be related to slight variations in salinity and temperatures of the fluid. The only exception is represented by the fluid trapped in the inclusions of Dol B from the Fontún locality (sample fc3fg). The measurements show slightly lower ice melting temperatures and variable homogenization temperatures. This dolomite is characterized by very low oxygen isotopic composition ($\delta^{18}O$ = -11) compared to the values of Dol B from the nearby localities ($\delta^{18}O$ between -6 and -4). Dol B is followed by Dol C, which is characterized by non-luminescent colour and a similarily low oxygen isotopic composition. The fluid trapped in Dol C is characterised by a very low salinity and distinctly higher homogenization temperature (Fig. 6.4A and 6.4B) compared to the fluid inclusions within Dol B in the same sample. No Raman spectra are available due to the high background signal related to the flat and irregular shape of the fluid inclusions. This fluid has been observed only locally, in the already mentioned sample locality (fc3fg, Fontún locality). The ample spread of T_H values

and the data distribution may also indicate re-equilibration of the inclusions due to higher temperature. These data are difficult to interpret. The fluid inclusions trapped in Dol B in the same sample show a certain variability, as indicated by higher T_H values between 70 and 130°C, Fig. 6.3H), never reaching, however, the higher temperatures recorded in Dol C (values between 120°C and 175°C). On the other side, similar diluted fluids to the ones trapped in Dol C have been observed in some cases, but only limited to the outer, Fe-oxihydroxide-rich rim of Dol B II. In one case, a gradient has been also observed from high salinity-lower homogenization temperatures in the core of Dol B II to low salinity-higher homogenization temperatures in the outer rim. This might mean that the eventual thermal event responsible for the higher temperature peaks reported in Dol C was only partly able to reset the inclusions in the outmost rim of Dol B II phase, which probably came into contact with the fluid. Alternatively, the cracking of the fluid inclusions may be responsible of the higher homogenization temperatures in the Dol B II.

The very close spatial association between the dedolomitized Fe oxy-hydroxide-rich zone and the inclusion-rich zones of Dol C may also indicate that the inclusions were trapped during dissolution and re-crystallization of the dolomite during the alteration event, which caused the oxidation of the iron-rich outmost zone of Dol B II. A shown in Figs. 6.1H and 6.1I, Dol B II is characterized by high iron content, as demonstrated by the non-luminescent colour in CL. The red dull CL colour, which is characteristic of the inclusion-rich zones of Dol C, may indicate dissolution and reprecipitation from a fluid with slightly different composition.

6.5. Salinity calculations

Raman spectroscopy at low temperatures combined with low temperature microthermometry revealed the presence of ice, hydrohalite and at least one additional phase, presumably a salt-hydrate. As mentioned earlier, the unknown phase could not be identified, due to the lack of experimental data for complex, highly saline fluid inclusions.

According to the data available, the system H_2O-NaCl-$CaCl_2$ represents the most likely model composition of the fluid inclusions. Magnesium surely represented one of the main components of the dolomitizing fluid at the time of dolomitization, but its concentration in the fluid trapped in the inclusion is strongly controlled by Mg fractionation during dolomitization (see paragraph 6.7).

For this reason salinity is calculated in the ternary system H_2O-NaCl-$CaCl_2$, according to the state equation from Nader et al. (1996) (see chapter 3, paragraph 3.8.4 for details). The values range from 27.4 to 28.5 NaCl+$CaCl_2$ eq. mass %. The exact proportion between the salts is reported in Tab. 6.2. However, this proportion is in part artificial as the salinity is calculated as eq. mass %. For comparison, the salinity was also calculated in $CaCl_2$ eq. mass %. The calculation in this system was necessary in

Sample	Volum fraction	T_H	T_M ice	T_M HH	Salinity NaCl +CaCl$_2$ eq. wt. %	Salinity CaCl$_2$ wt. % eq.
fc3sm p3f9	0.96	101	-39			27.7 mass% eq. CaCl$_2$
fc3sm p3f2	0.93	108	-31	-5	8.6 mass % eq. NaCl 19.6 mass % eq. CaCl$_2$	25.1 mass% eq. CaCl$_2$
fc3sm p3f3	0.97	106	-27	-12	13 mass % eq. NaCl 14.1 mass % eq. CaCl$_2$	23.6 mass% eq. CaCl$_2$
fc3sm p3f4	0.94	86	-32			25.5 mass% eq.CaCl$_2$
fc3sm p3fx	-	-	-30	-5	9.6 mass % eq. NaCl 18.3 mass % eq. CaCl$_2$	24.8 mass% eq. CaCl$_2$
fc3sm p3f6	0.95	90	-31			25.1 mass% eq. CaCl$_2$
fc3lann p1f6	0.95	122	-32.5	-4	7.5 mass. % eq. NaCl 21.0 mass. %eq. CaCl$_2$	25.7 mass% eq. CaCl$_2$
fc3lann p1f5	0.95	75	-31	-3.5	8.7 mass. % eq. NaCl 19.6 mass. %eq. CaCl$_2$	25.1 mass% eq. CaCl$_2$
fc3lann p1f4	0.93	96	-37.5			27.3 mass% eq. CaCl$_2$
fc3lann p1f11	0.95	100	-29			24.4 mass% eq. CaCl$_2$
fc3lann p3f2bis	0.95	80	-35	-9	9.8 mass. % eq. NaCl 17.6 mass. %eq. CaCl$_2$	26.5 mass% eq. CaCl$_2$
fc3lann p4f2	0.96	76	-34			26.2 mass% eq. CaCl$_2$
fc3lann p3f1	0.96	82	-31.5			25.3 mass% eq. CaCl2
fc3lann p3f5	0.93	91	-33.5	-10	6.5 mass. % eq. NaCl 22.3 mass. %eq. CaCl$_2$	26.0 mass% eq. CaCl2
fcxsm p4f1	0.96	81	-29	-5	10.6 mass. % eq. NaCl 17.0 mass. %eq. CaCl$_2$	24.4 mass% eq. CaCl$_2$
fcxsm p1f1	0.92	102	-30	-4	9.6 mass. % eq. NaCl 18.3 mass. %eq. CaCl$_2$	24.8 mass% eq. CaCl$_2$
fcxsm p1f2	0.94	107	-29	-6	10.6 mass. % eq. NaCl 17.0 mass. %eq. CaCl$_2$	24.4 mass% eq. CaCl$_2$
fcxsm p1f6	0.95	70	-36			26.8 mass% eq. CaCl$_2$
fcxsm p2f1	0.95	83	-30	-7	9.4 mass. % eq. NaCl 18.7 mass. %eq. CaCl$_2$	24.8 mass% eq. CaCl$_2$
fcxsm p1f7	0.96	88	-39			27.7 mass% eq. CaCl$_2$
fcxsm p3f1	0.95	102	-30			24.8 mass% eq. CaCl$_2$

Tab. 6.2. Salinity calculation of the most representative fluid inclusions.

particular for the inclusions in which hydrohalite did not nucleate, so that the salinity could not be expressed in NaCl-CaCl$_2$. mass % eq.

The salinity values for the most representative inclusions, of which accurate Raman data are available, are reported in Tab. 6.2.

6.6. Fluid inclusions in the dolomitized Carboniferous carbonate succession

Comparison between the fluid inclusions data of the dolomites sampled from the Cambrian rocks and from the Carboniferous dolomitized lithologies (Gasparrini 2003, Gasparrini et al. 2006a, b) reveals strong similarities. The dolomites, hosted in the precursor rocks of different ages, are also petrographically and geochemically similar, with abundant void-filling Dol B phases bearing numerous aqueous inclusions. These consistencies indicate compositional similarities between the fluids responsible for the dolomitization of the two carbonate successions. However, homogenization temperatures of Dol B from the Carboniferous-hosted dolomite show values (100°C to 150°C, Gasparrini 2003, Gasparrini et al. 2006a), whose mean is generally higher than the ones in the Cambrian Dol B (80°C to 110°C).

The model composition and the salinity of the dolomitizing fluid were calculated with the same methodology. Similar highly saline fluids were observed in the fluid inclusions in Dol B in both dolomitized carbonate rocks from the Cambrian and Carboniferous formations. Furthermore, the inclusions show a very similar metastable behaviour, causing the nucleation of the unknown salt-hydrate phase (HX), which melts in the same temperature range. A similar fluid, or, in alternative, a similar origin of the fluid, can be postulated for the dolomitization process affecting the two carbonate successions.

6.7. Crush-leach tests

Crush-leach analyses were carried out on 5 Cambrian dolomite samples and, for comparison, on 8 Carboniferous dolomite samples. Br, Na, Cl, K, Li, Ca and Mg were measured. All the data are presented in Tab. 6.3. The values have been recalculated to the best estimate of their concentration in the fluid inclusions, from the salinity determined by microthermometry and Cl$^-$ concentration in the crush-leach solution (Tab. 6.4), using the following relations:

microthermometry Cl concentration (ppm) / analysed Cl concentration = **F**

_____

concentration in the fluid inclusion = **F** * elemental crush-leach analyses (ppm)

This correction was possible only for the samples where accurate microthermometric measurements were available.

The method has some limitations. As already discussed, it is a bulk analysis method, which does not allow the distinction between different generations of fluid inclusions in the mineral phases. In this case, secondary inclusions have not been observed in the mineral phases analysed, except monophase liquid fluid inclusions. These inclusions are probably related to the last exposure phase, and if formed during meteoric diagenesis, are not able to affect the elemental ratios but only to dilute the total concentration. Secondly, the determination of salinity is dependent on the model system composition used and it may represent only a rough approximation, especially when dealing with complex and highly saline systems. Although accurate salinity determinations were carried out combining normal microthermometry measurements with low temperature Raman spectroscopy (see paragraph 6.3), the model composition is still a limiting factor.

Halogen ratios, specifically Cl/Br, are useful indicators of the source of salinity, especially if seawater is supposed to be one of the main component of the fluid. Cl and Br are conservative in solution and their concentrations are not affected by water/rock interaction, as long as halite dissolution and/or precipitation are not involved. In contrast to Cl and Br, elements such as Na, K and Li easily change their original concentration by fluid-rock interactions (Fontes and Matray 1993).
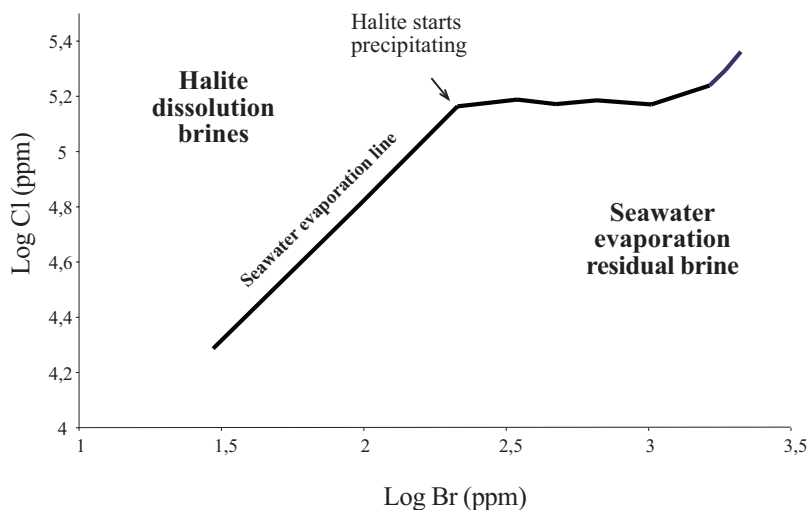
Fig. 6.12. Log Cl versus Log Br diagram showing the evaporation trend of seawater. According to their Cl/Br ratios, two broad brine types can be distinguished: the seawater evaporation residual brines and the halite dissolution brines.

According to the microthermometric data, the fluid trapped in Dol B is a very dense fluid characterised by a salinity well in excess of seawater salinity. Potential processes for generating such a high salinity include subaerial evaporation of seawater and subsurface dissolution of evaporite. During evaporation of seawater, the Cl and Br concentrations rise constantly, but the Cl/Br ratio is maintained constant until halite begins to precipitate (Fig. 6.12, Tab. 6.4). As halite

Sample	fc3lann Dol B	fcxsm Dol B	fcxsm Dol A	fc1fg Dol B	fc1fg Dol A	cabd2b Dol A	cabd2b Dol B	mpbd2m Dol B	mpbd2m Dol A	vcAd1t Dol B	vcbd1t Dol A	cubd1m Dol B	cubd1m Dol A
Formation	Láncara	Láncara	Láncara	Láncara	Láncara	Barcaliente	Barcaliente	Barcaliente	Barcaliente	Barcaliente	Barcaliente	Barcaliente	Barcaliente
salinity	25 $CaCl_2$	25 $CaCl_2$	25 $CaCl_2$	25 $CaCl_2$	25 $CaCl_2$	27 $CaCl_2$	27 $CaCl_2$	26 $CaCl_2$	26 $CaCl_2$	28 $CaCl_2$	26 $CaCl_2$	27 $CaCl_2$	27 $CaCl_2$
Cl (ppm)	188002	188002	188002	188002	188002	172496	172496	166107	166107	178884	166107	172496	172496
Na	6924	11099	9955	4873	5715	8354	6317	6919	5192	4180	3223	7260	5874
K	2598	3465	2965	877	1095	2648	910	2189	1734	1025	857	2134	1128
Li	32	10.5	8.9	3.9	4.6	41	41	7.2	6.5	3.4	2.5	6.2	6
Cl	36052	42453	35237	16664	19506	33848	36182	27533	18154	18736	13498	32940	29520
Br	387	362	300	207	348	344	445	294	190	251	174	381	303
Ca		12469	8492		4702							12198	10909
Mg		263	377		217							197	153
Charge anions		1196	992		549							928	832
Charge cations		1223	970		535							1002	847
Cl/Br (molar)	210	264	265	181	126	222	183	211	215	168	175	195	220
Na/Br (molar)	62	107	115	82	57	84	49	82	95	58	64	66	67
Na/Cl (molar)	0.3	0.4	0.4	0.5	0.5	0.4	0.3	0.4	0.4	0.3	0.4	0.3	0.3
Na/Li (molar)	65	319	338	377	375	61	46	290	241	371	389	353	295
Na/K (molar)	4.5	5.4	5.7	9.5	8.9	5.4	11.8	5.4	5.1	6.9	6.4	5.8	8.9

Tab. 6.3. Crush-leach measurements of Cambrian and Carboniferous hosted dolomite samples.

Sample	Factor	Na	K	Li	Cl	Br	Log Br	Log Cl	Na/Br (w)	Na/Cl (w)	Na/Li (w)	Na/K (w)
cubd1m Dol A	5.78	33975	6524	35	170743	1753	3.24	5.23	19.39	0.20	979	5.21
cubd1m Dol B	5.18	37584	11047	32	170524	1972	3.29	5.23	19.06	0.22	1171	3.40
vcbd1t Dol A	12.15	39158	10412	30	163993	2114	3.33	5.21	18.52	0.24	1289	3.76
vcAd1t Dol B	9.42	39381	9657	32	176519	2365	3.37	5.25	16.65	0.22	1229	4.08
mpbd2m Dol A	9.06	47014	15702	59	164387	1720	3.24	5.22	27.33	0.29	799	2.99
mpbd2m Dol B	5.97	41301	13067	43	164352	1755	3.24	5.22	23.53	0.25	961	3.16
cabd2b Dol B	4.71	29751	4283	193	170400	2096	3.32	5.23	14.20	0.17	154	6.95
cabd2b Dol A	5.04	42147	13356	207	170761	1735	3.24	5.23	24.29	0.25	204	3.16
fc1fg Dol A	9.47	54117	10369	44	184707	3295	3.52	5.27	16.42	0.29	1242	5.22
fc1fg Dol B	11.14	54302	9773	43	185695	2307	3.36	5.27	23.54	0.29	1249	5.56
fcxsm Dol A	5.29	52665	15686	47	186415	1587	3.20	5.27	33.18	0.28	1119	3.36
fcxsm Dol B	4.39	48736	15215	46	186412	1590	3.20	5.27	30.66	0.26	1057	3.20
fc3lann Dol B	5.16	35725	13401	165	186005	1997	3.30	5.27	17.89	0.19	216	2.67

Tab. 6.4. Recalculated crush-leach measurements (see text for details).

precipitation proceeds, the Cl/Br ratio constantly decreases. Br is preferentially enriched in the residual brine because it is less compatible with the structure of halite (distribution coefficient of Br into halite is 0.032, Holser 1979).

In Fig. 6.13A the Na/Cl vs. Cl/Br ratios during seawater evaporation are shown and used according to that of Kesler et al. (1995). The halogen content of the fluid inclusions indicate that the fluid, involved in the dolomitization of both Cambrian and Carboniferous rocks, was seawater which has evaporated past the point where halite precipitation finishes. At this salinity, K-salts are expected to start precipitating (Fontes and Matray 1993). All data plot close to the seawater evaporation line, suggesting that Na was not significantly removed from the solution as a consequence of water-rock interaction.

The Na/K vs. Cl/Br diagram (Fig. 6.13B) can be used in conjunction with the Na/Cl vs. Cl/Br values. The data show some more variability and do not align perfectly along the seawater evaporation line. Nevertheless, all of the samples have roughly the expected Na/K ratios for the degree of evaporation indicated by the Cl/Br ratios, showing that the original seawater values were modified only to a minor extent during water-rock interaction.

In the Cl/Br (molar) vs. Cl (ppm) diagram the data plot only partly on the evaporation line (Fig. 6.13C), having mostly slightly higher Cl/Br ratios than the seawater evaporation line.

In the Log (Cl) vs. Log (Br) diagram, the values are recalculated compositions (Fig. 6.13D). The data plot again along the seawater evaporation line and are consistent with an origin of the dolomitizing fluid from seawater, which has been further evaporated beyond halite precipitation.
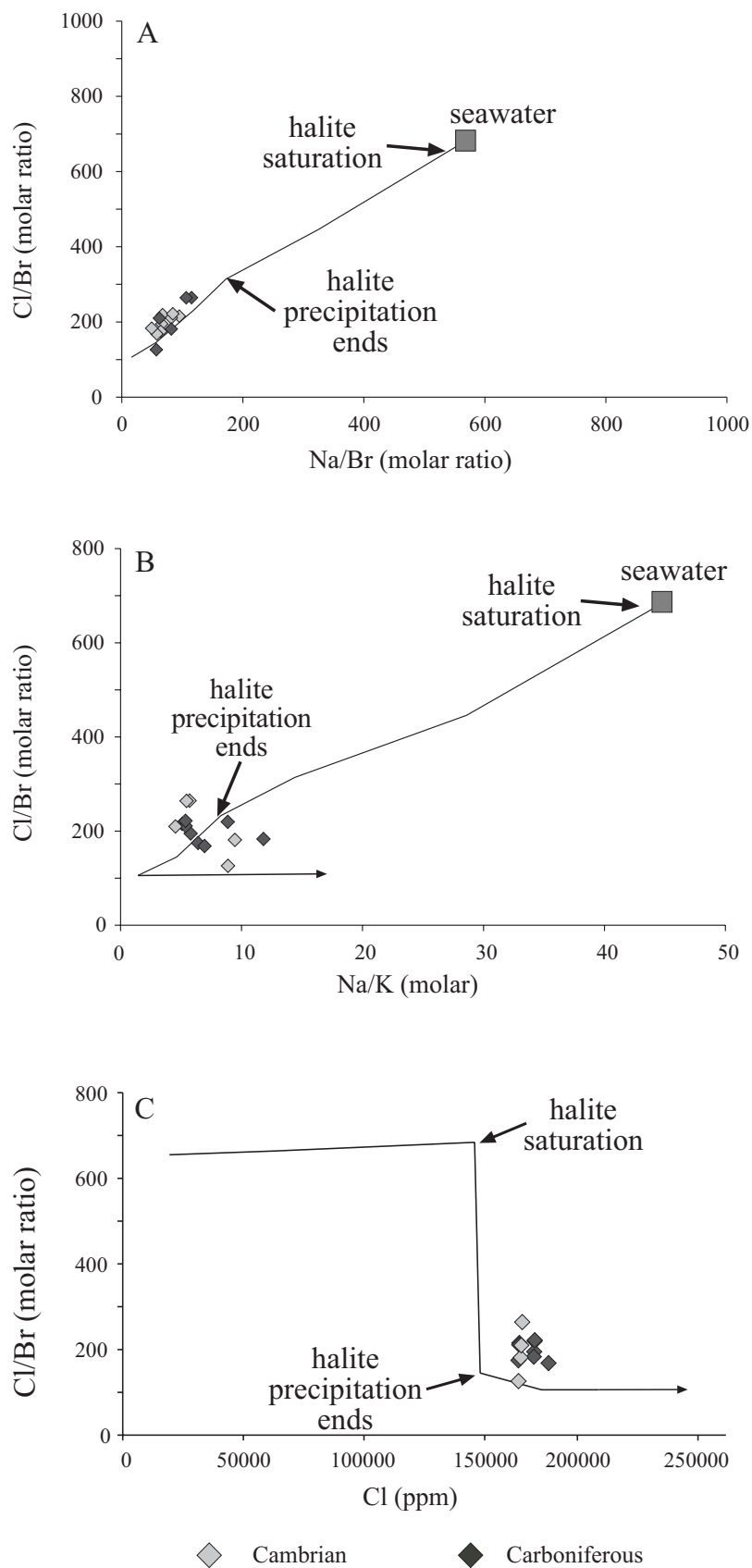
Fig.6.13. Crush-leach fluid composition of Dol B from Cambrian and Carboniferous rocks. For comparison, the seawater evaporation trend is also shown. A) Na/Cl vs. Cl/Br diagram; B) Na/K vs. Cl/Br; C) Cl/Br (molar) vs. Cl (ppm).
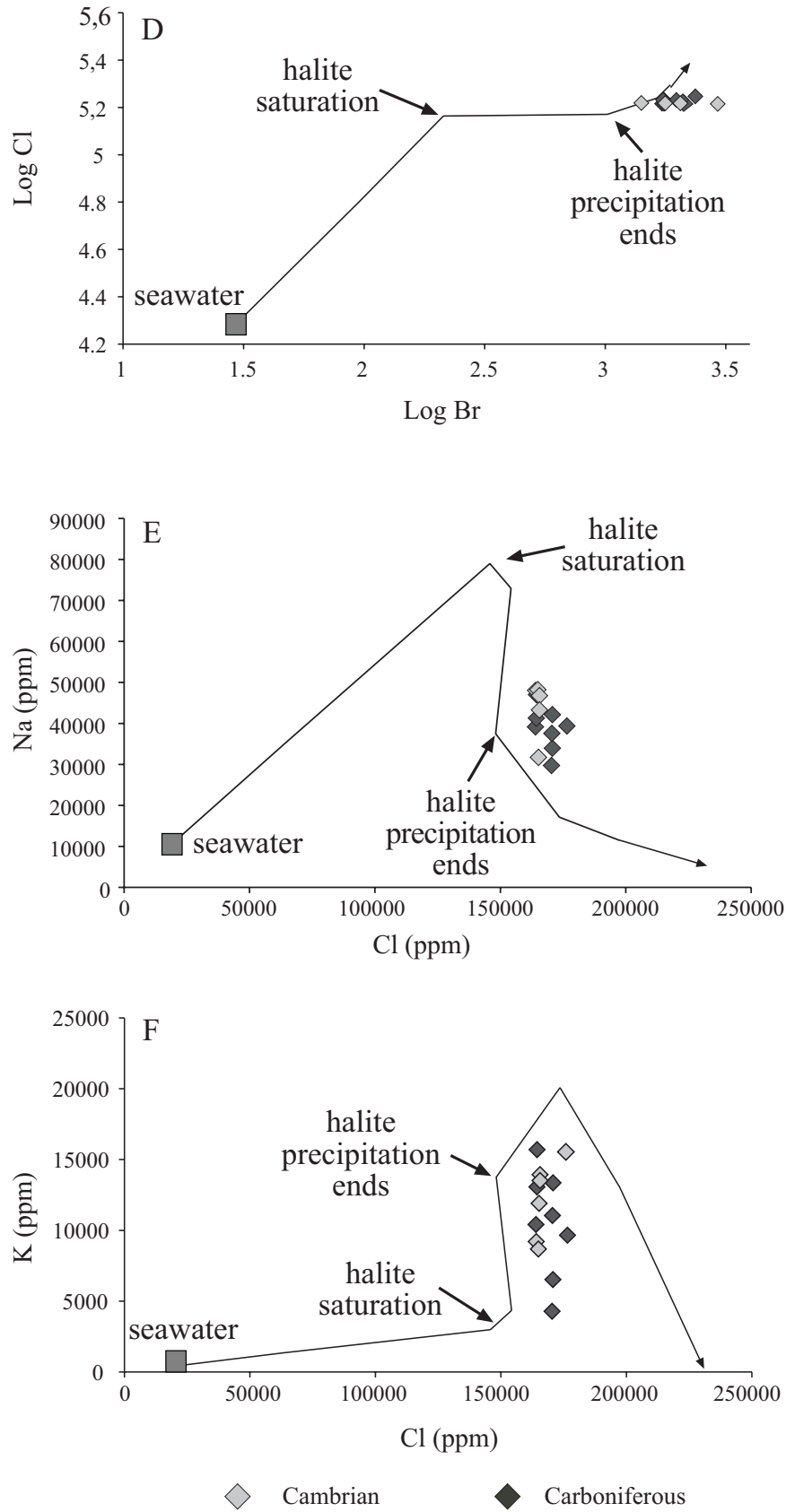
Fig.6.13. Continuation. D) Log (Cl) vs. Log (Br) diagram; E) Na vs. Cl (recalculated concentrations); F) K vs. Cl (recalculated concentrations).

The Na vs. Cl and K vs. Cl concentrations of the reconstructed fluid inclusions are plotted in Figs. 6.13E and 6.13F. For both elements there is some deviation from the value expected from evaporation of seawater: the data do not plot along the seawater evaporation line and the fluid appears to have lost K and gained Na in comparison to the seawater composition expected from the salinity of the fluid. This trend might partly be a burial effect, connected to the conversion of smectite to illite within the thick lower Paleozoic clastic sedimentary succession. This conversion results in depleting the fluid in K and enriching it in Na (Chaudhuri and Clauer 1993), which would explain also the slightly radiogenic Sr composition of the fluid that has been involved in the dolomitization of both the Cambrian and Carboniferous limestones. According to this reaction, the magnitude of the K decrease should, however, balance the magnitude of Na increase, which seems not to be the case. Some other factors might have been involved as well.

I have to mention, however, that part of the deviation of the data from the seawater evaporation line may also be due to uncertainties of the microthermometrically measured chloride concentrations, which were used to recalculate the elemental concentration in the crush-leach results. The visible shift of the data to the right with respect to the seawater evaporation line, in the diagrams Na vs. Cl and K vs. Cl, may at least be partly due to an error as small as 2-3 eq. mass % in the salinity calculation. The K and Na concentrations are in fact comparable to the concentration expected for the degree of evaporation assumed from the Cl/Br ratios of the data set (126 to 265, Tab. 6.3A).

The measured Na/Li weight ratios range from 154 to 1,298 (Tab. 6.3A). The Na/Li for evaporated seawater with the salinity of the fluid should have values around 13,000 (weight ratios) (after the end of halite precipitation). Interaction with clastic rocks might have increased the Li content of the fluids, therefore considerably, pointing again to a possible interaction of the fluids with clastic successions as discussed above.

The Ca and Mg contents were estimated from the methanol leach, in order to reduce the contamination due to dissolution of the host mineral. Dolomite is in fact insoluble in methanol. The fluids appear to be Ca-rich and this is in contrast to the Cl/Br ratios, which indicate highly evaporated seawater, that should be characterized by a very high concentration of Mg relative to Ca. The charge balance between the anions and the cations is very reliable and excludes the possibility of contamination. For a correct interpretation of the data, it has to be kept in mind that Ca and Mg strongly modifies their concentration during dolomitization. Depending on which reaction is used (see chapter 1, paragraph 1.3), dolomitization has the effect of decreasing the Mg content of the fluid and increase (reaction 1.2) or keep invariant the Ca content. The overall effect in both cases is the decrease of the Mg/Ca ratios.

6.8. P-t trapping condition

The P-t trapping conditions were calculated following the procedure explained in chapter 3, paragraphs 3.8.4 and 3.8.5. The fluid trapped in Dol B consists of a single homogeneous liquid phase. During subsequent cooling, the fluid inclusion is forced to follow an isochore until it crosses the liquid-vapour curve, where a vapour bubble should theoretically segregate into the inclusion. From this point on, the fluid inclusion will follow the liquid-vapour curve until it reaches the room P-t conditions. The trapping pressure and temperature of the fluid inclusions will result from the intersection between the isochores and the gradient.
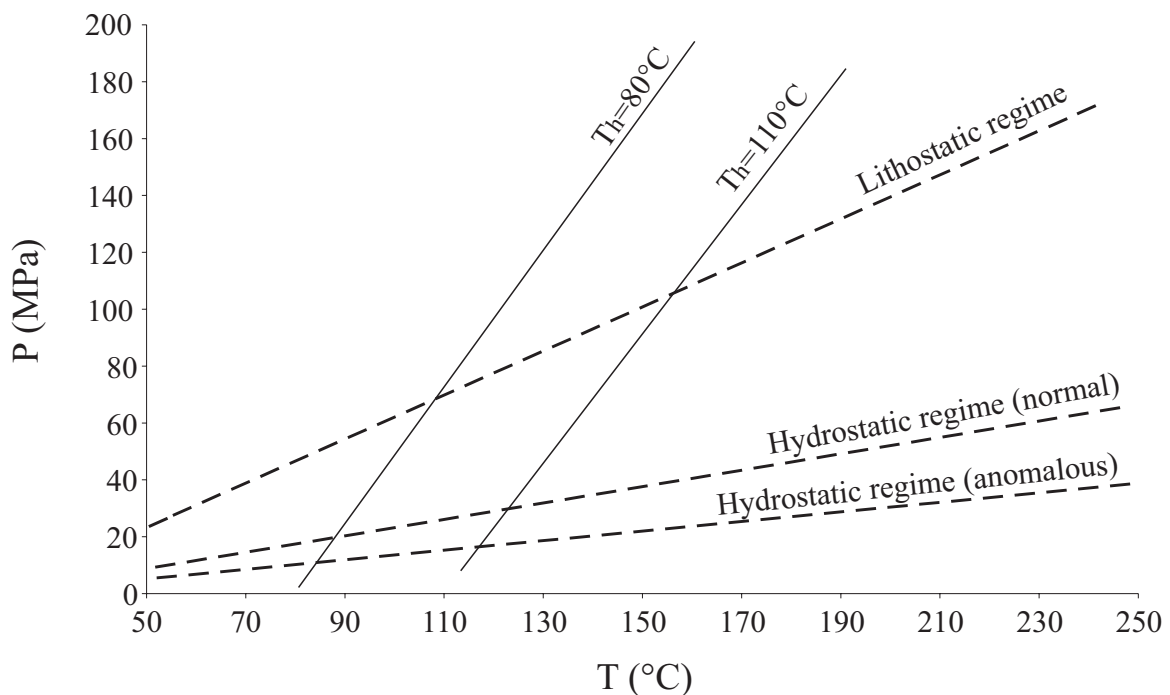
Fig. 6.14. Pressure - temperature trapping conditions of fluid inclusions of known density and TH for three different geothermal gradients: lithostatic, hydrostatic (normal) and hydrostatic (anomalous). The P-t trapping conditions are the intersections of the two isochores (calculated for TH of 80°C and 110°C) and the geothermal gradient.

The method may lead to significant errors due to the chosen P/t gradient (hydrostatic or lithostatic). In open systems, characterized by high water/rock ratios (the most likely setting for massive dolomitization), hydrostatic conditions can be considered more realistic than lithostatic ones; big amounts of fluids have to circulate through the succession in order to provide the requested Mg for accomplishing the massive dolomitization of calcium carbonate.

Isochores were constructed using a model composition of 14 $CaCl_2$+14 NaCl eq. mass %. The used model composition represents an average between the salinity calculated from the fluid inclusion microthermometry (≈28 NaCl+$CaCl_2$ eq. mass %) and the charge balance requirements from the crush-leach data, considering the Cl⁻ concentration of the crush leach and the Ca/Na mass ratio (which is

more or less 1:1, see values for the Cambrian samples in Tab. 6.3). Two different temperatures of homogenization, at 80°C and 110°C, were used, which represent the lower and the upper values of 90% of the measured inclusions. The anomalous high and low values of the data distributions were not considered representative. A "normal" geothermal gradient of 35°C/km and surface temperature of 20°C has been used to calculate the hydrostatic and lithostatic thermobaric gradients, assuming a linear relation between pressure (depth) and temperature (Fig. 6.14). The burial depth in a purely hydrostatic regime (10.1 MPa/km) is estimated at 2.0 km (corresponding to a pressure of 19.9 MPa), for a T_H of 80°C, and at 3.0 km (corresponding to a pressure of 29.9 MPa) for a Th of about 110°C. The pressure corrected trapping temperatures for the two homogenization temperatures of 80°C and 110°C are 88.2°C and 122.7°C respectively.

As it will be discussed in the next chapter, the geological setting in which the dolomitization event occurred was probably characterised by an "anomalous" geothermal gradient, which could have reached, at least locally and for limited periods of time, values as high as 80°C/km (see chapter 7, paragraph 7.3). In Fig. 6.14, for comparison, a geothermal gradient of 60°C/km, assuming a hydrostatic regime, is plotted.

The use of this "anomalous" geothermal gradient has the effect of decreasing the burial depth at which the inclusions were trapped: the burial depth is now between 1.1 km (corresponding to a pressure of 11.1 MPa) for a T_H of 80°C, and 1.6 km (corresponding to a pressure of 16.6 MPa) for a T_H of about 110°C. Consequently, the pressure corrected trapping temperatures are also decreased in comparison to the temperatures calculated with the "normal" geothermal regime of 35°C/km: for the two homogenization temperature of 80°C and 110°C the trapping temperatures would shift to 84.5 °C and 116.9°C.

In conclusions, the use of higher geothermal gradients results in the decrease of the pressure-correction and the decrease of the burial depth. The homogenisation temperature conditions can be considered the minimum P-t of trapping, whereas the calculated trapping conditions represent the maximum P-t possible for the dolomitizing fluids.

Chapter 7 - Discussion

7.1. The Cambrian dolomites

The carbonate succession of the Cambrian Láncara Fm. has been affected by (at least) two dolomitization events of different age. These events have produced two distinct dolomite lithologies (Fig. 7.1):

1) stratabound early diagenetic dolomite, beige in colour, occurring at the base of the lower part of the lower member of the Láncara Fm. Algal lamination, fenestral cavities, fine crystal size and very low porosity confirm the early diagenetic origin of these dolostones, which probably formed in a environment similar to a sabkha;

2) epigenetic dolomite, commonly characterized by abundant saddle dolomite void-filling phases and zebra structures. These petrographic characteristics together with the typical geochemical evidences (high T_H, low $\delta^{18}O$, radiogenic Sr) indicate a late burial origin.

The main characteristics of the two different dolomite types will be briefly discussed in the following paragraph, in order to critically review the evidences supporting the previous interpretations.

7.1.1. Lower member dolomite

Sabkha dolomites are usually associated with evaporite deposits, which are absent in the outcropping Cambrian sedimentary succession. Evaporites could have been dissolved or more likely removed during the onset of the Variscan thrusts. The thrusts are localized preferentially at the base of the Láncara Fm. and might have used an evaporite horizon as detachment level. In the Barrios de Luna area, however, where the Láncara Fm. is in stratigraphic contact with the underlying Herrería Fm., no indication of evaporite solution has been found.

Sabkha dolostones are in general Ca-rich and poorly ordered and characterized by positive oxygen isotope ratios and variable carbon isotopic ratios (which may be easily influenced by the incorporation of carbon derived from organic activity and methanogenesis). Nevertheless, sabkha dolostones are in
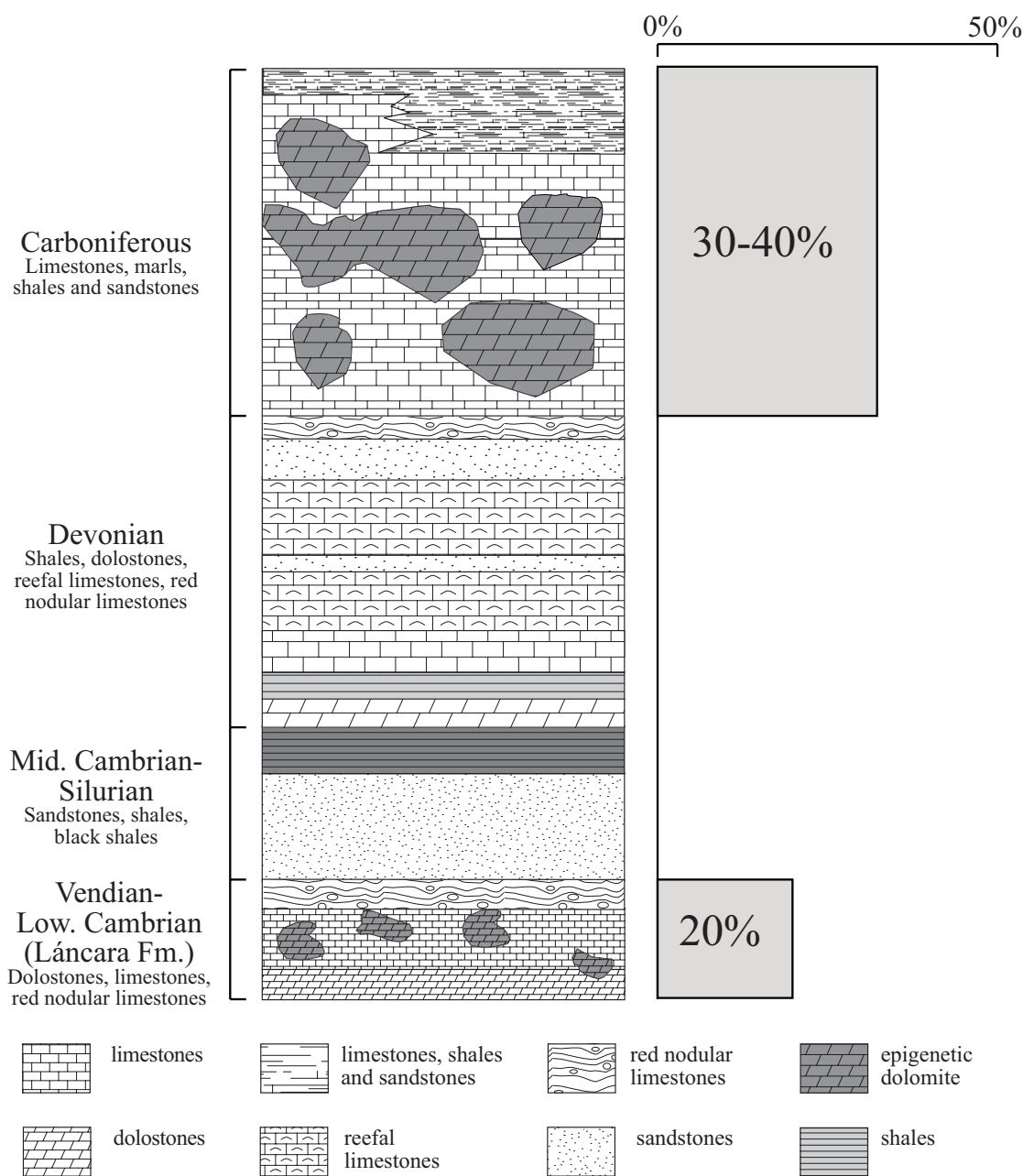
Fig. 7.1. Stratigraphic distribution and volume estimation of the dolomitized bodies in the Paleozoic sedimentary succession of the Cantabrian Zone in the study area.

general very unstable and usually recrystallize during burial. This characteristic reduces the possibility to preserve original isotopic and trace element composition. The geochemical signature of the Láncara lower member dolostone (ample negative $\delta^{18}O$ spread, ample slightly radiogenic $^{87}Sr/^{86}Sr$ spread, variable Fe and Mn content) confirms that re-equilibration during diagenesis occurred. The carbon isotopes are, on the other side, less susceptible to modification during burial, and preserve more easily the original depositional signature (see chapter 5, paragraph 5.4.1).

7.1.2. Late burial dolomitization

The second dolomitization event affecting the Láncara Fm. is of burial origin, as indicated by its petrography and geochemistry: it is fabric destructive, with only rare remnants of former sedimentary features left. Limestone-dolomite contacts are very sharp and cut stratification surfaces and sedimentary structures. The additional features observed in the studied rocks, which are typical for burial dolomitization (Gregg and Sibley 1984, Gregg 1985, Taylor and Sibley 1986, Mountjoy and Amthor 1994), are coarse crystallinity, non-planar texture, abundant saddle dolomite and zebra structures. The stoichiometry and the trace element signature also confirm the burial setting (see chapter 5, paragraphs 5.2 and 5.3.1).

This dolomite generation replaces preferentially the glauconitic packstone facies occurring in the basal part of the upper member of the Láncara Fm., and the underlying fenestral limestone facies of the lower member. The sabkha dolostone typical of the lower member is affected only rarely by this late dolomitization event (see chapter 4, paragraph 4.3).

The burial dolomitization in the Cambrian is volumetrically not impressive, especially when compared with the larger volumes of dolomitized Namurian and Westfalian rocks (Fig. 7.1). It affects limited volumes of rocks, usually not exceeding a few hundreds of cubic meters. The phenomenon is widespread on a regional scale and is complete, without undolomitized remnants of the precursor limestone within the dolomitized body.

Two dolomite types were recognized: matrix-replacive Dol A and void-filling Dol B. As no evidence of earlier diagenetic dolomitization has been observed in the mainly dolomitized lithology (i.e. the glauconitic packstone), the origin of Dol A as re-equilibration of a precursor dolomite phase can be excluded. In contrast, some part of the fenestral limestone facies contains replacements of two earlier dolomite phases (see chapter 4, paragraph 4.2).

The transition from Dol A to Dol B is generally gradual and both phases exhibit the same cathodoluminescence colour, with the exception the outer rim of void-filling Dol B II (the last Dol B generation) . Dissolution and corrosion were never observed at the contact between Dol A and Dol B. A continuous dolomitization process evolved in a nearly isochemical system, from a replacive stage towards a void-filling stage. It can be hypothesized that Dol B precipitated in an environment characterized by higher water/rock ratio.

The ample regional spread of $\delta^{18}O$ is of unclear origin. Lower values, between -8 and -13 PDB, are typical of the Bodón Unit (Villanueva, Campolongo and Viadango, see Fig. 4.1) and of the western part of the Somiedo-Correcilla Unit (Torrestio, Genestosa and Canseco, see chapter 4, Fig. 4.1). These samples contain abundant Dol B (which may locally reach 30-40% of the total volume) and do not contain measurable fluid inclusions.

The highest values (between -4 and -6‰ PDB) have been detected in the central part of the Correcilla Unit (Láncara de Luna, Aralla, Casares and San Martín, see chapter 4, Fig. 4.1). The samples from these localities are usually inclusion-rich, display zebra structures and contain abundant

open cavities. The late calcite cements fill to a minor extent the cavities. This calcite is probably of meteoric origin: the low $\delta^{13}C$ values indicates an influence of negative carbon derived from the decomposition of organic matter. The only exception is represented by the samples from the locality of Fontùn, in the Correcilla Unit (see chapter 4, Fig.4.1), which are characterized by anomalously low $\delta^{18}O$ values compared to the samples from nearby localities. Dol B from this locality contains few measurable fluid inclusions, with slightly lower salinity and comparable but slightly higher homogenization temperatures (see chapter 6, paragraph 6.2).

The $^{87}Sr/^{86}Sr$ ratios are distinctly higher than those of Cambrian seawater (and, consequently, higher than the those of seawater of all later ages), indicating the interaction of these brines with siliciclastic rocks. The strontium isotopic composition of the precursor lithologies is also more radiogenic relative to the Cambrian seawater. This evidence indicates that a first ^{87}Sr enrichment was already achieved during diagenetic recrystallization of the precursor limestone. The strontium isotopic composition of the matrix-replacive Dol A might have been slightly affected by the precursor lithology. The fairly similar strontium ratios show that the fluid flow paths did not change considerably from the time of replacement of the limestone and subsequent precipitation of Dol A to the time of Dol B emplacement.

7.2 Origin of matrix-replacing dolomite A

Dol A formed during the first fluid pulse, which used the previous discontinuities of the precursor limestone (fractures, bedding planes, laminations, stylolites). The fluid interacted with a heterogeneous substrate, due to the grain-size and the impurities present in the precursor limestone and in the early-dolomitized particles. Differences in the nucleation sites can explain the grain size and textural variation of Dol A (Gregg and Silbey 1984, Silbey and Gregg, 1987), which have been noticed in some samples.

The replacive burial dolomitization (Dol A) may have caused an increase of the porosity. This interpretation is valid only if we assume that the calcite replacement was a mole per mole process, which results in a volume loss of about 13% (Morrow 1990a). Pores and cavities are abundant in the dolomitized lithologies, at least in some localities, but they are usually associated to Dol B phase, where zebra structures are particularly well developed. Furthermore, the replacement among carbonates is often a volume per volume process, involving two separate but coeval chemical reactions: a) dissolution of primary mineral and b) precipitation of replacing mineral (Garrels and Dreyer 1952, Kinsman 1969, Land, 1980, Silbey 1982, Dockal 1988). For a volume per volume reaction the net dolomitization reaction can be written (Morrow 1990a)

$$1.75CaCO_3 + Mg^{2+} + 0.25CO_3^{2-} \leftrightarrow CaMg(CO_3)_2 + 0.75Ca^{2+} \tag{7.1}$$
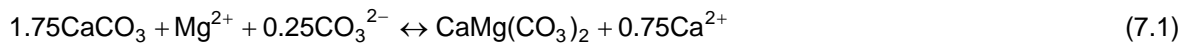
This reaction represents a composite between reaction 1.3 and 1.4 (chapter 1, paragraph 1.3), which can be seen as the end member of a series of reactions dependent on the degree to which there is a gain or a loss of rock volume during dolomitization. According to this reaction, an external source for Mg^{2+} as well as CO_3^{2-} is required.

This scenario cannot be excluded for the formation of the matrix-replacive dolomite and has the advantage of explaining the porosity distribution observed: the porosity increase, related to the formation of the pores and cavities, seems to be connected rather to the void-filling precipitation than the replacive dolomitization. As previously discussed, no porosity has been observed in Dol A phase, under normal microscopy and SEM. This evidence supports the volume per volume replacing reaction interpretation.

7.3 Origin of void-filling dolomite B

Void-filling dolomite generation (Dol B) generation followed replacive dolomite (Dol A) in a continuous process, as demonstrated by the petrography, the CL and the geochemistry (oxygen isotopic ratios, minor and trace elements). Dol B may have possibly precipitated directly from the dolomitizing fluid as a cement phase. This interpretation, although supported by several evidences, such as the saddle shape of the Dol B, the absence of solid inclusions and the abundant fluid inclusions (all typical characteristic of the cements), constitutes an oversimplification. In this respect, few considerations are necessary:

1- the amount of Dol B which precipitated is not easy to measure: the polymodal grain size distribution typical of Dol B does not allow, in most cases, a clear separation between Dol A and Dol B;

2- the is no geochemical evidence supporting the precipitation of Dol B from the dolomitizing fluid: all the geochemical indicators (oxygen and strontium isotopes, minor and trace elements) do not show any significant systematic change in the geochemical condition at the transition between the two dolomites A and B. Depletion in ^{18}O from matrix-replacive towards void-filling dolomites, which is a typical feature of many burial dolomites, may reflect an increasing temperature and/or a variation of the water-rock ratio. Matrix-replacive dolomite should be the phase more influenced by the oxygen isotopic composition of the precursor limestone (low water/rock ratio), relative to the void-filling phase. In the Cantabrian case, Dol A and Dol B are, however, geochemically indistinguishable: no systematic $\delta^{18}O$ difference has been observed between Dol A and Dol B in the Láncara Fm., which usually show very

similar values (see chapter 5, paragraph 5.4.1). Variation of the formation temperature from Dol A and Dol B has also not been observed: the few inclusions measured in Dol A show T_H similar to values from Dol B (see chapter 6, paragraph 6.2). The $^{87}Sr/^{86}Sr$ ratios of dolomites A and B are also very similar.

3- It has been known for a long time that quartz, metal sulphides and other minerals do not form directly from aqueous solution but rather through replacement of a series of intermediate phases (Morse and Casey 1988). This process is commonly referred to as the Ostwald's step rule. Recent hydrothermal laboratory experiments (Gaines 1974, Katz and Matthews 1977, Sibley 1990, Nordeng and Sibley 1994, Sibley et al. 1994) show that also dolomite forms after a relatively long induction period via so called VHMC (very high Mg calcite, with more than 36 mole % Mg), then non-stoichiometric dolomite and finally stoichiometric dolomite. This replacement can be very fast, especially in deep burial settings, being irrelevant for the investigation of ancient (Mesozoic and Paleozoic) dolomites (Machel 2004). The involvement of metastable intermediate phases cannot be excluded for either Dol A or Dol B.

A possible explanation for the textural transition from Dol A to Dol B (i.e. the absence of a sharp boundary between the two phases, as well as the gradual increasing grain-size of the Dol B sub generations) might be the variation of the dissolution/precipitation rate during the matrix-replacement dolomitization. This could have led to the void-filling precipitation: as the replacement process proceeds, increasing amounts of Ca are released into the solution. If the Mg supply and/or the Ca removal is no more efficient as before (for example at the final stages of the dolomitization process), it will progressively lower the Mg/Ca ratio of the fluid and consequently the dolomite precipitation rate, which is not able to balance the coeval calcite dissolution. Alternatively or in addition, it can be assumed that the CO_3^{2-} concentration in the dolomitizing fluid decreased during dolomitization, with the effect of changing from a volume per volume replacement to a mole per mole replacement. This scenario offers also a possible explanation for the formations of the cavities (which are only present in the Dol B), and for the interpretation of the geochemical data (which show only minor variation in the fluid/rock ratio between matrix-replacive and void-filling dolomite precipitation).

The crystal terminations of the last generation of Dol B (the Dol B II phase) contains more Fe, as indicated by the darker CL colour and the microprobe analyses, and are usually inclusion-free and finely zoned. A change in the fluid chemistry and/or in the fluid flow rate can be postulated, which brought the dolomitization process to an end.

7.4 Origin of dolomite C

Dolomite C is present only locally (Fontùn locality, in the Correcilla Unit, see chapter 4, Fig. 4.1) and postdates the Dol B. Its cathodoluminescence colour indicates geochemical conditions similar to the outer rim of the Dol B II phase (high Fe content and/or higher Fe/Mn concentrations). The T_H of the fluid inclusions trapped in Dol C shows distinctly higher values (between 128 and 175 °C, see chapter 6, Fig. 6.4B) compared to the Dol B fluid inclusions from the same locality. Petrographic evidence indicates that these fluid inclusions are probably of secondary origin and are related to the later oxidation episode responsible for the formation of the iron oxi-hydroxides (see chapter 6, paragraph 6.4).

The $\delta^{18}O$ values of Dol C are similar to the ones from Dol A and Dol B measured in the same sample. These values are anomalously low (around -11 $\delta^{18}O$ PDB) compared to the values of the samples of the nearby localities in the Correcilla Unit (see paragraph 7.1.2).

7.5. Origin of late calcite cements

Late calcite cements are present only locally. Petrographic evidence (see chapter 4, paragraph 4.3.2) and the very light carbon isotopic compositions (see chapter 5, paragraph 5.4.1) indicate possible precipitation of late calcite cements from fluids with a meteoric water signature, during exposure time. These cements correlate to Calcite II of Gasparrini et al. (2006b), which was also interpreted as late-stage meteoric in origin. The high-temperature Calcite I from the Carboniferous rocks, described by the same authors, has no equivalent in the Cambrian dolomitized successions.

7.6. Origin of dolomitizing fluids

The dolomitizing fluids were saline brines. Raman spectroscopy combined with microthermometry has revealed the presence of different cation species other than Na. Due to mass balance constraints, important concentrations of Mg characterized the fluid during dolomitization. As previously discussed (see chapter 6, paragraph 6.7), it is not possible to quantify the amount of Mg in the fluid inclusions due to the fact that Mg is the major element in dolomite and the concentration in the fluid is therefore modified during dolomitization.

Seawater (or modified seawater) is the only source of fluids sufficiently abundant and rich in Mg to

cause widespread dolomitization (Land 1985, Machel and Mountjoy 1986, Wilson et al. 1990, Spencer-Cervato and Mullis 1992). The Br/Cl ratios indicate that the fluids dolomitizing the Cantabrian rocks (both Cambrian and Carboniferous) were highly evaporated seawater, which was modified, to a minor degree, through fluid-rock interaction. The data show very high concentrations of Ca relative to Mg, which is in contrast to seawater that evaporated past the point of halite precipitation. Probably Mg was removed from the fluid and Ca was added during dolomitization.

Other Mg-rich hydrothermal fluids, described in the Cantabrian Zone, were responsible for the origin of the magnesite deposit of Valderrodero in Asturias, (Gutiérrez Claveron and García Iglesias 1982). The magnesite body were formed by metasomatism of the dolomitic member of the Herrería Formation. However, there is no evidence of a possible link between the formation of the magnesite deposits and the dolomitization of the Láncara Formation carbonates. The vicinity of the Valderrodero magnesite deposit to the igneous intrusions of Carlés, Ancellana and Salas-Belmonte suggests a possible magmatic origin of the Mg in the mineralizing fluids. According to the Sr isotopic composition, magmatic origin for our dolomitizing fluids can be excluded. (see chapter 5, paragraph 5.4.2).
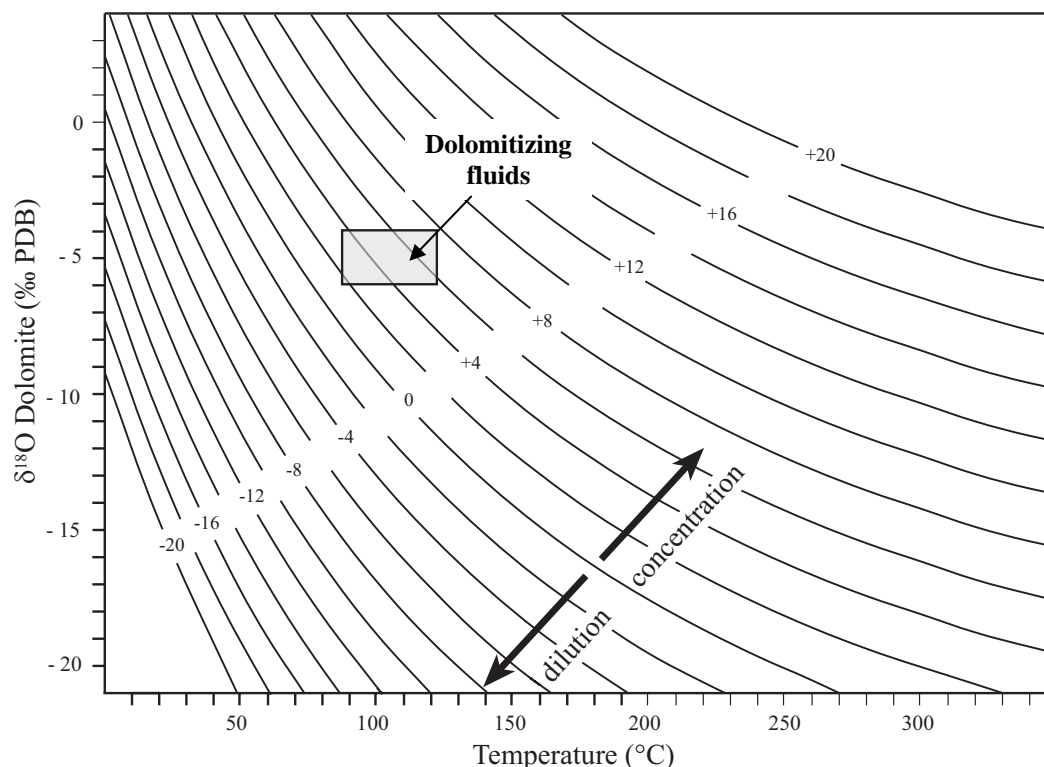
Fig. 7.2. Precipitation temperature vs. $\delta^{18}O$ values of Dol B. The $\delta^{18}O$ of the fluid in equilibrium with the dolomite phase was calculated using the equation of Land (1983).

It is well known that the O isotope composition of the dolomite phases and the temperature data from fluid inclusions can be used to calculate the oxygen isotopic composition of the dolomitizing fluid. Unfortunately, homogenization temperatures are available only for a few localities in the Correcilla Unit.

These dolomites display relatively low $\delta^{18}O$ (between -4 and -6‰ PDB) compared with the total range of data (between -4.02 to -13.29‰ PDB). The $\delta^{18}O$ of the fluid was calculated with the equation of Land (1983). In this calculation the pressure-corrected minimum and maximum trapping temperatures of the Dol B phase were used (84.5°C and 116.9°C, respectively; see chapter 6, paragraph, 6.8, Fig. 6.14), and the $\delta^{18}O$ between -4 and -6‰ PDB, corresponding only to the samples whose microthermometric data are available. The resulting oxygen isotopic composition of the fluid varies between 2 and 8‰ SMOW (Fig. 7.2): this composition is consistent with that of seawater enriched in ^{18}O during evaporation, in agreement with the crush-leach data.

Another mechanism able to increase the $\delta^{18}O$ of the basinal brines is the reaction of the fluids with carbonates and/or siliciclastic rocks (Clayton et al. 1966, Hitchon et al. 1971, Land and Prezbindowski 1981). The slightly radiogenic Sr isotopic ratios of the dolomite phases as well as of the precursor limestones indicate the presence of strontium from a crustal component. Nevertheless, the crush-leach analyses indicate that the fluid-rock interaction modified the fluid composition only to a certain degree. More probably, the distinctly negative oxygen isotopic composition is mostly due to different degree of evaporation of the seawater reservoir.

7.7. Age of dolomitization

The age of the dolomitization process can be constrained only indirectly. According to illite crystallinity data from the footwall of the basal thrust of the Somiedo-Correcilla Unit, the Láncara Formation reached a thermal peak during its burial history, prior to the emplacement of the Variscan thrusts (Aller et al. 1987, Bastida et al. 1999, Aller et al. 2005). During that time, the Lower Paleozoic succession underwent locally anchizonal conditions, with temperatures near or slightly exceeding 200°C. Fluid inclusion homogenization temperatures in the dolomites are well below this thermal peak, indicating that the dolomitization event took place during subsequent cooling or a second thermal peak after the emplacement of the Variscan nappes. If the dolomite had formed before the thermal peak was reached, the fluid inclusions would have at least partly re-equilibrated to higher temperature. The statistical distribution of the homogenization temperatures excludes this possibility (see chapter 6, paragraph 6.2). Furthermore, the field observations confirm a timing after the Variscan thrusting event: there is no evidence of involvement of this dolomite type in faulting and folding.

Geochemical and petrographic evidences indicate that the dolomitization of the Cambrian Láncara carbonates was directly related to the same event that produced the massive dolomitization affecting the Namurian and Westfalian carbonate succession (mostly restricted to the Bodón Unit). The geochemical data of the Cambrian- and the Carboniferous-hosted dolomites are compared in Tab. 7.1. In both cases, Sr, Fe, Mn and Na concentrations are very similar and consistent to a burial setting. Both

dolomite types are characterized by low $\delta^{18}O$ and a more radiogenic Sr isotopic composition compared to the seawater at the time of deposition of the precursor lithologies. The results of the crush-leach analyses, performed on samples from dolomitized Cambrian and Carboniferous rocks (see chapter 6, paragraph 6.7), indicate that the two dolomites were precipitated from a fluid of similar composition.

	Cambrian-hosted dolomite		**Carboniferous-hosted dolomite**	
	Dol A	**Dol B**	**Dol A**	**Dol B**
T_H (°C) (mode)		80 to 110		100 to 150
$\delta^{18}O$ (PDB)	-13.29 to - 4.20	-12.67 to -4.15	-10.58 to -2.96	-11.97 to -4.19
$\delta^{13}C$ (PDB)	-1.26 to 1.38	-1.12 to 1.19	1.86 to 5.42	1.74 to 5.30
$^{87}Sr/^{86}Sr$	0.7958 to 0.71168	0.70919 to 0.71114	0.70810 to 0.70921	0.70846 to 0.70908
Sr (ppm)	16 to 99	14 to 100	16 to 41	12 to 102
Fe (%)	0.22 to 4.58	0.27 to 1.82	0.08 to 0.61	0.06 to 0.55
Mn (ppm)	218 to 2496	483 to 1371	167 to 814	216 to 901
Na (%)	0.01to 0.04	0.01 to 0.04	0.02 to 0.05	0.01 to 0.06

Tab. 7.1. Comparison between geochemical data from the Cambrian-hosted dolomites and the Carboniferous-hosted dolomites.

The formation conditions determined from T_H of the fluid inclusions trapped in the "Cambrian-hosted dolomite" are distinctly lower than those from the "Carboniferous-hosted dolomite" (mode between 100 and 150°C). If the two dolomites are correctly interpreted as related to a coeval fluid flow event, the fluid inclusion data are another argument for the assumption that the dolomitization took place after the emplacement of the main thrust sheets, when the Cambrian succession of the Correcilla Unit overthrusted the Carboniferous succession of the Bodón Unit (Fig. 7.3).

Other indirect geological evidences can be used to further constrain the timing of the dolomitization event. The "Carboniferous-hosted" dolomite is the preferential host for small non-economic ore occurrences, deposited after the epigenetic dolomites in the paragenetic succession. The most important of these, Mina Profunda and Mina Providencia, close to the village of Carmenes, have been dated at 260-280 Ma, corresponding to the Middle-Late Early Permian (Paniagua et al. 1993). The period after the Variscan orogenesis and before the Middle Permian (or including it) is therefore the most likely time slot for the dolomitization. In this Late Stephanian-Early Permian time a second thermal peak occurred in the Cantabrian Zone, related to crustal thinning, intense volcanism and sparse plutonism associated with crustal delamination (Lepvrier and Martínez-García 1990, Gutiérrez-Alonso et al. 2004), resulting in an excellent scenario for dolomitization.
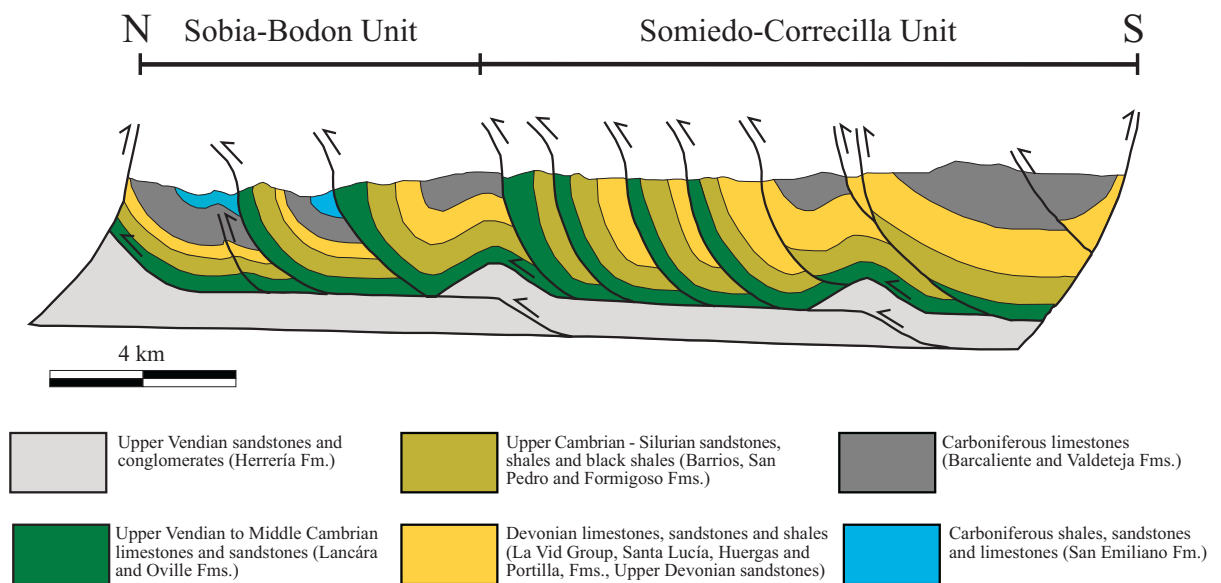
Fig. 7.3. Geological section of the southern part of Cantabrian Zone (along the Bernesga River) (Veselovsky 2004, modified).

Permian sediments do not crop out in the study area. The few Permo-Triassic sediments known, localized a few tens of km north of the study area, record the alternation of exposure and shallow water sedimentation under semiarid climatic conditions, characterized by restricted circulation and high evaporation rates. This setting may represent the most likely environment characterizing the Cantabrian Zone also during the Early Permian time.

The composition of the dolomitizing fluid, inferred by the crush-leach analyses, is in fact consistent with that of residual brines derived from highly evaporative seawater, which has passed the halite saturation point. The presence of thick halite strata of Permian age would confirm the hypothesis of an early Permian timing for the dolomitization. As mentioned before, Permian strata are not present in the study area. Nevertheless, older evaporites, or evidences of widespread evaporitic basins, that can be correlated to the formation of the Br-rich dense brines responsible of the widespread dolomitization of the Cambrian and Carboniferous carbonate succession in other geological periods, are missing in the Palaeozoic succession of the Cantabrian Zone. The lower age constraint on the dolomitizing process can be put at the post-Stephanian.

Evaporative seawater is extremely enriched in Mg and has the potential to filtrate deep into the basin. Eventually, convective circulation may arise if the geothermal gradient creates sufficient density contrast between the cool superficial and the warmer deeper fluids. The presence and extent of Permian basins in the Cantabrian Zone are hypothetical, however, and it is speculative therefore, if they could have provided a sufficient reservoir for fluids. Thick Triassic evaporites are known from the Basque area, but there are many arguments against a Triassic or later dolomitization, as discussed above.

The intra-montane Stephanian coal basins (such as the Cinera-Matallana Basin and the Sabero Coal Basin) overly the Westphalian deposits with an angular unconformity. The preserved sedimentary

thickness reaches from 1500 to 3000 meters (Colmenero et al. 1996, Heward 1978). In contrast with earlier authors (Evers 1967), Agueda et al. (1991) proposed that these today-isolated coal basins were probably interconnected during the Stephanian, forming a single foreland basin. The coals show a mostly burial-related coalification grade, controlled by an anomalous high geothermal gradient in the basin. Thermal modelling, based on vitrinite reflection data, indicates an overburden in excess of 1000 m at the time of maximum coalification, attributed by the authors to overlying Stephanian to Permian rocks (Fring et al. 2004). Fission tracks thermochronologic data (Carrière 2006) are consistent with a Permian thermal anomaly, which has been interpreted as related to an anomalous geothermal gradient. All these data reveal that sufficient accommodation was given to enable deposition of a thick Permian succession. This cover could have been subsequently eroded during the Alpidic tectonics, which strongly affected the area.

7.8. Dolomitization model

The main dolomitization models are here briefly critically reviewed in the frame of the geochemical and geological characteristics of dolomite of the Cantabrian Zone.

The high salinities measured in the fluid inclusions (8 times the salinity of seawater) are not consistent with hyposalinity dolomitization models, such as the mixing zone model (see chapter 1, paragraph 1.4), and with all the models which have normal seawater as principal dolomitization fluid. The high salinity and the Br/Cl ratios are consistent with the hypersaline environment of the reflux and Sabkha models (see chapter 1, paragraph 1.4), where the salinity of the fluid is controlled by evaporation. According to these models, dolomite forms in near surface and shallow burial diagenetic settings. Geochemical and petrographic evidences from the dolomites of the Cantabrian Zone (trapping temperature between 84.5°C and 116.9°C, very low $\delta^{18}O$, low Sr concentration, abundant saddle dolomite cements, zebra structures) indicate an intermediate to deep burial setting. Employing a "normal" geothermal gradient of 35°C/km, trapping depths between 2.0 km and 3.0 km have been calculated. As a distinctly higher geothermal gradient (approaching or exceeding 60°C/km) is likely, shallower levels are more realistic (1.1 to 1.6 km; see chapter 6, paragraph 6.8).

All of the most common burial dolomitization models (compaction flow, topography driven model, tectonically driven flow, thermal convection, seismic pumping) are essentially hydrologic models, which differ in the nature of the drivers and directions of the fluid flow (Morrow 1999). A combination of the different models are possible under certain conditions.

Topography driven flow can drive enormous quantities of meteoric water concentrating it by water-rock interaction (commonly dissolution of evaporites). The very high Br/Cl ratios of the fluid inclusions indicate that the dolomitizing fluids were mostly residual brines derived from the evaporation of seawater and that no appreciable dissolution of halite or other salts contributed to increase the salinity of the fluids. Tectonically driven flow and compaction flow have both the limit of the small amount of fluid, which can be provided for dolomitization, lacking a recharge mechanism. In the Cantabrian Zone,
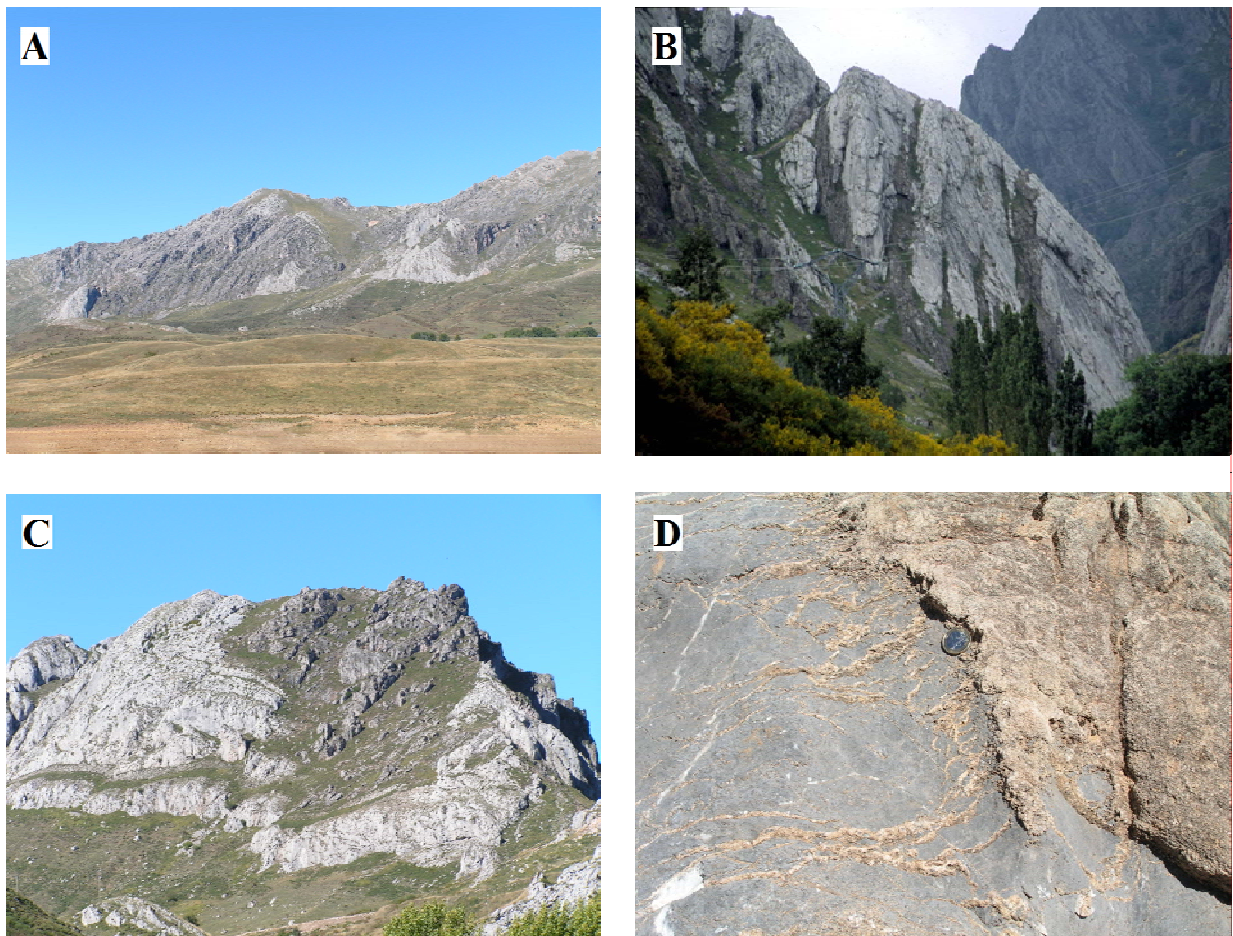
Fig. 7.4. A) Dolomitized Carboniferous succession in the area of San Martín de la Tercia; B) dike-like dolomite bodies in the Carboniferous of the Curueño Valley (courtesy of M. Gasparrini); C) mushroom-like dolomitic body in the Carboniferous close to the Viadango village; D) contact dolomitized/undolomitized rock from the Carboniferous succession.

they both could have played a secondary role together with other mechanisms.

Thermal convection provides an excellent mechanism for a long lasting, large-scale fluid circulation, which has all the requisites for dolomitization if kinetic limitations are overcome (Morrow 1998, Wilson et al. 2001). However, the very irregular shape of the dolomitized bodies, which are particularly evident in the Carboniferous dolomitized succession (Figs.7.4 A and B), does not correspond to the usual "mushroom-like" shape typical of the convective model, except in a few cases (Fig. 7.4C). The shape of the dolomitized bodies is probably strongly controlled by the permeability heterogeneity of the medium: the dolomitized lithologies were probably completely compacted and cemented at the time of dolomitization and the dolomitizing fluids used as main conduits discrete discontinuities such as stylolites, bedding planes and fractures of different size (Fig. 7.4D).

In the Cantabrian Zone, similar fluids caused the dolomitization of the Cambrian and the Carboniferous successions, implying an external fluid source and an efficient fluid circulation system active during the latest stages of the Variscan orogeny. A marine basin of Permian age under evaporitic condition is assumed to have provided highly concentrated fluids, which deeply filtrated into the Paleozoic successions. The fluids probably used a network composed by the pre-existing faults and

structures and the extensional structures formed as a consequence of the preceding oroclinal bending.

Due to the increased geothermal gradient, this fluid could have been involved into a thermal convective circulation, which had the potentiality to dolomitize important volumes of rocks on a regional scale. A gradient higher than the "normal" one (35°C/km) is more realistic in this geodynamic setting. The use of a higher geothermal gradient results in the decrease of the pressure-correction and the decrease of the burial depth (see chapter 6, paragraph 6.8).

The dolomite distribution in the study area allows some additional considerations about the typology of the dolomitizing fluid flow system. The third main carbonate interval in the Cantabrian Zone, the Devonian limestone of the Portilla and the Santa Lucia Fms. is almost undolomitized. These two formations are particularly well represented in the south of the study area (in the Correcilla Unit), where they form the main mountain ranges. Saddle dolomite cements with fluid compositions similar to the ones responsible for the dolomitization of the Cambrian and Carboniferous limestones were described from the Lower Devonian La Vid Group (Schneider 2001), but the volume of these dolomites is extremely low. In the Somiedo-Correcilla Unit, the Namurian-Westphalian limestones (Barcaliente and Valdeteja Fms.) are scarcely developed, with the exception of the Alba syncline, which is intensely dolomitized. On the other hand, in the Bodón Unit, in the northern part, the Namurian-Westphalian limestones represent the main carbonate interval and the Middle Devonian limestones are not well represented. The Cambrian succession is mostly dolomitized along the Somiedo-Correcilla thrust where it crops out regularly and represents the detachment level of this unit. It also occurs in the northern part of the Bodón unit, where it is much more discontinuous and tectonized.

A "simple" convective model is therefore not able to predict the distribution of the dolomitized bodies in the stratigraphic succession of the study area. The presence of particular CL patterns (described in chapter 3) and of zebra structures indicate that the dolomite was growing under some tectonic stress probably related to seismic activity. Seismic pumping of basinal brines along faults could have contributed to the dolomitization of the Cantabrian Zone .

The fluid flow pattern was certainly complicated by the presence of Variscan structures, which were reactivated in post Variscan time. Two important complex regional tectonic lines, i.e. the León Line in the north (which runs along the contact between the Bodón Unit and the Central Coal Basin), and the Sabero-Gordón Line in the south (in the Correcilla Unit) probably played an important role in controlling the fluid circulation and the tectono-thermal evolution of the area, as indicated by the distribution of the numerous ore deposits located in particular along the León Line.

7.9. Mass balance constraints

One of the most limiting factors in any dolomitization model, which is particularly important for ancient dolomites, is the quantification of the amount of fluids containing magnesium required to complete the dolomitization process. An estimation of this amount of fluid puts serious constraints to any interpretation of dolomite origin and formation.

Mass balance calculations have been carried out in the study area. The calculation is limited to the Namurian-Westphalian limestones of the Bodón Unit (Barcaliente and Valdeteja Fms.), where the dolomites are excellently exposed, forming an east-west striking mountain range, which crosses the whole study area. This succession probably constituted an excellent aquifer for the dolomitizing fluids, much more effective than the one corresponding to the relatively thin Cambrian carbonates of the Láncara Formation. The Cambrian succession was excluded in this calculation. Its limited volumes, anyway, would influence the total mass balance only to a minor extent. In addition, the estimation of the dolomitized/undolomitized ratio would be very complex for the Láncara Fm. carbonates, due to its more heterogeneous lithology and the presence of early dolomite phases.

The considerations given below are based on the data from the present study (i.e. crush-leach analyses, evaluation of the dolomitized rock volume) integrated with the results of Gasparrini et al. (2006a, b) on the "Carboniferous-hosted" dolomites.

For the rough quantification of the total amount of fluid the following approach has been carried out:

1- quantification of the dolomitized/non dolomitized rock ratio;
2- quantification of the volume of Namurian-Westphalian Carbonate rocks in the study area;
3- estimation of the Mg concentrations of the dolomitizing fluid;
4- estimation of the replacive/void filling dolomites ratio;
5- calculation of the amount of fluid needed for replacing;
6- calculation of the amount of fluid needed for void-filling.

7.9.1. Dolomitized rock volume calculation

An estimation of the dolomitized/undolomitized rock ratio has been made by means of mapping the dolomitized bodies in the study area, limited to the Namurian-Westphalian host limestones (Barcaliente and Valdeteja Fms.). The mapping was facilitated by the fact that the dolomitized rocks show a characteristic dark weathering colour, which is in contrast with undolomitized rocks, which have usually a light grey colour (Fig. 7.4A). The calculations were carried out on the digitized map of the study area, using DIANA image software. The map is shown in Fig. 7.5.

As the extent of the dolomitized bodies in the underground is unknown, a two-dimensional calculation was assumed as an approximation of the three-dimensional extension. The dolomite bodies are irregularly distributed along the study area. The most dolomitized areas correspond to the part of the range facing the east-west striking La Tercia Valley (between the villages of Carmenes in the east and Casares in the west, Fig. 7.4A), where the dolomitization locally affects the 100% of the total volume. Another fully dolomitized zone is located in the eastern part of the study area, south of the San Emiliano village. In the eastern part of the study area, corresponding to the Curueño Valley, the dolomitized bodies are limited in volume and usually have dike-like shapes (Fig. 7.4B). From the image analysis it resulted that about 33% of the total Namurian-Westphalian carbonate rocks outcropping were dolomitized.

7.9.2. Total carbonate rock volume calculation

The total volume of the Barcaliente and Valdeteja Fms. that was present at the time of dolomitization, can not be directly calculated from the geological maps and the stratigraphic thickness available in the literature. The area is particularly tectonized with its repetitive thrusted and folded successions. The recent geometry of the area is the product of Alpidic tectonic movements, which resulted in the reactivation of the main Variscan structures and the generally vertical inclination of the bedding and thrust planes. Consequently, it is not possible to calculate the amount of sedimentary succession which was eroded. For this reason, the volume of the carbonate rocks, which were affected by the dolomitization in this area, was calculated by mean of the 2D profile from the reverse basin model given by Dietrich (2005). In this model, the original thickness and geometry of the basin, in which the Barcaliente and Valdeteja Formations were deposited, was reconstructed. A 2D extension of 21.4 km^2, considering the sedimentation between 322 Ma and 312, was calculated for the Bodón transect (Fig. 7.6). The sedimentary thickness in the reverse basin model represents an overestimation of the real thickness of the Namurian-Westfalian carbonates at the time of dolomitization (see paragraph 7.7), due to loss of volume related to compaction after deposition but before dolomitization. As previously discussed (see paragraph 7.7), the overall thickness of the eroded sedimentary cover younger than Westfalian C is unclear in the study area. Furthermore, it is probable that the Barcaliente and Valdeteja Fms. were already fully mechanically and chemically compacted before the dolomitization event (postdating orogenesis).

The 3D extension was extrapolated from the 2D value (21.4 km^2) and the length of the Mountain Range constituted by the Barcaliente and Valdeteja Fms. in the study area, measured from the geological maps (approximately 68.4 km). A value of 1,464 km^3 was obtained.
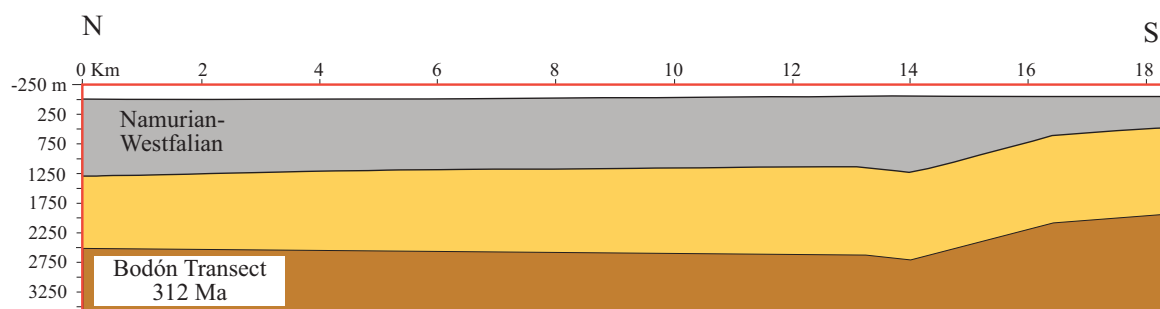
Fig. 7.6. 2D transect of the Cantabrian Basin at 312 Ma (Dietrich 2005, modified).

7.9.3. Estimation of the volume of replacive dolomite and void-filling dolomite

Considering that approximately 33% of the Barcaliente and Valdeteja Fms. were dolomitized in the study area, 483 km^3 of limestone were transformed into dolostone. The initial porosity of the limestone is considered to be very low (probably less than 1%) when dolomitization started (Gasparrini 2003, Gasparrini et al. 2006b), but the overall porosity and permeability of the limestones was surely

enhanced during dolomitization, due to tensional stress creating fractures and microfaults, which acted as main fluid conduits (see chapter 4, paragraph 4.3 for discussion).

In order to correctly quantify the total amount of replacive dolomite formed, it is necessary to establish which was the replacement process that took place: mole per mole or volume per volume. A mole per mole replacement would have increased the porosity. As previously discussed, the absence of microporosity in the Dol A phase exclude this dolomitization process; hence a volume per volume replacement is considered more appropriate to explain the Dol A formation.

The replacive vs. void-filling dolomite ratio varies widely in the study area, ranging from 5% up to 20%. A mean value of about 10% for the Dol B can be assumed as representative of all the study area. The porosity observed in the dolomitized rock, associated exclusively to the void-filling Dol B, is about 10-15 % of the total volume. In order to calculate the Dol A volume, about 20-25% of the total volume has therefore to be subtracted (volume of Dol B plus porosity).

In conclusions, the total amount of dolomite (replacive plus void-filling) ranges between 435 and 410.5 km^3. This volume corresponds to the precursor limestone total volume (483 km^3) subtracted the volume loss related due to dissolution (10-15%). The replacing dolomite volume is between 386.7 and 338 km^3, which corresponds to the total dolomitized volume minus the void-filling percentage (10%). The void-filling dolomite volume ranges between 48.3 and 72.5 km^3. The dolomite percentages are shown in Fig. 7.7.

7.9.4. Estimation of the Mg concentration of the dolomitizing fluid

The salinity of the dolomitizing fluid was established by means of fluid inclusion composition (microthermometry and Raman spectroscopy). Crush-leach indicates that the fluid derived from seawater, which has evaporated past the point where halite precipitation finishes and K-salts start precipitating (chapter 6, paragraph 6.8). As no direct estimation of the calcium and magnesium concentrations can be done directly from the crush-leach tests, the Mg and Ca content of the dolomitizing fluid have been extrapolated from the modern seawater evaporation trend, considering the degree of evaporation corresponding to the Cl/Br ratios of the crush-leach. This approach is valid only if no changes in the original concentrations are assumed (i.e mixing between different brines, dilution, halite dissolution). The crush leach test indicates that there was no important modification of the major ion content due to water-rock interaction and excludes dissolution of halite (which would have strongly increased the Cl/Br ratios). Mixing between the dolomitizing brines and less evaporated more diluted seawater-derived brines is also unlikely: this mixing would have shifted the data from the seawater evaporation trend forming a mixing line. Mixing with fresh meteoric-derived water would have diluted the fluid without changing the elemental ratios. The high salinity measured in the fluid inclusions is in contrast with this possibility.

The main elemental composition of seawater has changed during geological time (see following paragraph 7.10 for discussion). If we assume that the age of the seawater was probably Permian, as indicated by several direct and indirect geological evidences, the major ion composition of the Permian seawater can be considered similar to the composition of the modern seawater composition (Horita et al. 1991, Lowenstein et al. 2005). The dolomitizing fluid has a magnesium concentration equal to ca.

55000 ppm ($2.7*10^{-3}$ mol/cm^3), a calcium concentration close to 100 ppm ($0.003*10^{-3}$ mol/cm^3) and a density of ca. 1.2 g/cm^3, (Fontes and Matray 1993).
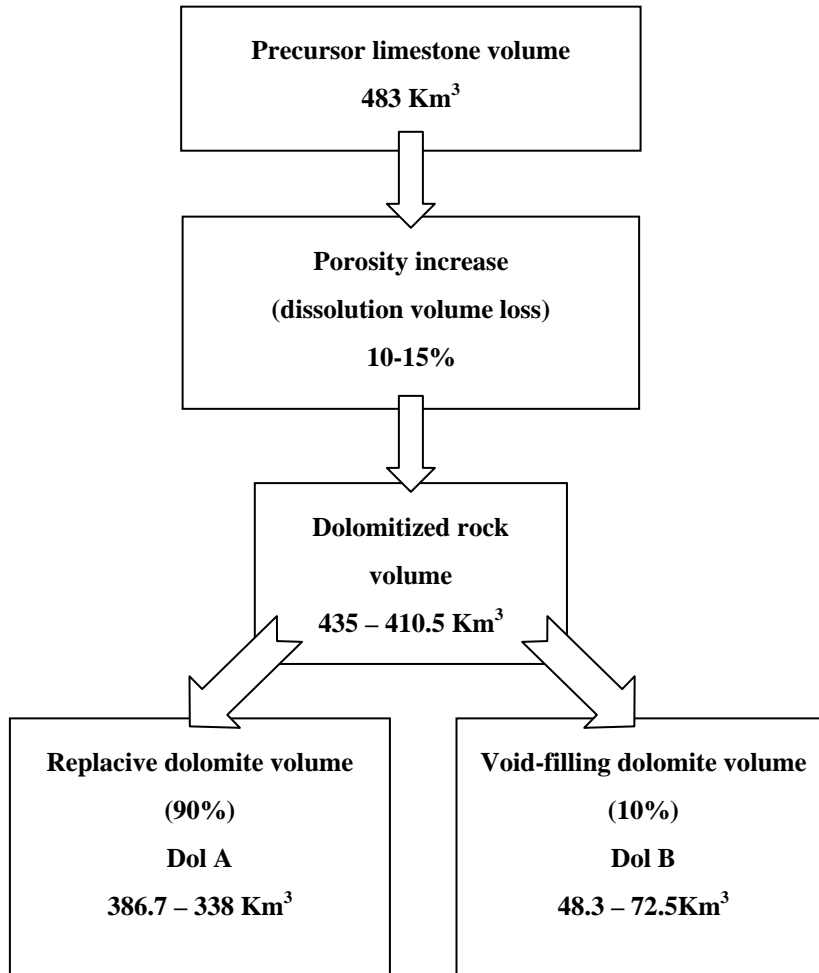
Fig. 7.7 Flow chart showing the different dolomitized rock volumes (see text for explanation).

7.9.5. Mass balance calculation – Replacive dolomite (Dol A)

As calculated above, the total amount of matrix-replacive Dol A is about 374 km^3, which contains $1.29*10^{16}$ moles of dolomite and exactly half moles of magnesium ($6.43*10^{15}$).

Not all the magnesium dissolved in the dolomitizing fluid is available for dolomitization. In order to continue the dolomitization process, the fluid must be supersaturated with respect to dolomite and undersaturated with respect to calcite. The dolomite-calcite equilibrium boundary depends on the Mg/Ca ratio, the temperature and on several other kinetic parameters, including salinity and CO_3^{2-}/Ca^{2+} ratios (see Fig. 1.2, chapter 1). The stoichiometry of reaction 7.1 (paragraph 7.2) and a temperature of about 150°C, determined by microthermometry (Gasparrini 2003, Gasparrini et al. 2006a), is used for the calculation. Considering that the reaction is approaching equilibrium, the sum of

_____

Ca and Mg before and after the reaction must be equal:

$$Mg_{df} + Ca_{d}f = Mg_{eq} + Ca_{eq} \qquad \text{(df = dolomitizing fluid; eq =equilibrium)} \qquad (7.2)$$

Substituting in the equation the Mg and Ca concentration of the dolomitization fluid ($Mg_{df} = 2.7*10^{-3}$ mol/cm^3; $Ca_{df} = 0.003*10^{-3}$ mol/cm^3) and considering that the equilibrium molar Ca/Mg ratio of approximately 8 at 150°C (Land 1985, Carpenter 1980), i.e. $Ca_{eq} = 8Mg_{eq}$, the equation becomes

$$2.7*10^{-3} + 0.003*10^{-3} = 8Mg_{eq} + Mg_{eq}$$

$$Mg^{eq} = 0.3*10^{-3} mol/cm^3$$

The amount of Mg available for dolomitization (Mg_{av}) is equal to the total amount of Mg in solution ($Mg_{df} = 2.7*10^{-3}$ mol/cm^3) minus Mg_{eq} ($0.3*10^{-3}$):

$$Mg_{av} = Mg_{df} - Mg_{eq} = 2.4*10^{-3} mol/cm^3$$

The ratio between the required (Mg_{req}) to the available (Mg_{av}) amount of Mg determines the amount of fluid (Fl_{dol}) needed to complete the dolomitization (Fl_{dol}):

$$Fl_{dol} = Mg_{eq}/Mg_{av}$$

$$Fl_{dol} = 5.92*10^{15} mol/2.4*10^{-3} mol/cm^3 = 2.8*10^{18} cm^3 = 2.8*10^{12} m^3$$

In conclusion, **$2.8*10^{12}$ m^3** of water containing 5.5 wt. % Mg has to be pumped through the limestone in order to provide enough magnesium to reach the observed amount of dolomitization. This calculation is valid only assuming that all the Mg dissolved into the dolomitizing fluid could have reached the dolomitization sites before being flushed out of the succession. The very sharp boundary between 100% dolomitized rocks and undolomitized rocks (Fig. 7.4D) shows that the dolomitization reaction continued until the residual brines had no more thermodynamic or kinetic potential to dolomitize further the carbonate succession further.

Another important parameter, which drastically decreases the amount of magnesium necessary to fully dolomitize a carbonate platform, is the presence of an early unstable precursor dolomite phases that would re-equilibrate during burial diagenesis to form more stable dolomite phases. The presence of such early diagenetic dolomite phases can be excluded for the Barcaliente and Valteteja Fms., where no evidence if early dolomite phases have been described (Gasparrini 2003, Gasparrini et al. 2006b). In the Láncara Fm., this scenario can be only partly excluded, as previously discussed: the late burial dolomitization event affects mostly the crinoidal wackestone of the upper member, which does not

display any evidence of an earlier dolomite phase, but also the lower member dolostone and the birdseye limestone facies, which was already partly dolomitized at the time the epigenetic dolomitization event took place.

It has to be kept in mind that the rough mass balance calculation given is a minimum quantification of the fluid, which has to be pumped through the limestone in order to accomplish the dolomitization. In this calculation the constraints related to the CO_3^{2-} has not been considered. According to a volume per volume replacement reaction, CO_3^{2-} has to be pumped through the limestone from an external source. Considering the stoichiometry of reaction 7.1 (paragraph 7.2), for any mole of dolomite forming, ¼ moles of CO_3^{2-} are necessary (in addition to the CO_3^{2-} derived from the dissolution of the calcite). Consequently, $3.25*10^{15}$ moles CO_3^{2-} are required in order to complete the process. The quantification of CO_3^{-2} in the dolomitizing solution is not easy to account. The fluid inclusion microthermometry and the crush-leach analyses indicate that Cl^- is the main anion present in solution. Carbonate and bicarbonate anions were not measured in the crush-leach but the charge balance between the anions and the cations is very reliable and excludes the possibility of important concentration of other anions in the leachate (see chapter 6, paragraph 6.7) . It cannot be excluded, however, that the CO_3^{2-} was exhausted during the dolomitization process. The carbonate (CO_3^{2-}) and bicarbonate (HCO_3^-) concentrations in seawater are very low when compared with other anions, but evaporation should increase the total alkalinity of seawater (Lazar et al. 1983). Sources of naturally occurring alkaline solutions containing high CO_3^{2-} include continental groundwater, which has been involved in alteration of siliceous rocks, or marine and continental waters that have been involved in anaerobic bacterial sulphate reduction (Lippmann 1973). Generation of the CO_3^{2-} by anaerobic sulphate reduction may have occurred in many burial environments (Morrow 1999). An increase in the CO_3^{2-}ion concentration, particularly in excess of calcium is an important variable for promoting dolomitization (Lippmann 1968, Davies et al. 1977). If a high concentration of CO_3^{2-} is assumed to be present in the dolomitizing fluid, the Cl^- dominated fluid inclusions may be the result of the strong depletion of the fluid relative to the carbonate ion during dolomitization.

7.9.6. Mass balance calculation – Void-filling dolomite (Dol B)

About 10-15 % of the total dolomitic body did not form as replacement of the precursor limestones but it precipitated as a void-filling phase (Dol B). The total volume related to void-filling dolomite ranges between 48.3 and 72.5 km^3. As previously discussed, Dol B did not precipitate directly from the dolomitizing fluid as a cement phase into an already open cavity. The process was probably preceded by dissolution of the precursor limestone in a similar way as for the matrix-replacive Dol A, but with a lower dissolution/precipitation rate. For this reason, the same approach used for the quantification of replacive dolomite can be applied also for the void-filling dolomite.

60^3km of dolomite contained approximately $1.03*10^{15}$ moles of Mg, corresponding to $2.51* 10^{16}$ grams. The magnesium available (Mg_{av}) in the dolomitizing fluid is equal to $2,4*10^{-3}$ mol/cm^3. The amount of fluid (Fl_{dol}) necessary to supply the Mg to complete the void-filling precipitation is equal to the ratio between the required (Mg_{req}) to the available (Mg_{av}) amount of Mg:

$$Fl_{dol} = 10.03 * 10^{15} \, mol/2.4 * 10^{-3} \, mol/cm^3 = 2.3 * 10^{17} \, cm^3 = 2.3 * 10^{11} \, m^3$$

About **2.3*10^11 m^3** of dolomitizing fluids in excess of the brines that caused calcite replacement are needed to provide the Mg necessary to complete the void-filling process. As for Dol A, also for the formation of Dol B the amount of CO_3^{2-} has to be considered; its concentration did not play a crucial role in terms of mass balance, however, because the volume of calcite dissolved probably exceeded the volume of dolomite precipitated.

Alternatively or in addition, a mole per mole replacement can be assumed for part of the the Dol B precipitation. As previously discussed in paragraph 7.2, the mole per mole and the volume per volume reactions can be seen as two end members of a series of reactions dependent if there is a gain or loss of rock volume during dolomitisation. A mole per mole reaction would increase the porosity of the dolomitized rock, as indicated by the numerous millimetre-scale pores associated with Dol B.

7.10. Massive burial dolomitization in the Paleozoic of Europe

Late to post Variscan burial massive dolomites were reported in several other regions in Central, Western and Southern Europe, such as Sardinia (Boni et al. 2000, Iannace et al. 2001), Belgium (Nielsen et al. 1998), Germany (Grobe and Machel 1996), Ireland (Wright et al. 1999), and Czech Republic (Suchy et al. 1996). These dolomites are mostly located in the external zone of the Variscan belt and replace Paleozoic carbonates ranging in age from Early Cambrian to Late Carboniferous. The dolomites share characteristics like comparable mineralogy and geochemistry, pervasive replacement patterns, fluid inclusions with high salinity and variable temperature, progressive depletion in $\delta^{18}O$ compared to their source limestone and radiogenic Sr values.

A late-Variscan hydrothermal event responsible for this widespread dolomitization process is assumed (Boni et al. 2000, Iannace et al. 2001), which was promoted by post-thrusting extensional tectonics and crustal thinning. Post-Variscan migration of highly saline fluids was widespread in central and western Europe (Behr et al. 1988, 1993, Wilkinson et al. 1995, Heijlen et al. 2001). One of the most important fluid flow events, responsible for the emplacement of Pb-Zn ore deposits in several districts in central and western Europe was dated as 270 Ma (Schneider 2000), which is surprisingly close to the age proposed for the dolomitization event in the Cantabrian Zone.

Permian seawater could have represented the common source for Mg-rich dolomitizing fluids. High evaporation rates of the seawater typical of Permian time increased the Mg/Ca ratios. Lower Permian evaporites are missing in the Cantabrian Zone and in most other European districts; they were reported recently from Russia and Ukraine (Kovalevich et al. 2002). On the other hand, thick Late Permian Zechstein evaporite deposits extend from the British Isles to Poland, reaching often a thickness of 1000 meters (Steward 1963).

Secular variations in major-ion chemistry (Mg^{2+}, Ca^{2+}, Na^+, K^+. SO_4^{2-} and Cl^-) of Phanerozoic seawater have been documented from fluid inclusions in marine halites (Kovalevich et al. 1998, 2002, Zimmermann 2000, Lowenstein et al. 2001, 2003, Brennan and Lowenstein 2002, Horita et al. 2002, Brennan et al. 2004), by the primary mineralogy of potash evaporites (Hardie 1996), by the magnesium content of fossil echinoderms (Dickson 2002) and the Sr concentration in biologic calcites (Steuber and Veizer 2002). The Phanerozoic has undergone two long-term fluctuations in major-ion composition (for example Mg^{2+}/Ca^{2+}) that are in phase with 100-200 My oscillation in sea level, icehouse-greenhouse climates and global volcanism. These fluctuations in the Phanerozoic seawater chemistry were explained by Hardie (1996) as the result of cyclical mixing between mid-ocean ridge hydrothermal brines and riverine water inflows, driven by changes in the rate of ocean crust production at the mid-ocean ridges.

Permian seawater had high Mg^{2+}/Ca^{2+} ratios (aragonite sea), with values very close to those of modern seawater (Horita et al. 1991, Lowenstein et al. 2001, 2005). Long-term variations in major-ion composition of seawater could have played a role in controlling global dolomitization rates, and Permian seawater as source of dolomitizing fluids might have had a potential higher than seawater of most of the other time periods in the Phanerozoic.

Chapter 8 - Conclusions

Several petrographic and geochemical methods have been applied on the study of the epigenetic dolomitization affecting the Láncara Fm. (Cantabrian Zone, NW Spain). The main conclusions are drawn on the basis of the results of the study.

1. The epigenetic dolomite occurring in the Láncara Fm. forms irregular bodies several meters thick, replacing principally the upper member glauconitic packstone and lower member birdseye limestone. These dolomites have often non-planar textures, variable carbon isotope composition, inherited from the precursor limestone, widely variable and negative oxygen composition, and slightly radiogenic strontium isotopes.

2. A first matrix-replacive dolomite phase (**Dol A**) is always associated with a second void-filling saddle dolomite phase (**Dol B**). Zebra structures are common.

3. Petrographic (CL) and geochemical evidences (trace elements, $\delta^{13}C$, $\delta^{18}O$, $^{87}Sr/^{86}Sr$) indicate that the two dolomite phases (A and B) formed in a diagenetic continuum.

4. Fluid inclusion microthermometry indicates that the Dol B phase formed at burial depth between 1.1 and 1.6 km.

5. Raman spectroscopy combined with microthermometry indicates that the dolomitizing fluid were highly saline brines (24.4 to 27.7 mass % eq. $CaCl_2$; 6.5 to 13 and 14.1 to 22.3 mass % eq. $NaCl + CaCl_2$). Several low temperature metastable behaviour of the fluid system could have been described and correctly interpreted.

6. The dolomitization affecting the Cambrian Láncara carbonates is petrographically and geochemically similar to the more extensive dolomitization process occurring in the Carboniferous thick carbonate succession of the Barcaliente and Valdeteja Fm. These *Carboniferous-hosted* dolomites formed at distinctly lower burial depth (3.9 ± 1.0 km,), as indicated by the fluid inclusion study of Gasparrini et al. (2006a).

7. Crush-leach analyses, performed on both *Cambrian-hosted* and *Carboniferous-hosted* dolomite samples show that the dolomitized fluids derived from evaporated seawater which have been modified by water-rock interaction but only to a minor extent.

8. The two dolomites (*Cambrian-hosted* and *Carboniferous-hosted*) have been interpreted related to similar and possible coeval dolomitizing fluid flow event.

9. Indirect geological evidences (temporal relation with the dated U ores and the main Variscan structures) point to Permian age for the onset of the dolomitizing event.

10. Mass balance calculations, restricted to the Carboniferous dolomitized succession, indicates that a minimum of $2.8*10^{12}$ m^3 (for Dol A) plus $2.3*10^{11}$ m^3 (for Dol B) of dolomitizing fluids are necessary to account for the total dolomitized rock volume in the study area.

References

Adams, J.E., Rhodes, M.L. (1960). Dolomitization by seepage-refluxion. Bulletin of the American Association of Petroleum Geologists, vol.44, p.1912-1920.

Agueda, J.A., Bahamonde, J.R., Barba, F.J., Brba, P., Colmenero, J.P., Fernandez, L.P., Salvador, C.I., Vera, C. (1991). Depositional environments in Westphalian coal-bearing successions of the Cantabrian Mountains, Northwest Spain. In: Bertrand (ed.), Coal; formation, occurrence and related properties; symposium. Bulletin de la Societe Geologique de France, Huitieme Serie, vol.162-2, p.325-333.

Allan, J.R., Wiggins, W.D. (1993). Dolomite reservoirs: geochemical techniques for evaluating origin and distribution. American Association of Petroleum Geologists, Continuing Education Course Notes, Series No.36, 129 p.

Aller, J. (1986). La estructura del sector meridional de las unidades del Aramo y Cuenca Carbonifera Central. Principado de Asturias, Consejería de Industria y Comercio, 180 p.

Aller, J., Brime, B. (1985). Deformacion y metamorphismo en la parte sur de la Cuenca Carbonifera Central (NO de Espana). Congres International de Stratigraphie et de Geologie du Carbonifére. 10, vol.3, p.541-548.

Aller, J., Bastida, F., Brime, C., Pérez-Estaún, A. (1987). Cleavage and its relation with metamorphic grade in the Cantabrian Zone (Hercynian of North-West Spain). Sciences Géologiques Bulletin, vol.40-3, p.255-272.

Aller, J., Valin, M.L., Garcia-Lopez, S., Brime C., Bastida, F. (2005). Superposition of tectono-thermal episodes in the southern Cantabrian Zone (Foreland Thrust and Fold of Iberian Variscides, NW Spain). Bulletin de la Societé Géologique de France, vol.176, p.487-497.

Alonso, J.L. (1987). Sequences of thrust and dicplacement in the superposed duplexes of the Esla Nappe Region (Cantabrian Zone, NW Spain). Journal of Structural Geology, vol.9-8, p.969-983.

Alonso, J.L., Pulgar, J.A. (1995). La estructura de la Zona Cantabrica. In: C. Aramburu and F. Bastida (eds.), Geología de Asturias. Trea, Gijón, p.103-112.

Amieux, P. (1982). La cathodoluminescence; methode d'etude sedimentologiques des carbonates. Bulletin des Centres de Recherches Exploration-Production Elf-Aquitaine, vol.6-2, p.437-483.

Amthor, J.E., Mountjoy, E.W., Machel, H.G. (1993). Subsurface dolomites in Upper Devonian Luduc Formation buildups, central part of Rimbey-Meadowbrook reef trend, Alberta, Canada. Bulletin of Canadian Petroleum Geologists, vol.41-2, p.164-185.

Apalategui, O. Eguiluz, L., Quesada, C. (1990). Ossa Morena. Structure. In: R. D. Dallmayer & Martinez-Garcia (eds.) Pre-Mesozoic Geology of Iberia. Springer Verlag, Berlin, p.280-291.

Aramburu, C. (1990). El Precambrico y el Paleozoico inferior. In: C. Aramburu and F. Bastida (eds.). Geología de Asturias. TREA, Gijón, p.35-50.

Bakker, R.J. (2002). Identification of salts in fluid inclusions by combined Raman Spectroscopy and low temperature microthermometry: PACROFI VIII, Pan American Conference on Research on Fluid Inclusions, Halifax, Abstracts, p.38-42.

Bakker, R.J. (2003). Package FLUID 1. Computer programs for analyses of fluid inclusion data and for modelling bulk fluid properties. Chemical Geolology, vol.194-1 and 194-3, p.2-23.

Bakker, R.J. (2004). Raman spectra of fluid and crystal mixtures in the system H_2O, H_2O-NaCl and H_2O-$MgCl_2$ at low temperatures: applications to fluid inclusion research. The Canadian Mineralogist, vol.42, p.1283-1314.

Bakker, R.J., Diamonds, L.W. (2006). Estimation of volume fractions of liquid and vapor phases in fluid inclusions, and definition of inclusion shapes. American Mineralogists, vol.91-4, p.635-657.

Banks, D.A., Yardley, B.W.D. (1992). Crush-leach analysis of fluid inclusions in small natural and synthetic samples. Geochimica et Cosmochimica Acta, vol.56, p.245-248.

Barber, D.J., Reeder, R.J., Smith, D.J. (1985). A TEM microstructural study of dolomite with curved paces (saddle dolomite). Contribution to Mineralogy and Petrology, vol.91, p.82-92.

Barnaby, R.J., Read, J.F. (1992). Dolomitization of a carbonate platform during late burial: Lower to Middle Cambrian Shady Dolomite, Virginia Appalachians. Journal of Sedimentary Petrology, vol.62, p.1023-1043.

References

Bastida, F., Marcos, A., Arboleya, M.L., Mendez, I. (1976). La Unidad de Peña Corada y su relación con el Manto del Esla (Zona Cantábrica, NO España). Breviora Geologica Astúrica, vol.20-4, p.49-55.

Bastida, F., Brime, C., García-López, S., Sarmiento, G.N. (1999). Tectono-thermal evolution in a region with thin-skinned tectonics: the western nappes in the Cantabrian Zone (Variscan belt of NW Spain). International Journal of Earth Science, vol.88, p.38-48.

Bathurst, R.G.C. (1975). Carbonate sediments and their diagenesis. Elsevier, Amsterdam, 658 p.

Behr, H.J., Kehrer, P., Rischmüller, H. (1988). The German Continental Deep Drilling Program, targets and state of work. AU: In: A. Boden (ed), Deep drilling in crystalline bedrock. Volume 2, review of deep drilling projects, technology, sciences and prospects for the future, p.64-81.

Behr, H.J., **Gerler, J.**, **HeinU.-F.**, **Reutel, C.J.** (1993). Tectonic brines und basement brines in den mitteleuropäischen Varisziden; Herkunft, metallogenetische Bedeutung und geologische Aktivität. In: H. Groos-Uffenorde, H. Jahnke and E. Schindler (eds), Otto Heinrich Walliser; Festschrift. Göttinger Arbeiten zur Geologie und Paläontologie, vol.58, p.3-28.

Behrens, E.W., Land, L.S. (1972). Subtidal Holocene dolomite, Baffin Bay, Texas. Journal of Sedimentary Petrology, vol.42, p.155-166.

Bein, A., Land, L.S. (1983). Carbonate sedimentation and diagenesis associated with Mg-Ca-chloride brines: The Permian San Andreas Formation in the Texas Panhandle. Journal of Sedimentary Petrology, vol.53, p.243-260.

Birck, J.L. (1986). Precision K-Rb-Sr isotopic analysis: application to Rb-Sr chronology. Chemical Geology, vol.56, p.73-83.

Boni, M., Parente, G., Bechstädt, T, De Vivo, B., Iannace, A. (2000). Hydrothermal dolomites in SW Sardinia: evidence for a widespread late Variscan fluid flow event. Sedimentary Geology, vol.131, p.181-200.

Brand, U., Veizer, J. (1980). Chemical diagenesis of a multicomponent carbonate system; 1, Trace elements. Journal of Sedimentary Petrology, vol.50-4, p.1219-1236.

Brennan, S.T., Lowenstein, T.K. (2002). The major-ion composition of Silurian seawater. Geochimica et Cosmochimica Acta, vol.66, p.2683-2700.

Brennan, S.T., Lowenstein, T.K., Horita, J. (2004). Seawater chemistry and the advent of biocalcification. Geology, vol.32, p.473-476

Brime, C., García-López, S., Bastida, F., Valín, M.L., Sanz-López, J., Aller, J. (2001). Transition from diagenesis to metamorphism near the front of the Variscan regional metamorphism (Cantabrian Zone, north-western Spain). Journal of Geology, vol.109, p.363-379.

Brown, R.J., Furrow, G.E. (1978). Recent dolomitic concretions of crustacean burrow origin from Loch Sunard,West Coast of Scotand: Journal of Sedimentary Petrology, vol.48, p.825-834.

Burke, W.H., Denison, R.E., Hetherington, E.A., Koepnick, R.B., Nelson, H.F., Otto, J.B. (1982). Variation of seawater [87]Sr/[86]Sr throughout Phanerozoic time. Geology, vol.10, p.516-519

Burns, S.J., McKenzie, J.A., Vasconcelos, C. (2000). Dolomite formation and biochemical cycles in the Phanerozoic. Sedimentology, vol.47-1s, p.49-61.

Carballo, J.D., Land L.S., Miser, D.E. (1987). Holocene dolomitization of supratidal sediments by active tidal pump, Sugarloaf Key, Florida. Journal of Sedimentary Petrology, vol.57, p.153-165.

Carpenter, A.B. (1976). Discussion: Dorag dolomitisation model: by K. Badiozamani. Journal of Sedimentary Petrology, vol.46, p.258-261.

Carpenter, A.B. (1980). The chemistry of dolomite formation I: the stability of dolomite. In: D. H. Zenger, J. B. Dunham and R. L. Ethington (eds.) Concept and models of dolomitisation. SEPM Special Publication vol.28, p.111-121.

Carrière, K. (2006). Neoproterozoic to Holocen tectonothermal evolution of the Southern Cantabrian Mountains, NW Iberia, as revealed by apatite fission-track thermocronology. Unpublished PhD thesis, Ruprecht-Karl Univerität Heidelberg, 289 p.

Cervato, C. (1990). Hydrothermal dolomitisation of Jurassic-cretaceous limestones in the Southern Alps (Italy); relation to tectonics and volcanism. Geology, vol.18, p.458-491.

Chaudhuri, S., Clauer, N. (1993). Strontium isotopic composition and potassium and rubidium contents of formation waters in sedimentary basins: clues to the origin of the solutes. Geochimica et Cosmochimica Acta, vol.57, p.429-437.

Clark, N.D. (1980). The diagenesis of Zechstein carbonate sediments. Contribution of Sedimentology, vol.9, p.167-203.

Clayton, R.N., Friedman, I., Graf, D.L., Mayeda, T.K., Meents, W.F., Shimp, N.F. (1966). The origin of saline formation waters: I. Isotopic composition. Journal of Geophysical Researce, vol.71, p.3869-3882.

Colménero, J.R., Prado, J. C. (1993). Coal Basins in the Cantabrian Mountains, northwestern Spain. International Journal of Coal Geology, vol.23, p.215-229.

Comte, P. (1936). Le Dévonien Inférieur du Léon. Compte Rendus Hebdomadaires des Seances de l'Academie des Sciences, vol.202-9, p.771-773.

Comte, P. (1937). La série cambrienne et silurienne du Léon. Compte Rendus Hebdomadaires des Seances de l'Academie des Sciences, vol.204-8, p.604-606.

Coniglio, M., Sherlock, R., Williams-Jones, A.E., Middleton, K., Frape, S.K. (1994). Burial and hydrothermal diagenesis of Ordovician carbonates from the Michigan Basin, Ontario, Canada. In: B. H. Purser, M. E. Tucker and D. H. Zenger (eds.), Dolomites - a volume in honour of Dolomieu. International Association of Sedimentologists Special Publication, vol.21, p.231-254.

Coplen, T.B., Kendall, C., Hopple, J. (1983). Comparison of stable isotope reference samples. Nature, vol.302, p.236-238.

Corretgé, L.G., Suárez, L.C. (1990). Cantabrian Zone. Igneous rocks. In: R. D. Dallmayer & Martinez-Garcia (eds.) Pre-mesozoic Geology of Iberia. Springer Verlag, Berlin, p.80-87.

Corretgé, L.G., Luque, C., Suárez, L.C. (1970). Los stock de la zona Salas-Belmonte (Asturias).Bolletino Geologico y Minero, vol.80-2, p.257-270.

Corretgé, L.G., Cienfuegos, I., Cuesta, A. et al. (1987). Granitoides de la Región Palentina (Cordillera Cantábrica, España). IX Reuniao sobre a Geologia do oeste peninsular, Memorias, Museu e Laboratorio Mineralogico e Geologico, Faculdade de Ciencias, Universidade do Porto, vol.1, p.469-498.

Crespo, J.L., Moro, M.C., Fadón, O., Cabrera, R., Fernández, A. (2000). The Salomón gold deposit (León, Spain). Journal of Geochemical Exploration, vol.71, p.191-208.

Crowford, M.L. (1981). Phase equilibria in aqueous fluid inclusions. In: L.S, Hollister and M.L. Crowford editors, Fluid Inclusions: Applications to Petrology. Mineralogical Association of Canada, Short Course Handbook vol.6, p.70-75.

Dana, E.S. (1955). A textbook of mineralogy. London, John Wiley and Sons, 851 p.

Davies, D.W., Lowenstein, T.K., Spencer, R.J. (1990). Melting behaviour of fluid inclusions in laboratory-grown halite crystals in the system $NaCl-H_2O-$, $NaCl-KCl-H_2O$, $NaCl-MgCl_2-H_2O$. Geochimica et Cosmochimica Acta, vol.54, p.591-601.

Davies, G.R., Smith, L.B. (2006). Structurally controlled hydrothermal dolomite reservoir facies: an overview. American Association of Petroleum Geologist Bulletin, vol.90-11, p.1641-1690.

Davies, P.J., Bubela, B., Ferguson, J. (1977). Simulation of Carbonate diagenetic processes: formation of dolomite , hunite and monohydro calcite by the reaction between nesquehonite and brine. Chemical Geology, vol.19, p.258-261.

Deffeyes, K.S., Lucia, F.J., Weyl, P.K. (1965). Dolomitization of Recent and Plio-Pleistocene sediments by marine evaporative waters on Bonaire, Netherlands Antilles. In: L.C. Pray and R.D. Murray eds., Dolomitization and Limestone Diageneis, a Symposium. Special Publication of the Society of the economic Paleontologists and Mineralogists, vol.13, p.71-88.

Dias, R., Ribero, A. (1995). The Ibero-Armorican Arc: a collision effect against an irregular continent? Tectonophysics, vol.246, p.113-128.

Dickson, J.A.D. (2002). Fossil echinoderms as monitor of the Mg/Ca ratio of Phanerozoic oceans. Science, vol.298, p.1222-1224.

Dietrich, B. (2005). Numerical modelling as a mean to enhance genetic sedimentary basin interpretation: a case study of the southern Cantabrian Basin (NW Spain). GAEA Heidelbergensis, vol.14, 263 p.

Díez Balda, M.A., Vegas, R., Gonzáles Loreido, F. (1990). Central-Iberian Zone. In: R. D. Dallmayer & Martinez-Garcia (eds.) Pre-mesozoic Geology of Iberia. Springer Verlag, Berlin, p.172-188.

Dockal, J.A. (1988). Thermodynamic and kinetic description of dolomitization of calcite and calcitization of dolomite (dedolomitization). Carbonates and Evaporites, vol.3-2, p.125-141.

Dolomieu, D. (1791). Sur le genre de pierres calcaires tréspeu effervescentesavec les acides et phosphorescentespar la collision. Journal Physique, vol.39, p.3-10.

Drever, J.I. (1982). The geochemistry of natural waters. Prentice-Hall, USA, 399 p.

Drivet, E., Mountjoy, E. W. (1997). Dolomitisation of the Leduc Formation (Upper Devonian), southern Rimbey-Meadowbrook reef trend, Alberta. Journal of Sedimentary Research vol.67-3, p.411-423.

_____

References

Dubessy J., Audeoud, D., Wilkins, R., Kosztolanyi, C. (1982). The use of the Raman Microprobe Mole in the determination of the electrolytes dissolved in the aqueous phase of fluid inclusions. Chemical Geology, vol.37-1,2, p.137-50.

Ebers, M. L., **Kopp, O.C.** (1979). Cathodoluminescent microstratigraphy in gangue dolomite, the Mascot-Jefferson City District, Tennessee. Economic Geology and the Bulletin of the Society of Economic Geologists, vol.74-4, p.908-918.

Emery, D., Robinson, A. (1993). Inorganic geochemistry.: Applications to Petroleum Geology. Blakwell, Oxford, 254 p.

Evers, H.J. (1967). Geology of the Leonides between the Bernesga and Porma rivers, Cantabrian mountains (NW Spain). Geologie en Mijnbouw, vol.46-12, p.483.

Fairbridge, R.W. (1957). The dolomite question. AU: BK: In: R. J. LeBlanc and J. G. Reeding, (eds.), Regional aspects of carbonate deposition-a symposium. Society of Economic Paleontologists and Mineralogists Special Publication, vol.5, p.125-178.

Fernández, L.P. (1995). El Carbonifero. In: C. Aramburu and F. Bastida (eds.). Geología de Asturias. TREA, Gijón, p.63-80.

Fernández Fernández, C.J. (1985). Las mineralizaciones (Cu)-Pb-Zn-Ba-Hg en rocas dominadamente calcáreas del Carbonífero, sector Norte de la región de Picos de Europa, Asturias. Características métalogenéticas en relación al tipo plomo-cinc-caliza. Compte Rendu X Congres International de Stratigraphie et de Geologie du Carbonifère, vol.3, p.105-119.

Fernández Fernández, C.J., Moreiras, D., Paniagua, A. (1985). Mineralogía y paragenesis mineral de la Mina Providencia (Cármenes, León). Trabajos de Geologia, vol.15, p.239-247.

Fernández-Suárez, J., Dunning, G. R.; Jenner, G.A., Gutiérrez-Alonso, G. (2000). Variscan collisional magmatism and deformation in NW Iberia: constraints from U-Pb geochronology of granitoids. Journal of the Geological Society of London, vol.157, p.565-576.

Fernández-Suárez, J., Gutiérrez-Alonso, G.; Cox, R., Jenner, G.A. (2002). Assembly of the Armorica Microplate: a strike-slip terrane delivery? Evidence from U-Pb ages of detrital zircons. Journal of Geology, vol.110, p.619-626.

Folk R.L., Land, L.S. (1975). Mg/Ca ratio and salinity, two controls over crystallization of dolomite. Bulletin of American Association of Petroleum Geologists, vol.59, p.60-68.

Fontboté, L. (1993). Self-organization fabrics in carbonate-hosted ore deposits: example of diagenetic crystallization rhythmites. In: P. Fenoll Hach-Alí and J. Torres-Ruiz, F. Grevilla (eds.), Current research in Geology applied to Ore deposits, Granada, University of Granada, p.11-14.

Fontboté, L., Amstutz, G.C. (1980). New observations on diagenetic crystallization rhythmitesin the carbonate facies of the Triassic of the Alpujárrides (Betic Cordillera, Spain): comparison with other diagenetic rhythmites . Revista Inst. Investigaviones Geológicas, vol.34, p.293-310.

Fontes, J.C., Matray, J.M. (1994). Geochemistry and origin of formational brines from the Paris Basin, France. 1. Brines associated with Triassic salts." Chemical Geology, vol.109, p.149-175.

Frankenfeld, H. (1983). El Manto de Montó-Arauz: interpretación estructural de la Región del Pisuega-Carrión (Zona Cantábriaca, NW de España). Trabajos de Geologia, vol.13, p.37-47.

Friedman, I.A.C., O'Neil, J.R. (1977). Compilation of stable isotope fractionation factors of geochemical interest. US Geological Survey Prof. Paper, 440 KK, p.1-12.

Frings, K. (2002). Palaeotemperatur –Anomalien in Spaetvariskisches Kohlenbecken am Beispiel des Ciñera-Matallana Beckens, Kantabrisches Gebirge, NW Spanien (CD-ROM). Gaea Heidelbergensis, vol.11, 136 p.

Frings, K., Lutz, R., de Wall, H., Warr, L.N. (2004). Coalification history of the Stephanian Cinera-Matallana pull-apart basin, NW Spain; combining anisotropy of vitrinite reflectance and thermal modelling. International Journal of Earth Sciences, vol.93-1, p.92-106.

Fritz, P., Smith, D.G.W. (1970). The isotopic composition of secondary dolomites. Geochimica et Cosmochimica Acta, vol.34-11, p.1161-1173.

Füchtbauer, H., Goldschmidt, H. (1966). Beziehungen zwiechen Calcium-gehalt und Bildungsbedingungen der Dolomite. Geologiche Rundschau, vol.55-1, p.29-40.

Gaines, A.M. (1974). Protodolomite syntesis at 100°C and atmospheric pressure. Science, vol.183, p. 518-520.

Gaines, A.M. (1980). Dolomitisation kinetics: recent experimental studies. In: D. H. Zenger, J. B. Dunham and R. L. Edhingtin (eds.), Concept and model of dolomitisation, Society of Economic Paleontologists and Mineralogists Special Publication, vol.28, p.81-86.

Galán Huertos, E., Rodas, M. (1973). Contribución a l'estudio mineralógico de los depositos de talco de Puebla de Lillo (León, España), Boletín geologicoy Minero, vol.84, p.347-365.

Galán, G., Suárez, L.C. (1989). Cortlandic enclaves associated with calcalkaline granites from Tapia, Asturias (Hercynian Belt, north-western Spain). Lithos, vol.23, p.233-245.

Galán, G., Pin, C., Duthou, J.L. (1996). Sr-Nd isotopic record of multistage interactions between mantle-derived magmas and crustal components in a collision context. The ultramafic-granitoid association from Vivero (Hercynian Belt, northwestern Spain). Chemical Geology, vol.131, p.67-91.

Gallastegui, G., Heredia, N., Rodríguez-Fernández, L. R., Cuesta, A. (1990)**.** El stock de Pena Prieta en el contexto del magmatismo de la unidad del Pisuerga-Carrion (Zona Cantabrica, N de Espana). Cuadernos do Laboratorio Xeoloxico de Laxe, vol.15, p.203-217.

García-Alcalde, J.L., Carls, P., Pardo Alonso, M.V., Sanz López, J., Soto, F., Truyols-Massoni, M., Valenzuela-Rios, J.I. (2002). Devonian. In: W. Gibbons and T. Moreno (eds.), The Geology of Spain. The Geological Society of London, p.67-91.

García de Figuerola, L. C., Peña, D. (1964) El afloramiento cuarzo-diorítico de Carlés (Asturias) y la prospección geoquímica del Cu en el mismo. Boletín de la Real Sociedad Española de Historia Natural, vol.62, p.91-106.

García-López, S., Brime, C., Bastida, F., Sarmiento, G.N. (1997). Simultaneous use of thermal indicators to analyse the transition from diagenesis to metamorphism: an example from the Variscan Belt of northwest Spain. Geological Magazine, vol.143-3, p.323-334.

García-López, S., Bastida, F., Brime, C., Aller, J., Valín, M.L., Sanz-López, J., Méndez, C.A., Menéndez-Alvarez, J.R. (1999). Los episodios metamórficos de la Zona Cantábrica y su contexto estructural. Trabajos de Geológia, vol.21, p.177-187.

García Ramos, J.C., Aramburu, C.; Brime, C. (1984). Kaolin tonstein of volcanic ash origin innthe Lower Ordovician of the Cantabrian Mountains (NW Spain). Trabajos de Geologia, vol.14, p.27-33.

Garven, G. (1985). The role of regional fluid flow in the genesis of the Pine Point Deposit, Western Canada sedimentary basin. Economic Geology and the Bulletin of the Society of Economic Geologists, vol.80-2, p.307-324.

Garven, G. (1995). Continental-scale groundwater flow and geologic processes. Annual Review of Earth and Planetary Sciences, vol.23, p.89-117.

Garven, G., Freeze, R.A. (1984a). Theoretical analysis of the role of groundwater flow in the genesis of stratabound ore deposits; 1, Mathematical and numerical model. American Journal of Science, vol.284-10, p.1085-1124.

Garven, G., Freeze, R.A. (1984b). Theoretical analysis of the role of groundwater flow in the genesis of stratabound ore deposits. 2. Quantitative results. American Journal of Science, vol.284-10, p.1125-1174.

Garven, G., Ge, S., Person, M.A, Sverjensky, D.A. (1993). Genesis of stratabound ore deposits in the Midcontinent basins of North America; 1, The role of regional groundwater flow. American Journal of Science, vol.293-6, p.497-568.

Gasparrini, M. (2003) Large-scale hydrothermal dolomitization in the southwestern Cantabrian Zone (NW Spain): causes and controls of the process and origin of the dolomitizing fluids. Unpbl. PhD thesis, University of Heidelberg, 193 p.

Gasparrini, M., Bakker, R.J., Bechstädt T. (2006a) Characterisation of dolomitizing fluids in the Carboniferous of the Cantabrian Zone (NW Spain): a fluid inclusion study with cryo-Raman spectroscopy.- Journal of Sedimentary Research, vol.76-12, p.1304-1322.

Gasparrini, M., Bechstädt, T., Boni, M. (2006b) Massive hydrothermal dolomite in the southwestern Cantabrian Zone (Spain) and its relation to the late Variscan evolution. Marine and Petroleum Geology, vol.3-5, p.543-568.

Garrels, R.M., Dreyer, R.M. (1952). Mechanism of limestone replacement at low temperatures and pressures. Geological Society of America Bulletin, vol.63-4, p.325-379.

Given, R.K., Wilkinson, B.H. (1987). Dolomite abundance and stratigraphic age constraints on rates and mechanisms of Phanerozoic dolostone formation. Journal of Sedimentary Petrology, vol.57, p.1068-1078.

Glover, E.D, Sippel, R.F. (1967). Synthesis of magnesium calcite. Geochemical and Cosmochimica Acta, vol. 33, p.603-613.

Goldsmith, J.R., Graf, D.L. (1958a). Structural and compositional variations in some natural dolomites. Journal of Geology, vol.66-6, p.678-693.

Goldsmith, J.R., Graf, D.L. (1958b). Relation between lattice constants and composition of the Ca-Mg carbonates. American Mineralogist, vol.43-1.2, p.84-101.

_____

References

Goldstein, R.H. (2003). Petrographic analysis of fluid inclusions. In: I. Samson, A. Anderson and D. Marshall editors, Fluid inclusions: Analysis and Interpretation. Mineralogical Association of Canada, Short Course Series Volume 32, p.9-53.

Goldstein, R.H., Reynolds, T.J. (1994). Systematics of fluid inclusions in diagenetic minerals. SEMP short course, vol.31, 198 p.

Gregg, J.M. (1983). On the formation and occurrence of saddle dolomite. Discussion. Journal of Sedimentary Petrology, vol.53, p.1025-1033.

Gregg, J.M. (1985). Regional epigenetic dolomitization in the Bonneterre Dolomite (Cambrian), southeestern Missouri. Geology, vol.13, p.503-506.

Gregg, J.M., Sibley, D.F. (1984). Epigenetic dolomitization and the origin of xenotipic dolomite texture. Journal of Sedimentary Petrology, vol.54-3, p.908-931.

Grobe, M., Machel, H.G. (1996). Petrographische und stabile Isotopendaten (C und O) fuer stoerungskontrollierte hydrothermale Mineralisation im devonischen Briloner Riffkomplex, Deutschland. Zentralblatt fuer Geologie und Palaeontologie, Teil I, vol.5-6, p.397-413.

Gutiérrez-Claverón, M., García Iglesias, J. (1982). El yacimiento de magnesita de Valderrodero (Asturias, Espana). Boletin Geologico y Minero, vol.XCIII-III, p.233-243

Gutiérrez-Alonso, G., Fernández-Suárez, J., Weil, A.B. (2004). Oroclinal bending lithospheric delamination. Geological Society of America Special Paper, vol.383, p.121-130.

Gutiérrez-Marco J.G., Robinson, M., Rábano, I., Sarmiento, G.N., San José Lancha, M.A., Herranz Araújo, P. (2002). Ordivician. In: W. Gibbons and T. Moreno (eds.), Geology of Spain. London, Geological Society, p.31-49.

Hardie, L.A. (1987). Dolomitization: a critical view of some current views. Journal of Sedimentary Petrology, vol.57, p.166-183.

Hardie, L.A. (1996). Secular variation in seawater chemistry: an explanation for the coupled secular variation in the mineralogies of marine limestones and potash evaporates over the past 600 my. Geology, vol.24, p.279-283.

Hardy, M., Ildefonse, J.P. (1981). Dolomitisation, chloritisation et talcification de la formation viseenne a facies griotte dans la region de Puebla de Lillo (Boñar, Espagne) In: 12e Assemblee generale de l'I.M.A.; II, Inclusions magmatiques, silicates, gemmes; Bulletin de Mineralogie, vol.104-4, p.445-451.

Hardy, R., Tucker, M. (1988). X-ray powder diffraction of sediments. In: M. Tucker (ed.),Techniques in sedimentology, p.191-228.

Hardy, M., Ildefonse, J.P., Fortune, J.P., Touray, J.C., García Iglesias, J. (1980). Genese du talc par diffusion simultaneé di magnesium et de la silice: cas des gites de Puebla de Lillo (Boñar, León, Espagne). Implicasions pour la prospection. Comptes rendus de l'Academie de Science de Paris, vol.290-12, p.731-734.

Heijlen, W., Muchez, P., Banks, D.A. (2001). Origin and evolution of high-salinity Zn-Pb mineralizing fluids in the Variscides of Belgium. Mineralium Deposita, vol.36, p.165-176.

Heward, A.P. (1978). Alluvial fan and lacustrine sediments from the Stephanian A and B (La Magdalena, Cinera-Matallana and Sabero coalfields), northern Spain. Sedimentology, vol.25-4, p.451-483.

Hitchon, B., Bachu, S., Underschulz, J.R. (1990). Regional subsurface hydrogeology, Peace River arch area, Alberta and British Columbia. Bulletin of Cannadian Petroleum Geologists, vol.38-A, p.196-217.

Holland, H.D., Zimmerman, H. (2001). The dolomite problem revisited. International Geology Review, vol.42, p.481-490.

Holser, W.T. (1979). Trace elements and isotopes in evaporates. Mineralogical Society of America Short Course Notes, vol.6, p.295-346.

Horita, J., Zimmerman, H., Holland, H.D. (2002). The chemical evolution of seawater during the Phanerozoic: implications from the record of marine evaporates. Geochimica et Cosmochimica Acta, vol.66, p.3733-3756.

Horita, J., Friedman, T.J., Lazar, B., Holland, H.D. (1991). The composition of Permian seawater. Geochimica et Cosmochimica Acta, vol.55, p.417-432.

Horwitz, E.P., Dietz, M.L., Fischer, D.E. (1991a). SREX: a new process for the extraction and recovery of strontium from acid nuclear waste streams. Solvant Exch., vol.9, p.1-25.

Horwitz, E.P., Dietz, M.L., Fischer, D.E. (1991b). Separation and preconcentration of Sr from biological, environmental and nuclear waste samples by extraction chromatography using a crown ether. Analytical Chemistry, vol.63, p.522-525.

Hower, J., **Eslinger, E**., **Hower, M.E**., **Perry, E.A**. (1976). Mechanism of burial metamorphism of argillaceous sediment; I. Mineralogical and chemical evidence. Geological Society of America Bulletin, vol.87-5, p.725-737.

Hsü, K.J. (1967). Chemistry of dolomite formation. In G.V. ChilingarH.J. Bissel, and R.W Fairbridge (eds.) Carbonate Rocks. Elsevier, Amsterdam, p.169-191.

Hurley, N.F., Budros, R. (1990). Albio-Scipioand Stoney Point fields – USA. Michigan Basin. In:E.A. Beaumont and N.H. Foster (eds.), Stratigraphic traps I. American Association of Petroleum Geologists, Atlas of Oil and Gas Field, p.1-37.

Iannace, A., Boni, M., Bechstaedt, T. (2001). Late Variscan fluid flow and hydrothermal dolomitization: an European prospective? In: A. Piestrzynski et al. (eds), Mineral deposits at the beginning of the 21st century. Proceedings of the Biennial SGA Meeting, vol.6, p.197-200.

Illing, L.V. (1959). Deposition and diagenesis of same Upper Paleozoic carbonate sediments in western Canada. Fifth World Petroleum Congress, New York, p. 23-52.

Jacobson, R.L., Usdowski, H.E. (1976). Partitioning of strontium between calcite, dolomite and liquids. Contribution to Mineralogy and Petrology, vol.59, p.171-185.

Julivert, M. (1971). Decollement tectonics in the Hercinian Cordillera of NW Spain. American Journal of Science, vol.270-1, p.1-29.

Julivert, M., Pamirez del Pozo, J., Truyols, J. (1971). Le réseau de failles et la couberture post.hercynienne dans les Asturies. In: Histoire structurale du Golfe de Gascogne. Puplications de l'Istutute Francais du Pétrole. Editions Tech 2, v.3.1-v3.4.

Julivert, M., Fontboté, J.M., Ribeiro, A., Conde, L. (1972). Mapa Tectonico de la Penisula Ibérica y Baleares. Instituto Geologico y Minero de España., 113 p.

Katz, A., Matthews, A. (1977). The dolomitization of $CaCO_3$: an experimental study at 252-295°C. Geochimica et Cosmochimica Acta, vol.41, p.297-308.

Keller, M. (1997). Evolution and sequence stratigraphy of an Early Devonian carbonate ramp, Cantabrian Mountain, northern Spain. Journal of Sedimentary Research, vol.67-4, p.638-652

Keller, M., Krumm, S. (1993). Variscan versus Caledonian and Precambrian metamorphic events in the Cantabrian Mountains, northern Spain. Zeitschrift Deutsche Geologische Gesellschaft, vol.144, p.88-103.

Kesler, S.E., Martini, A.M.; Appold, M.S., Walter, L.M., Huston, T.J., Furman, F.C. (1996) Na-Cl-Br systematics of fluid inclusions from Mississippi Valley-type deposits, Appalachian Basin: constraints on solute origin and migration paths. Geochimica et Cosmochimica Acta, vol.60-2, p.225-233.

Kinsman, D.J.J. (1969). Interpretation of Sr^{+2} concentrations in carbonate minerals and rocks. Journal of Sedimentary Petrology, vol.39-2, p.486-508.

Kovalevich, V.M., Peryt, T.M., Petrichenko, O.I. (1998). Secular variation in seawater chemistry during the Phanerozoic as indicated by fluid inclusions in halite. Journal of Geology, vol.106, p.695-712.

Kovalevich, V.M., Peryt, T.M., Carmona, V., Sydor, D.V., Vovnyuk, S.V., Halas, S. (2002). Evolution of Permian seawater: evidence from fluid inclusions in halite. Neues Jahrbuch Mineralogie Abhandlung, vol.178, p.27-62.

Kozlowsky, A. (1984). Calcium-rich inclusion solutions in fluorite from the Strzegom pegmatites, Lower Silesia. Acta Geoogica. Polonica., vol.34-1,2, p.131-138.

Kretz, R. (1982). A model for the distribution of trace elements between calcite and dolomite. Geochimica et Cosmochimica Acta, vol.46-10, p.1979-1981.

Kretz, R. (1992). Carousel model for the crystallization of saddle dolomite. Journal of Sedimentary Petrology, vol.62, p.551-574.

Krumgalz, B.S., Pogerelsky, R., Pitzer, K.S. (1996). Volumetric properties of single aqueous electrolytes from zero to saturation concentrations at 298,15 K represented by Pitzer ion-Interaction equation. J. Phy. Chem. Ref. Data, vol.25, p.663-689.

Land, L.S. (1980). The isotopic and trace element geochemistry of dolomite; the state of the art. In: D.H. Zenger, J.B. Dunham, E.L. Ethington (eds.), Concepts and models of dolomitization, Special Publication of the Society of Economic Paleontologists and Mineralogists, vol.28, p.87-110.

Land, L.S. (1983). The application of stable isotopes to studies of the origin of dolomite and problems of diagenesis of clastic sediments. In: M.A. Arthur, T.F. Anderson, I.R. Kaplan, J. Veizer and L.S. Land (eds.),

References

Stable isotopes in sedimentary geology. Society of Economic Paleontologists and Mineralogists Short Course, vol.10, p.4.1-4.22.

Land, L.S. (1984). Frio Sandstone diagenesis, Texas Gulf Coast; a regional isotopic study. American Association of Petroleum Geologists Memoir, vol.37, p.47-62.

Land, L.S. (1985). The origin of massive dolomite. Journal of Geological Education, vol.33, p.87-110.

Land L.S. (1991). Dolomitization of the Hope Gate Formation (N. Jamaica) by seawater: reassessment of mixing-zone dolomite. In: H.P. Taylor, J.R. O'Neil, I.R. Kaplan eds. Stable isotope geochemistry: a tribute to Samuel Epstein. Geochemical Society Special Publication, vol.3, p.121-133.

Land, L.S. (1992). The dolomite problem: Stable and radiogenic isotope clues. In: N.Claver and S.Chanduri (eds.) Signatures and Sedimentology Records, Lecture notes in Earth Science, Springer-Verlag, New York, vol.43, p.49-68.

Land, L.S., Hoops, G.K. (1973). Sodium in carbonate sediments: a possible index to the salinity of diagenetic fluids. Journal of Sedimentary Petrology, vol.43, p.614-617.

Land, L.S., Prezbindowski, D.R. (1981). The origin and evolution of saline formation waters: Lower cretaceous carbonates, south-central Texas and southern new Mexico. J. Hydrogeology, vol.54, p.51-74.

Lazar, B., Starinsky, A, Katz, A., Sass, E., Ben-Yaakov, S. (1983). The carbonate system in hypersaline solutions: alkalinity and $CaCO_3$ solubility of evaporated seawater..Limnology and Oceanography, vol.28-5, p.978-986.

Leeder, M.R. (1988). Devono-Carboniferous river systems and sediment dispersal from the orogenic belts and cratons of NW Europe. In:A.L. Harris and D.J. Fettes (eds.), The Caledonian-Appalachian Orogen. Geological Society of London, vol.38, p.549-558.

Lepvrier, C., Martínez-García, E. (1990). Fault development and stress evolution of the post-Hercynian Asturian Basin (Asturias and Cantabria, NW Spain). Tectonophysics, vol.184, p.345-356.

Liebermann, O. (1967). Synthesis of dolomite. Nature, vol. 213, p.241-245.

Linnemann, U., Heuse, T. (2000). The Ordovician of the Schwarzburg Anticline: Geotectonic setting, biostratigraphy and sequence stratigraphy (Saxoturingian Terrane, Germany). Zeitschrift der Deutschen Geologischen Gesellschaft, vol.151, p.471-491.

Lippmann, F. (1968). Syntesys of $BaMg(CO_3)_2$ (Norsehite) at 20°C and the formation of dolomite in sediments. In: G.Muller, G.M. Friedman eds. Recent Development in Carbonate Sedimentology in Central Europe. Springer-Verlag, New York, p.33-37.

Lippmann, F. (1973). Sedimentary carbonate minerals. Springer-Verlag, Berlin, p.228.

Loeschke, J. (1982). Late Hercynian igneous rocks of the southeastern Cantabrian Mountains (NW Spain). In: J. Kullmann, R. Schönenberg and J. Wiedmann (eds.), Subsidenz-Entwicklung im kantabrischen Variszikum und an passiven Kontinentalraendern der Kreide. Neues Jahrebuch fuer Geologie und Palaeontologie Abhandlungen, vol.163-2, p.260-271.

Loeschke, J. (1983). Igneous and pyroclastic rocks in Devonian and Lower Carboniferous strata of the Cantabrian Mountains (NW Spain). Neues Jahrbuch fuer Geologie und Palaeontologie Monatshefte, vol.8, p.495-504.

Loeschke, J. (1986). Magmatismus und Orogenese im Kantabrischen Gebirge Spaniens. °6 Jahrestagung der Geologischen vereinigung, Giessen.

Loeschke, J., **Zeidler, N.** (1982). Early Palaeozoic sills in the Cantabrian Mountains (Spain) and their geotectonic environment. Neues Jahrbuch fuer Geologie und Palaeontologie. Monatshefte, vol.7, p.419-439.

Lohmann, K.C. (1988). Application of carbon and oxygen isotopic techniques for unravelling the diagenetic history of carbonate sequences. In: J.R. Allan and P.M. Harris (eds.), Stable isotopes, Trace Elements and Fluid Inclusion Workshop,Chevron Oil Field research Co. unpublished report, p.1-49.

Long, J.V.P., Agrell, S.O. (1965). The cathodoluminescence of minerals in thin section. Mineralogical Magazine, vol.34, p.318-325.

Loredo, J., García Iglesias, J. (1988). El yacimiento aurífero de Carlés (Asturias). Boletín de la Sociedad Española de Mineralogía, vol.11-1, p.47-54.

Lotze, F. (1945). Zur Gliederung der Varisciden der Iberischen Meseta. Geotektonische Forschungen, vol.6, p. 78-92.

Lowenstein, T.K., Timofeeff, M.N., Brennan, S.T., Hardie, L.A., Demicco, R.V. (2001). Oscillation in Phanerozoic seawater chemistry: evidence from fluid inclusions in salt deposits. Science, vol.295, p.1086-1088.

Lowenstein, T.K., Hardie, L.A., Timofeeff, M.N., Demicco, R.V. (2003). Secular variation in seawater chemistry and the origin of calcium chloride basinal brines. Geology, vol.31, p.627-644.

Lowenstein, T.K., Timofeeff, M.N., Kovalevych, V.M., Horita, J. (2005). The major-ion composition of Permian seawater. Geochimica et Cosmochimica Acta, vol.69-7, p.1701-1719.

Lugli, S., Torres-Ruiz, J, Garuti, G., Olmedo, F. (2000). Petrography and Geochemistry of the Eugui magnesite deposit (Western Pyrenees, Spain): evidences for the development of a peculiar zebra banding by dolomite replacement. Economic Geology, vol.95, p.1775-1791.

Lumsden, D.N. (1979). Discrepancy between thin section and X-ray estimates of dolomite in limestones. Journal of Sedimentary Geology, vol.49, p.429-436.

Luque, C. (1985). Las mineralizaciones de mercurio de la Cordillera Cantábrica. Unpublished PhD thesis, Universidad de Oviedo.

Luque, C., Martínez García, E. (1983). Depósitos minerales en el Carbonífero de la Cordillera Cantábrica. In: C. Martínez Díaz (coord.), Carbonífero y Permico de España. Instituto Geológico y Minero de España, p.163-177.

Luque, C., Martínez García, E. (1985). Análisis tectometalogenetico de las mineralizaciones en el Carbonífero de la Zona Cantábrica, (NW de l'España). Compte Rendu du X Congres International de Stratigraphie et de Geologie du Carbonifere, vol.3, p.95-104.

Luque, C., Martínez García, E., Ruiz, F. (1990). The Cantabrian Zone. Metallogenesis. In: R. D. Dallmayer & Martinez-Garcia (eds.) Pre-mesozoic Geology of Iberia. Springer Verlag, Berlin, p.80-87.

Machel, H.G. (1987). Saddle dolomite as a by-product of stylolitization and thermochemical sulfate reduction. Geology, vol.15-10, p.936-940.

Machel, H.G. (2004). Concept and models of dolomitization. In: C. J.R. Braithwaite, G. Rizzi and G. Darke (eds.), The geometry and petrogenesis of dolomite hydrocarbon reservoirs. Geological Society of London Special Publication, vol.235, p.7-63.

Machel, H.G., Anderson, J.H. (1987). Pervasive subsurface dolomitization of the Nisku Formation in central Alberta. Journal of Sedimentary Petrology, vol.59, p.891-911.

Machel, H.G., Burton, E.A. (1991). Factors governing cathodoluminescence in calcite and dolomite and their implications for studies of carbonate diagenesis. In: C.E. Barker and O.C. Koop (eds.), Luminescence microscopy and spectroscopy: qualitative and quantitative applications. Society of Economic paleontologists and Mineralogists Short Course vol.25, p.37-57.

Machel, H.G., Cavell, P.A. (1999). Low-flux, tectonically-induced squeegee fluid flow ("hot flash") into the Rocky Mountain foreland basin. Bulletin of Canadian Petroleum Geology, vol.47-4, p.510-533.

Machel, H.G., Lonnee, J. (2002). Hydrothermal dolomite – a product of poor definition and imagination. Sedimentary Geology, vol.152, p.163-171.

Machel, H.G., Mountjoy, E.W. (1986). Chemistry and environment of dolomitization: a reappraisal. Earth Science Review, vol.23, p.175-222.

Machel, H.G., Mountjoy, E.W. (1987). General constraints on extensive pervasive dolomitisation and their application to the to the Devonian carbonate of Western Canada. Bulletin of Canadian Petroleum Geologists, vol. 35, p.143-158.

Machel, H.G., Mountjoy, E. W., Amthor, J.E. (1996). Mass balance anf fluid flow constrains on regional-scale dolomitization, Late Devonian, Western Canada Sedimentary Basin. Bulletin of Canadian Petroleum Geologists, vol.44-3, p.566-571.

Marcos, A. (1979). Facies differentiation caused by wrench deformation along a deep-seated fault szstem (León Line), Cantabrian Mountains, North Spain. Discussion. Tectonophysics, vol.60, p.303-309.

Mariano, A.N., Ring, P. J. (1975). Europium-activated cathodoluminescence in minerals. Geochimica et Cosmochimica Acta, vol.39-5, p.649-660.

Marquínez, J., Marcos, A. (1984). La estructura de la Unidad del Gildar-Montó (Cordillera Cantabriaca). Trabajos de Geologia, vol.14, p.53-64.

Martínez García, E. (1981). Tectónica y mineralizaciones pérmicas en la Cordillera Cantábrica oriental (Noroeste de España). Cuadernos do Laboratorio Xeoloxico de Laxe, vol.2, p.263-271.

Martínez Garcia, E. (1983). El Pérmico en la Cordillera Cantábrica. In: D. C. Martínez (ed.), Carbonífero y Pérmico de España. IGME, Madrid, p.389-402.

Martínez García, E., Tejerina, E. (1985). FLuorspar deposits associated with Carboniferous and Permian in Asturias and León, northwest Spain. In: A. T. Cross (ed.), Compte Rendu IX Congres International de Stratigraphie et de Geologie du Carbonífère, vol.4, p.467-478.

References

Matte, P. (1986). Tectonics and plate tectonic model for the Variscan belt of Europe. Tectonophysics, vol.126, p.329-374.

Matte, P. (1991). Accretionary history and crustal evolution of the Variscan belt in western Europe. Tectonophysics, vol.196, p.309-337.

Matte, P. (2001). The Variscan collage and orogeny (480-290 Ma) and the tectonic definition of the Armonican microplate: a review. Terra Nova, vol.13, p.122-128.

Mattes, B.W., Mountjoy, E.W. (1980). Burial dolomitization of the Upper Devonian Miette buildup, Jasper National Park, Alberta. In: D.H. Zenger, J.B. Dunham and R.L. Ethington (Eds.), Concepts and models of dolomitization. SEPM Special Publication, vol.28, p.259-297.

McKenzie, J. A. (1991). The dolomite problem; an outstanding controversy. In: D. W Mueller, J. A. McKenzie and H. Weissert (eds.), Controversies in modern geology, evolution of geological theories in sedimentology, Earth history and tectonics. Academic Press, London, p.37-54.

McKenzie, J.A., Hsü, K.J., Schneider, J.F. (1980). Movement of subsurface waters under the Sabkha, Abu Dhabi, UAE, and its relation to evaporative dolomite genesis. In: D. H. Zenger, J. B. Dunham and R. L. Edhingtin (eds.), Concept and model of dolomitisation, Society of Economic Paleontologists and Mineralogists Special Publication, vol.28, p.11-30.

Merino, E. (1984). Survey of geochemical self-patterning phenomena. In: G.Nicolis and F Baras (eds.), Chemical instabilities. Dordrecht, Reidel Publishing Company NATO ASI series C, vol.120, p.305-328.

Montañez, I. P. (1994). Late diagenetic dolomitization of Lower Ordovician, upper Knox carbonates: a record of the hydrotdynamic evolution of the southern Appalachian Basin. American Association of Petroleum Geologists, vol.78-8, p.1210-1238.

Montañez, I.P., Osleger, D.O., Banner, J.L., Mack, L.E., Musgrove, M. (2000). Evolution of the Sr and C isotope composition of Cambrian Oceans. GSA Today, vol.10-5, p.1-7.

Morrow, D.W. (1978). The influence of the Mg/Ca ratio and salinity on dolomitisation in evaporative basins. Canadian Petroleum Geology Bulletin, vol.26, p.389-392.

Morrow, D.W. (1990a). Dolomite - Part 1: the chemistry of dolomitization and dolomite precipitation. In: I. A. McIlreath and D. W. Morrow (eds.), Diagenesis. Geoscience Canada Reprint Series, vol.4, p.113-124.

Morrow, D.W. (1990b). Dolomite - Part 2: dolomitization models and ancient dolostones. In: I. A. McIlreath and D. W. Morrow (eds.), Diagenesis. Geoscience Canada Reprint Series, vol.4, p.125-139.

Morrow, D.W., Aulstead, K.L. (1995). The Manetoe Dolomite; a Cretaceous-Tertiary or a Paleozoic event? Fluid inclusion and isotopic evidence. Bulletin of Canadian Petroleum geology, vol.43-3, p.267-280.

Morrow, D.W., Cummings, G.L., Aulstead, K.L. (1990). The gas-bearing Devonian Manetoe facies, Yukon and Northwest Terrirories, Geological Survey of Canada Bulletin, vol.400, p.267-280.

Morse, J.W., Casey, W.H. (1988). Ostwald processes and mineral paragenesis in sediments. American Journal of Science, vol.288-6, p.537-560.

Mountjoy, E.W., Amthor, J.E. (1994). Has burial dolomitization come from age? Same answers from the Western Canada Sedimentary Basin. In: B.H. Purser, M.E. Tucker (Eds.), Dolomites – a volume in honour of Dolomieu. International Association of Sedimentologists Special Publications, vol.21, p.203-229.

Nader, J. (1996). CalcicBrine: a Microsoft Excel 5.0 Add-in for calculating salinities from microthermometric data in the system NaCl-CaCl$_2$-H$_2$O. Pacrofi XI, Wisconsin, p.87-89.

Nielsen, P., Swennen, R., Muchez, P., Keppens, E. (1998). Origin of Dinantian zebra dolomites south of the Brabant-Wales Massif, Belgium. Sedimentology, vol.45, p.727-743.

Nordeng, S. H., Sibley, D. F. (2003). The induction period and dolomite kinetics in experimental and natural systems. 12th Bathurst Meeting, International Conference of Carbonate Sedimentologists, vol.74.

Northrop, D.A., **Clayton, R.N**. (1966). Oxygen-isotope fractionations in systems containing dolomite. Journal of Geology, vol.74-2, p.174-196.

Oliver, J. (1986). Fluid expelled tectonically from orogenic belts: their role in hydrocarbon migration and other geological phenomena. Geology, vol.14, p.99-102.

O'Neil, J.R., Epstein, S. (1966). Oxigen isotope fractionation in the system dolomite-calcite-carbon dioxide. Science, vol.152, p.198-201.

Orti, F., **García-Veigas, J., Rosell, L., Jurado, M.J., Utrilla, R.** (1996). Formaciones salinas de la cuencas triasica en la península Ibérica: caracterización petrológica y geoquímica. Cuadernos de Geología Ibérica, vol.20, p.13-35.

Paniagua, A. (1993). Mineralizaciones asociadas a estructuras tardihercinicas en la rama sur de la Zona Cantábrica. Unpublished Ph.D. thesis, Universidad de Oviedo, Spain, 377 p.

Paniagua, A. (1998). Gold showing and deposits of th Palentian Zone (NW Spain)In: D. Arias, A Martín-Izard, and A. Paniagua (eds.). Gold in NW Spain. Departimiento de Geologia, Universidad de Oviedo, p.112-123.

Paniagua, A., Rodriguez Pevida L.S. (1988). Génesis y evolución de las mineralizaciones de Cu-Co-Ni-U-Pb-Zn-Au-Ag- ligadas a estructuras tardihercínicas en el área de Pajares-Villamanín-Boñar (N de León) Boletín de la Sociedad Española de Mineralogía, vol.11-2, p.118-119.

Paniagua, A., Loredo, J., Garcia Iglesias J. (1988a). Epithermal (Cu-Co-Ni) mineralization in the Aramo Mine (Cantabrian Mountains, Spain). Correlation between paragenetic and fluid inclusion data. Bulletin de Mineralogie, vol.111, p.383-391.

Paniagua, A., Rodríguez Pevida, L.S., Gutiérrez Villarias, J.L. (1988b). Mineralizaciones As-Sb-Au asociadas a rocas ignea filonianas del NE de Leon: las minas de Buron. Boletín de la Sociedad española de Mineralogía, vol.11-1, p.35-46.

Paniagua, A., Fontboté, L., Hach-Alí, F., Fallik, A.E., Moreiras, D.B., Corretgé, L.G. (1993) Tectonic setting, mineralogical characteristic, geochemical signatures and age datig of a new type of epithermal carbonate-hosted, precious metal-five elements deposits: the Villamanin area (CZ, N Spain). In: P. Fenoll Hach-Ali, J. Torres-Ruiz, F. Gervilla (eds.), Current Research in Geology applied to ore deposits, 2nd biennal SGA Meeting, Granada, p.531-535.

Paniagua, A., Rodríguez Pevida, L.S., Loredo, J., Fontboté, L., Fenoll-Hach-Ali, P. (1996). Un yacimiento de Au en carbonatos del órogeno hercínico: el área de Salomón (N León). Geogaceta, vol.20-7, p.1605-1608.

Patterson, R.J. (1972). Hydrogeology and carbonate diagenesis on costal sabkha in the Persian Gulf. Unpublished Ph.D Thesis, Princeston University, U.S.A., 498 p.

Patterson, R.J., Kinsman, D.J.J. (1982). Formation of diagenetic dolomite in sabkha along the Persian Gulf. Bulletin of American Association of Petroleum Geologists, vol.65, p.1457-1475.

Pérez Estaún, A. (1990). Cantabrian and Palentian Zone. Stratigraphy. In: R. D. Dallmayer & Martinez-Garcia (eds.) Pre-mesozoic Geology of Iberia. Springer Verlag, Berlin, p.10.

Pérez Estaún, A., Bastida, F. (1990). Cantabrian Zone. Structure. In: R. D. Dallmayer & Martinez-Garcia (eds.) Pre-mesozoic Geology of Iberia. Springer Verlag, Berlin, p.55-69.

Pérez Estaún, A., Bastida, F., Alonso, J.L., Marquínez, J., Aller, J., Alvarez Marrón, J., Marcos, A., Pulgar, J.A. (1988). A thin skinned tectonics model for an arcuate fold and thrust belt : the Cantabrian Zone. Tectonics, vol.7-3, p.517-537.

Prado, J.G. (1972). Nota sobra la petrografía de la zona de Viñon (Asturias). Studia geologica Salmanticensia, vol.7, p.7-32.

Purser, B.H., Tucker, M.E., Zenger, D.H. (1994a). Problems, progress and future research concerning dolomites and dolomitisation. In: B. H. Purser, M. E. Tucker and D. H. Zenger (eds.), Dolomites - a volume in honour of Dolomieu. International Association of Sedimentologists Special Publication, vol.21, p.3-20.

Quing, H., Mounjoy, E.W. (1994). Formation of coarsely crystalline, hydrothermal dolomite reservoir in the Presqu'ile Barrier, western Canada Sedimentary Basin. American Association of Petroleum Geologists, vol.78-1, p.55-77.

Radke, B. M., Mathis, R.L. (1980). On the formation and occurrence of saddle dolomite. Journal of Sedimentary Petrology, vol.50-4, p.1149-1168.

Raven, J.G.M., Van der Pluijm, B.A. (1986). Metamorphic fluids and transtension in the Cantabrian Mountains of northern Spain: an application of the conodont colour alteration index. Geological. Magazine., vol.123(6), p.673-681.

Ribeiro, A., Quesada, C., Dallmeyer, R.D. (1990). Geodynamic evolution of the Iberian Massif. In: R.D. Dellmeyer and E. Martínez-García (eds.), pre-mesozoic Geology of Iberia, Sringer-Verlag, Berlin, p.399-409

Robardet, M. (2002). Alternative approach to the Variscan Belt in southwestern Europe: preorogenic paleobiogeographical constraints. In: J. R. Martinez Catalan, R. D. Jr. Hatcher, R. Arenas and F. Díaz García (eds.), Variscan Appalachian dynamics: the building of the Late Paleozoic basement, Geological Society of America Special Paper, vol.364, p.1-15.

Robardet, M., Gutierrez Marco, J.C. (2002). Silurian. In: W. Gibbons and T.Moreno (eds.), The Geology of Spain, p.51-66.

Robie, R.A., Hemingway, B.S., Fisher, J.B. (1978). Thermodinamics property of minerals and related substances at 298.15°K and 1 bar pressure and at higher temperatures. United States Geological Survey Bulletin, vol.1452, 456 p.

References

Rodríguez Fernández, R., Heredia, N., Lobato, L., Velando, F. (1985). Memoria de la Hojas Geologica. E. 1:50.000 n° 106. (16-7), Camporredondo de Alba. IGME, p.98.

Roedder, E. (1984). Fluid inclusions. Reviews in Mineralogy, vol.12, 646 p.

Rosenberg, P.E., Holland, H.D. (1964). Calcite-dolomite-magnesite stability relations in solutions at elevated temperatures. Science, vol.145, p.700-701.

Samson, I.M., Anderson, A.J., Marshall, D.D. (eds.) (2003). Fluid inclusions. Analysis and interpretation. Mineralogical Association of Canada Short Course Series vol.32, 374 p.

Samson, I.M., Walker, R.T. (2000). Cryogenic Raman Spectroscopy studies in the system NaCl-CaCl2-H2O. The Canadian Mineralogist, vol.38, p.35-43.

Sánchez de la Torre, L., Agueda-Villar, J. A., Colménero, J. R., Manjon, M. (1977). La serie Permo-tríassica en la región de Villaviciosa. Cuadernos de Geología Ibérica, vol.4, p.329-338.

Sánchez de la Torre, L., Àgueda, J., Colménero, J.R., García-Ramos, J.C., Gonzáles-Lastra, J. (1983). Evolución sedimentaria y paleogeográfica del Carbonifero en la Cordillera Cantábrica. In: D. C.Martínez (ed.), Carbonífero y Pérmico de España. IGME, Madrid, p.133-150.

Schneider, J. (2000). Indirekte Rb-Sr-Chronometrie postorogener Hydrothermalsysteme und assoziierter Gangmineralisationen im Rhenohercynikum. Unpublished PhD thesis, Universität Giessen, Germany.

Schönenberg, R., Neugebauer, J. (1997). Einfürung in der Geologie Europas. Freiburg, Rombach, 384 p.

Searl, A. (1989). Saddle dolomite: a new view of its nature and origin. Mineralogical Magazine, vol.53, p.547-555.

Sheppard, S.M.F., Schwarcz, H.P. (1970). Fractionation of carbon and oxygen isotopes and magnesium between coexisting metamorphic calcite and dolomite. Contributions to Mineralogy and Petrology, vol.26-3, p.161-198.

Shepherd, T.J., Rankin, A.H., Alderon, D.H.M. (1985). A practical guide to fluid inclusion studies. Blakie & son, 239 p.

Shinn, E.A. (1968). Practical significance of birds-eyes structures in carbonate rocks. Journal of Sedimentary Petrology, vol. 38, p.215-223.

Shinn, E.A., Ginsburg, R.N., Lloyd, R.M. (1965). Recent supratidal dolomite from Andros Island, Bahamas. In: L.C. Pray and R.D. Murray eds., Dolomitization and Limestone Diageneis, a Symposium. Society of Economic Paleontologists and Mineralogists Special Publication, vol. 13, p.112-123.

Sibley, D.F. (1982). The origin of common dolomite fabrics: clues from the Pliocene. Journal of Sedimentary Petrology, vol.52-4, p.1087-110.

Sibley, D.F. (1990). Unstable to stable transformations during dolomitisation. Journal of geology, vol. 98, p.739-748.

Sibley, D.F. Gregg., J.M. (1987). Classification of dolomite rock textures. Journal of Sedimentary Petrology, vol.57-6, p.967-975.

Sibley, D.F., Nordeng, S.H., Brkowsky, M.L. (1990). Dolomitization setting in hydrothermal bombs and natural setting. Journal of Sedimentary Research, vol.64A, p.630-637.

Silva, J.B., Oliveira, J.T., Ribeiro, A. (1990). South Potuguese Zone. Stucturat outline. In: R.D. Dallmayer & Martinez-Garcia (eds.) Pre-mesozoic Geology of Iberia. Springer Verlag, Berlin, p.248-362.

Smith, D.B. (1981). Bryozoan-algal patch reefs in the Upper Permian magnesian limestones of Yorkshire, Northeast England. In: D.F. Toomey ed., European Fossil Reef Models. Society of Economic Paleontologist and Mineralogists Special Publication, vol.30. p.187-202.

Sommer, S.E. (1972). Cathodoluminescence of carbonates; 2, Geological applications. Chemical Geology, vol.9-4, p.275-284.

Spencer-Cervato, C., Mullis, J. (1992). Chemical study of tectonically-controlled hydrothermal dolomitization: an example from the Lessini Mountains, Italy. Geologisches Rundschau, vol.81-2, p.347-370.

Sperber, C.M., Wilkinson, B.H., Peacor, D.R. (1984). Rock composition, dolomite stoichiometry and rock/water reactions in dolomitic carbonate rocks, Journal of Geology, vol.92, p.609-622.

Stanley, S.M., Hardie, L.A. (1999). Hypercalcification: paleontology links, plate tectonics and geochemistry to sedimentology. GSA Today, vol.9-2, p.2-7.

Stel, J. H. (1975). The influence of hurricanes on the quiet depositional conditions in the Lower Emsian La Vid shales of Colle (NW Spain). Leidse Geologishe Mededelinge, vol.49, p.475-486.

Steuber, A.M., Pushkar, P., Hetherington, E.A. (1987). A strontium isotopic study of formation waters from the Illinois basin, USA. Applied Geochemistry, vol.2, p.477-494.

Steuber, T., Veizer, J. (2002). Phanerozoic record of plate tectonic control of seawater chemistry and carbonate sedimentation. Geology, vol.30, p.1123-1126.

Steward, F.H. (1963). Marine evaporites. United States Geological Survey Professional Paper, vol.440-Y, 52 p.

Suchy, V., Rozkosny, I., Zák, K., Francu, J. (1996). Epigenetic dolomitisation of the Prídolí formation (Upper Silurian), the Barradian Basin, Czech Republic: implications for burial history of Lower Paleozoic strata. Geologische Rundschau vol.85, p.264-277.

Tait, J.A., Bachtadse, V., Franke, W. Soffel, H.C. (1997). Geodynamic evolution of the European Variscan fold belt: paleomagnetic and geological constraints. Geologische Rundschau, vol.86, p.585-598.

Tait, J., Schaetz, M., Bacheadse, V., Soffel, H. (2000). Paleomagnetism and Paleozoic paleogeography of Gondwana and European terranes. In: W. Franke, V. Haak, O. Onckel and D. Tanner (eds.), Orogenic processes: quantification and modelling in the Variscan belt. Geological Society of London, vol.179, p.21-34.

Taylor, T.R., Silbey, D.F. (1986). Petrographic and geochemical characteristics of dolomite types and the origin of ferroan dolomite in the Treton Formation, Ordovician, Michigan Basin, USA. Sedimentology, vol.33, p.61-86.

Tornos, F., Spiro, B.F. (2000). The geology and isotope geochemistry of the talc deposits of Puebla de Lillo (Cantabrian Zone, northern Spain). Economic Geology, vol.95, p.1277-1296.

Tosal, J.M. (1968). Relaciones zócalo-cobertera en el limite de las provincias de Oviedo y Santander. Breiviora Geologica Astúrica, vol.12-9, p.9-14.

Truyóls, J., Arbizu, M.A., García, Alcalde, J.L., García López, S., Méndez Bedia, I., Soto, F., Truyóls Massoni, M. (1990). Cantabrian and Palentian Zone. Stratigraphy. In: R. D. Dallmayer & Martinez-Garcia (eds.) Pre-Mesozoic Geology of Iberia. Springer Verlag, Berlin, p.9-19.

Tucker, M.E. (1990). Dolomites and dolomitization processes. In: M.E. Tucker, V. P. Wright, J. A. and D. Dickson, Carbonate sedimentology. Blackwell, Oxford, p.365-400.

Tucker, M.E., Wright, V.P. Dickson, J.A.D. (1990). Carbonate sedimentology. Blackwell, Oxford, 482 p.

Usdowsky, E. (1994). Synthesis of dolomite and geochemical implications. In. B. H. Purser, M. E. Tucker and D. H. Zenger (eds.), Dolomites - a volume in honour of Dolomieu. International Association of Sedimentologists Special Publication, vol.21, p.345-360.

Vahrenkamp, V.C., Swart, P.K. (1990). New distribution coefficient for the incorporation of strontium into dolomite and its implications for the formation of ancient dolomites. Geology (Boulder), vol.18-5, p.387-391.

Veizer, J. (1983a). Trace elements and isotopes in sedimentary carbonates. In:. BA: R.J. Reeder (ed.), Carbonates; mineralogy and chemistry. Reviews in Mineralogy, vol.11, p.265-299.

Veizer, J. (1983b). Chemical diagenesis of carbonates; theory and application of trace element technique. SEPM Short Course, vol.10, p.3.1-3.100.

Veizer, J., Hoefs, J. (1976). The nature of $^{18}O/^{16}O$ and $^{13}C/^{12}C$ secular trends in sedimentary carbonate rocks. Geochimica et Cosmochimica Acta, vol.40, p.1387-1395.

Veselovsky Z. (2004). Integrated numerical modelling of a polyhistory basin, Southern Cantabrian Basin (Paleozoic, NW Spain). GAEA heidelbergensis, vol.13, 225 p.

Wacher, E., Hayes, J.M. (1985). Exchange of oxygen isotopes in carbon-dioxide-phosphoric acid systems. Chemical Geology, vol.52, p.365-374.

Wallace, A.M., Both, R.A., Morales-Ruano, S., Fenoll Hach-Alí, P., Leeds, T. (1994). Zebra textures from carbonate hosted sulfides deposits: sheet cavity networks produced by fracture and solution enlargement. Economic Geology, vol.89, p.1183-1191.

Warr, L.N., Marschik, R. (1996). The growth of illite in the Paleozoic rocks of the Cantabrian Zone, NW Spain: Evidences for fluid activity? Graduiertenkolleg 237 "Einwirkung fluider Phasen auf Locker- und Festgesteine", Symposium Poster.

Weil, A.B., Van der Voo, R., Van der Pluijm, B.A., Parés, J.M. (2000). The formation of an orocline by multiphased deformation: a paleomagnetic investigation of the Cantabrian-Asturias arc hinge-zone (northern Spain). Journal of Structural Geology, vol.22, p.735-756.

Weil, A.B., Van der Voo, R., Van der Pluijm, B.A., Parés, J.M. (2001). Oroclinal bending and evidence against the Pangea megashear: the Cantabria-Asturias arc (northern Spain). Geology, vol.29, p.991-994.

Weil, A.B., Gutiérrez-Alonso, G., Fernández-Suárez, J. (2003). Oroclinal bending lithospheric delamination. GSA Annual Meeting, Seattle, 2003.

_____

References

Wendte, J., Qing, H., Dravis, J.J., Moore, S.L.O., Stasius, L. D., Ward, G. (1998). High temperature saline (thermoflux) dolomitization of Devonian Swan Hills platform and bank carbonates, Wild River area, west-central Alberta. Bulletin of Canadian Petroleum Geologists, vol.46-2, p.210-265.

White, D.E. (1957). Thermal waters of volcanic origin. Geological Society of America Bulletin, vol.68, p.1637-1658.

Wickstrom, L.H. (1996). Play MOF: mIddle Ordovician fractured carbonates. In: J.B Roen and B.J. Walker (eds.), The atlas of major Appalachian gas plays. West Virginia Geological and Economic Survey Publication, vol.25, p.172-176.

Wickstrom, L.H., Gray, J.D., Stieglitz, R.D. (1992). Stratigraphy, structure and production history of the TrentoncLimestone (Ordovician)cand adjacent strata in northwestern Ohio. Ohio Geological Survey Report of Investigations, vol.143, 78 p.

Wilkinson, J.J., Jenkin, G.R.T., Fallick, R.P. (1995). Oxigen and hydrogen isotopic evolution of Variscan crustal fluids, U.K. Chemical Geology, vol.123, p.239-254.

Wilson, A.M., Sanford, W.E., Whitacker, F.A., Smart, P.L. (2001) Spatial patterns of diagenesis during geothermal circulation in carbonate platforms. American Journal of Science, vol.301, p.727-752.

Wilson, E.N., Lawrence, A.H., Philips, O.M. (1990) Dolomitization front geometry fluid flow patterns and the origin of massive dolomite: the Triassic Latemar buildup, northtern Italy. American Journal of Science, vol.290, p.741-796.

Windley, B.F. (1995). The evolving continents. Jhon Wiley & Sons, Chichester, 525 p.

Wood, R.J., Hewett, T.A. (1982). Fluid convection and mass transfer in porous sandstones; a theoretical model. Geochimica et Cosmochimica Acta, vol.46-10, p.1707-1713.

Wright, W.R., Somerville, I.D., Greg, J.M., Shelton, K.L. (1999). Dolomite CL, $\delta^{18}O$ and $\delta^{13}C$ data from Irish Midlands and Dublin Basin, Carboniferous. In C.J. Stanley et al. (eds.), Proceedings of the Biennial SGA Meeting, vol.5, p.913-916.

Ypma, P.J.M., Evers, H.J., Woensdregt, C.F. (1968). Mineralogy and geology of the Providencia Mine (Leon, Spain), type locality of Villamaninite. Neues Jahrbuch fuer Geologie und Palaeontologie Monatshefte, vol.6, p.174-191.

Zamarreño, I. (1972). Las lithofacies carbonatadas del Cambrico de la Zona Cantabrica (NW España) y su distribucion paleogeografica. Trabajos de Geologia, vol.5, 118 p.

Zeeh, S. (1995). Complex replacement of saddle dolomite by fluorite within zebra dolomites. Mineralium Deposita, vol.30, p.469-475.

Zenger, D.H. (1983). Burial dolomitization in the Lost Burro Formation (Devonian), east-central California, and the significance of late diagenetic dolomitization. Geology, vol.11-9, p.519-522.

Zhang, Y.G., Frantz, J.D. (1987). Determination of the homogenization temperatures and densities of supercritical fluids in the system $NaCl-KCl-CaCl_2-H_2O$ using syntetic fluid inclusions. Chemical Geology, vol.64, p.335-350.

Zimmerman, H. (2000). Tertiary seawater chemistry: implications from primary fluid inclusions in marine halite. American Journal of Science, vol.300, p.723-767.

Appendix

Appendix 1 - XRD

Analysed samples and results of XRD analyses: peaks positions, stoichiometry (N) and degree of order (OR).

Sample	Phase	Locality	I_{015}	I_{110}	d_{104}	N	OR
fc1 fg	Dol A	Fontún	374	825	2.8903	51.43	0.45
fc1 fg	Dol B	Fontún	419	789	2.8901	51.37	0.50
fc0 lann	Dol A	Láncara	998	1627	2.8885	50.83	0.61
fc1 lann	Dol A	Láncara	1351	1606	2.8853	49.77	0.84
fc1 lans	Dol A	Láncara	1072	1657	2.8874	50.47	0.65
fc3 lans	Dol A	Láncara	1226	1527	2.8845	49.50	0.80
fc1 lans	Dol A	Láncara	1357	1820	2.8848	49.60	0.75
fcx sm	Dol A	San Martin	434	831	2.8894	51.13	0.52
fcx sm	Dol B	San Martín	481	914	2.8871	50.37	0.53
fc4 sm	Dol A	San Martín	956	1393	2.8861	50.03	0.69
fc5 sm	Dol A	San Martín	1353	2046	2.8869	50.30	0.66
fc6 sm	Dol A	San Martín	1486	1659	2.8862	50.07	0.90
fc1 cas	Dol A	Casares	487	908	2.8940	52.67	0.54
fc1 cas	Dol B	Casares	537	872	2.8923	52.1	0.61
81fc04	Dol A	Campolongo	361	720	2.8866	50.20	0.50
fd2 vil	Dol B	Villanueva	381	796	2.8885	50.83	0.48
86fc04	Dol A	Villanueva	319	622	2.8848	49.60	0.51
86fc04	Dol B	Villanueva	332	660	2.8866	50.20	0.50
fd5 cos	Dol A	Cospedal	591	1407	2.8866	50.20	0.42
fd5 cos	Dol B	Cospedal	352	719	2.8883	50.77	0.49
fd1 gen	Dol A	Genestosa	316	699	2.8903	51.43	0.45
fd1 gen	Dol B	Genestosa	491	769	2.8885	50.83	0.64
fd5 tor	Dol A	Torrestio	361	773	2.8866	50.20	0.47
fd5 tor	Dol B	Torrestio	362	763	2.8885	50.83	0.47
97fc04	Dol B	Montuerto	260	621	2.8866	50.20	0.42
91fc04	Dol A	Montuerto	311	727	2.8885	50.83	0.43
91fc04	Dol B	Montuerto	621	1410	2.8903	51.43	0.44
83fc04	Low. memb. Ds	Campolongo	279	854	2.8885	50.83	0.33
57fc04	Low. memb. Ds	Cospedal	309	645	2.8848	49.60	0.48
fd2 col	Low. memb. Ds	Collada	1206	1902	2.8872	50.40	0.63
fc1 bar	Low. memb. Ds	Barrios de Luna	351	1287	2.8941	52.70	0.27
fc2 bar	Low. memb. Ds	Barrios de Luna	1007	1674	2.8886	50.87	0.60
fc2 bar	Low. memb. Ds	Barrios de Luna	475	1071	2.8910	51.67	0.44
fc4 bar	Low. memb. Ds	Barrios de Luna	909	1763	2.8898	51.27	0.52
fc5 bar	Low. memb. Ds	Barrios de Luna	923	1485	2.8878	50.60	0.62
fd1 bar 2	Low. memb. Ds	Barrios de Luna	561	1168	2.8953	53.10	0.48
fd3 bar2	Low. memb. Ds	Barrios de Luna	801	1244	2.8893	51.10	0.64
fd4 bar2	Low. memb. Ds	Barrios de Luna	716	1321	2.8904	51.47	0.54
fc1 bar3	Low. memb. Ds	Barrios de Luna	760	1483	2.8902	51.40	0.51
fd2 leo	Low. memb. Ds	León Line	744	1684	2.8911	51.70	0.44
fc1 sm	Low. memb. Ds	San Martín	980	1648	2.8849	49.63	0.59
fc5 cruz	Low. memb. Ds	Rodiezmo	560	1368	2.8907	51.57	0.41
1 val	Low. memb. Ds	Valdorria	829	1563	2.8921	52.03	0.53
1 gete	Low. memb. Ds	Gete	1191	1753	2.8885	50.83	0.68
2 noc	Low. memb. Ds	Nocedo	961	1449	2.8903	51.43	0.66

Appendix

Sample	Phase	Locality	I_{015}	I_{110}	d_{104}	N	OR
1 mon	Low. memb. Ds	Montuerto	752	1450	2.8939	52.63	0.52
1 cueto	Low. memb. Ds	Cueto Arcuno	1140	1967	2.8885	50.83	0.58
2 mon	Low. memb. Ds	Montuerto	685	1536	2.8921	52.03	0.45
99fc04	Low. memb. Ds	Nocedo	177	495	2.8903	51.43	0.36
85fc04	Low. memb. Ds	Villanueva	245	598	2.8866	50.20	0.41

Appendix 2 – Microprobe analyses

Analysed samples and results of the microprobe analyses. The measured points are shown in Fig. 5.3, chapter 5, paragraph 5.3.1.

Point	Sample	phase	Mg (at)	Ca (at)	Fe (at)	Mn (at)	total
1	fc8 sm	Dol A	0.987	1.004	0.004	0.001	1.996
2	fc8 sm	Dol B	0.996	1.018	0.004	0.001	2.020
3	fc8 sm	Dol B	1.005	0.994	0.007	0.001	2.007
4	fc8 sm	Dol B	0.982	0.987	0.017	0.001	1.987
5	fc8 sm	Dol B	0.902	1.000	0.056	0.002	1.960
6	fc8 sm	Dol B	0.942	0.971	0.042	0.001	1.958
7	fc8 sm	Dol B	0.956	0.977	0.036	0.002	1.970
8	fc8 sm	Dol B	0.859	0.983	0.130	0.005	1.978
9	fc8 sm	Dol B	0.929	0.982	0.050	0.002	1.964
10	fc8 sm	Dol B	0.912	0.978	0.069	0.003	1.962
11	fc8 sm	Dol B	0.983	0.992	0.020	0.001	1.996
12	fc8 sm	Dol B	0.988	0.994	0.006	0.001	1.990
13	fc8 sm	Dol B	0.990	0.993	0.005	0.001	1.989
14	fc8 sm	Dol B	1.009	1.001	0.007	0.001	2.019
15	fc8 sm	Dol B	0.994	0.999	0.010	0.001	2.004
16	fc8 sm	Dol B	1.008	1.004	0.007	0.001	2.021
17	fc8 sm	Dol B	0.971	0.991	0.016	0.001	1.980
18	fc8 sm	Dol B	0.846	1.001	0.142	0.005	1.993
19	fc8 sm	Dol B	0.825	1.000	0.145	0.005	1.975
20	fc8 sm	Dol B	0.850	0.998	0.142	0.005	1.996
21	fc8 sm	Dol B	0.954	0.963	0.035	0.001	1.953
22	fc8 sm	Dol B	0.937	0.980	0.059	0.003	1.980
23	fd5 torr	Dol B	0.962	0.970	0.023	0.002	1.958
24	fd5 torr	Dol B	0.975	0.964	0.025	0.002	1.968
25	fd5 torr	Dol B	0.838	0.983	0.135	0.009	1.966
26	fd5 torr	Dol B	0.833	0.978	0.133	0.008	1.954
27	fd5 torr	Dol B	0.909	0.969	0.067	0.007	1.953
28	fd5 torr	Dol B	0.936	0.956	0.042	0.005	1.938
29	fd5 torr	Dol B	0.859	0.995	0.129	0.009	1.992
30	fd5 torr	Dol B	0.844	1.002	0.141	0.010	1.997
31	fd5 torr	Dol B	0.891	0.998	0.099	0.005	1.993
32	fd5 torr	Dol B	0.974	0.976	0.031	0.002	1.986
33	fd5 torr	Dol B	0.970	0.974	0.017	0.001	1.963
34	fd5 torr	Dol B	0.974	0.967	0.021	0.002	1.966
35	fd5 torr	Dol B	0.970	0.963	0.016	0.001	1.952
36	fd5 torr	Dol B	0.990	0.965	0.019	0.001	1.976
37	fd5 torr	Dol A	0.968	0.969	0.019	0.002	1.959
38	fd5 torr	Dol A	0.983	0.970	0.016	0.001	1.973
39	fd5 cos	Dol B	0.957	0.982	0.030	0.004	1.974
40	fd5 cos	Dol B	0.960	0.983	0.028	0.003	1.975
41	fd5 cos	Dol B	0.955	0.984	0.029	0.003	1.971
42	fd5 cos	Dol B	0.959	0.979	0.029	0.003	1.970
43	fd5 cos	Dol B	0.957	0.976	0.029	0.004	1.968
44	fd5 cos	Dol B	0.957	0.978	0.028	0.004	1.968
45	fd5 cos	Dol B	0.959	0.978	0.031	0.003	1.971
46	fd5 cos	Dol B	0.950	0.975	0.038	0.004	1.967
47	fd5 cos	Dol B	0.963	0.981	0.028	0.003	1.976
48	fd5 cos	Dol B	0.966	0.991	0.032	0.003	1.993
49	fd5 cos	Dol B	0.965	0.973	0.030	0.003	1.972
50	fd5 cos	Dol B	0.967	0.977	0.030	0.003	1.976
51	fd5 cos	Dol B	0.955	0.982	0.030	0.003	1.971
52	fd5 cos	Dol B	0.958	0.978	0.030	0.003	1.970

Point	Sample	Phase	Mg (at)	Ca (at)	Fe (at)	Mn (at)	total
53	fd5 cos	Dol B	0.971	0.979	0.029	0.004	1.983
54	fd5 cos	Dol B	0.953	0.985	0.035	0.003	1.976
55	fd5 cos	Dol B	0.966	0.980	0.030	0.003	1.980
56	fd5 cos	Dol B	0.930	0.981	0.071	0.006	1.988
57	fd5 cos	Dol B	0.909	0.987	0.068	0.007	1.971
58	fd5 cos	Dol B	0.929	0.978	0.051	0.004	1.963
59	fd5 cos	Dol B	0.946	0.986	0.046	0.004	1.984
60	fd5 cos	Dol B	0.920	1.007	0.056	0.004	1.988
61	fd5 cos	Dol B	0.897	1.012	0.068	0.006	1.986
62	fd5 cos	Dol B	0.910	1.000	0.070	0.007	1.988
63	fd5 cos	Dol B	0.928	0.979	0.056	0.004	1.967
64	fd5 cos	Dol B	0.910	0.986	0.083	0.007	1.986
65	fd5 cos	Dol B	0.904	0.976	0.090	0.006	1.976
66	fd5 cos	Dol B	0.931	0.980	0.070	0.004	1.987
67	fd5 cos	Dol B	0.958	0.982	0.032	0.004	1.976
68	fd5 cos	Dol B	0.960	0.970	0.032	0.003	1.965
69	fd5 cos	Dol B	0.945	0.992	0.049	0.006	1.993
70	fd5 cos	Dol B	0.895	0.976	0.086	0.007	1.964
71	fd5 cos	Dol B	0.964	0.985	0.033	0.003	1.986
72	fd5 cos	Dol B	0.963	0.985	0.031	0.003	1.982
73	fd5 cos	Dol B	0.956	0.982	0.032	0.003	1.973
74	fd5 cos	Dol B	0.904	0.994	0.086	0.006	1.991
75	fd5 cos	Dol B	0.973	0.987	0.030	0.003	1.992
76	fd5 cos	Dol B	0.963	0.988	0.030	0.003	1.986
77	fd5 cos	Dol B	0.968	0.989	0.029	0.002	1.988
78	fd5 cos	Dol B	0.963	0.989	0.034	0.004	1.990
79	fd5 cos	Dol B	0.902	0.981	0.087	0.006	1.976
80	fd5 cos	Dol B	0.900	1.001	0.086	0.007	1.994
81	fd5 cos	Dol B	0.903	1.008	0.071	0.009	1.991
82	fd5 cos	Dol B	0.853	1.011	0.133	0.010	2.009
83	fd5 cos	Dol B	0.921	0.999	0.056	0.004	1.982
84	fd5 cos	Dol B	0.232	1.751	0.037	0.015	2.036
85	fd5 cos	Dol B	0.920	1.016	0.040	0.004	1.981
86	fd5 cos	Dol B	0.940	0.995	0.049	0.004	1.989
87	fd5 cos	Dol B	0.927	1.009	0.056	0.006	2.000
88	fd5 cos	Dol B	0.919	0.996	0.050	0.005	1.970
89	fd1 gen	Dol A	0.978	0.978	0.017	0.001	1.974
90	fd1 gen	Dol B	0.984	0.975	0.019	0.002	1.979
91	fd1 gen	Dol B	0.976	0.978	0.017	0.002	1.973
92	fd1 gen	Dol B	0.964	0.978	0.018	0.002	1.962
93	fd1 gen	Dol B	0.959	0.967	0.017	0.002	1.944
94	fd1 gen	Dol B	0.967	0.976	0.018	0.002	1.963
95	fd1 gen	Dol B	0.977	0.980	0.018	0.002	1.976
96	fd1 gen	Dol B	0.977	0.978	0.018	0.002	1.975
97	fd1 gen	Dol B	0.971	0.976	0.018	0.002	1.968
98	fd1 gen	Dol B	0.971	0.985	0.019	0.002	1.976
99	fd1 gen	Dol B	0.974	0.983	0.020	0.002	1.979
100	fd1 gen	Dol B	0.979	0.977	0.019	0.002	1.978
101	fd1 gen	Dol B	0.968	0.973	0.024	0.002	1.967
102	fd1 gen	Dol B	0.960	0.982	0.034	0.003	1.980
103	fd1 gen	Dol B	0.940	0.972	0.045	0.003	1.962
104	fd1 gen	Dol B	0.920	0.969	0.061	0.004	1.954
105	fd1 gen	Dol B	0.925	0.974	0.070	0.004	1.973
106	fd1 gen	Dol B	0.915	0.972	0.067	0.004	1.958
107	fd1 gen	Dol B	0.919	0.973	0.062	0.003	1.957
108	fd1 gen	Dol B	0.904	0.987	0.084	0.004	1.980
109	fd1 gen	Dol B	0.874	0.989	0.106	0.006	1.975
110	fd1 gen	Dol B	0.875	0.990	0.107	0.007	1.979
111	fd1 gen	Dol B	0.888	0.990	0.096	0.007	1.983
112	fd1 gen	Dol B	0.870	0.983	0.115	0.007	1.974

Point	Sample	phase	Mg (at)	Ca (at)	Fe (at)	Mn (at)	total
113	fd1 gen	Dol B	0.837	0.998	0.141	0.010	1.987
114	fd1 gen	Dol B	0.830	0.998	0.141	0.010	1.979
115	fd1 gen	Dol B	0.846	1.004	0.134	0.009	1.992
116	fd1 gen	Dol B	0.901	0.989	0.087	0.008	1.984
117	fd1 gen	Dol B	0.911	0.985	0.068	0.008	1.972
118	fd1 gen	Dol B	0.934	0.990	0.050	0.006	1.979
119	fd1 gen	Dol B	0.935	0.982	0.042	0.004	1.963
120	fd1 gen	Dol B	0.836	0.999	0.138	0.010	1.983
121	fd1 gen	Dol B	0.844	1.000	0.130	0.010	1.986
122	fd1 gen	Dol B	0.877	1.007	0.099	0.010	1.993
123	fd1 gen	Dol B	0.874	0.999	0.093	0.008	1.975
124	fd1 gen	Dol B	0.884	0.984	0.085	0.007	1.960
125	fd1 gen	Dol B	0.886	0.977	0.079	0.005	1.946
126	fd1 gen	Dol B	0.882	0.985	0.094	0.006	1.969
127	fd1 gen	Dol B	0.860	0.992	0.109	0.011	1.973
128	fd1 gen	Dol B	0.908	0.982	0.065	0.007	1.963
129	fd1 gen	Dol B	0.891	0.982	0.074	0.009	1.956
130	fd1 gen	Dol B	0.910	0.990	0.070	0.007	1.978
131	fd1 gen	Dol B	0.868	1.001	0.092	0.007	1.968
132	fd1 gen	Dol B	0.922	0.987	0.046	0.003	1.961
133	fd1 gen	Dol B	0.934	0.986	0.043	0.003	1.967
134	fd1 gen	Dol B	0.951	0.983	0.039	0.003	1.977
135	fd1 gen	Dol B	0.927	0.987	0.041	0.003	1.958
136	fd1 gen	Dol B	0.936	0.992	0.038	0.003	1.971
137	fd1 gen	Dol B	0.925	1.007	0.044	0.004	1.981
138	fd1 gen	Dol B	0.931	0.996	0.041	0.003	1.971
139	fd1 gen	Dol B	0.939	0.995	0.033	0.003	1.970
140	fd1 gen	Dol B	0.947	0.989	0.036	0.003	1.976
141	fd1 gen	Dol B	0.933	0.984	0.039	0.004	1.961
142	fd1 gen	Dol B	0.931	0.986	0.041	0.004	1.963
143	fd1 gen	Dol B	0.937	0.995	0.038	0.004	1.974

Appendix 3 – ICP-ES

Analysed samples and results of the ICP-ES analyses for the most representative elements.

Sample	Description	Locality	Mn (ppm)	Fe (wt. %)	Sr (ppm)	Na (%)
fcx sm	Dol A	13	666	0.26	28	0.02
fcx sm	Dol B I	13	718	0.28	32	0.04
fcx sm	Dol B II	13	692	0.98	23	0.01
fc3 sm	Dol A	13	218	0.28	20	0.02
fc3 sm	Dol A	13	240	0.22	16	0.02
fc3 sm	Dol B	13	483	0.69	16	0.01
fc4 sm	Low. memb. Ds	13	458	0.34	36	0.02
fc2 sm	Low. memb. Ds	13	135	0.21	12	0.01
fc1 cas	Dol A	12	524	0.39	26	0.02
fc1 cas	Dol B	12	547	0.27	20	0.02
fc4 cas	Dol A	12	654	0.22	31	0.02
fc1 fg	Dol A	16	731	0.56	22	0.01
fc1 fg	Dol B	16	721	0.57	47	0.01
fc4 tun	Ls	10	142	0.12	146	0.01
fc5 tun	Low. memb. Ds	10	354	0.94	62	0.01
fc6 tun	Birdseye Ls	10	223	0.24	93	<.01
18 tun	Gx Ls	10	263	0.24	177	0.01
26 tun	Dol A	10	325	0.5	13	0.02
30 tun	Birdseye Ls	10	123	0.16	130	0.01
fc5 cruz	Low. memb. Ds	14	427	0.78	56	0.01
fc2c cruz	Birdseye Ls	14	151	0.21	134	0.01
fc3 cruz	Birdseye Ls	14	137	0.17	119	< .01
fc0 lann	Dol A	9	549	0.63	15	0.01
fc1 lann	Dol A	9	366	0.23	25	0.02
fc0 gen	Dol B	2	702	0.75	29	0.01
58 cos	Dol B	3	1159	1.41	30	0.01
59 cos	Dol A	3	1284	0.95	61	0.01
56 cos	Birdseye Ls	3	50	0.04	154	<.01
108 car	Dol A	20	644	0.91	57	0.03
109 car	Low. memb. Ds	20	538	1.07	90	0.02
110 gete	Dol A	19	1279	1.65	32	0.01
110 gete	Dol B	19	1371	1.77	14	0.01
fc1 gete	Low. memb. Ds	19	260	0.64	61	0.01
112 gete	Low. memb. Ds	19	543	0.87	45	0.01
fc2 barr	Low. memb. Ds	8	1090	1.53	133	0.01
fc2 barr	Low. memb. Ds	8	950	1.44	142	0.02
46 barr	Gx Ls	8	129	0.32	229	0.01
47 barr	Birdeye Ls	8	97	0.07	235	<.01
106 cueto	Dol B	25	1244	1.67	26	0.02
fc1 cueto	Low. memb. Ds	25	244	0.74	75	0.02
104 cueto	Low. memb. Ds	25	490	1.46	105	0.01
103 noc	Dol A	27	2496	4.58	52	0.03
fc2 noc	Low. memb. Ds	27	393	0.36	119	0.01
99 noc	Low. memb. Ds	27	340	0.46	120	0.02
100 noc	Low. memb. Ds	27	3043	4	43	0.02
fc1 noc	Birdseye Ls	27	204	0.11	281	0.01
101 noc	Birdseye Ls	27	144	0.09	249	<.01
102 noc	Gx Ls	27	149	0.09	245	0.01
91 mon	Dol A	28	1813	2.51	40	0.01
91 mon	Dol B	28	1348	1.82	52	0.01
96 mon	Dol A	28	1111	1.52	38	0.02
97 mon	Dol A	28	2088	2.56	27	0.03
fc1 mon	Low. memb. Ds	28	917	0.64	86	0.01

Sample	Description	Locality	Mn (ppm)	Fe (%)	Sr (ppm)	Na (%)
fc2 mon	Low. memb. Ds	28	808	0.62	96	0.02
fc3 mon	Low. memb. Ds	28	924	0.93	95	0.02
92 mon	Birdseye Ls	28	76	0.1	184	<.01
94 mon	Gx Ls	28	323	0.2	145	0.01
88 val	Dol A	29	1110	3.51	43	0.04
90 val	Low. memb. Ds	29	1430	0.68	95	0.01
89 val	Gx Ls	15	176	0.09	375	0.01
81 cam	Dol B	15	584	0.54	60	0.01
81 cam	Dol A	15	931	1.12	84	0.02
86 vill	Dol A	22	499	0.44	99	0.01
86 vill	Dol B	22	649	0.87	100	0.01
85 vill	Low. memb. Ds	22	318	0.62	100	0.02

Appendix 4 – Stable isotope analyses

Analysed samples and results of the stable isotope analyses.

Sample	Description	Locality	$\delta^{18}O$	$\delta^{13}C$	Sample	Description	Locality	$\delta^{18}O$	$\delta^{13}C$
4 cruz	Low. memb. Ds	14	-9.09	-0.56	fcx sm	Dol A	13	-4.66	-1.24
6 cruz	Dol A	14	-11.31	-1.07	fcx sm	Dol BI	13	-4.20	-1.12
6 cruz	Dol B	14	-11.75	-0.64	fcx sm	Dol BII	13	-5.15	-0.88
fc1 cruz	Gx Ls	14	-10.48	0.65	fcx sm	Dol A	13	-4.68	-1.26
fc1 cruz	Calcite vein	14	-14.44	0.78	fcx sm	Dol BI	13	-4.25	-0.89
fc2 cruz	Birdseye Ls	14	-8.55	-0.40	fc8(2) sm	Dol A	13	-4.54	0.62
fc2 cruz	Ls	14	-8.49	-0.82	fc8(2) sm	Dol B	13	-5.07	0.51
fc2 cruz	Calcite vein	14	-13.87	-2.62	fc8 sm	Dol A	13	-5.42	0.63
fc3 cruz	Birdeye Ls	14	-8.61	-0.67	fc8 sm	Dol B	13	-7.26	0.52
fc3 cruz	Birdseye Ls	14	-9.26	-0.65	fc7 sm	Dol A	13	-4.80	0.52
fc3 cruz	Calcite vein	14	-15.05	-3.73	fc6 sm	Dol A	13	-5.33	-0.04
fc4 cruz	Ls	14	-8.69	-0.37	fc3 sm	Dol B	13	-5.46	-0.96
fc5 cruz	Low. memb. Ds	14	-9.42	-0.93	fc3 sm	Dol A	13	-5.88	-0.90
fc7 cruz	Low. memb. Ds	14	-8.47	-0.01	fc3 sm	Dol A	13	-5.28	-0.99
fc1b cruz	Gx Ls	14	-8.52	0.69	fc2 sm	Low. memb. Ds	13	-7.02	-0.97
fc1b cruz	Calcite vein	14	-13.55	0.62	fc1 sm	Low. memb. Ds	13	-6.33	-0.59
fc6b cruz	Birdseye Ls (matrix)	14	-8.37	-0.49	fc1 sm	Low. memb. Ds	13	-5.87	-0.87
fc6b cruz	Birdseye Ls (cements)	14	-11.47	-0.32	fcx sm	Calcite	13	-7.14	-5.10
fc6a cruz	Dol A	14	-9.54	0.44	fc7 sm	Calcite	13	-8.96	-1.40
fc6a cruz	Dol B	14	-10.13	-0.58	fc1 gf	Dol A	16	-9.89	1.19
18 tun	Gx Ls	10	-10.04	0.08	fc1 fg	Dol A	16	-9.88	1.25
19 tun	Gx Ls	10	-8.75	1.04	fc1 fg	Dol B I	16	-10.00	1.19
20 tun	Gx Ls	10	-6.60	0.92	fc1 fg	Dol B I	16	-10.04	1.15
21 tun	Birdseye Ls (matrix)	10	-8.99	0.71	fc1 fg	Dol B II	16	-11.88	-0.07
21 tun	Birdseye Ls (cements)	10	-12.36	-0.32	fc1 fg	Dol B II	16	-11.71	-0.22
25 tun	Dol A	10	-5.75	0.22	fc3 fg	Dol A	16	-9.84	1.27
25 tun	Dol A	10	-5.94	0.07	fc3 fg	Dol B	16	-11.69	0.22
26 tun	Dol A	10	-5.33	1.09	fc0 lann	Dol A	9	-5.23	-0.49
26(2) tun	Dol A	10	-5.45	0.99	fc2 lann	Dol A	9	-4.98	-0.28
28 tun	Low. memb. Ds	10	-8.00	0.46	fc2 lann	Dol A	9	-4.72	-0.35
29 tun	Birdseye Ls	10	-9.64	0.02	fc2 lann	Dol A	9	-5.09	-0.28
30 tun	Birdseye Ls	10	-9.49	0.10	fc2 lann	Dol A	9	-5.10	-0.23
32 tun	Ls	10	-8.36	0.08	fc2 lann	Dol A	9	-4.96	-0.23
33 tun	Dol A	10	-6.17	1.03	fc2 lann	Dol B	9	-4.56	-0.32
fc4 tun	Birdseye Ls	10	-9.46	0.11	fc2 lann	Dol B	9	-4.82	-0.38
fc4 tun	Calcite vein	10	-13.20	-0.46	fc2 lann	Dol B	9	-4.93	-0.30
fc1b tun	Dol A	10	-5.42	0.94	fc3 lann	Dol A	9	-4.20	0.37
fc3b tun	Dol A	10	-4.75	0.03	fc3 lann	Dol B	9	-4.27	0.35
fc3b tun	Dol B	10	-4.15	-0.06	fc3 lans	Dol A	9	-4.78	-0.76
fc3b tun	Dol	10	-6.46	0.35	fc3 lans	Dol A	9	-5.51	-0.34
fc5 tun	Low. memb. Ds	10	-8.89	0.52	fc3 lans	Dol B	9	-6.50	-1.08
fc6 tun	Low. memb. Ds	10	-10.06	0.17	fc4 lans	Dol A	9	-5.36	-1.00
fc1 cas	Dol A	12	-4.72	-0.61	fc5 lans	Dol A	9	-5.33	-0.21
fc1 cas	Dol B	12	-4.29	-0.40	fc5 lans	Dol B	9	-5.03	-0.23
fc1 cas	Calcite	12	-13.05	-1.39	fc6 lans	Dol A	9	-5.93	-0.24
15 cas	Dol A	12	-5.74	-0.37	fc6 lans	Dol B	9	-5.43	-0.25
15 cas	Dol A	12	-5.72	-0.32	fc4 lans	Calcite	9	-7.48	-9.22
16 cas	Low. memb. Ds	12	-6.02	1.26	fc5 lans	Calcite	9	-7.67	-8.85
17 cas	Low. memb. Ds	12	-6.21	-0.08	fd3 gen	Dol A	2	-10.59	-0.20
fd1 via	Dol A	12	-7.82	1.02	fd3 gen	Dol B	2	-10.87	0.04
fd1 via	Dol B	12	-9.06	0.52	fd 1 gen	Dol A	2	-10.31	0.28
fcx sm	Dol A	13	-5.09	-0.77	fd 1 gen	Dol B	2	-10.81	0.17

Sample	Description	Locality	$\delta^{18}O$	$\delta^{13}C$
54 gen	Dol A	2	-9.81	0.29
54 gen	Dol B	2	-10.67	0.04
fd7 torr	Dol A	1	-10.56	0.15
fd7 torr	Dol B	1	-11.67	0.01
fd5 torr	Dol A	1	-10.25	0.03
fd5 torr	Dol B	1	-12.40	-0.15
fd2 torr	Dol A	1	-10.18	0.11
fd2 torr	Dol B	1	-10.25	0.04
55 tor	Dol B	1	-11.42	-0.21
56 cos	Birdseye Ls	3	-7.76	-0.65
57 cos	Low. memb. Ds	3	-10.45	-0.30
58 cos	Dol A	3	-11.94	0.36
58 cos	Dol B	3	-12.10	0.29
59 cos	Dol A	3	-13.29	-0.26
fd4 cos	Birdseye Ls (matrix)	3	-10.04	-0.55
fd4 cos	Birdseye Ls (cements)	3	-7.47	-0.30
fd5 cos	DolA	3	-12.83	0.46
fd5 cos	DolB	3	-12.67	0.51
81 cl	Dol A	15	-8.69	0.52
81 cl	Dol B	15	-8.91	0.73
82 cl	Dol A	15	-8.32	0.55
83 cl	Low. memb. Ds	15	-6.23	-1.57
81 cl	Dol A	15	-8.80	0.56
81 cl	Dol B	15	-9.25	0.69
fd3 cl	Low. memb. Ds	15	-6.88	-2.26
fd1 cl	Dol A	15	-9.09	0.53
fd1 cl	Dol B	15	-9.05	0.54
fd2 cl	Low. memb. Ds	15	-5.88	-0.21
fd2 cl	Calcite vein	15	-9.48	-0.48
fd3 cl	Black Ls	15	-6.02	-2.16
84 vil	Gx Ls	22	-6.17	0.87
85 vil	Low. memb. Ds	22	-5.14	-0.62
86 vil	Dol A	22	-8.50	0.45
86 vil	Dol B	22	-8.55	0.59
86 vil	Dol A	22	-8.47	0.34
fd1 vil	Low. memb. Ds	22	-5.31	-0.33
fd1(b) vil	Low. memb. Ds	22	-4.71	-0.69
fd2 vil	Dol A	22	-8.44	0.30
fd2 vil	Dol B	22	-8.58	0.31
fd3 vil	Gx Ls	22	-6.73	0.84
87 can	Low. memb. Ds	23	-6.12	-2.42
fd1 can	Gx Ls	23	-8.35	0.38
fd2 can	Low. memb. Ds	23	-5.49	-1.21
2 mon	Low. memb. Ds	28	-5.90	-0.58
91 mon	Dol A	28	-10.12	0.22
91 mon	Dol B	28	-11.36	-0.32
91 mon	Dol A	28	-9.68	0.04
91 mon	Dol B	28	-11.77	-0.04
92 mon	Ls	28	-10.00	-0.40
94 mon	Gx Ls	28	-10.56	-0.11
95/2 mon	Dol A	28	-5.84	0.58
95/2 mon	Dol B	28	-5.71	0.61
98 mon	Calcite vein	28	-11.98	-3.82

Sample	Description	Locality	$\delta^{18}O$	$\delta^{13}C$
99 noc	Low. memb. Ds	27	-6.16	-1.18
101 noc	Birdseye Ls	27	-9.51	-0.52
101 noc	Birdseye Ls	27	-9.45	-0.55
102 noc	Gx Ls	27	-10.68	0.95
102 noc	Calcite vein	27	-12.95	0.67
103 noc	Dol A	27	-8.63	-0.97
1 noc	Birdseye Ls	27	-10.32	-0.37
2 noc	Low. memb. Ds	27	-5.93	-0.45
104 cueto	Low. memb. Ds	25	-6.57	-1.52
105 cueto	Low. memb. Ds	25	-5.76	-0.19
106 cueto	Dol A	25	-7.61	0.48
106 cueto	Dol B	25	-8.96	0.47
107 cueto	Dol A	25	-5.08	1.38
1 cueto	Low. memb. Ds	25	-6.78	-1.25
88 val	Dol A	29	-7.95	-0.10
89 val	Gx Ls	29	-8.04	0.58
90 val	low. memb. Dol.	29	-7.59	0.05
108 car	Dol A	20	-7.26	0.85
108 car	Dol B	20	-8.80	0.68
109 car	Low. memb. Ds	20	-5.10	0.15
110 gete	Dol A	19	-8.81	0.82
110 gete	Dol B	19	-9.08	0.71
111 gete	Low. memb. Ds	19	-5.78	-0.57
112 gete	Low. memb. Ds	19	-9.25	-0.13
113 gete	Low. memb. Ds	19	-9.01	-0.20
40 barr	Birdseye Ls	8	-14.07	0.27
43 barr	Low. memb. Ds	8	-5.39	-0.66
44 barr	Low. memb. Ds	8	-6.67	-0.90
45 barr	Low. memb. Ds	8	-6.96	-0.16
fc2 barr	Low. memb. Ds	8	-7.03	-1.05
fc4 barr	Low. memb. Ds	8	-7.18	1.04
fc5 barr	Low. memb. Ds	8	-5.48	-0.41
46 barr	Gx Ls	8	-9.45	0.35
47 barr	Birdseye Ls	8	-10.05	0.24
48 barr	Low. memb. Ds	8	-9.17	-0.48
50 barr	Low. memb. Ds	8	-6.02	1.30
78 rab	Low. memb. Ds	7	-9.55	0.27
80 rab	Dol A	7	-7.68	0.96
80 rab	Dol A	7	-7.77	0.87
67 vilsec	Ls	6	-11.82	0.28
69 vilsec	Gx Ls	6	-8.82	1.46
70 vilsec	Low. memb. Ds	6	-8.03	0.01
63 rio	Ls	5	-8.93	0.80
65 rio	Ls	5	-10.21	-0.29
65 rio	Calcite vein	5	-12.24	-3.18
fd1 leo	Gx Ls	21	-7.47	1.58
fd2 leo	Low. memb. Ds	21	-4.96	-0.29
fd2 leo_2	Low. memb. Ds	21	-5.80	0.41
fc2 cin	Gx Ls	17	-8.48	1.30
fc6 cin	Ls	17	-10.05	-0.12
fc2 vdv	Ls	17	-9.30	0.17
fc5 vdv	Ls	18	-9.26	-0.21

Appendix 5 – Sr isotopic analyses

^{87}Sr/^{86}Sr and Sr concentration (ppm) of different carbonate cement phases and lithologies.

Sample	Description	Locality	^{87}Sr/^{86}Sr	Conc Sr (ppm)
fc102 noc	Gx Ls	Nocedo	0.71080	279.33
fc101 noc	Birdseye Ls	Nocedo	0.70966	232.24
fc99 noc	Low. memb. Ds	Nocedo	0.71020	145.33
fc97 mon	Dol B	Montuerto	0.70917	30.25
fc94 mon	Gx Ls	Montuerto	0.70973	160.42
fc92 mon	Ls	Montuerto	0.70928	210.97
fc91 mon	Dol A	Montuerto	0.70961	69.60
fc91 mon	Dol B	Montuerto	0.70985	65.07
fc86 vill	Dol A	Villanueva	0.70958	105.28
fc86 vill	Dol B	Villanueva	0.70919	129.87
fc85 vill	Low. memb. Ds	Villanueva	0.70954	114.94
fc84 vill	Gx Ls	Villanueva	0.70983	379.52
fc81 camp	Dol B	Campolongo	0.70959	73.94
fc82 camp	Gx Ls	Campolongo	0.70922	274.11
fc83 camp	Low. memb. Ds	Campolongo	0.70979	85.89
fc56 cosp	Birdseye Ls	Cospedal	0.70898	174.70
fc57 cosp	Low. memb. Ds	Cospedal	0.71065	29.25
fc58 cosp	Dol A	Cospedal	0.71068	43.68
fc58 cosp	Dol B	Cospedal	0.71002	37.33
fc2 barr	Low. memb. Ds	Barrios del Luna	0.70990	103.68
fc46 barr	Gx Ls	Barrios de Luna	0.70997	244.29
fc47 barr	Ls	Barrios de Luna	0.70914	259.90
fc50 barr	Low. memb. Ds	Barrios de Luna	0.71013	80.21
fc51 barr	Low. memb. Ds	Barrios de Luna	0.70980	251.29
fc52 barr	Dolomite vein	Barrios de Luna	0.71062	75.26
fc1a cruz	Gx Ls	Rodiezmo	0.71107	202.67
fc5 cruz	Low. memb. Ds	Rodiezmo	0.70967	64.64
fc4 tun	Ls	Tunnel Aralla	0.70894	156.29
fc5 tun	Ls	Tunnel Aralla	0.71187	65.88
fc1 sm	Low. memb. Ds	San Martín	0.70932	28.89
fc1 sm	Saddle Dol. cememt	San Martín	0.70942	24.24
fc2 sm	Low. memb. Ds	San Martín	0.70914	24.41
fc3 sm	Dol A	San Martín	0.71075	17.55
fc3 sm	Dol B	San Martín	0.71005	14.88
fc8 sm	Dol A	San Martín	0.71168	18.88
fc8 sm	Dol B	San Martín	0.71114	27.21
fc2 lann	Dol A	Láncara	0.71074	29.93
fc2 lann	Dol B	Láncara	0.71029	25.25
fc3 lann	Dol A	Láncara	0.71040	24.44
fd1_5	Dol A	Torrestio	0.71026	40.41
fd1_5	Dol B	Torrestio	0.71007	29.68
fd1 gen	Dol A	Genestosa	0.71024	38.68
fd1 gen	Dol B	Genestosa	0.71001	53.41
fc1 fg	Dol A	Fontún	0.71008	43.04
fc1 fg	Dol B I	Fontún	0.70919	25.91
fc1 fg	Dol B II	Fontún	0.70996	87.42
fc1 cas	Dol A	Casares	0.70991	30.00
fc1 cas	Dol B	Casares	0.70943	27.45
fc1 cas	Calcite cements	Casares	0.70982	24.82

^{87}Sr/^{86}Sr, ^{87}Rb/^{86}Sr, Sr and Rb concentrations (ppm) of different sylicoclastic and igneous rocks.

Sample	Lithology	Locality	^{87}Sr/^{86}Sr	Conc Sr (ppm)	^{87}Rb/^{86}Sr	Conc Rb (ppm)
Mora	Black shales	Mora de Luna	0.73645	99.797	4.326	148.78
Herreria	Sandstone	Irede de Luna	0.76203	24.271	8.823	73.62
Herreria	Siltstone	Irede de Luna	0.88093	35.124	29.595	353.29
Oville	Sandstone	Ciñera	0.73289	59.487	2.688	55.14
Oville	Siltstone	Ciñera	0.73819	197.01	4.27	288.41
Formigoso	Black shales	Barrios de Luna	0.76327	89.64	8.056	248.26
Formigoso	Black shales	Mina Providencia	0.75382	72.289	6.476	161.15
San Pedro	Sandstone	Mina Providencia	0.71045	63.456	0.199	4.35
San Pedro	Shales	La Vid	0.73136	150.21	4.397	227.78
Olleros	Sandstone	Peredilla	0.72072	140.4	2.305	111.72
San Emiliano	Sandstone	Mina Profunda	0.72212	91.838	2.113	66.99
San Emiliano	Siltstone	Mina Profunda	0.72799	59.941	3.325	68.74
Diorite		Ciñera-Matallana Basin	0.70918	403.1	0.139	19.3

Appendix 6 - Fluid inclusion microthermometry

Analysed samples and result of the fluid inclusions microthermometry. Sample localities are shown in Tab. 4.1, chapter 4, paragraph 4.2.

Sample	Inc. n.	Loc.	Lith.	Phase	T_M ice	T_M HH	T_H
fcx sm		13	BE Ls				
	p1f1	13		Dol B	-36.5	-4	102
	p1f2	13		Dol B	-36.5	-6	107
	p1f3	13		Dol B	-38		80
	p1f4	13		Dol B	-30		
	p1f5	13		Dol B			
	p1f6	13		Dol B	-36		70
	p1f7	13		Dol B	-37.8		88
	p1f8	13		Dol B	-38.5		89
	p1f9	13		Dol B	-38		84
	p1f10	13		Dol B	-38		90
	p1f11	13		Dol B			
	p1f12	13		Dol B			104
	p1f13	13		Dol B			83
	p1f14	13		Dol B	-30.5		81
	p1f15	13		Dol B	-30		83
	p1f16	13		Dol B	-30		81
	p1f17	13		Dol B	-30		92
	p1f18	13		Dol B	-30		83
	p2f1	13		Dol B	-30	-7	83
	p2f2	13		Dol B	-37		78
	p2f3	13		Dol B			
	p2f4	13		Dol B	-36		116
	p2f4bis	13		Dol B	-28		76
	p2f5	13		Dol B			
	p3f1	13		Dol B	-30		102
	p3f2	13		Dol B	-30		100
	p3f3	13		Dol B			106
	p3f4	13		Dol B	-27	-7	
	p3f5	13		Dol B			104
	p3f6	13		Dol B	-29		90
	p3f7	13		Dol B			70
	p3f8	13		Dol B	-39		90
	p3f9	13		Dol B	-29		78
	p3f10	13		Dol B			86
	p3f11	13		Dol B			90
	p3f12	13		Dol B	-36.5		30
	p3f13	13		Dol B	-26		95
	p3f14	13		Dol B	-31		100
	p3f15	13		Dol B	-30		90
	p4f1_1	13		Dol B	-29	-5	81
	p4f1_2	13		Dol B			77
	p4f1_3	13		Dol B			84
	p4f1_4	13		Dol B			78
	p4f2_1	13		Dol B			95
	p4f2_2	13		Dol B			94
	p4f1_3	13		Dol B			94
	p4f3	13		Dol B	-29		
	p4f4	13		Dol B			
	p4f5	13		Dol B	-29		84
	p4f6	13		Dol B	-29		84
	p4f7	13				-34		100
fc3 lann		9	Gx Ls				
	p1f1	9		Dol B	-36		100.5
	p1f2	9		Dol B	-36		96.6
	p1f3	9		Dol B	-29		
	p1f4	9		Dol B	-37.6		96
	p1f5	9		Dol B	-31	-3.5	75
	p1f6	9		Dol B	-32.5	-4	122
	p1f6bis	9		Dol B			96
	p1f7	9		Dol B	-40		
	p1f8	9		Dol B	-36		100
	p1f11	9		Dol B	-29		100
	p2f13 a	9		Dol B	-28.5		
	p2f13 b	9		Dol B	-35.5		95
	p2f13 c	9		Dol B	-35		113
	p2f14	9		Dol B	-39		151
	p2f15	9		Dol B	-39		
	p2f16	9		Dol B			
	p2f17	9		Dol B			
	p2f18	9		Dol B	-30		103
	p3f1	9		Dol B	-31.5		82
	p3f2	9		Dol B	-32		75
	p3f2bis	9		Dol B	-35	-9	80
	p3f3	9		Dol B	-32		88
	p3f3bis	9		Dol B	-36		72
	p3f4	9		Dol B	-32		93
	p3f5	9		Dol B	-33.5	-10	91
	p3f6	9		Dol B	-33.8		92
	p3f7	9		Dol B	-33.5		74
	p3f8	9		Dol B			94
	p3f9	9		Dol B	-37		70
	p3f10	9		Dol B	-32		97
	p3f11	9		Dol B	-37.5		93
	p3f12	9		Dol B	-37.5		84
	p3f13	9		Dol B	-24.7		
	p4f1	9		Dol B	-34		85
	p4f2	9		Dol B	-33.8		76
	p4f3	9		Dol B	-34		92
	p4f4_1	9		Dol B	-34.5		63
	p4f4_2	9		Dol B	-36.5		79
	p4f4_3	9		Dol B	-36.5		84
	p4f5_1	9		Dol B	-34		111
	p4f5_2	9		Dol B	-34		100
	p4f5_3	9		Dol B	-34		84
	p4f6	9		Dol B	-34.2		77
	p4f7	9		Dol B	-36		75
	p4f8	9		Dol B	-35		81
	p4f9	9		Dol B	-35		74
fc8 sm		13	Gx Ls				
	p1f1	13		Dol B	-24		103
	p1f2	13		Dol B	-24		104
	p1f3	13		Dol B			105
	p1f4	13		Dol B			100
	p1f5	13		Dol B			99.5
fc3 sm		13	L.M. Ds				
	p1f1	13		Dol B	-34		100
	p1f2	13		Dol B	-34		105
	p1f3	13		Dol B	-29		101
	p1f4	13		Dol B			
	p1f5	13		Dol B	-27		112
	p1f6	13		Dol B	-26		133
	p1f7	13		Dol B	-25	-2	104
	p1f8	13		Dol B			86
	p1f9	13		Dol B			101
	p2f1	13		Dol B	-26		90

Sample	Inc. n.	Loc.	Lith.	Phase	T_M ice	T_M HH	T_H
	p2f2	13		Dol B	-32		110
	p2f3	13		Dol B	-31		
	p2f4	13		Dol B			90
	p2f5	13		Dol B	-27		70
	p3f1	13		Dol B	-31.5		101
	p3f2	13		Dol B	-31	-5	108
	p3f3	13		Dol B	-27	-12	106
	p3f4	13		Dol B	-32		86
	p3f5	13		Dol B	-29.5		106
	p3f6	13		Dol B	-31		90
	p3f7	13		Dol B	-24.5		120
	p3f8	13		Dol B			
	p3f9	13		Dol B	-39		91
	p3f10	13		Dol B	-35		98
	p3f11	13		Dol B	-27		115
	p3f12	13		Dol B			88
	p3f13	13		Dol B	-29		98
	p3f14	13		Dol B	-26	-10	108
	p3fx	13		Dol B	-30	-5	
fc3 cas		12	Gx Ls				
	p1f1	12		Dol B			
	p1f2	12		Dol B	-39		
	p1f3	12		Dol B	-34		
	p1f4	12		Dol B	-30		
	p1f5	12		Dol B	-32		95
	p1f6	12		Dol B	-34	-5	101
	p1f7	12		Dol B			93
	p1f7a	12		Dol B			91
	p1f7b	12		Dol B			91
	p1f7c	12		Dol B			93
	p1f7d	12		Dol B			91
	p1f7e	12		Dol B			89
	p1f7f	12		Dol B			91
	p1f7g	12		Dol B			98
	p1f7h	12		Dol B			
	p1f7i	12		Dol B			99
	p1f7l	12		Dol B			103
	p1f7m	12		Dol B			91
	p1f7n	12		Dol B			96
	p1f7o	12		Dol B			101
	p1f8	12		Dol B	-34		98
	p1f9	12		Dol B	-29.5		108
	p1f10	12		Dol B	-31		99
	p1f11	12		Dol B	-39		97
	p1f12a	12		Dol B			98
	p1f13	12		Dol B			
	p1f14	12		Dol B	-31.5		96
	p1f15	12		Dol B	-30		
	p1f16	12		Dol B	-37		97
	p1f16a	12		Dol B	-36		98
	p1f16b	12		Dol B			92
	p1f17	12		Dol B	-38		81
	p1f18	12		Dol B	-36.5		103
	p1f18a	12		Dol B	-37		
	p1f18b	12		Dol B	-27.5		95
	p1f18c	12		Dol B	-28		95

Sample	Inc. n.	Loc.	Lith.	Phase	T_M ice	T_M HH	T_H
	p1f18d	12		Dol B	-36		103
	p1f19	12		Dol B	-30	-2	100
	p1f20	12		Dol B	-36		95
	p2f1	12		Dol B	-28.5		97
	p2f2	12		Dol B	-34		95
	p2f3	12		Dol B	-34		94
	p3f1	12		Dol B	-36.5		100
	p3f2	12		Dol B	-36.5		100
	p3f2a	12					91
	p3f2b	12					93
	p3f2c	12					95
	p3f2d	12					96
fc1 fg		16	Gx Ls				
	f1	16		Dol B			78
	f3a	16		Dol B	-26.5		97
	f3b	16		Dol B			107
	f5a	16		Dol B	-26		98
	f5b	16		Dol B			100
	f5c	16		Dol B			104
	f5d	16		Dol B			110
	f8b	16		Dol B			118
	f8c	16		Dol B	-24		106
	p6f8	16		Dol B	-25		102
	p6f9	16		Dol B	-25		102
	p6f10	16		Dol B			105
	f10a	16		Dol B			98
	f10b	16		Dol B	-27		105
	f10c	16		Dol B	-28		120
	f11a	16		Dol B	-25		120
	f11b	16		Dol B	-27		130
	f11c	16		Dol B	-26		130
	f6	16		Dol C	-2		168
	f7	16		Dol C	-1		143
	f8a	16		Dol C	-2		145
	f2	16		Dol C	-3		171
	f4a	16		Dol C	-3		175
	f4b	16		Dol C			175
	f4c	16		Dol C			165
	f4d	16		Dol C			165
	f4e	16		Dol C			165
	f4f	16		Dol C			170
	f4g	16		Dol C			170
	p6f1	16		Dol C	-4.5		126
	p6f2	16		Dol C			130
	p6f3	16		Dol C			109
	p6f4	16		Dol C			132
	p6f5	16		Dol C			145
	p6f6	16		Dol C			134
	p6f7	16		Dol C			135
fc3 fg		16	Gx Ls				
	f12a	16		Dol C			160
	f12b	16		Dol C			>170
	f13	16		Dol C			98
	f9	16		Dol C	-1		

Appendix

List of abbreviation

N: North

E: East

S: South

W: West

°C: degree Celsius

t: temperature in °C

°K: degree Kevin

T: temperature in °K

P: pressure

s: seconds

kW: kilowatts

kV: kilovolts

mA:milliampers

MPa: Mega Pascals

ppm: part per million

CAI: Conodont alteration index

CL: Cathodoluminescence

XRD: X-ray diffraction

λ: wavelength

θ: angle of diffraction

d: lattice spacing

N: mole percent of $CaCO_3$

OR: Degree of order

Å: Angstrom

k_e: distribution coefficient

ICP-AES: Inductively coupled plasma atomic emission spectrometer

SEM: Scanning electron microscope

EDS: energy discriminating system for X-ray micro-analysis

EMPA: Electron microprobe analysis

WDS: wavelength dispersive spectroscopy

α: fractionation factor

R_A: the heavy/light isotopic ratio for phase A

spl: sample

st: standard

σ: standard deviation

PDB: *Belemnita americana* of the Peedee Formation in South Carolina

V-PDB: Vienna PDB

SMOW: Standard Mean Ocean Water

DIC: dissolved inorganic carbon

FI: fluid inclusions

T_H: homogenization temperature

T_M (ice): ice melting temperature

T_M (hh): hydrohalite melting temperature

T_e: eutectic temperature

eq. mass %: equivalent mass percentage

φ^{liq}: liquid7vapour fraction

Dol A: replacive dolomite

Dol B I: void fillinb dolomite generation I

Dol B II: void-filling dolomite generation II

Dol C: late dolomite cement

Ds: dolostone

EDs: epigenetic dolostone

Ls: limestone

MVT: Mississippi Valley Type

MM: microbial mat

BE: birdseyes

Epi: epiphyton

Ps: pisolite

Dx: dolomite

SDx: saddle dolomite

Cx: calcite

FCx: fibrous calcite

Gx : glauconite

Hiermit erlkäre ich, Fabio Lapponi, dass ich die vorgelegte Dissertation selbst verfasst und mich dabei keiner anderen als den von mir ausdrücklich bezeichneten Quellen und Hilfmittel bedient habe.

Weiterhin erlkäre ich, dass ich an keiner anderen Stelle ein Prüfungsverfahren beantragt bzw. die Dissertation in dieser oder anderen Form bereits anderweitig als Prüfungsarbeit verwendet oder einer anderen Fakultät als Dissertation vorgelegt habe.

Heidelberg, den 04.09.2007